Imperial College of Science, Technology and Medicine
Department of Mechanical Engineering

On dissipation intermittency and its modelling in terms of turbulence-chemistry interactions

Pankaj Yograj Vaishnavi

Submitted in part fulfilment of the requirements for the degree of
Doctor of Philosophy in Mechanical Engineering at
Imperial College London, December 2008

Abstract

A key challenge in combustion research is to model complex turbulence-chemistry interactions during extinction and re-ignition of non-premixed flames. These are caused when the scalar dissipation, χ, is above (or below) certain limits such that the diffusive temperature flux from the flame is much larger (or smaller) than chemical heat-release. χ is characterised by its small-scale intermittency, i.e. large fluctuations in χ are frequent and localised in space. This behaviour severely constrains its resolvability and has implications for modelling extinction/re-ignition processes. Scalar field statistics from the direct numerical simulation (DNS) database of a spatially-evolving, turbulent jet flame with multi-step chemistry by Pantano (2004) are studied using three different approaches, namely analysis of dissipation-spectra, direct investigation of dissipation contours and spatial filtering of the instantaneous dissipation signals. Out of these the spatial filtering method is found to be most suited for capturing the intermittent dissipation length scales and an Re_{δ}^{-1} scaling is proposed for 'adequate' χ-resolution in turbulent jet flame experiments/simulations. Furthermore, a Multiple Mapping Conditioning (MMC) approach with two reference variables is used to model extinction/re-ignition in inhomogeneous turbulent jet flames. A new sub-model for the convective velocity term is employed that does not need to presume Gaussian statistics and consistent closures for MMC drift and diffusion coefficients are derived. Effect of temperature fluctuations on scalar diffusivity is also accounted for. Joint scalar PDFs, conditional dissipation and conditional species predictions from MMC, and also conditional species concentrations from conventional singly- and doubly-conditioned moment closure (CMC1 and CMC2), are assessed against the Pantano DNS database. CMC1 expectedly over-predicts extinction and does not capture re-ignition, whereas extinction and re-ignition effects on species concentrations (including atomic H-radical) are captured satisfactorily using CMC2 and MMC. However, MMC scores over CMC2 because models for the joint scalar PDF evolution and conditional dissipation are self-contained in the former.

Acknowledgements

I would like to express my sincere gratitude to my supervisor, Prof. Andreas Kronenburg, for his guidance, encouragement, understanding and professionalism.

Many thanks are due to all my research colleagues, especially Jeremy, Philipp and the good old Sandeep, who made my last 3 and a half years at 503 MECH very fruitful and fun.

This work would not have been possible if it were not for the emotional support of my near and dear ones, especially my parents, to whom I am dedicating this work.

And finally many thanks and a lot of gratitude is due to Kshiti for putting up all these years.

mātaraṁ pitaraṁ cha samyajāmi

iyaṁ visṛṣṭiryata’ābabhūva yadi vā dadhé yadi vā na |
yo’asyādhyakṣaḥ paramé vyomantso’aṅga véda yadi vā na véda ||

Ṛgvéda 10.129.7

Contents

List of Tables

List of Figures

Nomenclature

Roman Symbols

A_r	Arrhenius pre-exponential constant for one-step reaction
$\mathcal{A}_o$	Characteristic dimensional reaction rate
$\mathcal{A}_i$	Dimensional pre-exponential Arrhenius parameter
A_i	Non-dimensionalised pre-exponential Arrhenius parameter
A_k	MMC drift coefficient
a_k	Velocity contribution to the MMC drift coefficient
a	Modelled velocity contribution for $k = 1$
$a_{p,q}^n$	Discretised value of a
$a_{\iota\varepsilon}$	Number of atoms of element ε in species ι
B_{kl}	MMC diffusion coefficient
B_{kl}^0	Temperature invariant MMC diffusion coefficient
C_{p_ι}	Specific heat at constant pressure for ι^{th} species
C_p	Specific heat at constant pressure of the gaseous mixture
C_ϕ	Mechanical to scalar time scale ratio
C_{ϕ_I}	Cumulative distribution of I^{th} scalar
C_θ	Cumulative distribution of the reference scalar
c_s	Acoustic propagation velocity in air
c_1, c_2	Acoustic propagation velocity in fuel and air streams
C_{pO_o}	Reference specific heat of oxygen at 298 K
C_ι	Non-dimensional concentration of ι^{th} species

C_G	Third-body concentration
$c_I, c_{II}, c_{III}, c_{IV}$	Global reaction sub-step coefficients
C_Z	Normalised cross-stream correlation coefficient in scalar turbulence
c_α	MMC modelling parameter based on conditional variance of dissipation
C_f	Scaling coefficient for c_α
D_I	Molecular diffusivity of the I^{th} scalar
D	Molecular diffusivity of the mixture fraction (or conserved scalar)
D_Z	One-dimensional dissipation spectrum
$\mathbb{D}_1$	Discretised drift coefficient using central-differencing
$\mathbb{D}_2$	Discretised diffusion coefficient using central-differencing
$e_{q,1}, e_{y,1}$	Conventional e_q, e_y terms for singly-conditioned CMC
$e_{q,2}, e_{y,2}$	Conventional e_q, e_y terms for doubly-conditioned CMC
$e_{q,MMC}, e_{y,MMC}$	Generalised e_q, e_y terms in MMC context
E_i	Activation energy for i^{th} global reaction sub-step
e_o	Regularisation parameter for H_2 concentration
E_Z	One-dimensional energy spectrum
$\mathcal{F}$	Normalised (unbounded) function of C, H and O mass-fractions
$\mathcal{F}_1, \mathcal{F}_2$	Fuel and air stream values of $\mathcal{F}$
f_{corr}	Stoichiometric sensible enthalpy correlation function
g_i	Body force along i^{th} coordinate direction
G_ι	Catalytic efficiency of ι^{th} species
$\mathcal{H}_\iota$	Enthalpy of the ι^{th} species
$\mathcal{H}$	Enthalpy of the gaseous mixture
$\mathcal{H}_1, \mathcal{H}_2$	Enthalpy values in the fuel and air streams
$\mathcal{H}_\iota^f$	Enthalpy of formation of the ι^{th} species
h_{s_ι}	Sensible enthalpy of the ι^{th} species
$h_s, \hat{h}_s$	Sensible enthalpy of the gaseous mixture, normalised value in $[0, 1]$
$h_{s_{max}}$	Maximum sensible enthalpy at stoichiometric
$\hat{h}_s^e$	Equilibrium profile of the sensible enthalpy
$\langle \hat{h}_s''^2 \vert \eta_1 \rangle$	Conditional variance of normalised sensible enthalpy

H	Jet nozzle width
h	Pilot width
$\imath$	$\sqrt{-1}$
J_i^I	Diffusive flux of the I^{th} scalar along the i^{th} coordinate direction
k_i	Reaction rate constant of the i^{th} global sub-step
K_{II}, K_{IV}	Additional reaction rate constants for steps (II) and (IV)
k_y	Cross-stream wavenumber in scalar turbulence
k^*	Normalised wavenumber using the Batchelor/Obukhov-Corrsin scale
k_{peak}	Wavenumber at peak in the dissipation spectrum
$k_{7.3\%}$	Wavenumber at 7.3% of the peak in the dissipation spectrum
L_{β_f}	Dissipation length scale at β_f fraction of the 'fully-resolved' limit
$L_{0.61}, L_{0.75}$	L_{β_f} values at $\beta_f = 0.61, 0.75$
L_λ	Taylor micro-scale
L_{integral}	Integral length-scale
L_1, L_2, L_3	Dimensions of the DNS grid along x-, y- and z-coordinates
l_T	Characteristic energy containing turbulent length-scale
l_c	Clustering parameter for reference-space grid
M_ι	Dimensional molecular weight of ι^{th} species
$M_\varepsilon, M_C, M_H, M_O$	Molecular weight of the $\varepsilon = \mathrm{C, H, O}$ elemental species
M_o	Reference molecular weight of Oxygen
$\bar{M}$	Average molecular weight of the gaseous mixture
m	Exponent of non-dimensionalised temperature ($= 0.7$)
n_s, n_r	Number of all scalars and major scalars (or reference variables)
n_ξ	Number of points on the reference grid ($= 64$)
N_{ij}, N_{IJ}	Scalar dissipation variable for $(i,j)^{th}$ and $(I,J)^{th}$ scalar pairs
N_s	Stoichiometric value of the scalar dissipation rate
N_{ij}^0	Temperature-invariant scalar dissipation variable
$\langle N_{11}^{0''2} \vert \eta_1 \rangle$	Conditional variance of scalar dissipation of mixture fraction
N_x, N_y, N_z	Number of points in the DNS grid along x-, y- and z-axes

N_T	Number of DNS time-steps for ensemble averaging
p	Static pressure
Δp	Pressure change due to acoustic disturbance
p_{real}	Constant dimensional pressure for fuel and air streams
$\mathbb{P}$	turbulent production via mean scalar gradient in the scalar variance budget
P_Z	marginal probability density function of mixture fraction
$P_{\boldsymbol{\theta}}$	Joint distribution of reference variables (bi-variate Gaussian)
$P_{\boldsymbol{\phi}}$	Joint scalar distribution
$P_{\boldsymbol{\phi}_{maj}}$	Joint distribution of major scalars
$P_{\mathbf{X}}$	Joint distribution of surrogate scalars
Q_ι, Q''_ι	Singly-conditioned mean and conditional fluctuation of ι^{th} species
$\mathcal{Q}_\iota, \mathcal{Q}''_\iota$	Doubly-conditioned mean and conditional fluctuation of ι^{th} species
R	Universal gas constant, $8.314 J\ mol^{-1}\ K^{-1}$
R_Z	Non-normalised cross-stream correlation coefficient in scalar turbulence
r	Cross-stream separation
$\mathcal{S}$	Turbulent strain rate
t	temporal coordinate
Δt	Lagrangian time-interval
t_o	Reference time-scale for non-dimensionalisation
T	Non-dimensionalised temperature
T_o	Reference temperature of fuel stream ($= 298K$)
T_{adia}, T_f	Adiabatic flame temperature ($= 2022K$), and its non-dimensionalised value
T_A	Activation temperature for one-step, infinitely fast, irreversible reaction
T^e	Equilibrium temperature profile
T_1, T_2	Non-dimensionalised fuel and air stream temperatures
$\mathbb{T}_I$	Turbulent transport term in the scalar variance budget
$\boldsymbol{u}$	Convective velocity vector
u_i, u_j	Velocity components in i^{th} and j^{th} coordinate directions
u_x, u_y, u_z	Velocity components in Cartesian coordinate directions

u'	RMS value of turbulent velocity fluctuations
u_K	Eddy turnover speed of Kolmogorov eddies
$\boldsymbol{U}$	Velocity conditioned on the reference space
U_x	Downstream velocity conditioned on the reference space
$\boldsymbol{U}^{(0)}$	Ensemble mean velocity
$\boldsymbol{U}_1^{(1)}, \boldsymbol{U}_2^{(1)}$	Coefficients for velocity model linear in the reference space
U_0, U_1	Coefficients of the velocity model linear in composition space
U_c, U_p, U_j	Velocities of efflux of the coflow, pilot and main jet
Δu	Difference between jet and coflow velocities
V	Characteristic velocity
v_F	Chemical coefficient of fuel in one-step irreversible reaction
$v_{\mathrm{O_2}}$	Chemical coefficient of oxygen
$v_{\mathrm{CO_2}}$	Chemical coefficient of carbon dioxide
$v_{\mathrm{H_2O}}$	Chemical coefficient of water
w_ι	Mass of the ι^{th} species in the gaseous mixture
w	Total mass of the gaseous mixture
$\mathcal{W}_I, \mathcal{W}_{II}, \mathcal{W}_{III}, \mathcal{W}_{IV}$	Reaction rates of global sub-steps
w_f	Filter width
W_I	Chemical source for I^{th} scalar conditioned on reference space
$\mathbf{x}$	Position vector
Δx	Streamwise grid size
x_i, x_j	i^{th} and j^{th} coordinate positions
x_c, y_c	Coordinates along the jet centre-line
$\mathbf{X}$	Set of all scalar mapping functions
X_I	Mapping function for the I^{th} scalar
X_I''	Conditional fluctuation about X_I in reference space
$X_{I_{p,q}}^n$	Discretised mapping function value for the I^{th} scalar
X_1^*, X_1^*	Stochastic values of surrogate scalars
y	Cross-stream coordinate direction

z	Spanwise coordinate direction
Z, Z_s	Mixture fraction/Conserved scalar and its stoichiometric value
$Z_\varepsilon, Z_C, Z_H, Z_O$	Conserved mass-fractions of elements $\varepsilon = \mathrm{C}, \mathrm{H}, \mathrm{O}$
Z_f	Filtered mixture fraction value

Greek Symbols

α	Thermal diffusivity constant
β_r	Temperature dependence exponent in the one-step irreversible reaction
β_i	Temperature dependence exponent in the i^{th} global reaction sub-step
β_m	Fraction of the local dissipation peak value
β_f	Ratio of the filtered value with the 'fully-resolved' dissipation limit
β_Δ	Value of β_f at grid size
γ	Adiabatic index
$\boldsymbol{\delta}_{ij}$	Kronecker delta function
$\delta_{0.5}$	Half-width of the jet
δ, δ_o	Non-dimensionalised and dimensional diffusion thickness of the flame
Δ_{3d}	Local grid size for three-dimensional DNS grid
$\Delta_x, \Delta_y, \Delta_z$	One-dimensional grid discretisations along the Cartesian axes
Δ	Local grid size in the $x-y$ plane
$\Delta_{x,f}, \Delta_{y,f}$	Filter widths in x- and y-coordinates
ϵ	viscous dissipation rate
ϵ_{max}	Largest fluctuations of the viscous dissipation rate
ζ_1, ζ_2	Sample space variables of ϑ_1, ϑ_2
η_K	Kolmogorov length-scale
$\eta_{K_{min}}$	Smallest possible values of the Kolmogorov scale
η_Z, η_{Z_s}	Characteristic dissipation length-scale and its spectral estimate
$\boldsymbol{\eta}$	Sample space of all scalars
$\boldsymbol{\eta}_{maj}, \boldsymbol{\eta}_{min}$	Sample spaces of major and minor scalars
η_i, η_j	Sample space variables of i^{th} and j^{th} major scalars
η_1, η_2	Sample space variables of mixture fraction and sensible enthalpy
$\boldsymbol{\theta}$	Reference space
θ_1, θ_2	Reference variables for mixture fraction and sensible enthalpy
θ_1^*, θ_2^*	Stochastic values of the reference variables

$\vartheta, \vartheta_1, \vartheta_2$	Arbitrary turbulent quantities
κ	Turbulent kinetic energy
$\lambda_{2d}, \lambda_{3d}$	Planar- and volumetric-estimates of dissipation scales from level-sets
Λ	Reynolds number scaling coefficient for intermittent dissipation scales
Λ_0	Reynolds number scaling coefficient for mean dissipation scales
Λ_{3d}	Reynolds number scaling coefficient for corrected dissipation layer thicknesses
μ	Dynamic viscosity
μ_χ	Ensemble average of scalar dissipation
ν	Kinematic viscosity
ν_o	Reference value of kinematic viscosity at $298K$
$\boldsymbol{\xi}$	Sample space of reference variables
ξ_1, ξ_2	Reference sample spaces for mixture fraction and sensible enthalpy
ξ_{1_p}	Discretised value on the reference grid
$\Delta\xi_p, \Delta\xi_q$	Local grid sizes on the reference grid
$\Delta\xi_{n_\xi}, \Delta\xi_0$	Grid sizes at the extremities of the reference grid
π	$\simeq 3.141592$
ρ	Density of the gaseous mixture
ρ_o	Reference density value of air at $298K$
ρ_ξ	Density conditionally averaged on the reference space
ϱ	Out-of-plane angle of the scalar gradient vector from planar dissipation layers
$\sigma_0, \sigma_1, \sigma_2$	Linear coefficients for the planar model for conditionally averaged temperature
σ_χ	Standard deviation of the scalar dissipation rate
Σ_I	Chemical production rate per unit mass conditioned on the reference space
τ	Turbulent eddy-turnover time scale
τ_c	Chemical time scale
τ_K	Kolmogorov time scale
τ_{res}	Scalar residence time scale
τ_{ij}	Reynolds stress tensor
$\boldsymbol{\phi}$	Set of all scalars

$\boldsymbol{\phi}_{maj}, \boldsymbol{\phi}_{min}$	Sets of major and minor scalars
ϕ_I	I^{th} scalar
ϕ_ι	ι^{th} species
ϕ_ι^e	ι^{th} species dependence on mixture fraction at equilibrium
Φ	Fuel-air equivalence ratio
φ	Exponential function in reference space
χ	Scalar dissipation rate of the mixture fraction
χ_{ij}	Scalar dissipation of any $(i,j)^{th}$ combination of major scalars
$\langle \chi_y \rangle$	Ensemble average of cross-stream scalar dissipation
$\langle \chi_y \rangle_s$	Spectral estimate of $\langle \chi_y \rangle$
χ_{max}	Global maximum of scalar dissipation
χ_{loc}	Local maximum of scalar dissipation
$\chi_{f,peak}$	Filtered scalar dissipation
$\chi_{\Delta,peak}$	Grid-resolved scalar dissipation
$\chi_{0,peak}$	'Fully-resolved' estimate of scalar dissipation
ψ	Statistical correlation coefficient
ω_H	Chemical source term for enthalpy of the mixture
ω_{h_s}	Chemical source term for sensible enthalpy of the mixture
ω_I	Chemical source term for the I^{th} scalar

Subscripts

DNS	Value from the DNS database
f	Filtered value
i	Global reaction sub-step index
I	Scalar field index
i, j	Major scalar indices
i, j, k	Coordinate indices
k, l, p, q	Reference manifold indices
MMC	Value from the MMC computation
o	Reference thermodynamic value for non-dimensionalisation
s	Estimate from dissipation spectra (used for mean values)
s	Stoichiometric value (used for instantaneous values)
ε	Chemical element index
ι	Minor scalar (chemical species) index
$\boldsymbol{\xi}$	Reference space
$\boldsymbol{\phi}$	Scalar space
$1, 2$	Fuel, Oxidiser stream index

Superscripts

0	Invariance in the reference manifold
e	Equilibrium concentration
n	Discrete n^{th} streamwise step
n'	Intermediate value after explicit sub-stepping at n

Operators

boldface	Vector

$\boldsymbol{\nabla}$	Gradient operator
$\delta_x, \delta_y, \delta_z$	Difference operators in coordinate directions
$\langle \ \rangle, -$	Statistical ensemble average
$\langle \ \vert \rangle$	Statistical conditional average
$\sim$	Density-weighed average
$'$	Superimposed Reynolds fluctuation
$''$	Superimposed Favre fluctuation

Shorthands

atm	Atmospheres
CMC	Conditional Moment Closure
CDF	Cumulative Distribution Function
Da	Damköhler number
DNS	Direct Numerical Simulation
FCM	Fast Chemistry Model
GAUSS	Gaussian distribution
J	Joule
K	Kelvin
Ka	Karlovitz number
Le	Lewis number
LES	Large Eddy Simulation
LFM	Laminar Flamelet Model
mm	Millimetres
mol	Mole
MMC	Multiple Mapping Conditioning
PDF	Partial Differential Equation
PDF	Probability Density Function
Pr	Prandtl number for air
Re	Jet-exit Reynolds number

Re_δ	Outer-scale turbulent Reynolds number
Re_λ	Taylor-scale turbulent Reynolds number
RMS	Root Mean Square
Sc	Schmidt number
STP	Standard Temperature and Pressure

Chapter 1

Introduction

1.1 Motivation

Combustion is one of the most important methods of harnessing energy (Peters, 2000). With the major contribution to the world's energy supply stemming from the use of fossil fuels, combustion is a primary technology for the generation of electricity and is also utilised in propulsion related devices. In spite of the on-going innovations in various other types of renewable/non-renewable energy sources, the contribution of fossil fuels to the global energy production is not expected to reduce in the near or mid-term future (Energy Review Report, 2006). It is also becoming increasingly evident that the products of Hydrocarbon combustion are responsible for a series of large-scale deleterious effects on the human environment. Various environmental and health hazards such as ozone depletion, smog, acid rains, respiratory ailments etc of major pollutants like nitrogen/sulfur oxides (NOx/SOx) or particulates are well-documented (Beer, 2000). Besides these, there is a steadily mounting body of scientific evidence (Energy Review Report, 2006) for global warming and climate change linked to anthropogenic carbon dioxide (CO2) emissions. In view of all the present and future combustion applications and their environmental impact, a deep understanding of the basic mechanisms of combustion is essential to improve the performance, reliability, safety, and environmental impact of combustion systems.

Various topics in combustion theory such as the gaseous deflagrations, effects of detailed chemistry, hydrodynamic theory, the interplay between the intrinsic instabilities and noise in wrinkled flames have seen a lot of progress (Bilger *et al.*, 2005; Buckmaster *et al.*, 2005; Westbrook *et al.*, 2005). Other aspects of study include anomalous characteristics of deflagrations in nonuniform flows, triple flame structures, combustion of solid propellants, theory of ignition, theory of gaseous detonations and turbulent combustion to name a few. The technological need for clean energy production, efficient propulsion and the associated environmental hazards has driven most of the research and development in this field to date. Supersonic propulsion and new methods of combustion using bio-derived and reduced carbon-content fuels are seen (Buckmaster *et al.*, 2005; Williams, 1994) as new thrust areas of application. In particular, the latter application will continue to complement the technological advancements in alternative energy sources (Energy Review Report, 2006).

Fluid turbulence is one of the oldest unresolved problems of classical mechanics and its complete physical description remains problematic in spite of numerous efforts of modern engineering science (Leslie, 1972; Bray, 1996). A major source of difficulty in the mathematical treatment and simulation of fluid-flow phenomena is the presence of very large ranges of length- and time-scales that occur even in nominally simple problems. Examples include the presence of a few molecular mean-free paths thick shock-wave region ahead of a wedge in supersonic flow or the bright-yellow soot formation zone in a standard laboratory bunsen flame. These phenomena are analogous in that the thickness of the aforesaid regions is very much smaller than their extent in other two spatial dimensions. Therefore, such flow events represent a wide range of characteristic spatial scales. Turbulence presents the ultimate hurdle of this type, because the fluid-flow in the state of turbulence is filled with simultaneously existing and interacting eddies and vortex tubes, of all sizes and in all three dimensions, representing local flow events on a very large range of scales of measurement/resolution (Cant, 1999). On the other hand, combustion in laminar (non-turbulent) flows is an intrinsically complex process involving a large range of chemical length and time scales. Some of the crucial chemical kinetics phenomena controlling flames take place in short periods over thin layers and are associated with very large gradients of reacting species concentration, temperature and density. Thus, the addition of chemical kinetics and thermodynamics (heat-release) to turbulent flow further complicates the problem due to the introduction new small scales of combustion, which in turn interact with the mixing scales of turbulence (Poinsot & Veynante, 2001).

The phenomenon of turbulence is ubiquitously present in all practical combustors (Libby & Williams, 1980; Pope, 1985; Kuznetsov & Sabelnikov, 1989; Klimenko & Bilger, 1999; Peters, 2000; Klimenko, 2003*b*; Bilger *et al.*, 2005), ranging from simple devices like a blow torch or domestic boilers to more complex industrial burners for process heating, spark-ignition/Diesel car engines, air-borne/stationary gas turbines, etc. The energy output of these combustion devices spans six orders-of-magnitude from 10^{-1} kWh to 10^{2} MWh (Cant & Mastorakos, 2008). Only a fraction of this order-of-magnitude increase in energy output is achieved by increasing the volume and the pressure rating of the combustor, while increasing the rate of the chemical reaction underlying the combustion process accounts for the rest of the energy increment. The evident increase in combustion efficiency per unit volume is a direct consequence of the increased rate of mixing and thermal transport caused by the turbulence in the working fluid of the combustor (Cant & Mastorakos, 2008). Therefore, understanding (and modelling) the complex interaction between fluid turbulence and the kinetics and thermodynamics of chemical reactions is a central pre-requisite for designing modern and efficient combustion chambers. Due to the mathematically intractable nature of the problem of turbulence, it would have been extremely difficult to make any progress in this matter without the availability of the modern tools of computational fluid dynamics (CFD) and turbulent combustion modelling to engineers (Libby & Williams, 1980; Kuznetsov & Sabelnikov, 1989; Peters, 2000; Bilger *et al.*, 2005). While significant progress has been made in the direct numerical simulation (DNS) of turbulence with a small number of reacting species and approximate evaluation of the chemical kinetics, a joint simulation of complex fluid flow turbulence and realistic chemistry will remain beyond the ability of the best supercomputers for some time. The lack of 'brute force' computational resources and the increasing industrial relevance of designing clean and efficient combustors has spurred the development of sophisticated and computationally inexpensive turbulent combustion models. The aim of these models is to simulate the turbulent flow-field statistics and the thermochemistry with adequate complexity and simultaneously capture the important turbulence-chemistry interactions with reliable accuracy.

A major classification of turbulent reacting flows, which aids their physical understanding and modelling, is based on whether the reactant species are fully mixed before ignition or not. Such flows are termed as turbulent *premixed* or *non-premixed* flows, respectively. It is easy to see that the reactants mix and burn simultaneously when they are not premixed and the fuel combustion process in such cases is completely dependent on the rate of scalar mixing. The primary aim of the present study is to understand and model the dynamics of turbulent scalar mixing and, as such, the focus throughout is limited to turbulent non-premixed combustion. Fig. 1.1 gives schematics of some characteristic industrial flames with non-premixed reactants, where the mixing process is aided by turbulence.

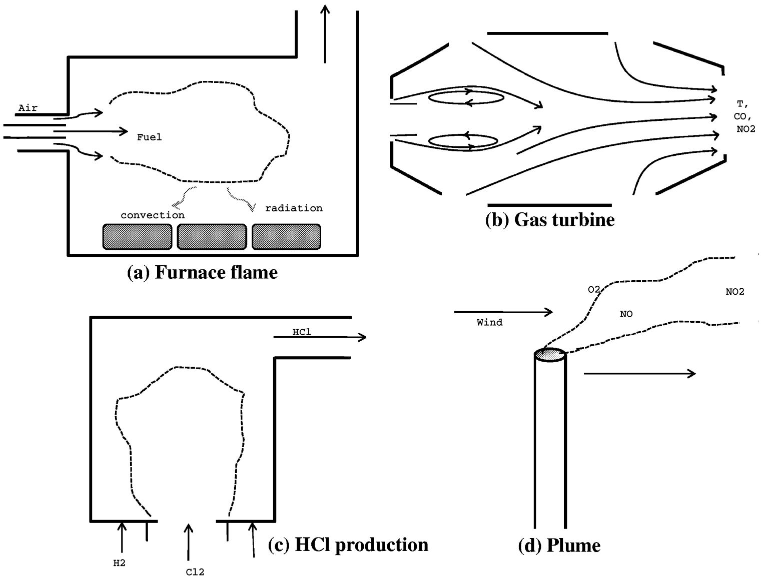

Figure 1.1: Schematic representations of turbulent non-premixed reacting flows in various industrial applications, viz. flame for furnace heating, aero-engine gas turbine, gaseous Hydrogen Chloride production and the atmospheric plume of a power-station. Adapted from Cant & Mastorakos (2008).

The instantaneous state of the fuel-oxidiser mixture in non-premixed combustion is quantified by a normalised measure of fuel concentration called the mixture fraction, which ranges from zero for the pure-oxidiser stream to unity for the pure-fuel stream. The transport equation for the mixture fraction has no chemical production component as it only describes the state of the mixing process and is, thus, advected like any other passive scalar by the turbulent (fluctuating) velocity field. The rate of dissipation of the resultant fluctuations in the mixture fraction is referred to as the scalar dissipation rate[1], and it quantifies the rate at which turbulent eddies enforce mixing between the reactants. The dissipation rate of the mixture fraction fluctuations is central to the description of turbulent mixing in non-premixed combustion (Bilger, 1980; Williams, 1985; Pitts *et al.*, 1999; Peters, 2000; Bilger, 2004).

Most of the contributions to the statistics for scalar dissipation come from the finest

---

[1] The text also refers to the same physical quantity as 'scalar dissipation' and sometimes only as 'dissipation'.

mixing scales of turbulence (Bilger, 2004; Sreenivasan, 2004), which necessitates high spatial-resolution for measuring this important quantity. In addition to the small-scale contributions to the dissipative process, its instantaneous statistics are highly intermittent, i.e. characterised by very large and frequent fluctuations. Therefore, reliable scalar dissipation rate measurement requires not just high spatial- but also high temporal-resolution. The problem of reliable measurements of scalar dissipation is further complicated by the trade-off between higher resolution, corresponding to smaller experimental probe-width, and greater signal-to-noise ratio. Thus, analysis of resolution requirements of the scalar dissipation in terms of esily measurable properties of turbulence, e.g. Reynolds number, is of paramount importance. Owing to these inherent experimental diagnostic limitations, studies like Buch & Dahm (1996, 1998), Pitts *et al.* (1999), Su & Clemens (2003) and Kushnir *et al.* (2006*b*) have attempted to characterise the scalar dissipation dynamics in non-reacting flows and extend the findings to turbulent combustion. All these approaches use individual numerical techniques to isolate the spatial-scales associated with scalar dissipation and no attempt was made in these studies to assess the computed dissipation scale statistics from individual methods against each other. Furthermore, the dissipation scaling criteria computed in the aforesaid studies are based on the assumption of self-similarity of jet flows in the far downstream region, whereas much stronger dissipative events are prevalent upstream owing to larger scalar gradients closer to the nozzle. The studies also fail to account for the effect of strong small-scale intermittency of the instantaneous scalar dissipation on its spatial-resolution. As explained in Sec. 1.3, all of these issues have been addressed in the present research.

In combustion related devices, the time-scales of mixing and combustion are crucial as they determine the dynamics of the coupling between the turbulence and thermochemistry and these relevant time-scales must be assessed appropriately (Kuo, 1986; Veynante & Vervisch, 2002; Bilger *et al.*, 2005). Prediction of the effects of such turbulence-chemistry coupling in non-premixed combustion is critically dependent on the values acquired by the ratio of the large-eddy turnover (or residence) time-scale of turbulence, τ_{res}, to the characteristic chemical time-scale, τ_c. This ratio is denoted by the Damköhler number, $Da = \tau_{res}/\tau_c$. Turbulent non-premixed combustion is asymptotically (Linán, 1974) limited by the two regimes of pure-mixing without reaction and infinitely fast[2] chemistry, which correspond to very small and very large Da values respectively. Assumptions of very small and very large values of this ratio are of little practical significance in turbulent combustion problems. The chemistry proceeds at finite rates comparable to the turbulent mixing dynamics in many real-world problems. For example, in the case of gas turbines, the avoidance of flame quenching/extinction is an important consideration from a safety point of view and equally important is the ability to relight the combustor if extinction does occur. The phenomena of extinction, re-ignition and pollutant formation are direct consequences of finite-rate chemistry and, hence, a majority of the current research on turbulent combustion modelling is focussed on such problems. A common assumption underlying such research is about the localisation of the combustion process in thin reaction zones that are physically aligned with the spatial contours of the stoichiometric mixture fraction value normal to the scalar-gradient vector (Turns, 1996). The thickness of these regions is presumed to be less than the smallest mixing scale of turbulence. Hence, the combustion localised within such regions is essentially laminar and they are termed as 'laminar flamelets' by Peters (1984). For non-premixed combustion in a laminar (non-fluctuating) velocity field, the amount of heat transported away from the reaction zone by diffusion is exactly balanced by the heat-release from combustion. In turbulent mixing, flamelet extinction (or re-ignition) occurs when local velocity fluctuations cause a much larger (smaller) diffusive heat flux away from the reaction zone than the chemical heat production. In other words, extinction or re-ignition implies that the rate of turbulent mixing

---

[2] This implies the reactants ignite and fully burn as soon as they are mixed.

(or scalar dissipation rate) is either far too high for the chemistry to catch up or so low that chemical reaction dominates, as described in the schematic in Fig. 1.2.

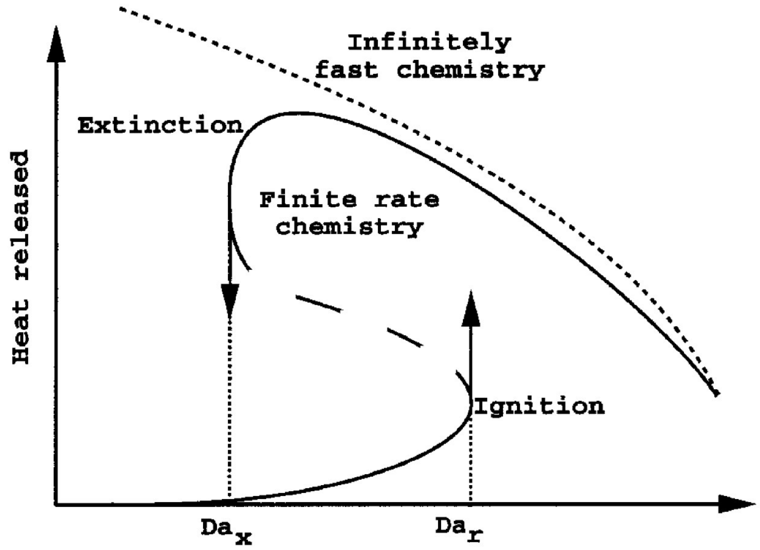

Figure 1.2: Typical *S-curve* heat-release response versus the Damköhler number, Da, for a non-premixed flame under turbulent strain. Adapted from Veynante & Vervisch (2002). The dashed line bounding the *S-curve* denotes the infinitely fast chemistry limit. Da_x and Da_r are critical Damköhler values at the quenching/extinction and ignition limits, respectively. The upper branch represents the increase in heat-release due to combustion as the reactants are mixed (and Da decreases), until the stirring becomes too fast for the chemical reaction to keep up with, leading to flame quenching at $Da = Da_x$. The lower branch signifies that any reduction in the mixing rate (increase in Da) makes chemical reaction easier to happen until the whole mixture re-ignites at $Da = Da_r$. The *S-curve* is broken at the middle branch indicating a low probability (Oberlack *et al.*, 2000) of response due to flame instability.

A series of modelling approaches, viz. fast chemistry model (FCM) by Bilger (1980), laminar flamelet model (LFM) by Peters (2000) and conditional moment closure (CMC) by Klimenko (1990); Klimenko & Bilger (1999), are directly based on mixture fraction as one of the major independent variables (Bilger, 1980). The strong dependence of the combustion process on the mixture fraction (especially at values close to stoichiometric) allows for a fairly accurate characterisation of the combustion process using these approaches. The governing equations for these models have a similar structure, i.e. a balance between the terms for the chemical production and diffusion in the mixture fraction space. Although the models differ in the specification of the modelling coefficients and the physical interpretation of the constituent terms. FCM is a simple and convenient model, but is restricted by the modelling requirement of fast and near-equilibrium state chemical reactions (Bilger, 1980). As explained before, this over-simplification is not at all suitable for determining important finite-chemistry effects. In its traditional formulation, LFM allows for larger deviations in species concentrations from their equilibrium values. Nonetheless, the model presumes all species concentrations as deterministic functions of the mixture fraction by disregarding all statistical deviations from the imposed functional dependence. Furthermore, it is only valid in the immediate neighbourhood of the thin reaction zone and is, therefore, not designed to specify reaction and turbulent transport processes in the rest of the flow. This is again a limitation in accurately predicting phenomena like pollutant formation that can depend on turbulent transport beyond the reaction zone. A notable advantage of the LFM model lies in its ability to predict the extinguishing effect of turbulent straining on the flamelet with reasonable accuracy, as the scalar dissipation term occurs explicitly in its governing equation. The LFM method has also been used in a Lagrangian framework (Mauss *et al.*, 1990) and with transient effects (Haworth *et al.*, 1988). The CMC model is a statistical generalisation of the LFM approach and operates with species concentrations that are conditionally averaged (but not functionally dependent) on the mixture fraction. CMC is designed to deal with both global and local transport processes but, in its singly-conditioned first-order formulation, neglects fluctuations of the scalar dissipation and the fluctuations around conditional means. Second-order CMC closures by Klimenko & Bilger (1999), Roomina & Bilger (2001) and Kim *et al.* (2002) employing conditional variance equations provide marginally better modelling in flames with local extinction and re-ignition. Better simulation of the extinction/re-ignition physics is provided by the doubly-conditioned CMC using either the scalar dissipation (Cha *et al.*, 2001) or, preferably, sensible enthalpy (Kronenburg, 2004) as the second conditioning variable. A key shortcoming of the doubly-conditioned CMC methods is the lack of closure for the important scalar dissipation variables that describe the turbulent mixing. Another powerful approach is represented by the probability density function (PDF) models (Dopazo, 1975; Pope, 1976, 1985). The PDF method involves the evaluation of the joint stochastic distribution of all chemical species and allows for a rigorous evaluation of the convective transport and the chemical source term. The joint PDF transport equation is also consistent with the coefficients of the CMC model for reactive species, whereas LFM is not constrained by the PDF conservation. Like CMC, the PDF methods need closure hypotheses to simulate turbulent mixing and require substantial computational resources to resolve the statistics for all key species.

Generalisation of the stochastic modelling framework that forms the basis for PDF and CMC concepts results in the Multiple Mapping Conditioning (MMC) approach by Klimenko & Pope (2003). The MMC model solves for the conditional expectations of all scalars, conditioned on a set of generic reference variables with a presumed (Gaussian) joint distribution. Knowledge of the joint reference distribution and the conditional expectations gives the actual scalar PDF. Both CMC and PDF governing equations can be recovered from the MMC framework, depending on how the variables in the reference manifold are chosen. The main advantage of using MMC over all other models for turbulent non-premixed combustion is the ease of modelling the MMC diffusion coefficients and, thereby, recovering the scalar dissipation rate. A few recent studies by Cleary & Kronenburg (2007*a*) and Kronenburg & Cleary (2008) have applied 'fully-closed' MMC to stationary homogeneous decaying turbulence for extinction/re-ignition modelling of a non-premixed flame. Due to the stationary homogeneous nature of turbulence no spatial convective transport model was required in these cases and there are no convincing models available for spatially evolving jet diffusion flames in the MMC literature. Furthermore, realistic flames involve thermal effects on the diffusion of chemical species, which also changes the way MMC diffusion coefficients are modelled.

1.2 Objectives

DNS and experimental work is expected to address some crucial questions on the phenomenology of small-scale mixing turbulence and its effect on non-premixed flames. Highly resolved, simultaneous measurements of all species concentrations and flow structures are necessary to assess the validity of closures and modelling assumptions needed for CMC/MMC approaches, and hence, DNS is better suited than experimental measurement for the evaluation of these closures. Given this background the primary aims of this study are summarised as follows:

- Investigate the small-scale intermittent statistics of turbulent scalar dissipation in the Pantano (2004) DNS and quantify the effect of intermittency on the resolution of dissipation rate in measurements/simulations in terms of a measurable bulk flow property, e.g. outer-scale Reynolds number.

- Demonstrate that the analysed DNS satisfies the resolution criterion for modelling scalar dissipation, so that the data can be reliably used to evaluate the closure modelling of extinction and re-ignition in flames.

- Carry out the CMC and MMC modelling of all scalar quantities in the inhomogeneous turbulent jet flame simulation of Pantano (2004) and demonstrate the accuracy of the MMC model (and its sub-models for velocity, drift, diffusion coefficients) in capturing the effects of extinction/re-ignition on the chemical species concentrations.

1.3 Contributions

The present research is broadly divided into two areas of contribution. Firstly, spatial length scales associated with the instantaneous scalar dissipation rate in the near-nozzle region are inferred numerically using a pre-computed DNS database of a turbulent jet flame. Three different computational methods are employed for this purpose, using the highly-resolved data of the profiles of mixture fraction and its scalar dissipation from the Pantano (2004) DNS of a three-dimensional, spatially-evolving jet flame at a moderate jet-exit Reynolds number. For the 'adequate' resolution of instantaneous scalar dissipation rate in turbulent reacting jets, a power-law scaling criterion in terms of a large-scale (measurable) property of turbulence like the outer-scale turbulent Reynolds number, Re_δ, is proposed by using the following methods:

- The discrete Fourier transforms (DFTs) of the cross-stream correlation coefficients for scalar turbulence are computed to yield the standard one-dimensional dissipation spectra. Analysis of the dissipation spectra shows an expected ${Re_\delta}^{-3/4}$ (Kolmogorov) scaling with the outer-scale Reynolds number.
- Similar to the approach used in Buch & Dahm (1996, 1998) and Su & Clemens (2003), thin, sheet-like three-dimensional scalar dissipation structures were directly investigated. These structures were identified within the computational domain using level-sets/contours of the scalar dissipation field, and their thicknesses were subsequently computed. The study shows, in accordance with experimental studies, that the captured dissipation-layer thickness also shows a Kolmogorov scaling with Re_δ.
- Lastly, spatial filters of varying widths were applied to the instantaneous mixture fraction field in order to model the averaging effect that takes place with

> some experimental measurement techniques (Barlow & Karpetis, 2005*b*,*a*). The filtered scalar dissipation rate was then calculated from the filtered scalar field. The peaks in the instantaneous filtered scalar dissipation profiles are observed to decrease exponentially with increasing filter width, yielding estimates of the 'true' value of instantaneous dissipation at that spatial location.

Unlike the dissipation length-scales obtained from the spectral analysis and the level-set method, the length scale estimates from the spatial-filtering method are found to be proportional to ${Re_\delta}^{-1}$. This is consistent (Sreenivasan, 2004; Yakhot, 2003) with the small-scale intermittency of scalar dissipation that cannot be captured by techniques that just resolve the conventional Batchelor/Obukhov-Corrsin scale. These results have implications when considering resolution requirements for simulating/measuring scalar dissipation length scales in DNS/experimental flows.

Secondly, extinction/re-ignition in an inhomogeneous turbulence jet flame is modelled using the MMC approach. The initial conditions and fluid properties of the MMC simulation are the same as that of the aforesaid Pantano (2004) flame. A new sub-model for the MMC convective transport term is proposed, which is not limited by the traditional MMC assumption by Klimenko & Pope (2003) of a Gaussian velocity field. Changes are also introduced in the way MMC diffusion coefficients are modelled in the presence of temperature fluctuations. Drift coefficients consistent with these amendments are derived from first principles for the MMC governing equation. Finally, predictions about the PDFs, scalar dissipation variables and species concentrations from the revised MMC model and those from the conventional singly- and doubly-conditional moment closure are assessed against the post-processed Pantano (2004) DNS data. The effects of flame extinction and re-ignition on the evolution of the joint-scalar PDF and species concentrations are very well predicted using MMC closure.

1.4 Thesis Organisation

The above mentioned research is organised as follows in this thesis. The next chapter surveys the existing fuild dynamics and, more specifically, turbulent combustion literature and builds the physical background for this research. This is achieved by starting from the Navier-Stokes (NS) mass/momentum/energy conservation equations, describing the effect of turbulence-chemistry interactions on the solution of those equations and the development of various modelling approaches to supplement the NS equations. Introductory discussion and literature review on the statistics and characteristic length scales of scalar dissipation is also presented in this chapter. The third chapter deals with the description of the Pantano (2004) DNS database which is used to analyse the small-scale intermittent statistics of scalar dissipation rate and, subsequently, to validate the full MMC/CMC closure of inhomogeneous turbulent non-premixed flames. Chapter 4 describes the various computational techniques used to analyse the dissipation statistics, compares the dissipation length scale statistics captured by all three methods and concludes by proposing a new Reynolds number scaling criterion to resolve the instantaneous dissipation field. Chapter 5 explains the MMC approach in further detail and posits the different sub-models for velocity, drift and diffusion coeffients and chemical source term used in the MMC closure of non-premixed combustion. The chapter also includes details on the numerical method and validation of the results against the DNS data. The conclusions chapter summarises the findings of the research undertaken on dissipation scaling and mapping closure and charts out the future work required in the relevant areas. Finally, the appendix gives the derivations of the generalised MMC governing equation and of the important sub-models used for its closure.

Chapter 2

Background Theory

The starting point for any soundly based analysis of turbulent reacting flows resides in the conservation laws for mass, momentum, scalar transport and internal energy that describe the three-dimensional motion of reactive gases. The system of equations, called the Navier-Stokes (NS) equations, formed by these conservation laws are used along with the gaseous equation of state to provide a comprehensive description of most turbulent reacting flows of practical interest.

The problem of developing an appropriate statistical formulation to compute turbulent quantities will be presented with an emphasis on determining the basic properties of relatively simple turbulent flames. Theoretical and experimental studies of turbulent flames have centred on idealisations of practically occurring situations (Bilger, 1976*a*,*b*, 1980, 1989). The particular idealisation (of furnace flames) represented by the planar jet diffusion flame will be considered in this study.

Relatively simplified theories have been derived (Kuo, 1986; Turns, 2000) for single phase, gaseous, high-to-moderate Reynolds number flows. Such assumptions avoid complexities involved in accounting for fuel droplets, particulates, soot formation and other such effects. Moreover, for gaseous reactants and products, the Prandtl and Schmidt numbers can be close to unity which can result in further simplifications (Peters, 2000). Another simplifying assumption is of no acoustic effects (i.e. low Mach number), ensuring that turbulent pressure fluctuations are not large enough to affect the rate of chemical reaction (Kakhi, 1994). Finally, a reduced four-step methane-air chemical reaction mechanism by Peters (2000) is used to counter the computational costs associated with detailed thermochemical descriptions.

The brief theory presented below aims to provide the physical properties of chemical species together with the appropriate boundary and initial conditions, the velocity field, temperature and species concentrations. For the case of laminar flows, this requires the solution of the conservation equations for mass, momentum, energy and chemical species. In turbulent flows, due to varying length and time scales, DNS of the exact transport equations would describe detailed behaviour of the flame at every instant, including even the smallest scale of fluctuation due to the turbulence and would provide invaluable information for theoretical framework (Hawkes *et al.*, 2006). However, the solution of these equations with initial conditions and boundary conditions appropriate to turbulent flows is computationally expensive. Moreover, DNS in the case of turbulent reacting flows results in further difficulties given the increased number of scalar transport equations necessary to describe the entirety of the transported scalar flow field and the coupling of highly non-linear thermochemically reacting systems (Kuo, 1986; Peters, 2000). Due to these reasons DNS is limited to relatively simple geometries and reduced chemistry models. An alternative approach is the large eddy simulation (LES), which provides a partial resolution of the turbulent flow motion by filtering out the small, dissipative scales and allowing for a coarser grid resolution. However, the problem of closure of turbulent fluxes at the sub-grid scales exists in LES. The limiting case of LES, where some of the largest energy-containing scales are revolved, is the Reynolds Averaged Navier-Stokes (RANS) simulation. In the present study, the closure problem for chemically reacting (non-premixed) flows is tackled using the conditional moment methods discussed in Chapter 5 and the input from RANS (or equivalently post-processed DNS data) is considered sufficient for the purpose of demonstration. Analogous sub-grid scale conditional moment closure models can also be derived, but they are beyond the scope of the present thesis.

In the coming sections the conservation equations for mass, momentum, energy, and chemical species are presented and the assumptions implemented to provide a closed set of equations for the set of velocity components, $\boldsymbol{u}(\mathbf{x}, t)$, and scalar quantities, $\boldsymbol{\phi}(\mathbf{x}, t)$. For clarity of presentation, all dependencies on spatio-temporal coordinates $\mathbf{x}$ and t are omitted from here on and exceptions are made where deemed necessary. Various flow field modelling approaches are discussed in brief. This is followed by a detailed discussion on the important scalar dissipation rate variable with special focus on its small-scale intermittent statistics and spatial resolution requirements. Finally various combustion modelling approaches are introduced and discussed.

2.0.1 Transport equations

Beginning with the NS equations, it can be shown that the properties at any point in the flame can be determined from the transport equations for the set of velocity components, $\boldsymbol{u}$, and the set of scalar mass fractions, $\boldsymbol{\phi}$. In mathematical terms,

$$\boldsymbol{\phi} = \{\phi_1, .., \phi_I, ..., \phi_{n_s}\}, \tag{2.1}$$

where n_s is the total number of scalar variables to be computed. Conceptually, the complete scalar set can be further sub-divided into the set of quantities that govern the mixing properties and the set of quantities that exclusively describe the chemistry of a turbulent non-premixed flame. The former includes the appropriate conserved scalars and the latter includes all the chemical species concentrations. In addition, thermodynamic properties like temperature[1] can also be placed in the former subset. Thus,

$$\boldsymbol{\phi}_{maj} = \{\phi_1, .., \phi_i, ..., \phi_{n_r}\} \tag{2.2}$$

and

$$\boldsymbol{\phi}_{min} = \{\phi_1, .., \phi_\iota, ..., \phi_{n_s - n_r}\}, \tag{2.3}$$

where the number of elements in the former subset is denoted by n_r, which puts the number of chemical species at $n_s - n_r$. In accordance with the literature (Klimenko & Pope, 2003), the individual elements of subsets $\boldsymbol{\phi}_{maj}$ and $\boldsymbol{\phi}_{min}$ are denoted by lower-case Roman and Greek subscripts, respectively, whereas the upper-case Roman character, I, is used to denote all the scalars together. This notation will be, henceforth, consistently followed throughout the text to denote the elements of the respective sets. Specifically, ϕ_1 and ϕ_2 are considered synonymous with the conserved scalar (or mixture fraction) and the sensible enthalpy, respectively. It will be shown in Chapter 5 that this conceptual division is of particular significance to the CMC/MMC closure modelling of turbulent non-premixed combustion.

The chemical and thermodynamic properties of a reacting system can be characterised by the mass fraction of each chemical species, ϕ_I, the mixture enthalpy $\mathcal{H}$, and the static pressure p. An equation of state relates these quantities to the density, ρ, and the velocity completes the description of the system of equations. These variables obey the following conservation equations:

---

[1] More generally, quantities sensitive to energy changes, like the sensible enthalpy, can be used.

$$\frac{\partial \rho}{\partial t} + \frac{\partial \rho u_i}{\partial x_i} = 0, \tag{2.4}$$

$$\frac{\partial \rho u_i}{\partial t} + \frac{\partial \rho u_j u_i}{\partial x_j} = -\frac{\partial p}{\partial x_i} - \frac{\partial \tau_{ij}}{\partial x_i} + \rho g_i, \tag{2.5}$$

$$\frac{\partial \rho \phi_I}{\partial t} + \frac{\partial \rho u_j \phi_I}{\partial x_j} = -\frac{\partial J_j^I}{\partial x_j} + \omega_I, \tag{2.6}$$

where g_i is the body force per unit volume in the i^{th} coordinate direction and J_j^I represents the molecular diffusion flux. Both the density ρ and the source term, ω_I, which represents the net formation rate of the I^{th} species per unit volume, are known functions of temperature and ϕ_I. The source term ω_I will be zero if ϕ_I is a conserved scalar like the mixture fraction. The stress term, $\partial \tau_{ij}/\partial x_j$ gives a description of the spatial stress gradients where τ_{ij} is the viscous stress tensor resulting from local deformation in Newtonian fluids and is dependent on local fluid-mechanical properties such that:

$$\tau_{ij} = \mu(\frac{\partial u_i}{\partial x_j} + \frac{\partial u_j}{\partial x_i}) - \frac{2}{3}\mu \frac{\partial u_k}{\partial x_k} \boldsymbol{\delta}_{ij}, \tag{2.7}$$

where μ is the dynamic viscosity of the fluid and $\boldsymbol{\delta}_{ij}$ denotes the Kronecker delta function. Cartesian tensor notation is used throughout and summation over repeated indices is implied. Fick's law is invoked in the derivation of the scalar equation and for most combustion processes, particularly for a binary mixture, the form of the molecular diffusion flux is given by (Peters, 2000; Meyer, 2001):

$$J_j^I = -\rho D_I \frac{\partial \phi_I}{\partial x_j}. \tag{2.8}$$

The next equation to be considered relates to the conservation of energy. It can take on a variety of forms with temperature, enthalpy, sensible enthalpy or internal energy as the principal variable. Confining our attention to low speed flows with a characteristic Mach number small compared to unity (< 0.3), the energy equation in terms of enthalpy (cf. (2.12)) is the most compact and is given by:

$$\frac{\partial \rho \mathcal{H}}{\partial t} + \frac{\partial \rho u_j \mathcal{H}}{\partial x_j} = \frac{\partial p}{\partial t} + \frac{\partial}{\partial x_j}\left(\rho \alpha \frac{\partial \mathcal{H}}{\partial x_j}\right) + \omega_{\mathcal{H}}, \tag{2.9}$$

Term $\omega_{\mathcal{H}}$, denoting the rate of enthalpy production, is given by,

$$\omega_{\mathcal{H}} = -\sum_{\iota=1}^{n_s - n_r}\left[\mathcal{H}_\iota \frac{\partial}{\partial x_j}\left(J_j^\iota + \rho \alpha \frac{\partial \phi_\iota}{\partial x_j}\right)\right]. \tag{2.10}$$

where the summation is done over the total number of chemically reactive species in the mixture and α is the thermal diffusivity of the gaseous mixture. $\mathcal{H}_\iota$ is the specific enthalpy of the ι^{th} reactive species and is considered to be a known function of the temperature T. The heat flux term in (2.9) include contributions from the conduction of heat arising from temperature gradients (Fourier's law) and the effect of enthalpy transport by the diffusive fluxes, J_j^ι. The kinetic energy per unit mass of the mixture is very small compared to the enthalpy per unit mass for low Mach number flows and is, thus, neglected in (2.9). Also neglected are the radiative heat transfer, the conversion of mechanical energy to heat by compressibility and viscous dissipation, work associated with the action of body forces and Soret effects as these usually represent a small fraction of the overall heat flow (Peters, 2000).

Equation (2.9) is analogous to (2.6) with $\omega_{\mathcal{H}}$ as the enthalpy source term. By invoking the assumption of unity Lewis number, defined as $Le_I = \alpha/D_I$ for all scalars, the source term $\omega_{\mathcal{H}}$ vanishes and (2.9) takes a form similar to the transport equation for a conserved scalar. $Le_I = 1$ implies that all species diffusivities are equal and equations (2.6) and (2.9) can be treated as a single system of equations. The Lewis number can also be expressed as a ratio of two other important dimensionless constants,

$$Le_I = \frac{Sc_I}{Pr}, \tag{2.11}$$

where $Sc_I = \nu/D_I$ is the Schmidt number for the I^{th} scalar and ν is the kinematic viscosity of the fluid. The Schmidt number expresses the relation between the diffusion of the momentum due to viscous forces and the diffusion of the species due to molecular diffusion. The Prandtl number, Pr, quantifies the relation between the diffusion of temperature and the dissipation of momentum. The unity Lewis number assumption is not always accurate and its implementation is ideally limited to specific simplified single phase flow cases (Kim & Williams, 1997). However, in hydrocarbon flames with sufficiently high Reynolds numbers, the molecular and the atomic hydrogen are the only species with Lewis numbers deviating significantly from unity. On the other hand the concentrations of these intermediate species are low in hydrocarbon flames and, while, the unity Lewis number assumption does not affect the flame structure significantly, it still may cause errors in predicting H and H_2.

The mixture enthalpy is related to the temperature via the following equation,

$$\mathcal{H} = \sum_{\iota=1}^{n_s-n_r} \phi_\iota \mathcal{H}_\iota, \tag{2.12}$$

where the specific enthalpy of species ι is given by,

$$\mathcal{H}_\iota = \mathcal{H}_\iota^f + \int_{T_o}^{T} C_{p_\iota} dT \qquad (2.13)$$

and $\mathcal{H}_\iota^f$ is the standard heat of formation of the ι^{th} species, T_o is a reference temperature which is usually the ambient temperature and C_{p_ι} is the specific heat capacity of the ι^{th} species at constant pressure. The standard heat of formation of any species is defined as the heat released when one kilomole of substance is formed from its elements and is generally calibrated at standard temperature and pressure (STP) conditions[2].

To express the temperature gradients in terms of the enthalpy gradients, the specific heat capacity at constant pressure of the mixture is first defined as:

$$C_p = \sum_{\iota=1}^{n_s - n_r} \phi_\iota C_{p_\iota}(T), \qquad (2.14)$$

where C_{p_ι} are the specific heats at constant pressure of the individual chemical species. Using (2.12), (2.13) and (2.14) it can be shown (Peters, 2000) that the enthalpy is expressed in terms of the specific heat capacity of the mixture as,

$$\mathcal{H} = \int_{T_o}^{T} C_p dT + \sum \phi_\iota \mathcal{H}_\iota^f. \qquad (2.15)$$

At this juncture it is important to introduce a new term,

---

[2] Equivalent to a temperature of 298 K and a pressure of 1 atm

$$h_s = \mathcal{H} - \sum \phi_\iota \mathcal{H}_\iota^f = \int_{T_o}^{T} C_p dT, \tag{2.16}$$

also known as the *sensible enthalpy* of the gaseous mixture. It is directly dependent on the temperature increment from the ambient value and the specific heat capacity of the mixture. The sensible enthalpy term is of great significance to conditional moment closure models (cf. Sec. 2.3.7) for turbulent combustion due to its strong temperature and mixture fraction sensitivity and the relative ease of modelling of its source term. The chemical production rate term for the sensible enthalpy of the gaseous mixture is given by,

$$\omega_{h_s} = -\sum_{\iota=1}^{n_s-n_r} \omega_\iota \mathcal{H}_\iota^f - \frac{\partial}{\partial x_j}\left[\sum_{\iota=1}^{n_s-n_r} \rho\alpha\left(1 - Le_\iota^{-1}\right) h_{s_\iota} \frac{\partial \phi_\iota}{\partial x_j}\right], \tag{2.17}$$

where $h_{s_\iota} = \mathcal{H}_\iota - \mathcal{H}_\iota^f$ is the ι^{th} species-specific sensible enthalpy. It is easy to see that the unity Lewis number assumption reduces the above source term to a compact form, viz. $-\sum_{\iota=1}^{n_s-n_r} \omega_\iota \mathcal{H}_\iota^f$. As mentioned earlier, the Lewis numbers of major species in hydrocrabon flames do not deviate much from unity and this simplification holds for them. However, it is largely accurate even for intermediates like H and H_2 with Lewis numbers much less than unity, due to their small concentrations.

Finally, the system of equations is closed by the equation of state that relates density to temperature as,

$$p = \rho R T \sum_{\iota=1}^{n_s-n_r} \frac{\phi_\iota}{M_\iota}, \tag{2.18}$$

where M_ι denotes the molecular weight of the ι^{th} chemical species. The low Mach number assumption removes the pressure dependency which originates from the mean flow or by turbulent fluctuations (Kakhi, 1994). As a result, coupling of the momentum and scalar fields is assumed to take place primarily through the density field determined from the equation of state where $\rho = \rho(\phi_\iota, \mathcal{H}, p)$. Temperature is also functionally dependent on the same variables where $T = T(\phi_\iota, \mathcal{H}, p)$ through an auxiliary relation. Since the reaction rate source terms (ω_ι) are algebraic functions of p, ρ, T and ϕ_ι, ω_ι need only be expressed as a function of the same set of three variables.

It is possible to scale pressure variation and its effect on the source term. It is easily shown through dimensional analysis, that the low Mach number assumption removes the dependence of the source term on pressure variations, Δp, caused by the mean flow and turbulent fluctuations. The magnitude of these variations can be estimated as follows (Kakhi, 1994):

$$\Delta p \propto \rho V^2 = Ma^2(\rho c_s^2) \qquad \textit{and} \qquad \frac{\Delta p}{p} \propto Ma^2 \tag{2.19}$$

where V is a characteristic velocity, Ma is the Mach number, $c_s = (\gamma p/\rho)^{1/2}$ is the speed of sound and the adiabatic index, γ, is the ratio of specific heats at constant pressure and volume. Equation (2.19) clearly shows that at low Mach numbers, the influence of pressure fluctuations will be negligible. Therefore the pressure fluctuations term $(\partial p/\partial t)$ in the energy equation (2.9) can be neglected as this term only plays a role in the propagation of the acoustic waves. Though the pressure term is disregarded in the current work, effects of pressure variations can be significant at low Mach numbers in confined flows, e.g. in describing engine cycles of internal combustion engines (Libby & Williams, 1980).

2.0.2 Reynolds and Favre Averaging

A statistically averaged set of equations is more advantageous due to the computational expense involved in resolving the instantaneous variables in (2.4) to (2.18) directly. The typical approach involves the decomposition of an arbitrary turbulent quantity, ϑ, into its mean and fluctuating parts as follows:

$$\vartheta = \overline{\vartheta} + \vartheta', \tag{2.20}$$

where the mean can be defined either through time averaging,

$$\overline{\vartheta}(\mathbf{x}) = \lim_{\Delta t \to 0} \frac{1}{\Delta t} \int_{t}^{t+\Delta t} \vartheta(\mathbf{x}, t) dt, \tag{2.21}$$

or through an ensemble average,

$$\langle \vartheta(\mathbf{x}, t) \rangle = \lim_{N \to \infty} \frac{1}{N} \sum_{i=1}^{N} \vartheta^{(i)}(\mathbf{x}, t), \tag{2.22}$$

where $i = 1, ...N$ denotes individual realisations. As a consequence of the ergodic theorem (Pope, 2000), both averaging methods, denoted by the overbar and angular-bracket operators, are equivalent so long as the turbulence is statistically stationary. Henceforth in the text, all mean/averaged quantities will be understood to be functions of the spatial coordinates, $\mathbf{x}$, alone. In the case of variable density flows, Reynolds averaging produces many unresolved fluctuating density related terms. It is often convenient to introduce a density weighted average, namely the Favre average, such that all fluid mechanical quantities, except pressure, are density weighted as follows,

$$\widetilde{\vartheta} = \frac{\overline{\rho\vartheta}}{\overline{\rho}}, \tag{2.23}$$

where the bar indicates conventional time averaging and the tilde is the Favre-averaging operator. Therefore rewriting (2.20) for Favre-averages and fluctuations around it gives,

$$\vartheta = \widetilde{\vartheta} + \vartheta''. \tag{2.24}$$

Here a double-prime superscript is used to denote the fluctuations around the Favre-mean. The nature of these fluctuations is such that their mean value is non-zero whereas a mass average makes the term vanish, i.e. $\overline{\rho\vartheta''} = 0$. An advantage when considering variable density flow is that fluctuating density terms arising from time averaging disappear through Favre averaging, resulting in convenient simplifications. For example, the relative expressions for a typical non-linear convective term arising out of Reynolds and Favre averaging of the momentum conservation equation (2.5) are given by (Libby & Williams, 1980),

$$\overline{\rho u_i u_j} = \overline{\rho u_i}\,\overline{u}_j + \overline{\rho}\,\overline{u_i' u_j'} + \overline{u}_i\overline{\rho' u_j'} + \overline{u_j}\,\overline{\rho' u_i'} + \overline{\rho u_i' u_j'} = \overline{\rho}\tilde{u}_i\tilde{u}_j + \overline{\rho u_i'' u_j''}, \tag{2.25}$$

which implies that Favre averaging automatically incorporates these various modes of momentum exchange into a small number of terms making the approach relatively simple. This is evidently useful in flows with large density variations. The relative simplicity encountered in Favre averaging makes it the preferred choice in describing the required transport equations for solving turbulent reacting flows. Using the definition of Favre averaging in (2.23) and (2.24), the velocity and scalars (i.e. enthalpy and species mass fractions) can be decomposed into their mean (bulk) and fluctuating (turbulence) components. Favre decomposition and statistical averaging on the conservation equations leads to the following ensemble averaged equations (Kuo, 1986):

$$\frac{\partial \overline{\rho}}{\partial t} + \frac{\partial \overline{\rho}\tilde{u}_l}{\partial x_l} = 0 \tag{2.26}$$

$$\frac{\partial \overline{\rho}\tilde{u}_i}{\partial t} + \frac{\partial \overline{\rho}\tilde{u}_i\tilde{u}_l}{\partial x_l} = -\frac{\partial \overline{p}}{\partial x_i} - \frac{\partial \overline{\rho}\widetilde{u_i''u_l''}}{\partial x_l} - \frac{\partial \widetilde{\tau_{il}}}{\partial x_l} + \overline{\rho}\tilde{g}_i \tag{2.27}$$

$$\frac{\partial \overline{\rho}\tilde{\phi}_I}{\partial t} + \frac{\partial \overline{\rho}\tilde{u}_l\tilde{\phi}_I}{\partial x_l} = -\frac{\partial \overline{\rho}\widetilde{u_l''\phi_I''}}{\partial x_l} - \frac{\partial \tilde{J}_l^I}{\partial x_l} + \overline{\varpi}_I \tag{2.28}$$

In the context of homogeneous turbulence, gradients of mean diffusion terms such as the direct molecular stresses, $\frac{\partial \widetilde{\tau_{il}}}{\partial x_l}$, and the diffusive flux, $\frac{\partial \tilde{J}_l^I}{\partial x_l}$, are negligible and the above equations take a form which is identical to their Reynolds averaged counterparts. From a modelling point of view, the various unknowns in these equations, are the turbulent Reynolds stresses in the momentum equation, $\widetilde{u_i''u_l''}$, the turbulent scalar fluxes $\widetilde{u_i''\phi_I''}$ and the source term in the scalar transport equations $\overline{\varpi}_I$. The turbulent Reynolds stress and scalar flux terms are traditionally closed using the gradient transport approximation. However, the mean production rate $\overline{\varpi}_\iota$ of the ι^{th} species per unit volume is particularly complicated and is discussed next.

2.0.3 Mean Reaction Rates

The averaged source term in (2.28) creates several difficulties due to its nonlinear dependence on temperature and species concentrations. Consequently, the averaging procedure results in a production of higher moment terms that are statistical correlations of two or more fluctuating components (Bilger, 1980). This problem can be illustrated in the limit of an infinitely fast one-step irreversible chemical reaction,

$$vFuel + Air \rightarrow (1+v)Products \tag{2.29}$$

for which the simplified Arrhenius form of the rate of production ω_F of the fuel can be written as

$$\omega_F = -A_r \rho^2 T^{\beta_r} \phi_F \phi_O \exp\left(\frac{-T_A}{T}\right), \tag{2.30}$$

where A_r is the Arrhenius pre-exponential constant, T_A is the activation temperature of the reaction and ϕ_F, ϕ_O are the respective mass fractions of the fuel and oxidiser (air). Reynolds averaging (2.30) by rewriting the species and temperature quantities in terms of their mean and fluctuating components and expanding about the mean states gives,

$$\overline{\omega}_F = -A_r \overline{\rho}^2 \bar{T}^{\beta_r} \widetilde{\phi_F} \widetilde{\phi_O} exp\left(\frac{-T_A}{\overline{T}}\right) \left[1 + \frac{\overline{\rho'^2}}{\overline{\rho^2}} + \frac{\overline{\phi'_F \phi'_O}}{\overline{\phi}_F \overline{\phi}_O} + 2\frac{\overline{\rho' \phi'_F}}{\overline{\rho}\overline{\phi}_F} + \frac{T_a}{T}\left(\frac{\overline{\phi'_F T'}}{\overline{\phi}_F \overline{T}} + ...\right)\right], \tag{2.31}$$

where the continuation ... is for moments of third and higher order and the prime indicates a fluctuation about the mean. Higher order moment terms now appear as a result of averaging the expression. These terms are usually not of negligible magnitude and must be retained, e.g. in cases of very rapid reactions in weak turbulence, where the root-mean-square (RMS) of fluctuations in species concentration are larger than its mean (O'Brien, 1980). Therefore any moment closure model of $\overline{\omega}_F$ should retain most higher-order terms occurring in (2.31). This constraint makes the use of moment methods very difficult as every higher-order moment represents a separate closure problem and would ideally require the solution of its own transport equation.

The next section briefly reviews the relative merits of various flow field modelling approaches, viz. DNS, LES and moment closures and introduces the important scalar dissipation parameter to describe turbulent mixing. The statistics of dissipation length scales and numerical approaches used for estimating these are discussed before going on to the combustion modelling in detail.

2.1 Flow Field Modelling Approaches

2.1.1 Direct Numerical Simulation

As explained in Sec. 1.1, turbulent combustion is one of the many themes that is talked about in practical applications. With the continuous developments of numerical combustion, it has become apparent that the unsteady, three dimensional nature of the interaction between turbulence and the flame must be modelled (Bray, 1996; Kerstein, 2002). Comprehensive studies of unsteady phenomena controlling turbulence/chemistry interactions are in their infancy. However, with the growth of computational power previously unthinkable DNS flame calculations can be attempted (Hawkes *et al.*, 2006; Thevenin, 2005; Vervisch, 2000; Pantano, 2004; Westbrook *et al.*, 2005) allowing basic mechanisms controlling flame/turbulence interactions to be investigated. However, the computational expense involved still requires simplifying assumptions such as low turbulence Reynolds numbers and simplified chemical kinetics. In some cases, the solution of two-dimensional flows is also required. Even with such simplified approximations, the results are encouraging (Hawkes *et al.*, 2006; Pantano, 2004; Westbrook *et al.*, 2005) and provide a better basis for model developments, where in the past modellers depended partly on intuition.

DNS makes use of instantaneous conservation equations discussed in the previous section, where the future state of the flow can in principle be determined precisely, given exact knowledge of the initial and boundary conditions. In the case of turbulent combustion DNS, the solution of the three-dimensional Navier-Stokes equations and the equations for chemical species transport are solved. However, the additional equations mean that a smaller number of grid points must be used as compared to isothermal flows due to the increased computational time.

A complete turbulent flow simulation using DNS necessitates the resolution of the finest scales of turbulence. This is esential when analysing highly non-equilibrium processes such as extinction/re-ignition (Sreenivasan, 2004; Sreedhara & Lakshmisha, 2000). DNS studies combined with experimental investigation will enable the development and validation of current and future closures for reacting flows, especially in the modelling of strongly intermittent quantities like scalar dissipation that require the knowledge of small-scale statistics. For reproducing the small-scale statistics faithfully DNS studies with very high numerical accuracy are required. Both pseudo-spectral methods (Sreedhara & Lakshmisha, 2000) and finite difference methods with spectral-like resolution (Lele, 1992; Poinsot & Veynante, 2001) have been used to perform high-resolution simulations. Examples of well-resolved

DNS studies of turbulent reacting flows include the CH_4-air jet flame by Pantano (2004), hydrogen jet lifted flame by Mizobuchi *et al.* (2005) and a skeletal CO/H_2 jet flame by Hawkes *et al.* (2006). Direct numerical simulations are unlikely to be in practical use for industrial design calculations in the near future and their main role is as a research tool to provide fundamental insight on turbulent reacting flows and aid the development of improved statistical sub-models, e.g. for turbulent mixing. Closures can then be applied in engineering codes for use in the design of practical combustors. Description of the attributes of the Pantano (2004) DNS used for the present study is detailed in the next chapter.

2.1.2 Large Eddy Simulation

A major difficulty with DNS is the limitation to low or moderate Reynolds number flows and simplistic geometries. This led to the widespread interest in large eddy simulation (LES) for turbulent reacting flows which can be applied to a variety of more complex geometries and elevated Reynolds number flows. The use of LES for solving turbulent reacting flow problems has increased dramatically within the last decade. Large scale structures that are well resolved in LES are geometry dependent in a manner that is difficult to capture through single point Reynolds averaged flow models (Bray, 1996). These large structures control to an extent the entrainment rate in a mixing layer which will also clearly affect the composition of the reactive gas pockets.

Whereas in DNS, much of the computational expense goes into the description of the small dissipative motions, LES focuses more on the dynamics of the larger-scale motions which are explicitly computed. In LES, large three-dimensional unsteady turbulent motions are directly represented and small-scale (high pass filtered) quantities are modelled. Though the small scales are removed through filtering, the near-universality of dissipation rates and other small-scale processes makes them arguably easier to describe in a subgrid scale turbulence model. In LES, localised spatial averaging is imposed by means of a spatial filter function (Pope, 2000). Large eddy simulation sets out like DNS to resolve eddying motions in both space and time, but the computational cells are too large to resolve the smaller scales of motion. In fact such differencing on a discrete grid is equivalent to obtaining a filtered field where the filter scale is equal to the grid size. This implicitly filtered field which is modelled in LES is a representation of a spatially filtered DNS calculation producing a mean velocity from an unfiltered instantaneous velocity.

A subgrid scale model is introduced to describe the subgrid Reynolds stresses which arise from the spatial averaging process. The correlation coefficient can be split up into a resolved part and a fine structure contribution. This fine scale contribution is key to the accuracy of LES. Cost wise, LES lies between one point Reynolds stress models and DNS and is motivated by the limitations of both these approaches. Albeit the computational cost for LES is still high, notably when including time-averaged information, its application to turbulent reacting flows has become increasingly important (Bray, 1996; Janicka & Sadiki, 2005; Kempf *et al.*, 2006). Nonetheless, there are still drawbacks with respect to modelling flow, chemistry and turbulence-chemistry interactions. Kinetic energy and scalar dissipation which occurs at the smaller scales must be modelled as does the coupling between molecular mixing and chemical kinetics. Even though models for small scale turbulent motions must be applied in a similar fashion to RANS, LES offers significant improvement because large scale perturbations are explicitly captured. LES in reacting flows can in principle better model acoustic disturbances notably combustion instabilities, a problem which occurs frequently in combustion-related devices (Varoquie *et al.*, 2002; Westbrook *et al.*, 2005). However, LES has not yet reached the maturity required for implementation in a model intended for practical combustors with complex geometry and chemistry and the implications for LES are continuously being assessed (Pope, 2004; Bilger *et al.*, 2005).

2.1.3 Moment Closures

The system of Reynolds/Favre averaged transport equations for a group of turbulence variables contain higher-order statistical correlation terms that are not accounted for in that system of equations. This is the closure problem of turbulence which exists for all combinations of statistical quantities. It reflects the fact that the physical variables can provide only a partial description of turbulence because they are affected by influences other than those that their transport equations describe. Statistical closures approximate these influences in terms of the known quantities within the group by providing extra equations for the unknown random variables.

In principle, a higher level closure that considers a larger number of variables describing turbulent statistics is potentially more accurate than a low level closure as the former can afford a more complete flow specification (Hanjalic, 1994; Lumley, 1978; Pope, 2000; Speziale, 1995). For incompressible flows, a second order closure represents a better resolved flow field as transport equations for second moment quantities such as $\widetilde{u_i''u_j''}$, $\widetilde{u_i''\phi_I''}$, $\widetilde{\phi_I''\phi_J''}$ and the dissipation rate of turbulent kinetic energy, $\widetilde{\epsilon}$, are solved for. Higher-order triple correlation terms are modelled in terms of the mean quantities and second moments. The accuracy of the set of equations will depend on the type of closure modelling implemented. Possible closures to the Reynolds stress, dissipation and scalar equations are considered in the following subsection.

2.1.4 Turbulence Scale Models

To close the set of equations, the Reynolds stresses are often modelled as a function of a characteristic turbulence velocity, a turbulence length scale and a turbulent viscosity coefficient, where viscosity is a function of the characteristic length and velocity parameters. Zero equation models solve a partial differential equation like (2.27) for the mean velocity field and use an algebraic model to relate the fluctuating quantities to the mean flow. Simple moment closure modelling of scalar turbulence follows the same pattern but requires analogous mixing parameters, viz. the characteristic mixing length scale and turbulent species diffusivity. Models of this type work well enough in simple quasi-steady flows for which the adjusted constants have been calibrated. The assumption is that the turbulence is in equilibrium with the local mean conditions and the history of turbulence (Pope, 2000) ix not explicitly considered. These models do not work well for problems in which the mean conditions change abruptly, e.g. local extinction and re-ignition of turbulent flames.

One-equation models include partial differential equations for the characteristic turbulence velocity. Two-equation models add a further equation for the turbulence length scale. The additional partial differential equations describe the evolution of quantities that are required to calculate the stress tensor in the mean flow equations. Such models are described as scale evolution models (Lumley, 1978) and relate turbulent transport to a combination of the local features of the mean flow and one or two parameters of the turbulence. As a result, the evolution model takes explicit account of the history of the turbulence scales. However, they are still equilibrium models in that they assume that the mean field and the turbulence parameters are in local equilibrium. Evolution equations generally give a reasonable first order approximation of the turbulence in simple separated flows or flows with gradual changes in boundary conditions but fail in flows with strong rotations, density gradients and high temperature fluctuations (Sloan *et al.*, 1986).

2.1.5 Second Moment Closures

In second moment methods, the Reynolds stresses are obtained by solution of its own transport equations (Kuo, 1986). Higher order closure approximations are employed which enable the full anisotropic characteristics of the Reynolds stresses to be modelled. Analogous transport equations for turbulent scalar fluxes, $\widetilde{\boldsymbol{u}''\boldsymbol{\phi}''}$, can be derived and modelled along the same lines. Second moment quantities like scalar fluxes are crucial to the description of turbulent transport processes, whereas the strength of the mixing turbulence is quantified in terms of the variance of the scalar concentration. Since the scope of the present thesis is limited to the dynamics of the turbulent mixing field, only the generalised Favre-averaged transport equation for the scalar variance is discussed here.

$$\underbrace{\frac{\partial\overline{\rho}\widetilde{\phi_I''^2}}{\partial t}}_{I}+\underbrace{\frac{\partial\overline{\rho}\widetilde{u}_i\widetilde{\phi_I''^2}}{\partial x_i}}_{II}=\underbrace{\mathbb{T}_I}_{III}+\underbrace{\mathbb{P}}_{IV}+\underbrace{\overline{u_i''\omega_I}}_{V}-\underbrace{\overline{\rho}\tilde{\chi}_{II}}_{VI}, \tag{2.32}$$

where

$$\mathbb{T}_I=-\frac{\partial\overline{\rho}\widetilde{u_i''\phi_I''^2}}{\partial x_i}\qquad\mathbb{P}=-2\overline{\rho}\widetilde{u_i''\phi_I''}\frac{\partial\tilde{\phi}_I}{\partial x_i}. \tag{2.33}$$

The terms on the right-hand side of (2.32) represent, in order, turbulent transport [term *III*], turbulent production via the mean scalar gradient [term *IV*], scalar-mean formation/reaction rate correlation [term V] and the mean scalar dissipation of the I^{th} species [term VI]. The rate of dissipation of fluctuations of an arbitrary I^{th} scalar, represented by χ_{II}, has already been introduced in Sec. 1.1 as a key concept in modelling extinction/re-ignition phenomena in turbulent non-premixed flames (Bilger, 1980; Williams, 1985; Pitts *et al.*, 1999; Peters, 2000; Bilger, 2004) and according to (Peters, 2000) is mathematically given by,

$$\chi_{II} = 2D_I \boldsymbol{\nabla}\phi_I'' \cdot \boldsymbol{\nabla}\phi_I'' \simeq 2D_I \boldsymbol{\nabla}\phi_I \cdot \boldsymbol{\nabla}\phi_I, \tag{2.34}$$

where D_I is the diffusion coefficient for the I^{th} scalar and the two indices in the subscript for χ represent the gradients of the respective scalars on the right-hand side of (2.34). According to (2.34), χ_{II} is directly proportional to the square of the magnitude of the scalar gradient, $\boldsymbol{\nabla}\phi_I$, quantifying the extensive rate-of-strain imposed on the local scalar distribution by the turbulent eddies. The scalar variance budget in (2.32) implies that the mean scalar dissipation gives the rate at which the variance of scalar fluctuations is destroyed in a turbulently advected scalar field. Other authors like Veynante & Vervisch (2002) also define the mean scalar dissipation rate as the rate of decay of 'scalar energy' or $\widetilde{\phi_I''^2}/2$, which gives

$$N_{II} = \frac{\chi_{II}}{2} = D_I \boldsymbol{\nabla}\phi_I \cdot \boldsymbol{\nabla}\phi_I \tag{2.35}$$

.

The subscript notation for N follows the same convention as that for χ. It follows from the aforesaid definition that the rate of scalar dissipation has an inverse-time dimensionality and governs the local residence time-scale of turbulent mixing. Therefore, the averaged scalar dissipation, $\widetilde{\chi_{II}}$, can be expressed in terms of the mean viscous dissipation rate, $\widetilde{\epsilon}$, by assuming a direct proportionality (Spalding, 1971; Tennekes & Lumley, 1974) between the turbulent scalar (mixing) and fluid-mechanical time scales,

$$\widetilde{\chi_{II}} = C_\phi \frac{\widetilde{\phi_I''^2}}{\tau}. \tag{2.36}$$

Here, the C_ϕ parameter is the mechanical to scalar time scale ratio, $\tau = \widetilde{\kappa}/\widetilde{\epsilon}$ is the characteristic turbulent eddy-turnover time based on the Kolmogorov (1941) scaling estimate and $\widetilde{\kappa}$ is the turbulent kinetic energy. For non-reacting turbulence, the C_ϕ parameter varies depending on the flow conditions (Warhaft & Lumley, 1978; Warhaft, 1980), but a value of 2.0 is generally used (Newman *et al.*, 1981; Pope, 1985).

2.2 Scalar dissipation statistics

The general concept of the dissipation rate of turbulent fluctuations of an arbitrary scalar was introduced in the previous section. Characterising the mixing dynamics of conserved scalars is of particular significance to the studies of passive/reacting turbulent flows (Dimotakis, 2005). According to (2.34), the mathematical form for the scalar dissipation rate of any conserved scalar, Z, in passive scalar turbulence[3] is given by

$$\chi = 2D\boldsymbol{\nabla} Z \cdot \boldsymbol{\nabla} Z, \tag{2.37}$$

where D is the diffusivity of the conserved scalar (or mixture fraction). Henceforth

---

[3] The turbulent reacting flow counterpart for the conserved scalar is the mixture fraction, formally introduced in the next section

in the text, all instances of χ (or $N = \chi/2$) without subscripts refer to the scalar dissipation rate of the conserved scalar or mixture fraction. Before moving on to the discussion of closure modelling for turbulent non-premixed combustion, it is necessary to review the small-scale statistics of the scalar dissipation variable that plays a key role in these modelling approaches. This section reviews studies concerning the small-scale statistics and intermittency of scalar dissipation with a special focus on its spatial resolution requirements and classifies computational approaches to analyse the characteristic dissipation length scales. Application of these methods to post-process dissipation statistics from highly resolved DNS studies is also discussed. This is followed by the description of the combustion models in the next section.

While there is good evidence to suggest that the statistics of scalar dissipation have some properties of near-universal nature (Monin & Yaglom, 1971; Tennekes & Lumley, 1974; Newman *et al.*, 1981; Nelkin, 1994; Sreenivasan & Antonia, 1997; Wang *et al.*, 1999) that can be applied to many mixing environments, including the ocean, the atmosphere and internal flows of engineering importance, the departures from the universal behaviour (specifically for the inertial-subrange) have also been well documented (Frisch, 1991; Sreenivasan & Stolovitzky, 1996; Noullez *et al.*, 1997). Frisch (1995) gives a detailed review of these aspects in the theory of small-scale turbulence. In this study, we concentrate primarily on results pertaining to reacting flows, for which turbulent scalar mixing is less well-studied in spite of its crucial role in such flows (Bilger, 1980). Understanding the statistical properties of a random quantity like scalar dissipation is the starting point to develop improved models for mixing and for non-premixed combustion. It is experimentally observed that the strongly intermittent behaviour of scalar dissipation is somewhat similar to that of the instantaneous turbulent viscous dissipation (Sreenivasan, 2004). In other words, a frequent occurrence of instantaneous values much larger than the mean is observed. This observation is quantified in Fig. 2.1, which shows that dissipative events at over 4.5 standard deviations from the mean are a thousand times more likely to occur than similarly large fluctuations in a common Gaussian process. However, the frequency and magnitudes of the fluctuations in scalar dissipation are characteristically larger than those in viscous dissipation. Nonetheless, both variables show a skewed probability distribution that has a large tail. It follows from various studies (Batchelor & Townsend, 1949; Grant *et al.*, 1962; Meneveau & Sreenivasan, 1991) that the average value of the viscous dissipation is not completely representative of its physical characteristics, and the reader is referred to recent reviews by Sreenivasan (2004) and Schumacher *et al.* (2005). Attempts to incorporate the high-variability properties of viscous dissipation into a turbulence theory led to the well-known work of Kolmogorov (1962). In this respect, Oboukhov (1949) and Corrsin (1951) were the first to naturally assume that many aspects of turbulent mixing are similar to turbulence itself and predicted the scaling of the inertial subranges of structure functions and spectra.

Experimental measurement of the scalar dissipation entails the difficult task of obtaining the instantaneous spatial derivative (in at least one dimension) of the mixture fraction with sufficient resolution such that these frequent large-magnitude excursions are not overlooked (Gibson, 1991). The experimental study by Dahm & Southerland (1997) gives an assessment of the accuracy of Taylor's hypothesis in approximating the magnitude of the scalar dissipation rate from such one- or two-dimensional spatio-temporal measurements of the scalar gradients. Furthermore, the study quantifies the extent of the departure from the true magnitudes using such measurements and gives a generalised analytical framework to maximise the correlation between the measured and true dissipation rates. There have been many other recent attempts (experimental and numerical studies) to quantify scalar dissipation in turbulent axisymmetric and planar jets, like those by Dahm *et al.* (1991), Buch & Dahm (1996), Buch & Dahm (1998), Dahm & Southerland (1999), Pitts *et al.*

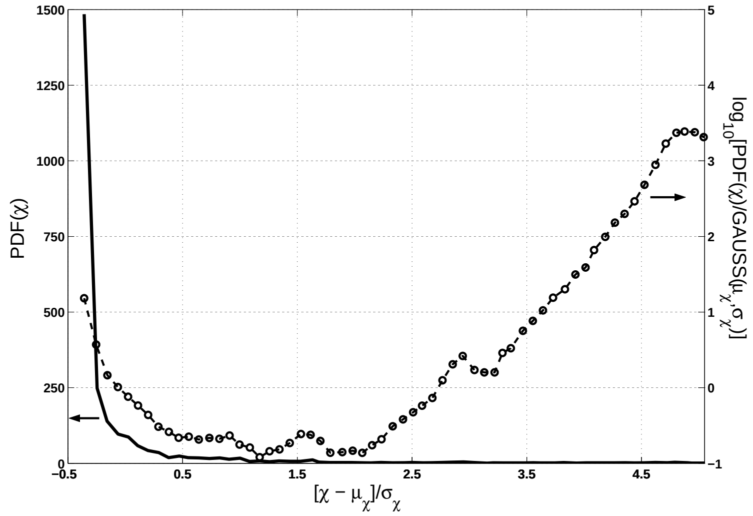

Figure 2.1: Illustration of the small-scale intermittency of scalar dissipation rate computed at an arbitrarily chosen spatial location ($x/H = 2.8, y/H = 5.2$) from the Pantano (2004) DNS dataset described in Chapter 3. Notation μ_χ and σ_χ denote the mean and standard deviation of the scalar dissipation rate at the aforesaid spatial location. The solid line is the probability density of the instantaneous scalar dissipation rate and the dashed line denotes the ratio of the actual probability density to the Gaussian density computed at the same mean and standard deviation (or variance).

(1999), Tsurikov & Clemens (2002), Su & Clemens (2003) and Barlow & Karpetis (2005*b*). An additional difficulty encountered in reacting flows is that the mixture fraction itself does not exist on its own as part of the experimental flow. It is generally derived from the composition of the mixture (Bilger *et al.*, 1990). This requires simultaneous measurements of multiple species concentrations in a high-temperature environment as a prelude to obtaining the scalar dissipation. This interest is motivated by a desire to characterise this fundamental turbulence property and to model its behaviour owing to its key role in mixture-fraction based models for turbulent non-premixed or partially-premixed combustion.

2.2.1 Average and instantaneous dissipation length scales

The Kolmogorov length scale of turbulence is defined as

$$\eta_K = \left(\frac{\nu^3}{\langle \epsilon \rangle} \right)^{1/4}, \tag{2.38}$$

where $\langle \epsilon \rangle$ denotes the mean of the turbulence kinetic energy dissipation rate, $\epsilon (\mathbf{x}, t)$, and ν is the kinematic viscosity. The mechanism of formation of turbulent fluid-elements with a characteristic thickness of η_K can be explained in terms of the vorticity transport equation that describes the evolution of the vorticity field subject to the balance between vortex-stretching due to the mean strain-rate field (resulting in an elongation and thinning of the vortex-tube structures) and the re-connection effects induced by viscous-diffusion. The result is a vortex tube with $\mathrm{O}(\eta_K)$ thickness, characterising the length-scale at which the viscous dissipation of turbulent kinetic energy predominates.

The average dissipation length-scale η_K is undoubtedly important from a theoretical and practical standpoint. However, due to the attested departure from Gaussianity in the dissipation range (Monin & Yaglom, 1971), it is unable to fully characterise the distribution of dissipation scales in turbulent flow. This multiplicity of dissipation length-scales is characteristic of the small-scale intermittency and its physical explanation involves the addition of a new feature to the traditional eddy-cascade picture of turbulence by Kolmogorov (1941).

She *et al.* (1990) and She (1991) describe the canonical picture of turbulence as consisting of a hierarchy of small-scale coherent structures in addition to the known random eddy-cascade with near-Gaussian statistics. These coherent structures are local and intermittent and, thus, show strongly non-Gaussian statistics. The aforesaid mechanism of formation of coherent vortex structures, based on the strain-diffusion balance, is supplemented in the revised picture. She *et al.* (1990) describe that the coherent vortex structures are subjected to an additional strain field caused by the vortex structures themselves in the event of large vorticity magnitudes. To

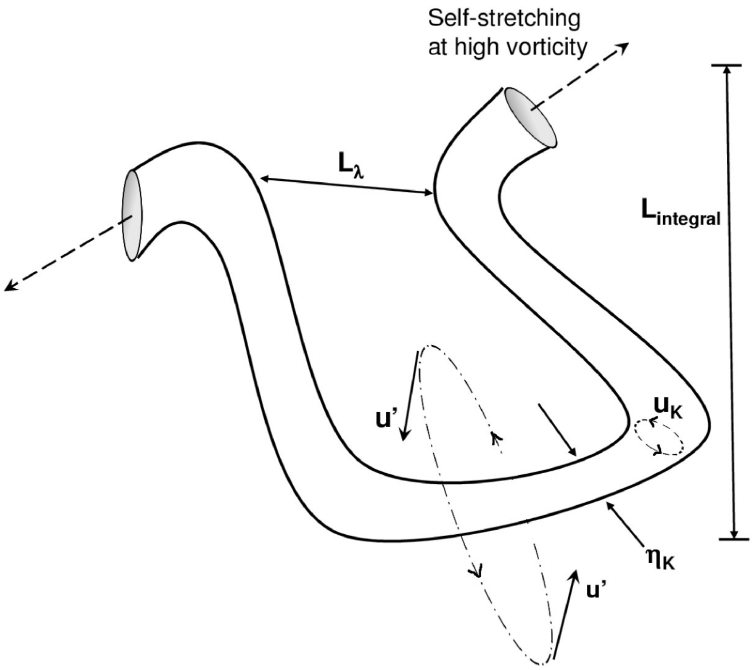

Figure 2.2: Schematic representation of the strain-diffusion balance for a coherent vortex-tube structure in mixing turbulence. The dimensions of the structure in terms of the characteristic velocities and length-scales of turbulence are illustrated. Here, u_K denotes the eddy-turnover velocity at the Kolmogorov scales and L_λ is the Taylor microscale.

account for this *self-stretching* component of strain-rate, the strain-rate tensor is subdivided into the *self-stretching* and mean-strain components. The former component becomes dominant at high vorticity (or, equivalently, large velocity-gradient) magnitudes. The balance between the dominant *self-stretching* component of strain-rate and the viscous diffusion leads to the formation of structures with sub-Kolmogorov thicknesses and results in the wide dissipation length-scale distribution characteristic of intermittency. It is important to note here that the descriptions of turbulence intermittency in Kolmogorov (1962) and related studies *presume* the dissipation-scale statistics as lognormal-like. Unlike She *et al.* (1990) and She (1991), these descriptions do not fully explain/model the turbulence dynamics underlying such statistics.

For the reasons described above and in some circumstances, it becomes useful to define a *local*, instantaneous, viscous dissipation length scale, called the *local* Kolmogorov scale by Schumacher *et al.* (2005) and denoted here by η'_K. The concept of a locally-defined, fluctuating dissipation length-scale is not new, and has also been put forth in the multifractal analysis of the small-scale turbulence structure by Frisch & Vergassola (1991). This local quantity follows from (2.38) according to the same dimensional arguments used to define η_K, giving $\eta'_K(\mathbf{x},t) \sim (\nu^3/\epsilon(\mathbf{x},t))^{1/4}$. Since ν is not expected to have very intermittent statistics, it largely depends on some smooth function of the temperature, the majority of the variability of η'_K results from the statistics of ϵ. The abundance of local values of ϵ that are much larger than $\langle\epsilon\rangle$ (owing to its intermittent distribution) gives rise to a significant range of instantaneous dissipation length scales smaller than η_K. Accurately measuring the probability distribution function (or PDF) of ϵ requires that the minimum measuring scale, $\eta_{K_{\min}} \sim (\nu^3/\epsilon_{\max})^{1/4}$, be such that the probability that $\epsilon > \epsilon_{\max}$ is very small, say 1% (Sreenivasan, 2004).

The same argument of small-scale intermittency can be extended to turbulent mixing dynamics, as explained in reviews by Sreenivasan (1991, 2004) and Bilger (2004), to hypothesise the existence and significance of *local* scalar dissipation length scales, or $\eta_Z = \eta_K \cdot Sc^{-3/4}$, where η_Z denotes the Obukhov-Corrsin scale. This expression is valid for Schmidt numbers, Sc, smaller than one, and Sc is defined as $Sc = \nu/D$ (Tennekes & Lumley, 1974). For large Schmidt numbers, $Sc \geq 1$, the corresponding balance of turbulent stretching and molecular diffusion leads to the Batchelor (1959) scale, defined as $\eta_Z = \eta_K \cdot Sc^{-1/2}$. While the definition of the Batchelor scale is strictly valid for Schmidt numbers greater than or equal to unity (Buch & Dahm, 1998), the label is commonly used to imply the finest mixing scale in the turbulence and combustion literature. Henceforth, for the sake of convenience, all references to the Batchelor scale will imply the finest mixing length scale in the broadest sense, whereas the symbol η_Z will be used to denote the specific

Schmidt number scaling for the present case of $Sc = 0.7$. It should be noted that the difference in value between the Batchelor and Obukhov-Corrsin scales is negligible for Schmidt numbers of order unity.

2.2.2 Categorisation of the measurement methods

The experimental or numerical measurement of spatial-scales associated with scalar dissipation can be broadly categorised into approaches that either involve the computation of two-point spatial correlations of scalar fluctuations (scalar spectra), or the determination of the spatial distribution of the scalar dissipation using scalar-gradients.

The method involving scalar spectra uses the standard eddy-cascade theory of turbulence to arrive at estimates for the Batchelor length scale and is described in Sec. 4.1. On the other hand, information about the spatial-distribution of χ can, in turn, be acquired through two independent approaches used in the literature that either compute the spatial variation of χ by plotting its iso-contours or level-sets at various fractional-values of the local peak, keeping the grid-size fixed, or that model the decay of the local peak-values in the χ-profiles for incremental increases in the effective spatial-discretisation (or filter-width) of the sampling volume.

The former level-set (fixed filter-width) approach has been used in various numerical and experimental studies, like those by Buch & Dahm (1996, 1998), Kushnir *et al.* (2006*b*), Su & Clemens (2003) and Tsurikov & Clemens (2002), to investigate the thin, planar, three-dimensional scalar dissipation structures and ascertain their thicknesses. The thicknesses thus computed are characterised as the spatial-scales associated with scalar dissipation. The application of this approach to the present study has been detailed in Sec. 4.2. Other experimental studies by Barlow & Karpetis (2005*a*,*b*) estimate χ using the latter spatial-filtering approach. As described further in Sec. 4.3, this method in particular seems better suited for characterising the small-scale intermittency of the scalar dissipation process.

2.2.3 The DNS database

Traditionally, simulations involving the solution of the scalar advection-diffusion equation with the Navier-Stokes equations have resolved no more than the Batchelor scale. Experiments in non-reacting flows by Buch & Dahm (1996, 1998), Pitts *et al.* (1999) and Su & Clemens (2003) among others have also suggested that accurate measurements of the scalar dissipation rate require a spatial resolution comparable to (or even smaller than) the Batchelor scale, using scaling laws and self-similarity arguments. However, as Barlow & Karpetis (2005*b*) suggest, applicability of these scaling relationships to estimate the Batchelor scale in laboratory-scale flames is unclear. Such estimates are hinged on the assumption of self-similarity of the flow that is valid only far downstream, if present at all in common flame geometries (Sreenivasan, 2004). Furthermore, owing to the reasons described in the preceding section, the intermittent character of the scalar dissipation process introduces additional constraints on its spatial resolution and the Batchelor scale estimate is no longer enough for moments higher than the mean. Hence, various reviews by Bilger (2004), Sreenivasan (2004), Barlow & Karpetis (2005*b*), and Schumacher *et al.* (2005) concur that published χ-measurements from experiments or simulations of turbulent jet-flames can frequently have questionable spatial resolution, especially at high Reynolds numbers.

Many recent well-resolved simulations of turbulent scalar mixing that exist in literature are in the low (Yeung *et al.*, 2004; Schumacher *et al.*, 2005; Kushnir *et al.*, 2006*b*) and moderate (She *et al.*, 1993; Wang *et al.*, 1999; Vedula *et al.*, 2001) Reynolds number range, with perhaps the recent exception of Yeung *et al.* (2005).

However, they all tackle the problem of turbulent mixing in its simplest form, i.e. between passive scalars. Donzis *et al.* (2005) gives a good account of the attributes of such DNS studies to date. For the low-to-moderate Reynolds number range evidenced in the present DNS, the small scale evolution for reacting cases can be expected to markedly differ from the evolution in non-reacting cases owing to dilatation and relaminarisation of the flow. DNS of constant density flows can therefore not be used to quantify dissipative structures in reaction zones for such Reynolds numbers. However, DNS studies for the complex case of turbulent mixing with reaction, e.g. in the aforesaid case of turbulent jet-flames (Boersma, 1999) or in channel flows (Brethouwer & Nieuwstadt, 2001), tend to be invariably limited to the low-to-moderate range of Reynolds numbers with simplistic chemistry and resolution limited to about η_K. Even the relatively good resolution of the turbulent diffusion flame DNS by Mizobuchi *et al.* (2005), using a varying $23 - 400$ million grid-point computational domain, is incapable of reproducing intermittency effects accurately owing to the high Reynolds number it attempts to simulate and is, therefore, unsuitable for our present purpose. Therefore, an extremely well-resolved DNS of a turbulent reacting jet at a moderate jet-exit Reynolds number of 3000 and with relatively detailed 4-step chemistry (Pantano, 2004) has been chosen in the present study to implement the numerical approaches mentioned in Sec. 2.2.2. Further relevant details on the DNS can be found in Chapter 3. It is important to note that Kolmogorov's first hypothesis regarding the universal behaviour of the fine dissipation length scales holds in the low-to-moderate Reynolds number range (She *et al.*, 1993; Saddoughi & Veeravalli, 1994; Nelkin, 1994; Pope, 2000; Yeung *et al.*, 2004; Kushnir *et al.*, 2006*b*; Wang *et al.*, 2007*b*). This justifies the rationale of the present study that concerns itself with the spatial-scales of dissipation and does not depend on the existence of a well-defined inertial subrange in the turbulence spectrum. The reader is referred to Secs. 4.1.2 and 4.1.3 in Chapter 4 for further discussion on this important issue.

2.3 Combustion Models

Reacting flows are more complex that isothermal flows due to the variable density effects that result from the heat release due to chemical reactions. This in turn affects the velocity flow field which alters the chemistry. This coupling through the effect of turbulence-chemistry interactions is the key to properly modelling turbulent reacting flows. Generally, chemical reactions take place in a shorter time compared to turbulent mixing rates which produce large temporal and spatial fluctuations in the flow field. As mentioned earlier, the treatment of the reaction source term is the cause of most of the difficulty due to its non-linearity through the Arrhenius expression. Such turbulence fluctuations of species mass fractions that appeared in (2.31) produce order of magnitude changes in the chemical reaction rates which alter individual species mass fractions and surrounding temperature. For computationally tractable equations, higher moments are dropped from the mean source term, which results in large errors, notably when the activation energy is larger. The various combustion models used in literature to approach the problem of modelling the turbulence-chemistry interactions are introduced and discussed in this section.

2.3.1 Combustion Regimes

Combustion requires that fuel and oxidiser be mixed at the molecular level. In turbulent non-premixed combustion specifically, the way in which this process happens depends on the turbulent mixing process. Once a range of different size eddies has developed, strain and shear at the interface between the eddies enhances the mixing process. Similarly, an eddy break up process will increase strain and shear and steepen the concentration gradients at the interface between the unmixed reactants, where molecular mixing of fuel and oxidiser generally takes place. As chemical reactions consume the fuel and oxidiser and steepen the gradients at the interface, the mixing process is further modified. Thus classical scaling laws for isothermal flows, such as Reynolds number independence in open jets, are no longer valid. This is further complicated by the fact that various chemical reactions occur on different time scales, leading to chemical and turbulent interaction at the large scales of the inertial subrange. Furthermore, heat release by combustion induces an increase in temperature which in turn accelerates combustion chemistry. The chain branching and breaking reactions sensitive to temperature changes can cause ignition and extinction phenomena. Therefore, identifying different combustion regimes through local time and length scales forms the basis for establishing various combustion models in turbulent reacting flows, as their formulation usually involves various combustion regime assumptions.

The laminar flamelet approach (Peters, 2000) covers both premixed and non-premixed regimes of combustion and its main feature is the assumption of relatively fast chemistry. Within the context of turbulent flames, these flamelets appear as an ensemble of thin, locally laminar, one-dimensional structures embedded within the turbulent flow field. A criterion for the chemistry to be fast is then determined with respect to the relevant time and length scales of the chemistry and turbulence. Provided that the characteristic time scale of the thermochemistry is small in comparison to the Kolmogorov time scale, the combustive process is assumed to be completed within the turn over time of the smallest eddies.

Characteristic time and length scales for turbulence are well established (Pope, 2000) where a typical large eddy integral time and length scale is equal to $\tau_{res} = \widetilde{\kappa}/\widetilde{\epsilon}$ and $l_T = \widetilde{\kappa}^{3/2}/\widetilde{\epsilon}$ respectively. The typical turbulent Reynolds number is then equal to $Re = \widetilde{\kappa}^{1/2} l_T/\nu \equiv \widetilde{\kappa}^2/\widetilde{\epsilon}\nu$. In the description of turbulent combustion it is necessary to define further nondimensional parameters namely the Damköhler number (Da) and the Karlovitz number (Ka). The former (cf. Sec. 1.1) corresponds to the ratio of the turbulent residence time scale τ_{res} to the chemical time scale, τ_c. The residence time scale of turbulence is usually considered to be in direct proportion with the integral length scale and is governed by the rate of scalar dissipation through (2.36). The Damköhler number is a measure of the importance of the interaction between chemistry and turbulence. Most combustion models are placed at the extremes of the Da number. For example if $Da << 1$, the turbulence is much faster than the chemistry and vice versa. The former regime is the *well-stirred reactor*, where products and reactants are rapidly mixed.

On the other hand, the Karlovitz number corresponds to the ratio of chemical time scale τ_c and smallest (Kolmogorov) turbulent time scale, τ_K.

$$Ka \equiv \frac{\tau_c}{\tau_K} \tag{2.39}$$

If $Ka << 1$ the chemical reactions occur much faster than all turbulent scales. Turbulence does not alter the flame structure and the chemical region is in laminar conditions. The Karlovitz number can be linked to the Damköhler number as follows:

$$Ka = \frac{1}{Da}\widetilde{\kappa}\left(\frac{\widetilde{\epsilon}}{\nu}\right)^{(1/2)} \tag{2.40}$$

Using their definitions, the Re, Da and Ka numbers can be combined and are related by $Re = Da^2 Ka^2$ provided that the Schmidt number ($Sc = \nu/D$) is unity and thus only two out of the three parameters are independent. For $Da >> 1$ and $Ka < 1$, the chemical time scale is shorter than any turbulent time scale This condition, also known as the Klimov-Williams limit, is the laminar flamelet regime. In this regime, the turbulence is unlikely to affect the inner flame structure which remains close to a laminar flame wrinkled by the effect of turbulent eddies.

For $\tau_K < \tau_c < \tau_{res}$, the turbulent integral time scale is still larger than the chemical time. However the small scales of turbulence (Kolmogorov) are smaller than the flame thickness and will influence the inner flame structure. For example, the flame will be quenched as a result of exceeding flame stretch induced by the Kolmogorov scales. For non-premixed flames (Bray & Peters, 1993) define a flamelet regime in mixture fraction space, Z. Provided that the mixture fraction variance, $\widetilde{Z''^2}$ about the mean stoichiometry is small, it is readily established that reactions are sufficiently fast everywhere and reaction zones are connected. Conversely, if the variance is pronounced, the diffusion flame structure will separate.

An important phenomenon in diffusion flames is the extinction which occurs on the upper branch of the *S-curve* in Fig. 1.2 when the Da is decreased by increasing the main jet velocity for example. Commonly, a critical value is reached where this phenomenon occurs which causes a rapid transition to the lower branch. By defining the residence time as $\tau_{res} = 1/\mathcal{S}$, where $\mathcal{S}$ is a strain rate parameter along the fuel and air interface, increasing the strain rate (or decreasing Da in Fig. 1.2) will cause the flame to extinguish provided that τ_c is larger or comparable to τ_K.

2.3.2 Conserved Scalar Formalism

The laminar flame concept describes turbulent diffusion flames as an ensemble of stretched laminar flamelets (Peters, 2000) where profiles from laminar diffusion flame simulations are used to calculate mean and variances in turbulent flames. These laminar flames are typically characterised by a single conserved scalar, namely the mixture fraction, Z. Writing $a_{\iota\varepsilon}$ as the number of atoms of element ε in a molecule of species ι, w_ι as the mass of the ι^{th} chemical species and M_ε as the molecular weight of the element, the mass of all atoms of ε in the system is given by,

$$w_\varepsilon = \sum_{\iota=1}^{n_s-n_r} \frac{a_{\iota\varepsilon} M_\varepsilon}{M_\iota} w_\iota \tag{2.41}$$

Therefore, the mass fraction of element ε in the gaseous mixture of mass w is

$$Z_\varepsilon = \frac{w_\varepsilon}{w} = \sum_{\iota=1}^{n_s-n_r} \frac{a_{\iota\varepsilon} M_\varepsilon}{M_\iota} \phi_\iota \tag{2.42}$$

The conservation equation for Z_ε is then given by:

$$\frac{\partial \rho Z_\varepsilon}{\partial t} + \frac{\partial \rho u_k Z_\varepsilon}{\partial x_k} = -\frac{\partial}{\partial x_k} \left(\sum_{\iota=1}^{n_s-n_r} \frac{a_{\iota\varepsilon} M_\varepsilon}{M_\iota} J_k^\iota \right) \tag{2.43}$$

Clearly the chemical source term is removed as a result of conserving mass fraction. Assuming Fickian diffusion and molecular diffusivity, D, (2.43) can be modified into the convenient form shown below:

$$\frac{\partial \rho Z_\varepsilon}{\partial t} + \frac{\partial \rho u_k Z_\varepsilon}{\partial x_k} = -\frac{\partial}{\partial x_k} \left(\rho D \frac{\partial Z_\varepsilon}{\partial x_k} \right) \tag{2.44}$$

The global chemical reaction equation for complete combustion for a hydrocarbon fuel C_iH_j can be written as (Peters, 2000):

$$\mathrm{v_F C_i H_j + v_{O_2} O_2 \rightarrow v_{CO_2} CO_2 + v_{H_2O} H_2O}, \tag{2.45}$$

where v with the subscripts denotes the chemical coefficients of the respective species in the above reaction. Let Z_C, Z_H and Z_O represent the elemental mass fractions of C, H, and O and M_C, M_H and M_O be their respective molecular weights. The normalised function, $\mathcal{F}$, where:

$$\mathcal{F} = \frac{Z_C}{i \cdot M_C} + \frac{Z_H}{j \cdot M_H} - 2\frac{Z_O}{v_{O_2} M_{O_2}} \tag{2.46}$$

will be zero provided the conditions are stoichiometric. The most commonly adopted definition of the mixture fraction is due to Bilger (1988), and is obtained by normalising the function, $\mathcal{F}$, such that it varies between zero and unity.

$$\begin{aligned} Z &= \frac{\mathcal{F} - \mathcal{F}_2}{\mathcal{F}_1 - \mathcal{F}_2} \\ &= \frac{Z_c/(iM_c) + Z_H/(jM_H) + 2(\phi_{O_2,2} - Z_O)/(v_{O_2} M_{O_2})}{Z_{C,1}/(iM_c) + Z_{H,1}/(jM_H) + 2(\phi_{O_2,2}/(v_{O_2} M_{O_2})} \\ &= \frac{2Z_C/M_C + 1/2Z_H/M_H + 2(Z_{O,2} - Z_O)/M_O}{2Z_C/M_C + 1/2Z_{H,1}/M_H + Z_{O,2} M_O} \end{aligned} \tag{2.47}$$

The subscripts 1 and 2 refer to the fuel and air streams, respectively. The formulation is often used to determine the mixture fraction from experimental or numerical data of mass fraction that are available. In the flow field calculation, Z is normalised to values between zero and unity in the pure air and fuel streams respectively. Its conservation equation is identical to (2.44) with Z replacing Z_ε as the conserved scalar. For unity Lewis numbers the transport equation (2.9) for the enthalpy also takes the same form as (2.44), provided we neglect the radiative source and the transient pressure terms in the former. This allows the enthalpy to be linearly related to the mixture fraction such that:

$$\mathcal{H} = \mathcal{H}_1 Z + \mathcal{H}_2(1 - Z) \tag{2.48}$$

where $\mathcal{H}_1$ and $\mathcal{H}_2$ are the enthalpy contents of the fuel and air streams, respectively.

2.3.3 Thermochemical Models

Any chemical element can be represented by a normalised scalar (Peters, 2000) as that represented in the previous section but there are restrictions that the presence of chemical elements impose on the combustion process. This can be more clearly seen through the Burke-Schumann solution and then the equilibrium solution, both of which are a function of such a conserved scalar, namely the mixture fraction. In the limit of an infinitely fast one-step irreversible reaction there exists a thin non-equilibrium region, usually within the shear layer where $Z = Z_s$. Outside this region the mass fractions are either negligible or piecewise linear functions of the conserved scalar Z,

$$\phi_F = \phi_{F,1}\left(\frac{Z - Z_s}{1 - Z_s}\right), \phi_O = 0, \qquad Z \geq Z_s \tag{2.49}$$

$$\phi_O = \phi_{O,2}\left(1 - \frac{Z}{Z_s}\right), \phi_F = 0, \qquad Z \le Z_s \tag{2.50}$$

Here $\phi_{F,1}$ and $\phi_{O,2}$ are the fixed mass fractions of pure fuel and oxidiser in the respective fuel and air streams. The Burke-Schumann solution of profiles of ϕ_F, ϕ_O and temperature for complete combustion are now linear functions of mixture fraction, with the assumption of a unity Lewis number, equal diffusivity, constant pressure and negligible radiative heat transfer. All species are in chemical equilibrium with one another. However, this is not true for real flames and nonequilibrium effects (e.g. extinction and re-ignition) must be accounted for to better represent actual measured species and temperature profiles. Some of the most promising techniques to predict the physics of extinction and re-ignition are based on:

- presumed probability density function (PDF) approach,
- the solution of the joint-PDF of the turbulent-combustion variables,
- steady and transient flamelet-based modelling (FM),
- conditional moment closure (CMC) of the advection-diffusion equations and
- solution of the transport equations for scalar surrogates or *mapping functions* conditioned on a set of reference variables with a presumed PDF.

2.3.4 Presumed PDF Approaches

The presumed PDF approach is based on the underlying assumption that the shape of the PDF is known and can be described as a function of a random variable, e.g. a conserved scalar, and its first two moments, namely the mean and the variance. Bilger (1980) showed that the shape of the scalar PDF is dependent upon the spatial

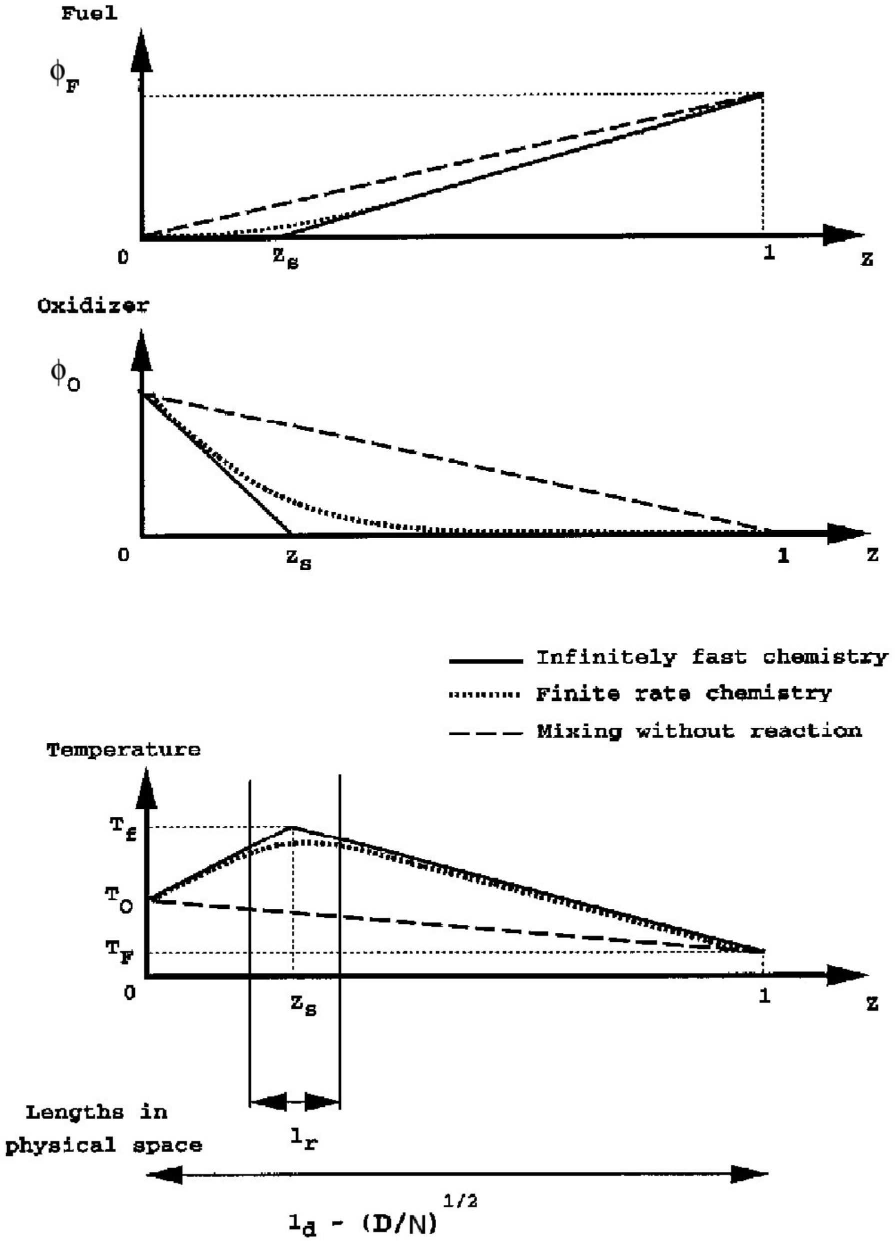

Figure 2.3: Schematic showing the inner structure of non-premixed flames. Variation of fuel and oxidiser mass fractions and temperature in the mixture fraction space is bounded by the inifinitely fast chemistry limit on the upper side and by the pure-mixing case on the lower side. l_d is the characteristic diffusive thickness and depends on the scalar dissipation rate, N, whereas the reaction zone thickness, l_r, depends on l_d and the Damköhler number. Figure reproduced from Veynante & Vervisch (2002).

location. Within the proximity of the shear layer, the PDF will tend to resemble a number of spikes due to intermittent effects resulting from the continuous entrainment of fresh unburnt fluid into the turbulent flow. Towards the core of the jet, the profiles are reminiscent of a Gaussian shape. When considering a function containing a greater number of random variables, determining an appropriate shape is more difficult and multivariate presumed PDF approaches are intrinsically complicated due to the required PDF needed to account for unrealisable scalar spaces (Borghi, 1988). Consider two arbitrary random variables, ϑ_1 and ϑ_2, with sample spaces, ζ_1 and ζ_2, respectively. Then the conditional average of ϑ_1 on ϑ_2 is given by, $\langle \vartheta_1 | \vartheta_2 = \zeta_2 \rangle$ and is related to the unconditional average, $\langle \vartheta_1 \rangle$ by,

$$\langle \vartheta_1 \rangle = \int_{-\infty}^{\infty} \langle \vartheta_1 | \vartheta_2 = \zeta_2 \rangle P_{\vartheta_2}(\zeta_2) d\zeta_2 \tag{2.51}$$

where P_{ϑ_2} is the marginal PDF of the conditioning variable, ϑ_2. In the same fashion, the mass fraction of a species in a turbulent flow can be written in such a way as to depend (conditionally) on the local value of mixture fraction, Z. Therefore it is possible to write an averaged species mass fraction conditional on mixture fraction such that:

$$\langle \phi_\iota \rangle = \int_{-\infty}^{\infty} \langle \phi_\iota | Z = \eta_1 \rangle P_Z(\eta_1) d\eta_1 = \int_{-\infty}^{\infty} \langle \phi_\iota | \eta_1 \rangle P_Z(\eta_1) d\eta_1 \tag{2.52}$$

Following the nomenclature for the scalar mass fractions introduced in Sec. 2.0.1, consistent subscript notation is used for their sample space variables denoted by $\boldsymbol{\eta}_{maj} = \{\eta_1, .., \eta_i, ..., \eta_{n_r}\}$. Therefore, η_1 in (2.52) denotes the sample space of the mixture fraction, $\phi_1 \equiv Z$. The reactive scalars can be modelled in terms of their fluctuations in mixture fraction space using the above equation. Klimenko & Bilger (1999) give the transport equation for the mixture fraction PDF, $P_Z(\eta_1)$, as

$$\frac{\partial \langle \rho | \eta_1 \rangle P_Z(\eta_1)}{\partial t} + \boldsymbol{\nabla} \cdot \langle \rho \boldsymbol{u} | \eta_1 \rangle P_Z(\eta_1) = -\frac{\partial^2 \langle \rho N | \eta_1 \rangle P_Z(\eta_1)}{\partial \eta_1^2}, \tag{2.53}$$

where N is the dissipation rate of the mixture fraction defined in (2.37). Presuming the shape of the PDF simplifies the problem of solving this partial differential equation. Instead, only the mean and variance transport equations for the mixture fraction are solved for. The mean thermochemical properties are then obtained by assuming the chemical equilibrium of a laminar flame profile and integrating using the presumed shape PDF over the sample mixture fraction space to obtain Favre averaged mean values. Previous studies have shown (Borghi, 1988; Peters, 2000) that the optimal shape which best describes the major parts of the flow is a beta-PDF profile. The difficulty with such an approach lies in the fact that concentrations of minor species such as CO and NO which are time dependent, and usually slower in formation, are over-estimated as a result.

2.3.5 PDF Methods

The PDF method (Pope, 1985) is based on the computation of the joint stochastic distribution of all reactive and conserved scalars as the turbulent reacting flow evolves in space and time. There are several recognisable types of PDF transport approaches which lead to closure, e.g. the joint scalar or joint velocity-scalar levels. The main advantage of PDF methods stems from the fact that the previously averaged non-linear source term now appears in its exact closed form in the PDF transport equation. Consequently multi-step chemical mechanisms for finite rate thermochemistry can be included without the need for approximations. Due to the dimensionality of the PDF, a finite volume technique is prohibitive and a stochastic approach, usually of a Monte Carlo type, featuring tracking of particles in a Lagrangian framework, is used to extract the evolution of the PDF. The advantage of such an approach is that the computational cost is linear with the number of solved random variables included in the PDF function. As a result, the computation becomes more tractable when considering a larger number of scalars, for instance with the use of augmented reduced chemical mechanisms. This allows for the inclusion of a sufficient number of species and a more complete description of extinction and ignition phenomena in combustion related devices (Lindstedt, 2000). The method can be effective in modelling the extinction and re-ignition processes as it (potentially) allows for an accurate evaluation of the extent of scalar fluctuations. However, there still remain some uncertainities about the universality of the mixing models used in this approach, especially due to the heuristic nature of the presumption of the C_ϕ value to adjust the mixing time scales. The need for mixing models is obviated in deterministic approaches like FM or CMC and their lower dimensionality makes them equally (if not more) desirable than PDF methods.

2.3.6 Flamelet Models

The nature of turbulent flows is such that the flamelets will themselves vary over space and time. So long as the reaction zone thickness remains below the Kolmogorov scale, combustion will occur in the semi-laminar flow trapped within that eddy and through convenient coordinate transformations, Peters (1984) obtains the following transport equation to be solved:

$$\rho \frac{\partial \phi_\iota}{\partial t} = \frac{\rho}{Le_\iota} N \frac{\partial^2 \phi_\iota}{\partial Z^2} + \omega_\iota, \tag{2.54}$$

In the context of (2.54), fluctuations of the species mass fraction, ϕ_ι, are negligible but the reaction rate, ω_ι, must now be considered. For the steady case, (2.54) can be integrated over mixture fraction space. However the numerical integration is too costly. Consequently, as the unsteady flamelet will clearly depend upon both Z and N, the PDF function is simply adjusted to include effects of scalar dissipation, which now has a statistical distribution attached to it. With this in mind, a more appropriate PDF is defined as a function of Z and N and by assuming that within the shear layers N approximately equals its stoichiometric value, N_s. Bilger (1980) first proposed a statistical independence between both random variables such that the joint PDF can be split into two components,

$$P_{Z,N_s} = P_{N_s} P_Z \tag{2.55}$$

In steady LFM (i.e. for $\partial \phi_\iota / \partial t = 0$), flamelet tables in the form of $\phi_\iota = \phi_\iota(Z, N)$ functions are pre-computed for a range of Z and N values appropriate to the flame under investigation. P_Z is generally taken to be a β-function, whereas the PDF for the scalar dissipation is required to be lognormal (Peters, 1984). Recent experiments and DNS data (Karpetis & Barlow, 2002; Hawkes *et al.*, 2006) corroborate this.

However, by neglecting the unsteady part of the flamelet equation, Pitsch (2000) shows that one cannot include the transient behaviour of flamelets, which inhibits the profiles from undergoing changes while they are transported convectively downstream of the jet nozzle exit. Both Peters (2000) and Pitsch (2000) argue that in a Lagrangian treatment of the flamelet development the streamwise location, x, of the flamelet is uniquely related to the time interval, Δt, of convection

$$\Delta t = \int_0^x \frac{1}{\langle u(x') | Z = Z_s \rangle} dx', \tag{2.56}$$

where one representative flamelet is solved simultaneously and coupled with the flow field calculation. In order to produce reasonable results, the input into the combustion model (to determine the flamelet table) must be well specified. This will depend on the axial velocity at the stoichiometric mixture, the mean mixture fraction and the variance of the mixture fraction. A stochastic mixing approach to predict the local scalar dissipation rate and a defined re-ignition parameter using simplified stochastic differential equations has also been devised recently (Pitsch *et al.*, 2003). This approach enhances the description of the effects of extinction and relight in unsteady LFM, but discrepancies remain when compared to DNS data.

2.3.7 Conditional Moment and Mapping Closures

In its traditional formulation the flamelet model does allow for moderate deviations of scalar concentrations from their equilibrium values (cf. Sec. 2.3.6). These deviations are limited to the reaction zone, which is presumed to be thin. This makes the model inherently unsuitable in describing reaction or transport processes outside of the thin reaction zone, such as those related to pollutant formation. Furthermore, the flamelet model assumes an explicit functional dependence of scalar concentrations on the mixture fraction and therefore neglects the scalar fluctuations around these values. On the other hand, CMC modelling (Klimenko & Bilger, 1999) approaches the problem by considering chemical species, or (minor) quantities, conditionally averaged on one or two (major[4]) quantities that govern the fluctuating behaviour of the turbulent reacting system. It follows that a suitable choice of major quantities amongst all scalars will result in negligible fluctuations around the aforesaid conditional means. Computing/presuming the joint distribution of only the major quantities, instead of the whole joint scalar-PDF, is required to model extinction and re-ignition phenomena in turbulent non-premixed flames. It is generally

---

[4] The 'major-minor' terminology is not common in CMC literature. This has been used here for explanatory consistency with MMC.

recognised that the fluctuations in the scalar concentrations (chemical species and temperature) for many finite-rate reactions in non-premixed combustion are mainly governed by the mixture fraction fluctuations. Therefore, the singly-conditioned CMC formalism recognises the mixture fraction as a major source of fluctuations and relaxes the flamelet assumption of expressing the species concentration as a function of Z. The species mass fractions exhibit relatively low variations about the mean conditioned on the mixture fraction i.e. $\langle \phi_\iota | Z = \eta_1 \rangle$. In the limit where these fluctuations about the conditional mean become negligible, the chemical source term in the Favre averaged species transport equation can be arguably re-written as $\langle \omega_\iota(\phi) | Z = \eta_1 \rangle \simeq \omega_\iota(\langle \phi | Z = \eta_1 \rangle)$. Consequently models for the conditional means terms combined with a presumed PDF in mixture fraction space are sufficient to provide closure.

Scalar conditional averages are modelled at a single point and time and denoted by $Q_\iota(\eta_1)$ which corresponds to a conditioning of species mass fraction with respect to the mixture fraction space variable η_1, where

$$Q_\iota(\eta_1) = \langle \phi_\iota | Z = \eta_1 \rangle \equiv \langle \phi_\iota | \eta_1 \rangle \tag{2.57}$$

and the conditional fluctuations, Q''_ι, complete the description

$$\phi_\iota = Q_\iota(\eta_1) + Q''_\iota. \tag{2.58}$$

By applying conditional statistics in the context of high Reynolds number flows, Klimenko & Bilger (1999) obtain the following transport equation for the ι^{th} singly-conditioned species mass fraction,

$$\rho_\eta \frac{\partial Q_\iota}{\partial t} + \langle \rho \boldsymbol{u} | \eta_1 \rangle \cdot \boldsymbol{\nabla} Q_\iota = \langle \omega_\iota | \eta_1 \rangle + \rho_\eta \langle D_\iota \boldsymbol{\nabla} Z \cdot \boldsymbol{\nabla} Z | \eta_1 \rangle \frac{\partial^2 Q_\iota}{\partial \eta_1^2} + e_{q,1} + e_{y,1}, \quad (2.59)$$

where

$$e_{q,1} = \left\langle \boldsymbol{\nabla} \cdot [\rho D_\iota \boldsymbol{\nabla} Q_\iota] + \rho D_\iota \boldsymbol{\nabla} Z \cdot \boldsymbol{\nabla} \frac{\partial Q_\iota}{\partial \eta_1} + \boldsymbol{\nabla} \cdot [\rho (D_\iota - D) \boldsymbol{\nabla} Z] \frac{\partial Q_\iota}{\partial \eta_1} \right| \left. \eta_1 \right\rangle, \quad (2.60)$$

and

$$e_{y,1} = - \left\langle \rho \frac{\partial Q_\iota''}{\partial t} + \rho \mathbf{u} \cdot \boldsymbol{\nabla} Q_\iota'' - \boldsymbol{\nabla} \cdot [\rho D \boldsymbol{\nabla} Q_\iota''] \right| \left. \eta_1 \right\rangle \quad (2.61)$$

Here, D_ι and D are the diffusivities of the ι^{th} species and the mixture fraction, respectively. Term $\rho_\eta = \langle \rho | \eta_1 \rangle$ denotes the conditionally averaged density, $\langle D_\iota \boldsymbol{\nabla} Z \cdot \boldsymbol{\nabla} Z | \eta_1 \rangle$ is the conditional scalar dissipation and $\langle \omega_\iota | \eta_1 \rangle$ is the conditional chemical source term. There is a clear similarity between the flamelet equation (2.54) and the singly-conditioned CMC equation (2.59), other than the convective terms in the latter. Both equations essentially describe the reactive-diffusive balance at the reaction zone of a non-premixed turbulent flame. However, the main difference between the two models is that the CMC equation does not require approximations as all variables are conditioned on mixture fraction, whereas the flamelet equations assume a very thin reaction zone and near-stoichiometric composition for scalar dissipation. Most of the terms in (2.59) are unclosed and require modelled approximations. A linear model is commonly used to model the conditional velocity (Klimenko & Bilger, 1999; Roomina & Bilger, 2001), and the singly-conditioned scalar dissipation rate is often modelled using amplitude mapping closure (Chen *et al.*, 1989; Girimaji, 1992). A simpler approach to approximate conditional dissipation by its unconditional mean value is also employed, but is accurate only in Gaussian turbulence (Klimenko & Bilger, 1999). Another closure strategy is to use a presumed form of the PDF and integrate the conditional PDF transport equation (2.53) in η_1-space.

Due to the reactive-diffusive structure of the non-premixed flames, the gradient of chemical species mass fraction with respect to the mixture fraction or $\partial Q_\iota/\partial\eta_1$, is negligible compared to species diffusion in the mixture fraction space, i.e. $\partial^2 Q_\iota/\partial\eta_1^2$, especially close to the stoichiometric composition. The same is not true of the diffusion in physical space, i.e. $\langle \boldsymbol{\nabla}\cdot[\rho D \boldsymbol{\nabla} Q_\iota]|\eta_1\rangle$, which is dominated by the convective transport, $\langle \rho \boldsymbol{u}|\eta_1\rangle \cdot \boldsymbol{\nabla} Q_\iota$. Combining these observations with the lack of differential diffusion effects implies that all constituents of the $e_{q,1}$ term can be safely neglected from (2.59) without seriously compromising the conditional species predictions. In addition, first-order CMC also assumes negligible fluctuations around the singly-conditioned mean, i.e. $e_{y,1} = 0$ and only uses the conditional averages in the computation of the reaction rate term. This has produced good results for a variety of non-premixed flows, e.g. simple jet flames (Smith *et al.*, 1993, 1995), lifted flames (Devaud & Bray, 2003), bluff-body flames (Kim *et al.*, 2000, 2007; Navarro-Martinez & Kronenburg, 2007), furnaces (Rogerson *et al.*, 2005) and enclosure fires (Cleary & Kent, 2005). However, singly-conditioned, first-order CMC is not capable of accurately predicting species concentrations in the presence of local extinction and re-ignition, due to large conditional fluctuations in such cases. Thus, either second-order closure (modelling of conditional variance terms) or double-conditioning (on mixture fraction and an additional variable) can be used to compensate for these shortcomings.

Second order closures applied to the source term have been incorporated and examined by Kim and co-workers (Kim & Huh, 2002; Kim *et al.*, 2002) and include equations for conditional variances and co-variances initially in the context of a reduced chemical mechanism. This is due to the difficulty of its computational implementation leaving an insufficient description of intermediate and minor species. Recently, Kim *et al.* (2004) applied a detailed chemical mechanism to predict the structure of a turbulent diffusion flame, comparing both first and second order closures. Kim *et al.* (2004) argued that higher order corrections do not influence major species so much and higher order closures should only be applied to key intermediate and minor species reactions since they are shown to have a beneficial effect on species such as CO and NO, leaving major species unchanged.

An alternative approach is to consider multiple conditioning variables to reduce the conditional fluctuations (Bilger, 1992). Scalar dissipation was clearly the initial choice as a direct consequence of its effect on scalar fluctuations. Studies by Cha and coworkers (Cha *et al.*, 2000, 2001) showed doubly-conditioned CMC as a better alternative to the singly-conditioned first-order and second-order closure assumptions for single-step chemistry. These studies followed the LFM approaches to propose the idea of scalar dissipation rate as a second conditioning variable, which results in good extinction modelling but predicts re-ignition too prematurely due to significant fluctuations around the doubly-conditioned mean of the dissipation rate of N. It has also been demonstrated (Kronenburg, 2004) that fluctuations of temperature from the mean doubly-conditioned on Z and N are large and as a result the reaction-rate closure becomes generally inaccurate. Instead, a more cogent argument has been made for reduced temperature (Bilger, 1992) or, more recently, sensible enthalpy, h_s (Kronenburg, 2004; Kronenburg & Papoutsakis, 2005; Kronenburg & Kostka, 2005), as a physically and computationally more viable alternative to N in doubly-conditioned moment closure. The exact form of the doubly-conditioned chemical species transport equation, with mixture fraction and sensible enthalpy as the conditioning variables has been derived by Kronenburg (2004) and for cases without differential diffusion it is given by,

$$
\begin{aligned}
\langle \rho | \eta_1, \eta_2 \rangle \tfrac{\partial \mathcal{Q}_\iota}{\partial t} + \langle \rho \boldsymbol{u} | \eta_1, \eta_2 \rangle \cdot \boldsymbol{\nabla} \mathcal{Q}_\iota \quad = \quad & \langle \omega_\iota | \eta_1, \eta_2 \rangle - \langle \omega_{h_s} | \eta_1, \eta_2 \rangle \tfrac{\partial \mathcal{Q}_\iota}{\partial \eta_2} + \\
& \langle \rho D_\iota \boldsymbol{\nabla} Z \cdot \boldsymbol{\nabla} Z | \eta_1, \eta_2 \rangle \tfrac{\partial^2 \mathcal{Q}_\iota}{\partial \eta_1^2} + \\
& 2 \langle \rho D_\iota \boldsymbol{\nabla} Z \cdot \boldsymbol{\nabla} h_s | \eta_1, \eta_2 \rangle \tfrac{\partial^2 \mathcal{Q}_\iota}{\partial \eta_1 \partial \eta_2} + \\
& \langle \rho D_\iota \boldsymbol{\nabla} h_s \cdot \boldsymbol{\nabla} h_s | \eta_1, \eta_2 \rangle \tfrac{\partial^2 \mathcal{Q}_\iota}{\partial \eta_2^2} + e_{q,2} + e_{y,2},
\end{aligned}
\tag{2.62}
$$

where the sample space for the sensible enthalpy variable, $\phi_2 \equiv h_s$, is given by η_2. The $\mathcal{Q}_\iota = \langle \phi_\iota | \eta_1, \eta_2 \rangle$ term denotes the doubly conditioned mean in the composition-enthalpy space and $\mathcal{Q}_\iota''$ represents the fluctuations around it. All terms of the type $\langle D_\iota \boldsymbol{\nabla} \phi_i \cdot \boldsymbol{\nabla} \phi_j | \eta_1, \eta_2 \rangle$, where $i, j = 1, 2$, in (2.62) represent the unclosed doubly conditioned dissipation variables. The expressions for $e_{q,2}$ and $e_{y,2}$ terms are simply extensions of the singly-conditioned case.

$$
\begin{aligned}
e_{q,2} \quad = \quad & \Big\langle \boldsymbol{\nabla} \cdot [\rho D_\iota \boldsymbol{\nabla} \mathcal{Q}_\iota] + \rho D_\iota \boldsymbol{\nabla} Z \cdot \boldsymbol{\nabla} \tfrac{\partial \mathcal{Q}_\iota}{\partial \eta_1} + \rho D_\iota \boldsymbol{\nabla} h_s \cdot \boldsymbol{\nabla} \tfrac{\partial \mathcal{Q}_\iota}{\partial \eta_2} + \\
& \boldsymbol{\nabla} \cdot [\rho (D_\iota - D) \boldsymbol{\nabla} Z] \tfrac{\partial \mathcal{Q}_\iota}{\partial \eta_1} + \boldsymbol{\nabla} \cdot [\rho (D_\iota - \alpha) \boldsymbol{\nabla} h_s] \tfrac{\partial \mathcal{Q}_\iota}{\partial \eta_2} \Big| \, \eta_1, \eta_2 \Big\rangle ,
\end{aligned}
\tag{2.63}
$$

and

$$
e_{y,2} = - \left\langle \rho \frac{\partial \mathcal{Q}_\iota''}{\partial t} + \rho \mathbf{u} \cdot \boldsymbol{\nabla} \mathcal{Q}_\iota'' - \boldsymbol{\nabla} \cdot [\rho D \boldsymbol{\nabla} \mathcal{Q}_\iota''] \right| \left. \eta_1, \eta_2 \right\rangle \tag{2.64}
$$

The double-conditioning introduces the new thermal diffusivity term, α, into the expression for $e_{q,2}$. The primary closure hypothesis of setting $e_{y,2} = 0$ is very well justified for conditioning by two scalars. On the other hand, unless differential diffusion effects predominate, closure of $e_{q,2} = 0$ follows the same order-of-magnitude reasoning given for the singly-conditioned CMC terms. This relatively recent approach has lead to some promising results (Kronenburg, 2004; Kronenburg & Papoutsakis, 2005) for two- and four-step chemistry in homogeneous decaying turbulence. However, the method faces a major shortcoming, viz. the lack of closure of the doubly-conditional scalar dissipation (Kronenburg, 2004) terms and of the joint-PDFs of Z and h_s. Assuming β-function shapes for the PDFs of the conditional sensible enthalpy, $\langle h_s|Z\rangle$, has been shown to give partially acceptable results (Kim *et al.*, 2002; Kronenburg & Papoutsakis, 2005). However, computing the correct PDF shape requires the provision of the conditional enthalpy variance, $\langle h_s''^2|Z\rangle$, and that in turn suffers from the deficient second-order closure modelling needed to solve the governing equations for $\langle h_s''^2|Z\rangle$ (Swaminathan & Bilger, 1999; Kim, 2002; Kim *et al.*, 2002).

Overall, CMC has proven to be a successful method of modelling turbulent jet flames. While doubly-conditioned CMC improves on the singly-conditioned CMC predictions for extinction and (more importantly) re-ignition phenomena by modelling the chemical source term accurately, it is limited by the lack of reliable closures for the scalar dissipation terms. The application of mapping closures has recently emerged in the context of turbulent non-premixed combustion. The mapping closure approach for passive scalar turbulence was initially discussed by Chen *et al.* (1989) and Pope (1991). For stochastically advected passive scalars in homogeneous turbulence, fluctuations are solved for by mapping the scalar distribution on to a set of alternative reference variables with a presumed (joint-Gaussian) PDF. Multiple mapping conditioning (MMC) applied to turbulent reacting flows (Klimenko & Pope, 2003) has ramified into *deterministic* MMC and *probabilistic* MMC, where in the case of the former minor fluctuations are ignored and, in the latter, they are treated with conventional stochastic mixing models. Major fluctuations are solved by mapping them to a set of prescribed stochastic reference variables. The aim is to provide an attractive compromise between CMC and joint PDF methods depending upon the number of major and minor species groupings that are chosen. A detailed discussion on the MMC methods can be found in Chapter 5.

The next chapter presents the relevant details on the numerical, thermodynamic and chemistry modelling implemented in the Pantano (2004) DNS. This DNS database is primarily used for the post-processing of the scalar dissipation statistics and for validating the combustion models implemented in the present study.

Chapter 3

Relevant attributes of the simulation

The following sections describe the various key parameters and attributes of the Pantano (2004) DNS. The physical setup of the three-dimensional turbulent jet flame simulation is described first, followed by detailed introductions to the thermodynamics and chemistry models used in the DNS. Finally, we explain the numerical resolution and extinction/reignition characteristics of the DNS that are particularly relevant to the present work.

3.1 Setup and Geometry

The present study makes use of the extensive database of a three-dimensional Direct Numerical Simulation (DNS) of a spatially-evolving planar turbulent jet flame by Pantano (2004). The simulation models the non-premixed combustion of methane (fuel stream) with air (coflow) using a four-step reduced chemical mechanism (Peters, 1985). To enhance flame stability at the inflow and avoid flame lift-off or

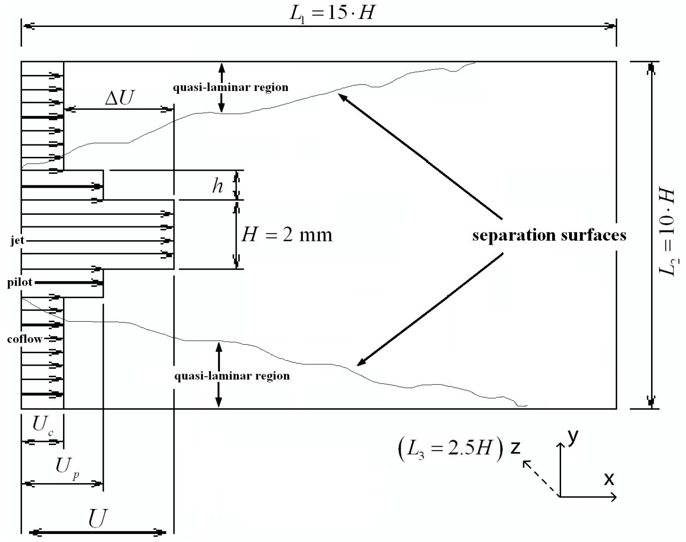

Figure 3.1: Schematic of the computational domain. The spanwise dimension L_3, not shown here, is orthogonal to the plane of the figure.

blow-out, a pilot is inserted between the jet core and the main co-flow. This pilot is implemented numerically as a thin, burning coflow at stoichiometric composition and with a high temperature, equal to the adiabatic flame temperature for the employed chemistry model. Moreover, the pilot streamwise velocity is slightly higher than that of the main coflow to avoid recirculation. This technique has been used by Wall *et al.* (2000) to stabilize round jet flames. The flame at these pilot conditions burns below the quenching rate of scalar dissipation and remains attached to the inflow of the domain.

The DNS solves the compressible Navier-Stokes equations Pantano *et al.* (2003) for 8 scalar and 5 fluid-mechanical fields at a moderately low Mach number (i.e. with negligible compressibility effects) on a large cuboidal computational grid of $(N_x = 1024) \times (N_y = 512) \times (N_z = 192)$ grid-points, where the x-, y- and z- Cartesian coordinate axes are aligned with the streamwise, cross-stream and spanwise directions, respectively. Fig. 3.1 shows the schematic of the computational domain. The domain size is L_1 in the streamwise direction, L_2 in the transverse/cross-stream direction and L_3 in the spanwise direction. The jet nozzle width is denoted by H

and that of the pilot is denoted by h. The fuel-jet is composed of a mixture of methane and nitrogen. The coflow is composed of air approximated as a mixture of oxygen and nitrogen. Both, methane and oxygen, mass fractions are equal to 0.23. The global chemistry step can be described by

$$\mathrm{CH_4} + 2\mathrm{O_2} \rightarrow \mathrm{CO_2} + 2\mathrm{H_2O} \tag{3.1}$$

3.2 Thermodynamics

The attributes of the DNS are given in Table 3.1. Here, U_j is the efflux velocity of the jet, $\Delta u = U_j - U_c$ is the velocity difference (at efflux) between the co-flow and the jet, c_1 and c_2 are the respective speeds of acoustic propagation in the fuel- and air- streams, ν_0 is the kinematic viscosity of air at STP conditions and Φ is the fuel-air equivalence ratio. The convective Mach number is denoted by M_c and defined as in Bogdanoff (1983) and Papamoschou & Roshko (1988). The value of M_c (cf. Table 3.1) is small enough so that compressibility effects are not important (Pantano *et al.*, 2003). The jet and coflow have the same density and the influence of density variation is exclusively associated with heat release. The pressure across the air and fuel streams is constant. This implies that the fuel-air temperature ratio is equal to the average molecular weight ratio of the air in the coflow to that of the fuel in the jet. Thus, the air temperature is 20% higher than the fuel temperature of $298K$. The latter value is maintained as the reference temperature level, T_o, corresponding to the mixture density, ρ_o. Specific heats of the species in the ideal gas mixture depend on temperature. The specific heats at constant pressure and enthalpy are obtained from NASA polynomial fits (McBride *et al.*, 1995). The values of these parameters give an adiabatic flame temperature of $T_{adia} = 2022\mathrm{K}$.

Table 3.1: Geometrical specifications of the computational domain of the analyzed DNS, including the general physical attributes of the simulated flow. The Taylor Reynolds number, Re_λ, is defined according to Pope (2000).

Geometrical attributes

Nozzle width	H	$\sim 2\,mm$
Pilot width	h	$0.325\,H$
Computational box dimensions	(L_1, L_2, L_3)	$(15\,H, 10\,H, 2.5\,H)$

Physical attributes

Co-flow and Pilot velocities	$U_c,\ U_p$	$0.029\,U_j,\ 0.29\,U_j$
Convective Mach number	$M_c = \Delta u / (c_1 + c_2)$	0.3
Damköhler number	$Da = H M_o \mathcal{A}_o / (\Delta u \rho_o)$	5000
Jet-exit Reynolds number	$Re = \Delta u H / \nu_0$	3000
centreline Taylor Reynolds nos.	Re_λ	38 to 58
Prandtl number for air	$Pr = \nu/\alpha$	0.7
Stoichiometric mixture fraction	$Z_s = 1/(\Phi + 1)$	0.2

Unless specified otherwise, all variables in the DNS formulation and used henceforth are non-dimensionalised with respect to reference length, mass, time, molar and temperature units. The reference molecular weight is that of oxygen, O_2, and is denoted by M_o. The time-scale associated with the chemistry is determined in terms of the characteristic reaction rate, $\mathcal{A}_o$, given by (3.18). The units of length, velocity, time, density, enthalpy and pressure are H, Δu, $t_o = H/\Delta u$, ρ_o, $C_{pOo} T_o$ and $\rho_o \Delta u^2$, respectively. Here C_{pOo} is the specific heat at constant pressure of oxygen at T_o.

The DNS introduces certain simplifications in the molecular transport properties. The viscosity μ is taken to be proportional to T^m, where T denotes the temperature with the exponent $m = 0.7$. All scalars are assumed to have diffusion coefficients, D_I with similar temperature dependence,

$$\rho D_I = \frac{T^m}{Re Pr Le_I}. \tag{3.2}$$

Here, ρ is the instantaneous, local density in the jet flow and $Re = 3000$ is the jet-exit Reynolds number of the flow at the nozzle conditions. The constancy of the Prandtl number is also imposed, and the value of $Pr = 0.7$ (for air) is used throughout. The reference values of D_I and the thermal diffusivity α at T_o are obtained from Smooke & Giovangigli (1991). The values of the Lewis numbers, $Le_I = \alpha/D_I$, of the different species are specified in Table 3.2. The thermal effects on species diffusivities are thereby taken into account in this simplified transport model. For mixture fraction and sensible enthalpy as the scalars, $D_I = D = \alpha$ and $Le_I = 1$ are used in (3.2).

The stoichiometric mixture fraction, Z_s, is given by

$$Z_s = \frac{1}{1+\Phi}. \tag{3.3}$$

It should be noted that the value of the stoichiometric mixture fraction, Z_s, in the present DNS is four to eight times larger than that for pure hydrocarbon-air flames due to the dilution of the hydrocarbon fuel with nitrogen. The non-dimensional sensible enthalpy of the mixture can be directly computed from the temperature values (non-dimensionalised by T_o) using the form for (2.16) as,

$$h_s = \int_1^T C_p dT, \tag{3.4}$$

where C_p is the non-dimensionalised value of the specific heat at constant pressure of the gaseous mixture and is related to the specific heats of individual species as in (2.14). The specific heats of the individual chemical species, $C_{p_\iota}(T)$, are expressed as polynomial functions of the temperature with coefficients given by McBride *et al.* (1995). For convenience, the non-dimensionalised value is further normalised with respect to the maximum sensible enthalpy at the adiabatic flame temperature, $T_f = T_{adia}/T_o$, given by $h_{s_{max}} = \int_1^{T_f} C_p dT$. Thus, the normalised value of the sensible enthalpy is given by

$$\hat{h}_s = h_s / h_{s_{max}} \tag{3.5}$$

such that $\hat{h}_s \in [0,1]$ just like the $[0,1]$ bounded mixture fraction. In the present study, the normalised value, $\hat{h}_s$, is used in lieu of the actual h_s value for computation. This, in turn, requires the sensible enthalpy gradient and chemical source terms be scaled by a factor of $1/h_{s_{max}}$ as well. Finally, the non-dimensional equation of state for the gaseous mixture is given by,

$$\frac{\rho T}{\bar{M}} = \frac{p_{real} M_o}{\rho_o R T_o} \tag{3.6}$$

where p_{real} is the dimensional gas pressure within the mixture and $R = 8.314\mathrm{Jmol}^{-1}\mathrm{K}^{-1}$ is the universal gas constant for ideal gases. $\bar{M}$ is the normalised average molecular weight of the gaseous mixture and is given in terms of the species molecular weights M_ι as,

$$\bar{M} = \left(M_o \sum_{\iota=1}^{n_s - n_r} \frac{\phi_\iota}{M_\iota} \right)^{-1} . \tag{3.7}$$

Since the pressure fluctuations due to acoustic effects are negligible in the DNS formulation and the density variation is exclusively associated with heat release, the right-hand side of (3.6) can be computed at inlet conditions of standard air temperature and pressure (i.e. $p_{real} = 1$ atm and $T_o = 298$ K) to give a non-dimensionalised value of ~ 1.01. Therefore, the density is computed directly as

Table 3.2: Constant Lewis numbers (Smooke & Giovangigli, 1991) of all the species involved in the reduced four-step chemistry model employed for the Pantano (2004) DNS.

Lewis numbers for the chemical species

CH_4	O_2	H_2O	CO_2	CO	H_2	H	N_2
0.97	1.11	0.83	1.39	1.10	0.30	0.18	1.00

function of temperature and the species mass fractions in the present study.

3.3 Chemistry

In order to reduce the computational cost associated with full chemistry models, the Pantano (2004) DNS uses a reduced mechanism of Peters (1985) for the combustion of methane. This is a four-step mechanism, derived from a skeletal C-1 mechanism by systematic application of quasi-steady state and partial equilibrium approximations and by truncating the resulting non-linear relationships between the mass fractions of the species in quasi-steady state. This renders the algebraic expressions of the reaction rates explicit. The mechanism involves 8 species, namely, CH_4, O2, H_2O, CO_2, CO, H_2, H and N_2. Thus, seven transport equations with non-zero reaction rates are solved along with the flow variables. The mass fraction of N_2 is obtained from the balance of all species and no transport equation is thus required for this inert species. Therefore the inert mass fraction of N_2 is

$$\phi_{\mathrm{N}_2} = 1 - \sum_{\iota \neq \mathrm{N}_2}^{n_s - n_r} \phi_\iota \tag{3.8}$$

where the index ι goes through all the other 7 chemical species and ϕ_ι denotes the ι^{th} mass fraction. Peters (1985) reduced mechanism can be represented by the following global reactions:

$$\begin{aligned} \mathrm{CH_4 + 2H + H_2O} &= \mathrm{CO + 4H_2} \quad (I) \\ \mathrm{CO + H_2O} &= \mathrm{CO_2 + H_2} \quad (II) \\ \mathrm{H + H + G} &= \mathrm{H_2 + G} \quad (III) \\ \mathrm{O_2 + 3H_2} &= \mathrm{2H + 2H_2O} \quad (IV) \end{aligned}$$

The reaction-rate expressions for the rates of production/consumption of the species are provided as algebraic expressions of the concentrations and temperature as in Seshadri & Peters (1988). The non-dimensional reaction rates corresponding to the global step-reactions above are,

$$\begin{aligned} \mathcal{W}_I &= k_{11} C_{\mathrm{CH_4}} C_{\mathrm{H}}, && (3.9) \\ \mathcal{W}_{II} &= k_{10} \frac{C_{\mathrm{H}}}{C_{\mathrm{H_2}}} \left(C_{\mathrm{CO}} C_{\mathrm{H_2O}} - C_{\mathrm{CO_2}} \frac{C_{\mathrm{H_2}}}{K_{II}} \right), && (3.10) \\ \mathcal{W}_{III} &= k_5 C_{\mathrm{O_2}} C_{\mathrm{H}} C_{\mathrm{G}}, && (3.11) \\ \mathcal{W}_{IV} &= k_1 C_{\mathrm{H}} \left(C_{\mathrm{O_2}} - C_{\mathrm{H}}^2 \frac{C_{\mathrm{H_2O}}^2}{C_{\mathrm{H_2}}^3} K_{IV} \right). && (3.12) \end{aligned}$$

The non-dimensional concentration of the ι^{th} chemical species, C_ι, is defined by

$$C_\iota = \frac{\rho \phi_\iota M_o}{M_\iota} \tag{3.13}$$

,

and the third body concentration, C_G, is defined as

$$C_G = \sum_{\iota=1}^{n_s - n_r} C_\iota G_\iota, \tag{3.14}$$

Table 3.3: Specific dimensional reaction rate parameters appearing in (3.15) for each reaction sub-step in the reduced chemistry model employed for the Pantano (2004) DNS. The values are taken from Seshadri & Peters (1988) and the units are in cm, mole, Kelvin and kJ.

Reaction rate parameters

Reaction	$\mathcal{A}_i$	β_i	E_i
k_1	1.2×10^{17}	-0.91	69.10
k_5	2.0×10^{18}	-0.8	0.0
k_{10}	1.2656×10^{7}	1.5247	60.042
k_{11}	2.2×10^{4}	3.0	36.6

with catalytic efficiencies $G_{CH4} = G_{H_2O} = 6.5$, $G_{O_2} = G_{N_2} = 0.4$, $G_{CO_2} = 1.5$, $G_{CO} = 0.75$ and $G_{H_2} = G_H = 1$ as given by Smooke & Giovangigli (1991).

The mechanism given by (I)-(IV) is a global representation of the chemistry and should not be confused with the actual paths that the reaction takes. These are not elementary reactions; their rates are expressed as algebraic functions of rates appearing in the skeletal C-1 mechanism. The reaction-rate constants, ${k_i}^1$, are given in the customary Arrhenius form,

$$k_i = A_i T^{\beta_i} exp\left(\frac{-E_i}{RTT_o}\right), \tag{3.15}$$

where A_i is the non-dimensionalised pre-exponential Arrhenius factor, E_i is the (dimensional) activation energy per unit mole for each reaction sub-step and T is the non-dimensionalised temperature. The remaining constants, K_{II} and K_{IV} in (respectively) (3.10) and (3.12) are determined according to the following expressions:

$$K_{II} = 0.0039512\, T^{0.8139}\, exp\left(\frac{16.6247}{T}\right), \tag{3.16}$$

---

[1] where $i = 1, 5, 10, 11$

Table 3.4: The reaction rate coefficients of all the chemical species for the reduced chemistry mechanism employed in the Pantano (2004) DNS. The coefficients are used to compute the rate of production of the ι^{th} chemical species using (3.19), in terms of the rates for the individual reaction sub-steps given by (3.9)-(3.12).

Species reaction rate coefficients

Chemical species	CH_4	O_2	H_2O	CO_2	CO	H_2	H
c_I	-1	0	-1	0	1	4	-2
c_{II}	0	0	-1	1	-1	1	0
c_{III}	0	0	0	0	0	1	-2
c_{IV}	0	-1	2	0	0	-3	2

$$K_{IV} = 2.7405\, T^{-0.2484}\, exp\left(\frac{19.262}{T}\right). \tag{3.17}$$

The values of the parameters appearing in (3.15) are obtained by non-dimensionalizing the dimensional rate constants reported in Table 3.3 by the largest of the rates at T_o, in this case, that of reaction k_5. This characteristic dimensional reaction rate (units of moles per unit volume and time) is given by

$$\mathcal{A}_o = \mathcal{A}_5 T_o^{\beta_5} exp\left(\frac{-E_5}{RT_o}\right)\cdot\left(\frac{\rho_o}{M_o}\right)^3 \tag{3.18}$$

Finally, the rates of production of each ι^{th} chemical species can be defined in terms of the rates of the individual reaction sub-steps (I)-(IV) using,

$$\omega_\iota = Da\frac{M_\iota}{M_o}\left(c_I\mathcal{W}_I + c_{II}\mathcal{W}_{II} + c_{III}\mathcal{W}_{III} + c_{IV}\mathcal{W}_{IV}\right), \tag{3.19}$$

where c_I-c_{IV} are the species-specific coefficients of the reaction rate model in (3.19) and their values are laid out in Table 3.4. The species reaction rate ω_ι is scaled by the constant Damköhler number specified in Table 3.1. A common difficulty encountered in the implementation of reduced mechanisms is the presence of algebraic terms in the denominator of the reaction rate expressions. When the denominator goes to zero, the reaction rate becomes infinitely large. In this case, the presence of the concentration of H_2 in the denominator of (3.10) and (3.12) leads to this undesired behaviour. In regions where there is no H_2, these expressions diverge to infinity and an appropriate regularization must be applied for numerical purposes. As suggested by Peters (1991), a common regularization is to add a small constant, e_o, to the denominator of (3.10) and (3.12) so that $1/C_{\mathrm{H}_2}$ becomes $1/(C_{\mathrm{H}_2} + e_o)$, in order to avoid the singularity. Pantano (2004) found that this regularization was sufficient for a one-dimensional flamelet test calculation but not in the full flame DNS, where shifting the hydrogen concentration by e_o was not satisfactory at all points of the computational domain. Compact regions with aphysically high values of the reaction rates were still prevalent far away from the flame. Keeping this in mind, the algebraic singularity in hydrogen concentration in the reduced chemistry model employed in the DNS has been regularised with,

$$\frac{1}{C_{\mathrm{H}_2}} \rightarrow \begin{cases} 0, & 0 \leqslant C_{\mathrm{H}_2} < e_o, \\ \tanh\left(\frac{C_{\mathrm{H}_2} - e_o}{e_o}\right) \frac{1}{3e_o}, & e_o \leqslant C_{\mathrm{H}_2} < 3e_o, \\ \frac{1}{C_{\mathrm{H}_2}}, & 3e_o \leqslant C_{\mathrm{H}_2}. \end{cases} \tag{3.20}$$

The same regularisation scheme for the H_2 concentration has been used in the present work while encoding the chemistry model for the CMC/MMC calculations described in Chapter 5. The value of e_o was chosen to be approximately equal to 1% of the maximum concentration of H_2 in the simulation, viz. $e_o \simeq 1.6 \times 10^5$. These choices allow a very smooth transition of the reaction rates from the flame region to the regions where C_{H_2} is zero.

3.4 Resolution and numerical characteristcs

This DNS uses a compact Padé scheme with sixth-order accuracy for the computation of the spatial derivatives (Lele, 1992). The scheme provides an improved resolution of the finer length scales without numerical dissipation. It is noted that the grid-discretisation employed in the DNS is fine enough to capture the instantaneous χ-distribution. This can be deduced from the distribution of the grid-normalised dissipation length scales that are shown in Fig. 4.16 in Sec. 4.4. This highly-resolved DNS models the jet flow close to the nozzle, a region important for flame stabilisation. The near-nozzle region of jet flames has remained virtually unstudied with respect to the scaling laws for the estimation of the smallest turbulence scales, but a better understanding of the spatial-resolution requirements for scalar dissipation in the stabilization region of the turbulent jet flame are as important as the well-studied self-similar regions further downstream.

The fuel consumption layer of the methane-air mechanism has been well resolved in the DNS in order to avoid numerical extinction (Seshadri & Peters, 1988) of the flame owing to the lack of resolution. A resolution of approximately 10 points across the fuel consumption layer was used for the DNS. The simulated turbulent jet flame is partially extinguished, predominantly at the centre of the domain, i.e. around $x = 7.5H$. In this region, the large-scale organised vortices shed from the shear layers have sufficient strength (large rate-of-strain) to extinguish the flame. Pantano (2004) uses the hydrogen radical field in the methane-air chemistry model to analyse of the topological structure of the flame reaction zone. Fig. 3.2 gives a good qualitative idea of the flame extinction/re-ignition characteristics in terms of the rendered instantaneous contours of the hydrogen radical mass fraction in three-dimensions. The extinguished regions are clearly visible in the centre of the domain as gaps in the hydrogen radical mass fraction, whereas the continuity of the surface close to

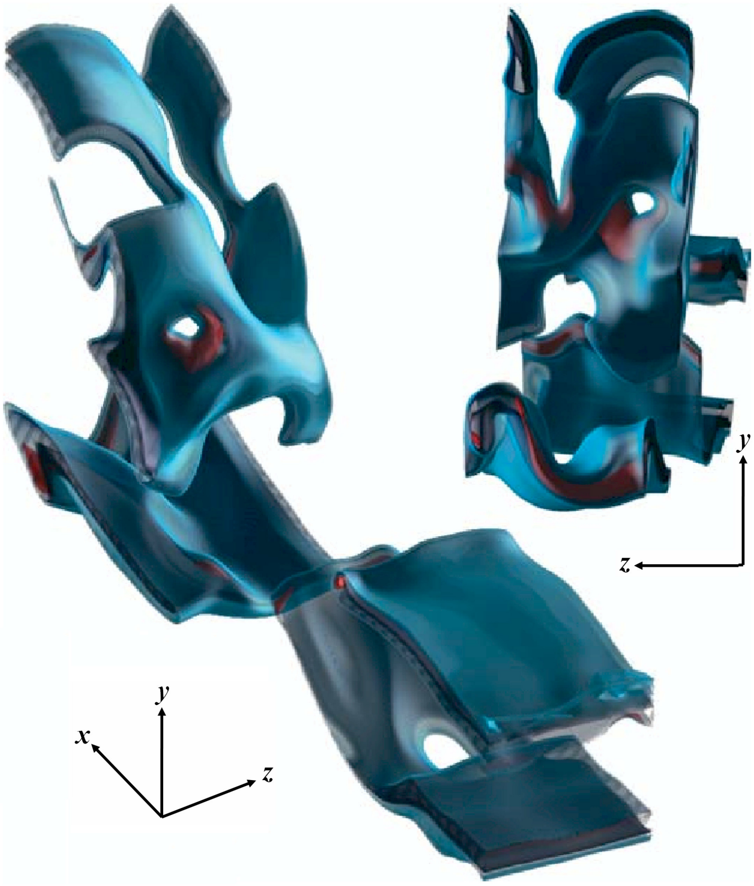

Figure 3.2: Three-dimensional rendering of the hydrogen radical mass fraction at an instant in time, reproduced from Pantano (2004). The axis orientations are as indicated next to each view.

the nozzle indicates a steadily burning pilot. Much of this continuity is regained far downstream as well, which signifies flame re-ignition.

The next chapter describes the application of the spectral analysis, level-set method and spatial-filtering techniques to the Pantano (2004) DNS data, in order to quantify the small-scale statistics of the instantaneous scalar dissipation rate field.

Chapter 4

Scalar dissipation scaling

The main motivation of the present study is to analyse the one-point statistics of instantaneous scalar dissipation using the computational methods categorised in Sec. 2.2.2 and to characterise the spatial length scales associated with dissipation in terms of easily measurable large-scale properties of the flow such as the outer-scale turbulent Reynolds number. The following sections outline a detailed description of the aforesaid approaches and the limitations involved in their implementation to the DNS database. The discussion of (and comparison between) the results from the different numerical methods is also detailed in the coming sections.

4.1 Spectral analysis

4.1.1 Cross-stream scalar dissipation spectra

The spectral theory of the turbulent velocity field has a direct analogy in turbulent scalar fields (Batchelor, 1959; Tennekes & Lumley, 1974). For sufficiently high Reynolds numbers and Schmidt numbers close to unity the form of the scalar spectra is similar to that of the velocity spectra.

In the present study, the one-dimensional scalar spectra, $E_Z(k_y)$, at wavenumber k_y is computed as the one-dimensional Fourier transform of the two-point cross-stream correlation, that is equivalent to the power spectrum of scalar fluctuations (Tennekes & Lumley, 1974; Pope, 2000) at various downstream locations. The two-point cross-stream correlation coefficient at any point (x_c, y_c) along the jet centreline is defined as,

$$R_Z(x_c, y_c, r) = \langle Z'(x_c, y_c, z, t) \cdot Z'(x_c, y_c + r, z, t) \rangle, \tag{4.1}$$

where r is the cross-stream distance and subscript c indicates jet centreline values. According to Pantano (2004), the average value is computed as a simultaneous mean in temporal (t-) and spanwise (z-) directions

$$\langle \vartheta \rangle (x, y) = \frac{1}{N_T N_z} \cdot \sum_{n=1}^{N_T} \sum_{k=1}^{N_z} \vartheta(x, y, z, t), \tag{4.2}$$

where N_T is the number of time steps and N_z is the number of spanwise planes over which the average of an arbitrary turbulent field $\vartheta(x, y, z, t)$ is computed. This is because the turbulent flow field at every time step and $z = constant$ spanwise section is considered as an independent realisation. Therefore, (4.2) represents the ensemble averaging of an arbitrary turbulent quantity ϑ. However, it should be noted that the true number of independent samples available to compute the averages at each (x, y) location will be over an order-of-magnitude less than $N_T \times N_z$, due to some spatial correlation in the turbulent quantities across the spanwise coordinate. Fig. 4.1 shows the plots of the normalised correlation coefficient,

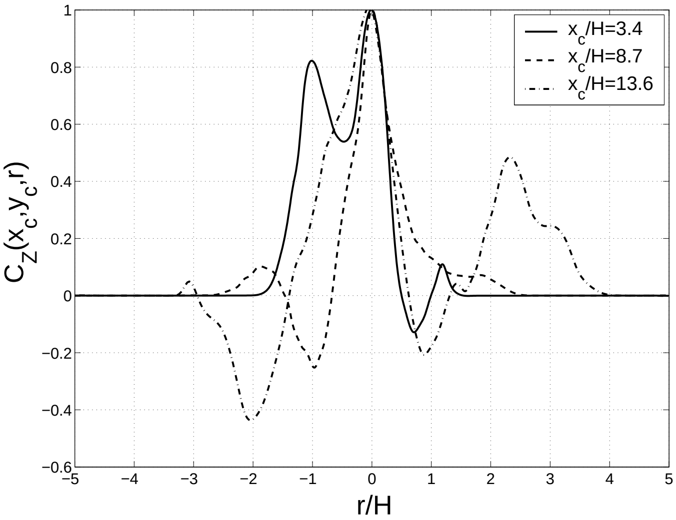

Figure 4.1: Variation of the normalised correlation coefficient $C_Z(x_c, y_c, r)$ with the cross-stream position vector r, at various downstream locations along the jet centreline ($y_c/H = 5.0$). All spatial quantities are shown in terms of jet-width, H. The one-dimensional dissipation spectra corresponding to the shown correlation coefficients are plotted in Fig. 4.3.

$$C_Z(x_c, y_c, r) = \frac{R_Z(x_c, y_c, r)}{\left[\langle Z'(x_c, y_c)^2\rangle \cdot \langle Z'(x_c, y_c + r)^2\rangle\right]^{1/2}}, \tag{4.3}$$

at various downstream locations along the jet centreline. Owing to the complex unstable nature of the studied flow and small-size of the computational domain ($x/H \leq 15$), the number of independent realisations is not enough to get R_Z profiles symmetric about the jet centreline. Therefore, isotropy about the centre-plane is not assumed while computing the correlation coefficients, i.e. in general $R_Z(x_c, y_c, r) \neq R_Z(x_c, y_c, -r)$.

The one-dimensional spectrum is defined as

$$E_Z(k_y) = \frac{1}{4\pi} \int_{-\infty}^{\infty} \exp\left(-\imath k_y r\right) R_Z(r) dr, \tag{4.4}$$

or equivalently by

$$R_Z(r) = 2\int_{-\infty}^{\infty} \exp\left(\imath k_y r\right) E_Z(k_y) dk_y, \tag{4.5}$$

where the dependence on x_c and y_c has been dropped for clarity. For homogeneous flow it is possible to relate $E_Z(k_y)$, using Parseval's identity, to the dissipation spectrum, giving

$$D_Z(k_y) = 2Dk_y^2 E_Z(k_y), \tag{4.6}$$

where the variation of the molecular diffusion coefficient, D, in the cross-stream direction due to changes in temperature has been neglected. The choice of locations for the spectral analysis is quite limited by the evolving nature of the simulated turbulent jet, where large portions of the upstream flow domain on either side of the jet are quasi-laminar (Pantano, 2004). Therefore, scalar correlations in such regions are of little interest. Owing to these constraints, the region along the centre of the evolving turbulent jet was chosen for the spectral analysis, where the local turbulent Reynolds number values are high enough for the existence of a 'universal' dissipation range (cf. Sec. 4.1.2 and Sec. 4.1.3).

It is recognised that the one-dimensional cross-stream spectra do not account for the streamwise and spanwise contributions of mixture fraction gradients to the total scalar dissipation. However, determination of the absolute values of scalar dissipation is not of primary concern here since the length scales will be determined by the largest gradients, some of which will be aligned with the cross-stream direction. In planar-jet turbulent flow (with purely streamwise forcing of the jet) the thin shear layers and, therefore, the thin and elongated scalar dissipation structures are predominantly orthogonal to the cross-stream direction in the near-nozzle region. Thus, the cross-stream scalar spectra are able to capture the average scales (or the average thicknesses of these structures) at which scalar fluctuations are dissipated for this flow. In addition, the grid resolution is finest in this direction, enabling the computation of $E_Z(k_y)$ at the highest possible wavenumbers. The reader should note, however, that the dissipation field becomes nearly isotropic far downstream (Buch & Dahm, 1998; Su & Clemens, 2003) and one-dimensional cross-stream spectra may not capture the smallest scales there.

It remains to say that the character of the simulated jet flame implies that a sizeable number of data-points in the quasi-laminar region outside the separation surfaces of the jet will not be relevant for the computation of the dissipation length-scales. An estimate of the region that contributes significantly to the data-processing algorithms can be based on the normalised correlation coefficient, C_Z, introduced earlier. The regions, where $|C_Z(x_c, y_c, r)|$ remains monotonically less than 1% of its centreline value of unity, correspond to quasi-laminar regions. Here the flow is largely uncorrelated with the turbulence within the jet and therefore does not affect the dissipation of scalar fluctuations. Based on this measure, about 75% of all data points contribute to the computation of the dissipation length scales. However, none of the methods described in the present study explicitly discards the quasi-laminar region of the computational domain for post-processing.

4.1.2 Batchelor length-scale computation

The 'universal' dissipation subrange of the standard, non-reactive, spectral theory of turbulence is defined as the region in wavenumber space beyond the diffusive roll-off limit. In terms of the non-dimensionalised wavenumber, k^*, which is computed by multiplying the wavenumber with the Kolmogorov- or Batchelor-scale, this subrange starts at $k^* \simeq 0.1$ (Pope, 2000).

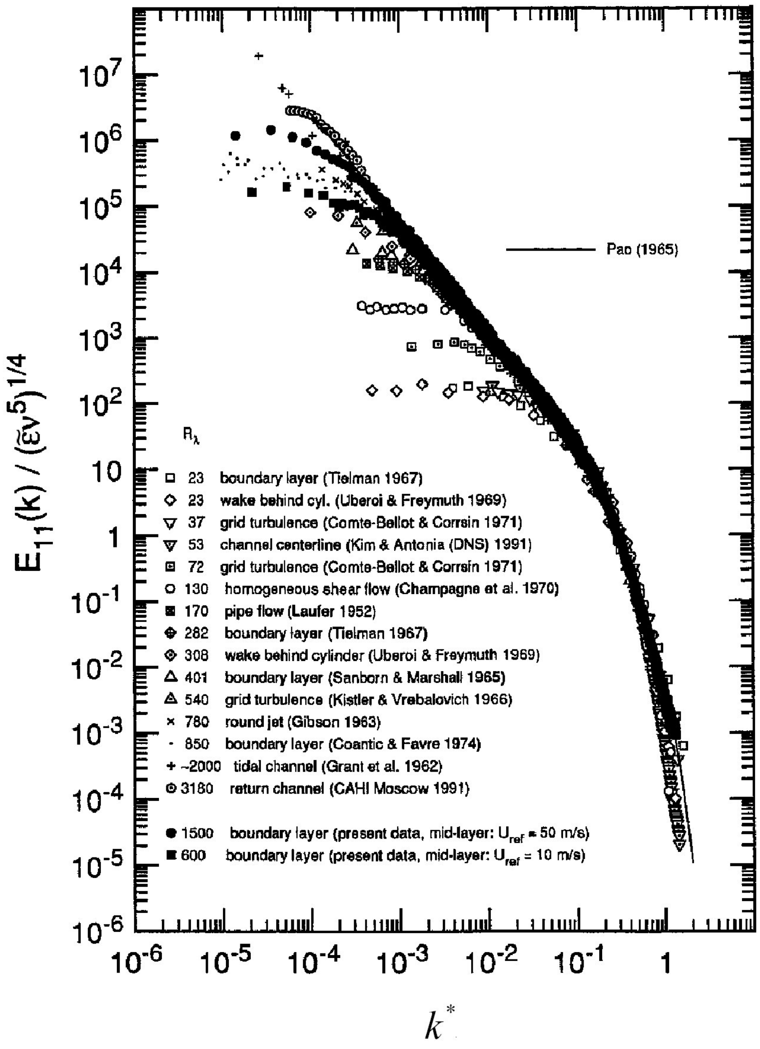

Figure 4.2: Experimental data showing the dissipation range collapse of suitably normalised one-dimensional turbulent energy spectra for a variety of turbulent flow cases at Taylor Reynolds numbers in the range of 23 to 3180. The plot has been reproduced from Saddoughi & Veeravalli (1994). Quantities on the y-axis, viz. $\tilde{\epsilon}$, ν and E_{11} denote the Favre-averaged dissipation rate, coefficient of viscosity and energy content of the turbulent fluctuations in a single velocity component, respectively. The corresponding non-dimensionalised wavenumber, k^*, is on the horizontal/x-axis.

Fig. 4.2 shows a comparison of various experimental results reported by Saddoughi & Veeravalli (1994), where the scaled one-dimensional spectra collapse on to a single curve at $k^* > 0.1$ for Taylor Reynolds numbers between 23 and 3180. In other words, they show a 'universal' dissipation range scaling. Furthermore, it is observed that the scaled one-dimensional dissipation spectrum (Pope, 2000) peaks at $k^* \simeq 0.26$. Since the peak-value occurs at $k^* > 0.1$, it can be used to define a *spectral* estimate of the Kolmogorov or Batchelor length-scale for the aforesaid range of Taylor Reynolds numbers. In the case of the scalar field, an analogy can be used to define a *spectral* scalar dissipation scale, according to

$$\eta_{Z_s} = \frac{[k^*]_{\mathrm{peak}}}{k_{\mathrm{peak}}} \simeq \frac{0.26}{k_{\mathrm{peak}}}, \tag{4.7}$$

where $k_y = k_{\mathrm{peak}}$ is the wavenumber of the peak in the computed cross-stream dissipation spectra. It can be shown that the area up to the $k^* = 1.0$ cut-off under the aforesaid one-dimensional dissipation spectrum contributes around 98% to the total mean dissipation. Recent high-resolution experiments (Wang *et al.*, 2007*a*,*b*) use a similar technique to arrive at the estimates of the Batchelor scale for axial jet-flames at locations ≥ 40 nozzle-diameters downstream. The value of the model spectrum of Pope (2000) at $k^* = 1.0$ corresponds to 7.3% of the peak dissipation level. Thus, the inverse of the wavenumber where the dissipation spectrum reaches 7.3% of its peak value is taken as the Batchelor scale estimate. This wavenumber is denoted $k_{7.3\%}$ and the corresponding Batchelor scale estimate is given by

$$\eta_{Z_s} \simeq \frac{1}{k_{7.3\%}}. \tag{4.8}$$

Wang *et al.* (2007*a*,*b*) use a somewhat more stringent estimate based on the wavenumber where the spectrum reaches 2% of its peak value.

Fig. 4.3 shows the computed non-dimensional scalar dissipation spectra. On scaling the wavenumber range for the dissipation spectra with η_{Z_s} obtained from (4.8), it is evident that the numerical cut-off limit in the spectra does not set in until well

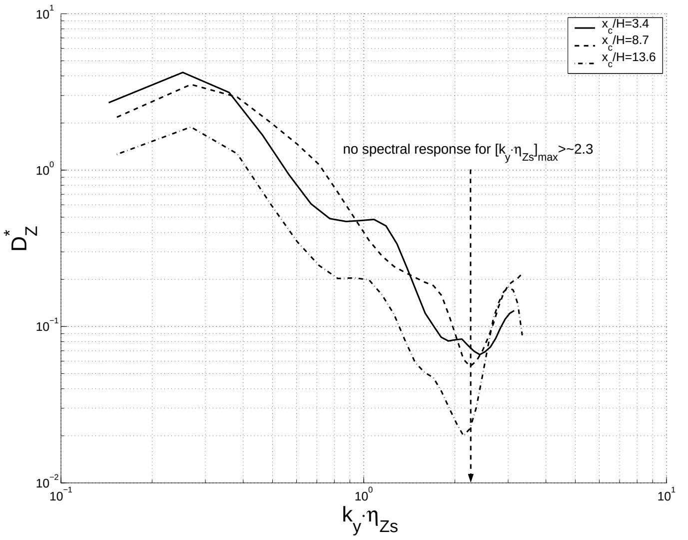

Figure 4.3: Scalar dissipation spectra in logarithmic coordinates at various downstream locations. The horizontal axis denotes the non-dimensional wavenumber $k_y \cdot \eta_{Z_s}$ and the vertical axis denotes the normalised scalar dissipation spectra, $D_Z^* = D_Z(k_y)/(\langle D\rangle\langle\chi_y\rangle\langle\epsilon\rangle^{-1/3}{\eta_{Z_s}}^{-1/3})$. The spectra were initially computed for 512 closely spaced values of k_y and averaged into 30 'bins' in the wavenumber space.

beyond the Batchelor scale (i.e. at $k_y \cdot \eta_{Z_s} \simeq 2.3$). As expected, the peaks for the *non-dimensionalised* spectra occur at $k_y \cdot \eta_{Z_s} \simeq 0.26$, with a slight shift to lower wave numbers for $x_c < 5H$. The vertical line indicates the approximate non-dimensional wavenumber limit (around $k_y \cdot \eta_{Z_s} = 2.3$) beyond which no more meaningful spectral response is obtained from the database. For wavenumbers beyond this limit, the turbulence energy spectrum becomes flat and represents a 'noise floor' (Wang *et al.*, 2007*a*). This in turn corresponds to an increase, proportional to ${k_y}^2$ (cf. Sec. 4.1.1), evidenced in the dissipation spectra beyond this limit.

The one-dimensional dissipation spectra computed above can be used to extract information regarding the average downstream evolution of the cross-stream scalar dissipation, which in turn provides estimates for the Batchelor length scales at the respective downstream locations. Analogous to the definition of viscous dissipation in wavenumber-space, the average scalar dissipation at any downstream centreline location can be recovered from the integral of the one-dimensional dissipation spec-

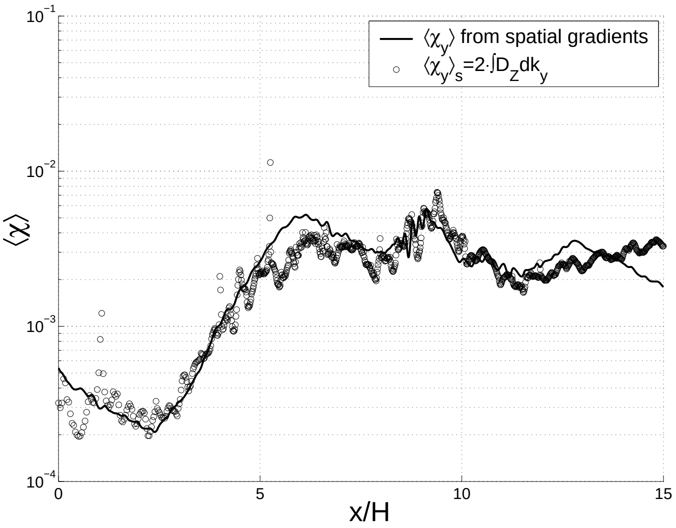

Figure 4.4: Comparison of the downstream evolutions (along the jet centre-plane) of the averaged scalar dissipation rates: calculated from cross-stream scalar-gradients, $\langle \chi_y \rangle$, and recovered from one-dimensional dissipation spectra, $\langle \chi_y \rangle_s$.

trum at that location (Tennekes & Lumley, 1974; Pope, 2000; Mathieu & Scott, 2000). The spectral estimate (denoted by the subscript s) of the average scalar dissipation rate is, therefore, given by

$$\langle \chi_y \rangle_s = 2 \int_0^\infty D_Z(k_y)\, dk_y, \tag{4.9}$$

where D_Z is defined in Sec. 4.1.1. The above identity is consistent with the factor of 2 used in (2.37). It must be noted that the spectral estimate of the average scalar dissipation rate corresponds only to the dominant cross-stream component of $\langle \chi_y \rangle$ given by the spatial-gradient along the y-coordinate only, i.e. $\langle \chi_y \rangle = \langle 2D\, (\partial Z/\partial y)^2 \rangle$. As expected, there is good agreement between the jet-centreline averaged scalar dissipation rate from spatial and spectral calculations, as functions of the downstream coordinate, in Fig. 4.4.

4.1.3 Reynolds number scaling

For the studied flow-configuration, the outer-scale Reynolds number, Re_δ, is defined as:

$$Re_\delta = \frac{\delta_{0.5} u'}{\nu}, \tag{4.10}$$

where $\delta_{0.5}$ is the outer-scale of the flow, proportional to the integral-scale of turbulence and computed as the jet half-width, i.e. the distance between the points where the average jet velocity falls to half its centreline value. Here, u' is the representative value of the turbulent velocity fluctuations and ν is the local kinematic viscosity. This parameter is used throughout the thesis to parameterise the dependence of the dissipation length scales on Reynolds number, as is customary in turbulence theory. Depending on the method of computation of the (instantaneous or mean) scalar dissipation length-scales (cf. Sec. 2.2.1), the u' value at any location will be taken as the instantaneous value or as the root-mean-square of the local distribution, respectively.

The non-reacting experimental data in Saddoughi & Veeravalli (1994) show that the departure from the universal behaviour at low Reynolds numbers mainly arises in the energy containing range (roughly $k^* > 0.003$), while the inertial-subrange (roughly $0.003 < k^* < 0.1$) is diminished. However, as described earlier in Sec. 4.1.2, the whole range of Reynolds numbers exhibits a 'universal' dissipation-range scaling at $k^* > 0.1$ (Nelkin, 1994; Pope, 2000) and shows excellent agreement with the non-dimensional spectrum.

A numerical simulation of isotropic turbulence by She *et al.* (1993) showed that the scaled spectra fall onto a universal curve at $k^* \geq 0.03$ for Taylor Reynolds numbers in the range of $15 \leq Re_\lambda \leq 200$. In addition, the DNS study of turbulent scalar mixing by Yeung *et al.* (2004) shows that Kolmogorov's first hypothesis regarding the dissipation range of the energy spectrum and, thus, its scaling given by (2.38) holds at Taylor Reynolds numbers between 8 and 38. The same scaling is obtained by Kushnir *et al.* (2006*b*) for dissipation 'filament' thicknesses when Taylor-scale Reynolds numbers equal 10 and 24. Hence, for our present case where Re_λ varies from around 20 to 67 throughout the computational domain (and from 38 to 58 along the centreline), it is expected that the spatial scales in the dissipation range still possess the 'universal' behaviour associated with Kolmogorov's first hypothesis despite the diminished inertial subrange at such low-to-moderate Reynolds numbers.

Conventionally, the finest mixing length scale is associated with the local turbulent Reynolds number, Re_δ, and Schmidt number via the relationship

$$\frac{\eta_Z}{\delta_{0.5}} = \Lambda_0 Sc^{-\frac{3}{4}} {Re_\delta}^{-\frac{3}{4}}, \tag{4.11}$$

where Λ_0 is the proportionality constant or the scaling coefficient. This relationship is based on dimensional arguments and it must be noted that the Re_δ-scaling in the above definition follows from Kolmogorov's first hypothesis, which holds (as remarked above) at the Reynolds numbers that can be found in the present DNS. The Batchelor scale definition in Pitts *et al.* (1999) assumes the left-hand-side in the above equation, i.e. $\eta_Z/\delta_{0.5}$, to be of the same order-of-magnitude as $Sc^{-3/4}{Re_\delta}^{-3/4}$ implying that $\Lambda_0 \simeq 1$. It should also be noted here that other experimental studies (Buch & Dahm, 1998; Su & Clemens, 2003) give values of Λ_0 in the range of 5 to 11 for the far-downstream self-similar regions of the jet.

To confirm the Re_δ-scaling of (4.11) for the present study, the η_Z term is substituted by its spectral estimate η_{Z_s} from (4.7) and (4.8) along the jet centreline. The resulting values of the scaling coefficient, Λ_0, are then plotted as functions of the

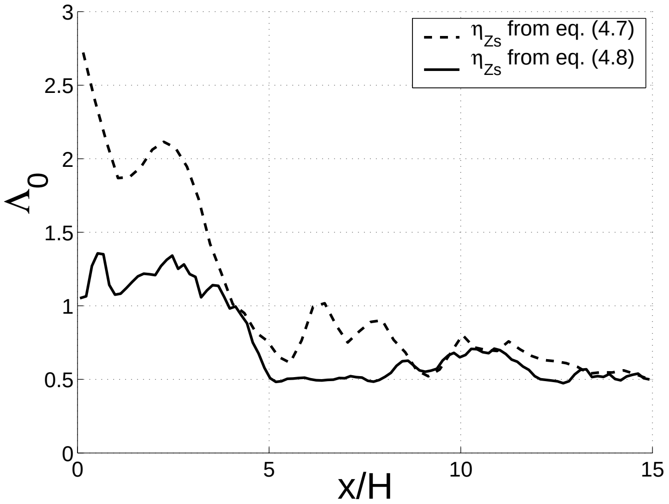

Figure 4.5: Downstream variation of Λ_0 values from (4.11). Computed by replacing η_Z with its spectrally recovered value η_{Z_s} from (4.7) and (4.8).

downstream positions in Fig. 4.5. The values computed using (4.7) slightly oscillate around a constant mean value of $\Lambda_0 \simeq 0.7$, except in the near inflow region ($x_c < 5H$) of the developing jet-flow, where cross-stream inhomogeneities are quite severe and the statistics of the velocity field are poorly reflected in those of Z. The Λ_0 values from (4.8) show a similar downstream evolution, however, with appreciably less fluctuations and remain around 0.5 for locations $x_c \geq 5H$.

In the region upstream of $x_c = 5H$, the jet-core has not broken up yet and there is a low amount of scalar mixing along the centreline. Consistently, the small scalar dissipation rate (i.e. the dissipation spectrum being confined to a relatively small range of wavenumbers) results in an over-estimation of the Batchelor scale from (4.7) and (4.8). This seems to be in agreement with the results from the DNS by She *et al.* (1993), where the computed k_{peak} wavenumber was found to be slightly smaller (at lower Reynolds numbers) than what the proportionality to $1/\eta_Z$ would imply. In other words, the Kolmogorov scale based on $0.26/k_{\text{peak}}$ is somewhat over-estimated when Taylor Reynolds numbers are low. However, the roughly constant values of Λ_0 seen for most of the downstream section ($\geq 5H$) in Fig. 4.5, corroborate that the spectrally computed estimates using (4.8) are representative of the Batchelor length scales in the flow.

4.2 Direct computation of scalar dissipation structures

A measurement method that is similar in spirit to the experimental technique described in Su (1998) and Su & Clemens (2003) has been utilised. Thin, sheet-like three-dimensional regions aligned with the regions of high shear within the computational domain are directly investigated, where most of the scalar dissipation process remains concentrated (Buch & Dahm, 1998; Tsurikov & Clemens, 2002). More recently, notable numerical studies of the small-scale topological structure of the turbulent scalar/dissipation field have been done by Wang & Peters (2006) and Kushnir *et al.* (2006*b*). In the former study, the approach has been to identify the regions, termed as 'dissipation elements', of monotonic increase (or decrease) of the fluctuating scalar concentration. Analysis of these 'dissipation elements' also confirms a high probability of alignment between scalar gradients and the most compressive rate of strain, as found in the shear-layers of the turbulent jet flow. The latter study by Kushnir *et al.* (2006*b*) analyses the topology of the two-dimensional scalar dissipation rate field using a sophisticated numerical algorithm described in Kushnir *et al.* (2006*a*). For all points on the two-dimensional field belonging to the regions delineated by a threshold value of the dissipation level-set, the algorithm computes a so-called 'proximity graph', which is updated on successive coarse-graining and can be used to quantify statistical properties like the density and convexity of the points at each level of resolution. Finally, a principal component analysis is carried out on these dissipation 'filaments' or 'sub-filaments' identified on the basis of the aforementioned statistical properties. The filament thickness is thus characterised by the eigenvalue of the eigenvector orthogonal to the direction of orientation of the filament.

4.2.1 Algorithm

An algorithm previously used by Buch & Dahm (1998) and Su & Clemens (2003) for the computation of the two-dimensional (planar) dissipation layer thicknesses with a correction for their three-dimensional orientation has been employed in the present study. The dissipation layers are identified as the contours or level-sets at fixed values of χ within the instantaneous $\chi(x, y)$ field. The fixed values are chosen as a fraction, β_m, of the local maxima in their neighbourhood (x, y) locations. The local thickness of a dissipation layer, λ_{2d}, at a given value of β_m quantifies the instantaneous two-dimensional dissipation length-scale. This two-dimensional dissipation length-scale estimate is then corrected by using the three-dimensional orientation of the scalar gradient vector in terms of the out-of-plane angle, ϱ, to give the three-dimensional length-scale estimate, λ_{3d}. The algorithm and all the parameters involved are described in more detail as follows.

The algorithm used for identifying the dissipation layers and computing their local thicknesses is shown schematically in Fig. 4.6. It essentially deals with a two-dimensional dissipation field in the $x - y$ plane. First, the global maximum of the scalar dissipation, χ_{max}, at a specific plane is determined. Second, all structures, where $\chi < 0.5\chi_{\text{max}}$, are discarded to isolate the regions of strongest dissipative behaviour. A parameter $\beta_m \equiv \chi/\chi_{\text{loc}}$ is introduced, which represents the fraction of the local maximum, χ_{loc}, at any point in the scalar dissipation field. The β_m parameter demarcates the local *spiky* topology of the dissipation field for our investigation and values between 50% and 90% are chosen for it. Finally, level-sets or

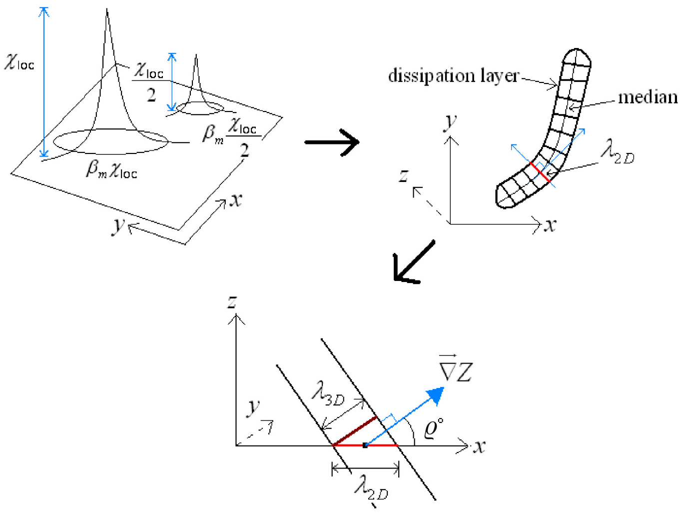

Figure 4.6: Schematic representation of the numerical method employed to investigate the instantaneous scalar dissipation structures in the three-dimensional computational domain and to compute their thicknesses. Symbols next to the contours indicate the constant values of χ used to compute the range of contours at a fixed fraction, β_m, of the local peak-values that vary from the global maximum of the planar χ-field, or χ_{max}, to $\chi_{max}/2$.

iso-contours of the remaining structures at the iso-level of $\beta_m \chi_{\mathrm{loc}}$ are determined. It was observed that for the present DNS test-case, scalar dissipation contours at values less than $\beta_m = 0.5$ tend to intersect and thus do not correspond to extreme and isolated dissipative events. This may be an effect of the relatively low Reynolds number range in the present DNS, as previous experimental studies of dissipation layers at high Reynolds numbers (Buch & Dahm, 1998) do not show this tendency at comparable values of β_m. However, only the finest scales of the scalar dissipation are of specific interest here and therefore, contours at values below $\chi/\chi_{loc} = 0.5$ are not of direct interest in the present study. On the other hand, the reasoning behind the choice of β_m no larger than 0.9 is purely computational. There are too few occurrences for $\beta_m > 0.9$ to obtain reasonably accurate statistics.

Once the two-dimensional dissipation layers depicted in Fig. 4.6 have been identified, each with its point-to-point connectivity, the algorithm processes the data to compute the median by recognising the elongated topology of the structure and

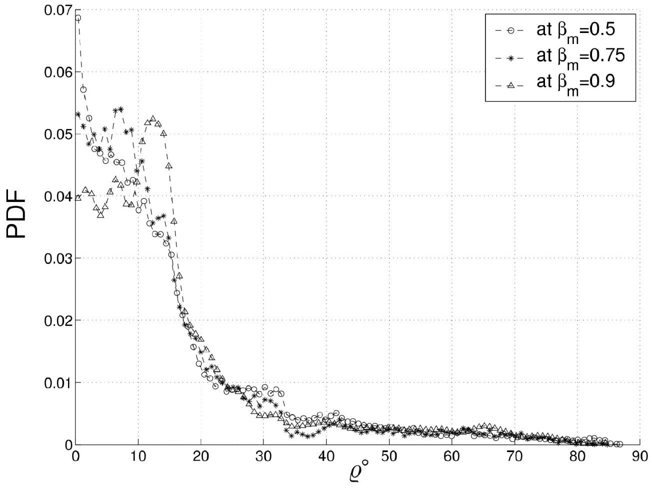

Figure 4.7: PDF of the out-of-plane angle ϱ of the scalar-gradient vector for a single computational time-step at different β_m values. The ϱ values have been computed at all dissipation-layer mid-points, for each β_m value, at a single computational time-step.

its corresponding *corners*. For each point on the contour, the nearest point that is not on its branch between the *corners* is taken as the *fellow-point* on the opposite branch. In order to remove computational noise, two points and two corresponding *fellow-points* are bunched and averaged to get a layer mid-point. The line joining these mid-points makes the median for each dissipation layer. Finally, the thickness attributed to each point on the median is computed by calculating the length of the segment orthogonal to the median at that point, whose end-points manage to be on or just inside the layer boundary in either direction. The measured two-dimensional layer thickness, λ_{2d}, at each layer mid-point, is corrected for three-dimensional orientation by the cosine of the out-of-plane angle of the $\boldsymbol{\nabla} Z$ vector (Su & Clemens, 2003), to give

$$\lambda_{3d} = \lambda_{2d} \cdot cos\varrho. \tag{4.12}$$

This projection becomes less reliable as the dissipation layers align less orthogonally with the plane ($x-y$) of the flame, i.e. as ϱ increases, owing to increasingly significant layer-curvature effects. In similar experimental studies by Su & Clemens (2003), the authors do not consider χ-level sets for which $\varrho > 60°$. However, the PDFs of the out-of-plane angle in Fig. 4.7 measured at all locations for different values of β_m show an extremely high preponderance (around 97%) of $\varrho \leq 60°$, which makes the correction largely reliable.

It is worth noting that the present algorithm introduces some simplifications in the computations of the dissipation layer thicknesses and it differs from the algorithm used by Buch & Dahm (1998) and Su & Clemens (2003) in two aspects. Firstly, the two-dimensional neighbourhood regions that define the dissipative structures may include more than one local maximum of χ for very low values of β_m. As a result, these regions would appear longer (more elongated) than the dissipation regions identified by Buch & Dahm (1998). Secondly, variation in the "local layer-normal dissipation maximum" (see Buch & Dahm (1998) for its definition) is unaccounted for along the dissipation layer and this leads to thinner structures than reported in Buch & Dahm (1998). However, due to our choice of relatively high values for β_m above, the neighbourhood regions tend to isolate the local maxima and the computed dissipation layer thicknesses will be similar for the two algorithms. In other words, the differences between the dissipation layer thicknesses reported from both algorithms will decrease with increasing β_m.

Fig. 4.8(a) shows the distribution of the corrected scalar dissipation layer thicknesses, λ_{3d}, normalised by the local grid-discretisation, $\Delta_{3d} = (\Delta_x \Delta_y \Delta_z)^{1/3}$, in the computational domain. The effective three-dimensional grid-spacing is denoted by Δ_{3d}, where Δ_x, Δ_y and Δ_z are the variable grid-discretisations in the respective coordinate directions. The detection of values smaller than the minimum grid spacing limit can be primarily associated with locations where the out-of-plane angle ϱ tends to 90°. This phenomenon is also amplified by the interpolation between grid

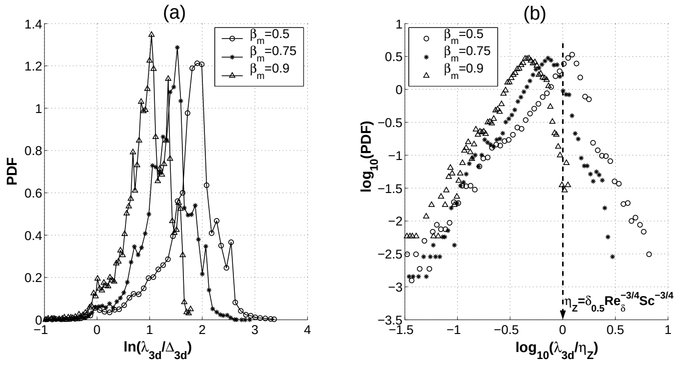

Figure 4.8: On the left, PDFs of the logarithm of the corrected (three-dimensional) scalar dissipation layer thicknesses are normalised with the effective grid-discretisation Δ_{3d} for $\beta_m = 0.5$, 0.75 and 0.9. The negative values for $\ln(\lambda_{3d}/\Delta_{3d})$ are numerical artefacts due to the thicknesses computed at the very few locations where $\varrho \to 90°$. On the right, PDFs of λ_{3d} are normalised by the dissipation length-scale η_Z from (4.11) with a unity scaling coefficient.

points near the corners of the dissipation layers when computing the iso-contours. However, owing to the very small number of such occurrences (cf. Fig. 4.7), their effect on the analysis is negligible.

In Fig. 4.8(b), the PDFs of the dissipation-layer thicknesses normalised by the magnitude of the local dissipation scale, η_Z, show a negative skews at all values of β_m. In other words, dissipation length-scales smaller than the most frequently-occurring scale (given by the peak of each PDF) are more likely to occur than those larger than the most frequently-occurring scale. This is in agreement with the results in Kushnir *et al.* (2006*b*), where a similar negative skew is observed in the normalised dissipation 'filament' thicknesses. In addition, Fig. 4.8(b) shows that the formation of dissipative structures with thicknesses of the order of η_Z is conditional on the chosen value of β_m. However, this dependence on β_m or any equivalent measure of spatial-resolution is not apparent in the analysis by Kushnir *et al.* (2006*b*). A majority of their computed dissipation 'filaments' are reported to be thicker than η_Z, an observation limited to lower β_m values in the present analysis.

A somewhat different analysis was employed by Schumacher *et al.* (2005). They used scalar-increments over the viscous-convective range between the Kolmogorov and Batchelor scales (for $Sc > 1$) that yielded a dissipation scale estimate slightly greater than η_Z. However, unlike Kushnir *et al.* (2006*b*), the actual distribution of dissipation length-scales is not captured in this analysis and this approach is therefore not used here.

4.2.2 Re_δ-scaling of dissipation layer thicknesses

In this section, a local Reynolds number definition has been used, where u' represents the local velocity fluctuation. This is necessary in order to account for the fluctuating nature of λ_{3d} and the necessity to relate instantaneous scales with Reynolds numbers based on instantaneous or local quantities. This is opposed to the analysis in Sec. 4.1.3 where a quantity computed from two-point correlations such as the dissipation spectrum requires Reynolds numbers based on averaged quantities such as the RMS Fig. 4.9 shows the scalar dissipation thickness as a function of Reynolds number. The whole range of Re_δ values is grouped into 60 bins and is plotted against the bin-average of $\lambda_{3d}/\left(\delta_{0.5}Sc^{-1/2}\right)$ in log-log coordinates. The least-squares fits for several values of β_m show a negative slope that approximates the value -0.75. This is consistent with a Kolmogorov type or ${Re_\delta}^{-3/4}$ scaling that is independent of β_m and the findings are in agreement with the experimental and numerical results of Buch & Dahm (1998), Su & Clemens (2003) and Kushnir *et al.* (2006*b*).

It is important to note that the amount of data samples for the dissipation layer thicknesses, i.e. the number of spatial locations within the computational domain where the thicknesses have been computed, decreases with increasing β_m as resolution constraints increase. For example, the sample size for $\beta_m = 0.5$, 0.75 and 0.9 is

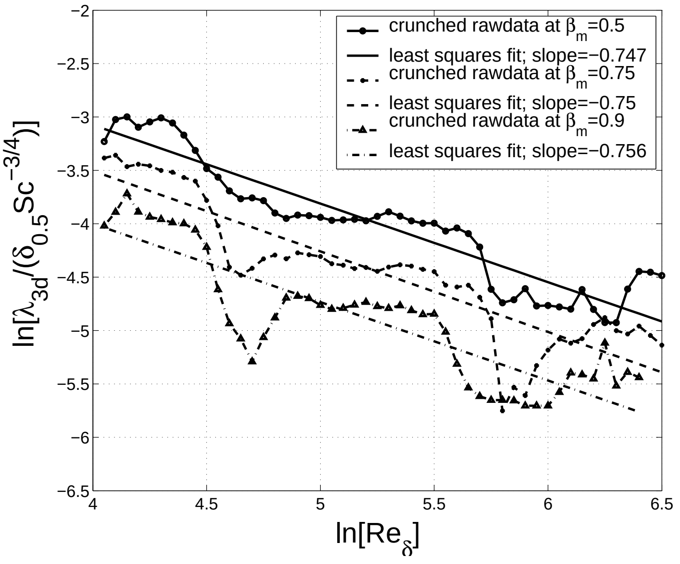

Figure 4.9: Observed ${Re_\delta}^{-0.75}$ scaling dependence for the corrected dissipation layer thicknesses, λ_{3d} in log-log coordinates. Data corresponding to a single computational time-step is shown at $\beta_m = 0.5$, 0.75 and 0.9.

around 40,000, 30,000 and 9,000 points, respectively. The data variability around the least-square fits in Fig. 4.9 is caused due to the discontinuous distribution of the dissipation layers along the streamwise direction at the β_m values chosen. Since the outer-scale Reynolds number is strongly correlated with the downstream evolution of the jet flow, this data variability is reflected in the means conditioned on Re_δ. Thus, as higher β_m values correspond to thinner and shorter layers, the variation increases with β_m.

4.2.3 Variation of scaling coefficient with β_m

Assuming the existence of a ${Re_\delta}^{-3/4}$ scaling of the dissipation layer thicknesses as evidenced in Fig. 4.9, the current formulation for λ_{3d} can be assumed to scale (similar to (4.11)) as

$$\lambda_{3d} = \Lambda_{3d}\delta_{0.5}Sc^{-\frac{3}{4}}{Re_\delta}^{-\frac{3}{4}}, \tag{4.13}$$

where Λ_{3d} is the scaling coefficient for the dissipation length scales, when expressed in terms of corrected three-dimensional scalar dissipation layer thicknesses. Values of the scaling coefficient, $\Lambda_{3d} \simeq 1.2$ *to* 0.55 determined by (the exponential of) the y-intercept of the least-square fits shown in Fig. 4.9, are observed to decrease over the investigated local χ-resolution range given by $\beta_m = 0.5$ to 0.9. The scatter around the mean (least-squares) estimate for Λ_{3d} is nearly Gaussian-distributed over the whole Reynolds number range. The standard deviation in the scaling coefficient values is around 30% of the mean for each β_m value. Thus, the interval $[0.4\Lambda_{3d}, 1.6\Lambda_{3d}]$ represents the 95.4% confidence interval associated with our Λ_{3d} estimates.

Evidently, the values for the scaling coefficient Λ_{3d} are smaller than those predicted in Buch & Dahm (1998) and Su & Clemens (2003), though it is of the same order as the Λ_0 value computed in Sec. 4.1.3. This may be explained on account of the following: in Buch & Dahm (1996, 1998) and Su & Clemens (2003) the dissipation layer thickness is defined as the distance across the layer between points where the dissipation rate is 20% of the local peak-value. This would be equivalent to a β_m value of $\beta_m = 20\%$ in the present study. However, the choice was made to compute the dissipation layers at much higher β_m values to isolate the most strongly dissipative regions. These regions determine the finest scales in the scalar field, which is a principal goal of this study. Relaxation of β_m to values of 20% would result in a thickening of the dissipation layers and would lead to a higher estimate for Λ_{3d}. Extrapolation of our results to β_m values of $0.1 - 0.2$ would yield Λ_{3d} being around $5.0 - 4.0$, which is much closer to the experimental estimates in Buch & Dahm (1998) and Su & Clemens (2003). Further contributing factors to the differences are the simplifications in the algorithm described in Sec. 4.2.1 and the fact that the experimental studies were for the self-similar regions in non-reacting turbulent jet flows. We stress that an exact determination of Λ_{3d} is not of primary interest here (and is, in fact, not possible due to its dependence on β_m). We seek to establish the validity of scaling relationships for the dissipative structures in turbulent reacting flows with low-to-moderate Reynolds numbers. These scaling relationships appear to be similar to scaling laws established for non-reacting flows.

4.3 Spatial-filtering analysis

Adequate spatial resolution to capture scalar dissipation means that the scalar gradient should remain sufficiently unchanged over the minimum length scale of discretisation or experimental probe-width employed for measurement. However, owing to small-scale intermittency, the fluctuations in scalar gradients (and hence in χ) can be many orders of magnitude higher than the mean and have a much higher probability of occurrence (i.e. they show a lognormal-like PDF) than those in the scalar (Sreenivasan, 2004). Sreenivasan (2004) proposes that the best way to deal with an intermittent variable like χ is to locally smooth it over a non-overlapping spatial interval (in other words, filter-width, w_f). The properties of the smoothed variable can then be studied as a function of w_f as it is extrapolated to the smallest scale of interest. In the present study, the analogy of the above approach with the experimental spatial-filtering technique of Barlow & Karpetis (2005*b*,*a*) is utilised. This is achieved by analysing the decay of the frequently occurring instantaneous *spikes* in χ resolved by the DNS as the size, w_f, of the applied numerical filter is increased beyond the computational grid-resolution. The type of decay with w_f is used to reconstruct the hypothetical 'fully-resolved' χ peak-values corresponding to zero filter-width. The ratio of the DNS-resolved instantaneous *spikes* in χ to the 'fully-resolved' reference limit is investigated.

4.3.1 Spatial-filtering method

Previous experimental studies of axisymmetric turbulent jet flames by Barlow & Karpetis (2005*b*) show that the peak-value of the logarithm of the mean cross-stream component of χ decreases linearly with increasing filter-width. As explained above, this linear decay is then exploited to calculate the 'fully-resolved' limiting value at zero filter-width. However, it should be pointed out that in the context of the numerical implementation of this technique to the present DNS, this 'fully-resolved' scalar dissipation is a hypothetical maximum that will most likely not exist at any point in the simulated flow. This theoretical value strictly serves as a good reference against which the resolution of the spatially-filtered χ peak-values is quantified. Thus, a suitable fraction of this reference is subsequently chosen as the effective length scale required for adequate resolution. However, based on the discussion in Sec. 2.2.1, the instantaneous length scales central to the idea of adequacy of χ-resolution cannot be captured by linear scaling of (the logarithm of) the mean dissipation, but of the instantaneous χ-field that exhibits small-scale intermittency. Therefore, the spatial-filtering method explores the instantaneous cross-stream profiles of scalar dissipation instead.

In the present DNS database, the planar, top-hat filtered mixture fraction $Z_f(x, y, z)$ given by

$$Z_f(x,y,z) = \frac{1}{\Delta_{x,f}\Delta_{y,f}} \int_{x-\frac{\Delta_{x,f}}{2}}^{x+\frac{\Delta_{x,f}}{2}} \int_{y-\frac{\Delta_{y,f}}{2}}^{y+\frac{\Delta_{y,f}}{2}} Z(x',y',z)\,dx'dy' \tag{4.14}$$

is considered, where $\Delta_{x,f}$ and $\Delta_{y,f}$ denote the filter width at any (x, y) position, with $w_f = \sqrt{\Delta_{x,f}\Delta_{y,f}}$. For the filtering operation the z dependence is dropped and, for simplicity, the scalar dissipation fields at every $x - y$ plane are considered as mutually independent realisations. The filtered instantaneous scalar dissipation rate

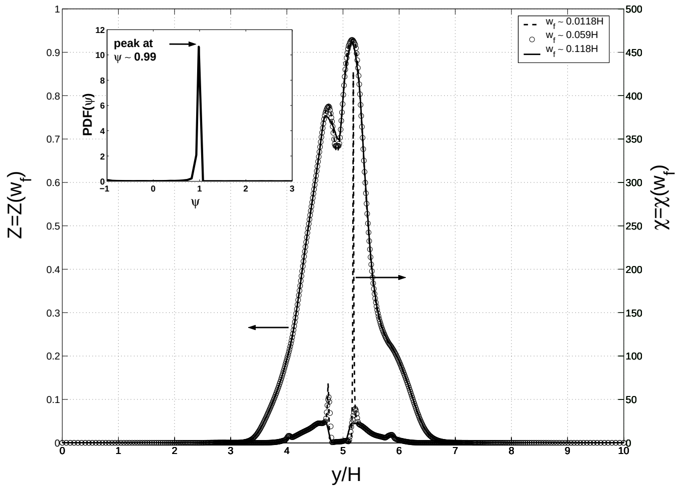

Figure 4.10: Variation of the instantaneous cross-stream profile of scalar dissipation rate, χ, and mixture fraction, Z, with increasing filter-width, w_f, at an arbitrarily chosen spatial location ($x/H = 2.8$, $z/H = 0.0$). The peak-value of the cross-stream χ profile appears to drop exponentially with a linear increase in w_f. The inset shows the PDF of the correlation coefficient, ψ, for the least-squares fit between the actual dependence of χ peak-values on w_f and the exponential-decay model in (4.16). ψ is computed for the χ peak-values at $1024/8 \times 192/3 \times 30$ cross-stream profiles throughout the present DNS database. The peak is observed for $\psi \simeq 0.99$. Negative signs have been appended to ψ values to indicate negative linear decay, i.e. for plots with $s > 0$.

is calculated from the spatially filtered mixture fraction field at each corresponding grid-point by central-differencing of (2.37),

$$\chi_f(x,y,z) = 2D\left(\left[\frac{\delta_x Z_f}{\Delta_{x,f}}\right]^2 + \left[\frac{\delta_y Z_f}{\Delta_{y,f}}\right]^2 + \left[\frac{\delta_z Z_f}{\Delta_z}\right]^2\right), \tag{4.15}$$

where δ_x, δ_y and δ_z are the central-difference operators for the respective coordinate directions. The smallest resolvable filter-width is given by $\Delta = \sqrt{\Delta_x \Delta_y}$, where $(\Delta_x, \Delta_y, \Delta_z)$ is the basic grid-discretisation used in the DNS, which varies from location to location owing to the clustering of the grid nodes in regions close to the shear layer. Successive iterations of spatial-filtering with successively larger filter-width values will smear out peak values of instantaneous Z (and hence χ).

4.3.2 Results and discussion

Effect of the filter width

Fig. 4.10 shows that spatial-filtering has a strong reducing effect on the instantaneous peaks of scalar dissipation, with the peak value decreasing drastically for increasing filter-width. However, the corresponding effect on instantaneous mixture fraction profiles is practically negligible. If an exponential decay of the maximum scalar dissipation is assumed as suggested by Barlow & Karpetis (2005*b*), it is possible to study the 'fully-resolved' scalar dissipation maxima as the filter-width is extrapolated to a sufficiently small value. In other words, the model is a linear variation of the type:

$$\ln\left(\chi_{f,\,\mathrm{peak}}\right) = \ln\left(\chi_{0,\,\mathrm{peak}}\right) + s \cdot w_f, \tag{4.16}$$

where $\chi_{f,\,\mathrm{peak}} = max\left(\chi(y)\right)$ is the maximum scalar dissipation value along the cross-stream direction for constant x and z (see Fig. 4.10 for illustration), $\ln\left(\chi_{0,\,\mathrm{peak}}\right)$ is the 'fully-resolved' χ value computed by extrapolating to zero filter-width and $s\,(< 0)$ is the slope of decay of the logarithm of the scalar dissipation peak value. The parameter s quantifies the effect of spatial-filtering on the χ peak-value.

For every downstream location, $N_z \times N_T$ realisations can be used to establish the linear relationship described in (4.16), where, $N_T = 30$ is the number of different time instants being considered. Following the method described by Barlow & Karpetis (2005*b*), values of $\ln\left(\chi_{f,\,\mathrm{peak}}\right)$ and the corresponding filter-width are accepted only in cases where the linear correlation coefficient of their least-squares fit, ψ, is 0.99 or better during the spatial-filtering operation. As is customary, $\psi = 0$ indicates completely uncorrelated variables and $\psi = 1$ implies perfect linear correlation. To reduce the number of cross-stream profiles to be processed from an extremely large value of $N_x \times N_z \times N_T \sim 5.9$ million, one χ-peak per cross-stream profile is assumed for each eighth grid-point along the streamwise direction and each third grid-point along the spanwise direction. Additionally, the condition on ψ limits the very large number of available spatio-temporal locations to around $75,500$ cases that show near-perfect linearity described by (4.16). The stringent demand on the choice of peak-values $\chi_{f,\,\mathrm{peak}}$, i.e. $\psi \rightarrow 1$ ensures exponential decay with increasing filter-width and the important intermittent statistics are thus captured. In addition, the PDF of the ψ-values for all the processed cross-stream profiles in Fig. 4.10 (inset) shows a very high preponderance of values around $\psi \simeq 0.99$. This justifies the validity of the exponential-decay model described by (4.16) in the present DNS.

The following qualitative observations come to light regarding the effects of spatial-filtering of the instantaneous χ profiles. First, the scalar dissipation values at the 'fully-resolved' limit are observed to be finite. Thus, the extrapolation of the peak scalar dissipation values to the 'fully-resolved' limit seems valid as shown by Barlow & Karpetis (2005*b*). Second, the PDF of the scalar dissipation peak value is well captured at the minimum filter width $w_f = \Delta$. Fig. 4.11 compares different PDFs that are obtained by varying the filter-width, w_f, in (4.14) and (4.15). The figure shows that the PDF of the scalar dissipation values at the 'fully-resolved' limit (i.e. $w_f \rightarrow 0$) does not show any appreciable change from the PDF captured at the grid-spacing (i.e. $w_f = \Delta$), indicating that the DNS grid captures the range of dissipation values quite well. For the larger filter width $w_f = 8\Delta$, the probability distribution shows a negative skewness as the probability of χ-values being smaller than the average increases. Third, on average, the effect of spatial-filtering on χ increases with downstream distance. It peaks at about the centre of the computational domain (around $x/H \simeq 7.5$) beyond which it slightly decreases as shown in Fig. 4.12. This seems to be directly linked with the trend shown by the outer-scale

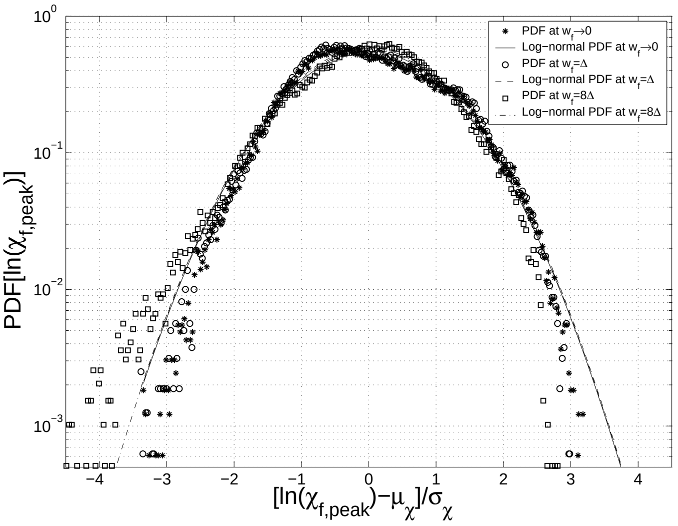

Figure 4.11: Dependence of the PDF of (the logarithms of) the filtered χ peak values, PDF($\ln \chi_{f,\,\mathrm{peak}}$), on the level of filter width given by the magnitude of $\frac{w_f}{\Delta}$. The symbols show the actual data at various filter-widths, whereas the curves show the corresponding log-normal PDFs for the same mean, μ_χ, and variance, σ_χ.

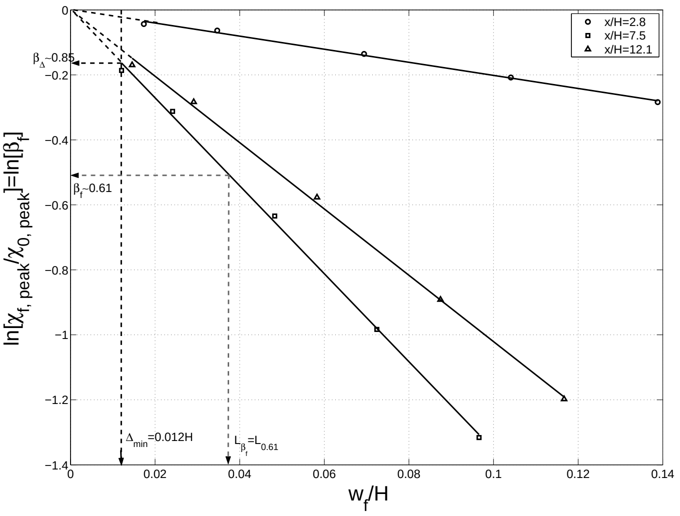

Figure 4.12: Averaged plots of the filtered χ peak-values normalised by the 'fully-resolved' limit with increasing filter-width in semi-log coordinates. The reported results indicate the mean variation, computed by averaging over the PDF (of all instantaneous spatio-temporal cases) corresponding to each of the three downstream stations. The horizontal lines indicate 85% and 61% recovery of the 'fully-resolved' χ value at $w_f = \Delta$ and $w_f = L_{0.61}$, respectively. Here, $\Delta = \sqrt{\Delta_x \cdot \Delta_y}$ indicates the non-uniform grid-discretisation employed in the DNS. The dotted portions of the linear plots represent the extrapolation at $w_f < \Delta$ and filter-widths corresponding to this region do not represent physically resolved dissipation length scales.

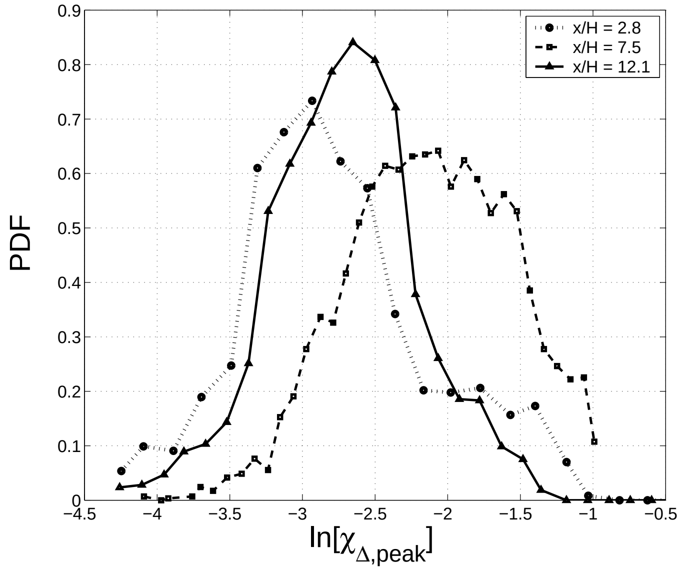

Figure 4.13: Dependence of the PDF of (the logarithms of) the χ peak-values that are resolved by the grid, i.e. $PDF\left(ln\chi_{\Delta,\,\mathrm{peak}}\right)$ on downstream distance.

turbulent Reynolds number, Re_δ, which also peaks in the centre of the computational domain and decreases slightly further downstream (Pantano, 2004). Finally, the magnitude of the spatial-filtering effect, s, is sensitive to the corresponding magnitudes of the dissipation peak-values resolved by the grid. This is demonstrated in Fig. 4.13. The downstream position with the largest average $\chi_{\Delta,\mathrm{peak}}$ corresponds to the downstream position with the largest gradient $|s|$, and the downstream position with the smallest average $\chi_{\Delta,\mathrm{peak}}$ corresponds to the downstream position with the smallest gradient $|s|$. This correlation holds throughout the flow. This implies that the decay of χ-peaks through filtering is correlated with the magnitudes of these peaks.

The local effects of spatial-filtering can be quantified by the parameter s or, equivalently, by the filter-widths required for resolving a fixed fraction (defined as β_f in (4.18) below) of $\ln\left(\chi_{0,\,\mathrm{peak}}\right)$. The observations made above imply that these effects are linked to the magnitudes of χ peak-values, which in turn are dependent on the turbulent Reynolds number Re_δ (Sreenivasan, 2004) owing to the intermittent nature of the χ field. The correlation between χ peak-values and the turbulent Reynolds number is also corroborated by Hawkes *et al.* (2006) in their turbulent jet flame DNS. Hawkes *et al.* (2006) reveal increasing levels of extinction and longer reignition times, caused by large dissipation fluctuations, with increases in the Reynolds number. These links are examined in detail next.

Choice of β_f

Following Barlow & Karpetis (2005*b*), a length scale to quantify the effects of spatial-filtering on χ can be defined. This length scale is the filter-width required to recover a sufficiently large fraction β_f of the (hypothetical) 'fully-resolved' scalar dissipation value, where $\beta_f = \chi_{f,\,\mathrm{peak}}/\chi_{0,\,\mathrm{peak}}$. The definition of the length scale L_{β_f} then follows from (4.16) as

$$L_{\beta_f} \equiv \frac{\ln(\beta_f)}{s}. \tag{4.17}$$

An appropriate value of β_f must be selected in (4.17) in order for L_{β_f} to be well defined. The statistics of the fractional value of $\chi_{0,\,\mathrm{peak}}$ that is actually resolved by the computational grid, i.e. the fraction $\beta_\Delta = \chi_{\Delta,\,\mathrm{peak}}/\chi_{0,\,\mathrm{peak}}$ for $w_f = \Delta$, can be used as guidance. Using (4.16), β_Δ can be written as

$$\beta_\Delta = \exp(s \cdot \Delta). \tag{4.18}$$

Fig. 4.14 shows the statistics of β_Δ for the whole DNS database. It is evident that the increasingly spiky behaviour of χ due to intermittency that is approximated here by the magnitude of the actually resolved peak-χ values or $\ln(\chi_{\Delta,\,\mathrm{peak}})$, correlates with the decreasing ability of the grid to locally resolve $\chi_{0,\,\mathrm{peak}}$ (i.e. decreasing β_Δ). It

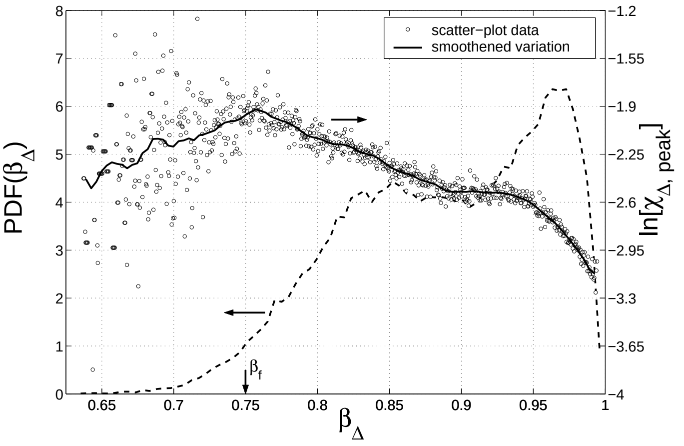

Figure 4.14: Variation of the fraction, β_Δ of the 'fully-resolved' value $\chi_{0,\,\mathrm{peak}}$ recovered by the local grid-discretisation (for $\psi > 0.99$) against the (logarithm of) magnitude of the peak-value resolved $\chi_{\Delta,\,\mathrm{peak}}$.

follows from (4.18) that for a fixed grid-discretisation Δ, the parameter β_Δ depends directly on the rate of spatial-filtering decay, s. Therefore, the correlation of β_Δ with $\chi_{\Delta,\,\mathrm{peak}}$ in Fig. 4.14 corroborates the preliminary observation made in Sec. 4.3.2 that larger χ peak-values tend to decay faster with filtering. In addition, Fig. 4.14 shows that most of the strongest spiky behaviour (or largest $\ln \chi_{\Delta,\,\mathrm{peak}}$ values) occurs in the vicinity of $\beta_\Delta \simeq 0.75$. Thus, in the context of the present DNS, there is no need to relax the definition of β_f below 0.75 for it to be deemed sufficient to capture the strongest dissipative events.

The very few spatio-temporal locations (around 2% of the total), characterised by $\beta_\Delta < (\beta_f = 0.75)$ in the PDF on Fig. 4.14, correspond to the extrapolated region shown in Fig. 4.12. Therefore, the dissipation length scale values, computed in terms of the filter-width at these locations, remain less than the local grid-size. However, these numerical artefacts are insignificant in number and have negligible effect on the analysis.

Re_δ scaling

Based on the spatial-filtering analysis of the scalar dissipation field it is seen that the defined length scale L_{β_f} is a representative measure of a wide variety of local dissipative events at $\beta_f = 0.75$. Examination of the scaling of the local instantaneous dissipation length scale, $L_{0.75}$, with Reynolds number requires a parameterisation at each spatio-temporal location. For the present analysis, the instantaneous Re_δ is again used, based on the fluctuating velocity component, u', instead of its root-mean-square value. This is consistent with the remarks made earlier in Sec. 4.2.2.

As commented in Sec. 2.2.1, many previous studies on the resolution requirements for χ like Buch & Dahm (1996, 1998); Pitts *et al.* (1999); Su & Clemens (2003), infer that the minimum length scale deemed adequate to characterise scalar dissipation is proportional to (if not of the same order as) the Batchelor scale. However, it follows from the discussion in the preceding sections that the length scales, $L_{0.75}$, representative of the instantaneous scalar dissipation peaks captured by the spatial-filtering technique, are equivalent to the *local*, minimum dissipation length scales of Sreenivasan (2004) or $\eta_{Z_{min}}$, that need to be resolved for capturing the intermittency of scalar dissipation. The Reynolds number scaling for these minimum length scales can be established by plotting $\ln\left(L_{0.75}/\left(\delta_{0.5}Sc^{-3/4}\right)\right)$ as function of $\ln\left(Re_\delta\right)$. Due to the large number of data points involved, the $\ln\left(Re_\delta\right)$ range is divided into 100 bins and the averaged value of $L_{0.75}/\left(\delta_{0.5}Sc^{-3/4}\right)$ is plotted against that of $\ln\left(Re_\delta\right)$ for each bin. The result is shown in Fig. 4.15 and the data reveal a slope of -1 in the double logarithmic plot. We therefore suggest a ${Re_\delta}^{-1}$ scaling for the length scale $L_{0.75}$, viz.

$$L_{0.75} = \Lambda \delta_{0.5} Sc^{-\frac{3}{4}} {Re_\delta}^{-1}. \tag{4.19}$$

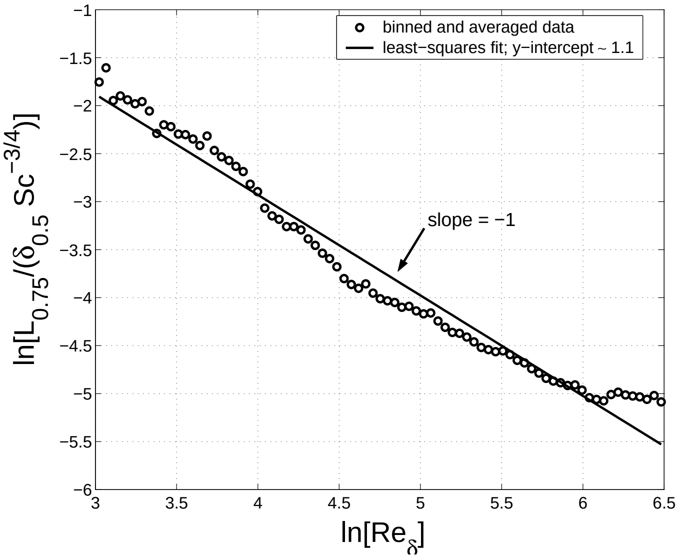

Figure 4.15: Linear scaling of $L_{0.75}/\left(\delta_{0.5}Sc^{-3/4}\right)$ with Re_δ in double-logarithmic coordinates. A slope of -1 is obtained after a least-squares fit.

This is consistent with scaling estimates for $\eta_{Z_{min}}$ by Sreenivasan & Meneveau (1988); Sreenivasan (2004) that are based on the theory of multifractals. A similar ${Re_\delta}^{-1}$ scaling estimate for the intermittent dissipation length-scales has also been derived by Yakhot (2003) using the theory of turbulence structure functions. The physical mechanism that leads to the small-scale intermittency and the corresponding deviation from ${Re_\delta}^{-3/4}$ scaling may be attributed to the *self-stretching* component of the strain-rate tensor as introduced in She *et al.* (1990).

It is important to note here that the proposed type of ${Re_\delta}^{-1}$-scaling is determined by the fixed statistics of the rate of spatial-filtering decay, s, and hence, it is insensitive to any change in the β_f value. On the other hand, the value of the scaling coefficient Λ is estimated to be around 3.0 and depends on the chosen value of $\beta_f = 0.75$ in our case.

We can conclude that the spatial filtering technique is capable of capturing most of the local, small-scale intermittent behaviour of χ and the present DNS database supports the estimates in Sreenivasan & Meneveau (1988), Yakhot (2003) and Sreenivasan (2004). The analysis indicates that the resolution requirements for scalar dissipation measurements are much more stringent than what the Batchelor scaling would suggest. It also implies that the number of DNS grid points necessary for spatial resolution of the finest (intermittent) structures scales with $N^3 \propto Re^3$ as opposed to the conventionally suggested $N^3 \propto Re^{9/4}$ scaling based on the Kolmogorov scale. The implications for the large-eddy or direct numerical simulations of turbulence due to the stringent scaling constraints imposed by dissipation intermittency have been discussed in detail by Yakhot & Sreenivasan (2005).

4.4 Comparison of the analyses

Differences in the length scale estimates that originate from the three methods presented above can be best summarised in a comparison of their probability distributions. Fig. 4.16 shows these PDFs of the normalised average and instantaneous dissipation length scales. The one-dimensional cross-stream spectral estimate of the mean dissipation length scale, η_{Z_s}, has been obtained using (4.8) at all downstream locations along the jet centreline, while the instantaneous and local dissipation length scales, $L_{0.75}$, are computed by spatial filtering of the peak values of the instantaneous cross-stream χ-profiles. Fig. 4.16 also includes the instantaneous normalised three-dimensional dissipation layer thickness, λ_{3d}, distribution. All values have been normalised with respect to the minimum grid-discretisation, $\Delta_y = 0.0118H$. Since the PDFs are computed using data from the entire computational domain rather than at any specific (x, y) location, they would not be affected by any lack of enough independent samples to compute statistical moments (as seen in Sec. 4.1.1).

Fig. 4.16 shows a very wide distribution of the dissipation length scales represented by $L_{0.75}$ compared to η_{Z_s} and λ_{3d}. It also demonstrates that the bulk of the finest

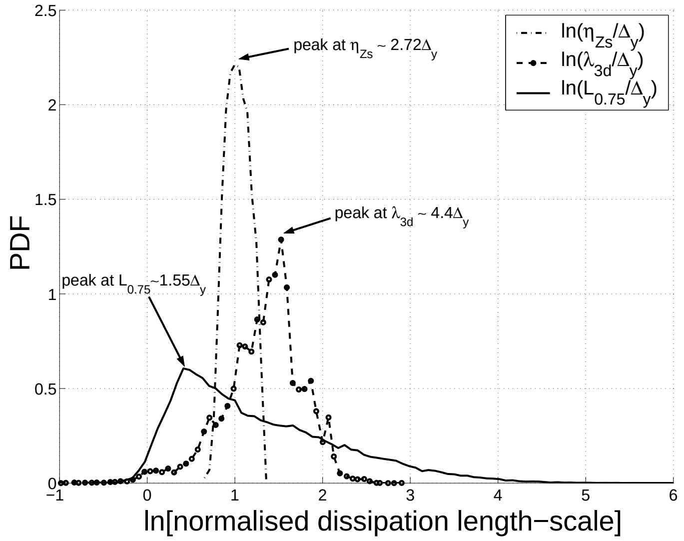

Figure 4.16: PDF of the normalised instantaneous and mean dissipation length scales and dissipation layer thicknesses, viz. η_{Z_s}, $L_{0.75}$ and λ_{3d} (computed at $\beta_m = 75\%$). Peak values are indicated as multiples of the cross-stream grid-discretisation. Negative values of the logarithms of the grid-normalised dissipation scales are numerical artefacts of the data-analysis algorithms that have been explained in Sec. 4.2.1 and Sec. 4.3.2.

mixing scales present in the flow (owing to the small-scale intermittency of χ) cannot be characterised by the Batchelor scale. The PDF of the instantaneous *local* dissipation scale, $L_{0.75}$, peaks at a noticeably lower value than that of the spectral dissipation scale estimate, η_{Z_s}, indicating the necessity for much more stringent resolution requirements than the commonly used scaling with the Batchelor scale. Furthermore, the relatively limited range of dissipation length scales given by η_{Z_s} and λ_{3d} seems to agree with the limited range of dissipation-layer thicknesses found for direct experimental measurements (Buch & Dahm, 1998).

The next chapter introduces the theory and numerical implementation details on the mapping closure method for modelling the transport of scalar statistics in turbulent non-premixed flames. Closures for all MMC sub-models are presented and the extinction/re-ignition predictions using MMC are compared with the CMC predictions and DNS data.

Chapter 5

Mapping closure approach

This chapter starts with a detailed review of the existing literature on the mapping closure formalism to model the conditional scalar transport equations. Later sections describe the governing MMC equations and discuss the closure of each unclosed term occurring therein. This study revises the standard MMC closure for downstream velocity, based on linearity in the reference space, to linearity in the composition space. This modelling amendment ensures that the PDF of downstream convective velocity is free to evolve from a non-Gaussian shape to Gaussian, rather than being constrained to follow Gaussian dynamics. The change is deemed necessary due to proximity of the flow to the nozzle, where Gaussianity does not apply. MMC drift coefficients consistent with the revised velocity modelling are derived from first principles. Other modelling improvements include the incorporation of temperature dependence of diffusivity. In addition to the MMC equations, the singly- and doubly-conditioned CMC equations (cf. Sec. 2.3.7) are also solved, with unclosed terms in CMC equations computed from the DNS. Details on the initialisation, numerical scheme and realisability constraints are also reported. Finally, MMC predictions of joint mixture fraction-sensible enthalpy PDF, doubly-conditioned dissipation variables and conditional species concentrations are compared with the DNS results and

CMC1/CMC2 as well.

5.1 Multiple mapping conditioning

Given the aforesaid background, multiple mapping conditioning has emerged (Klimenko & Pope, 2003; Klimenko, 2005) as a new modelling approach that combines the advantages of PDF and CMC methods. It effectively solves for the evolution of the joint PDF in the major manifold, which is used in conjunction with the conditional moment method to determine the dependent species concentrations. This is achieved by generalising the concept of mapping closures (Chen *et al.*, 1989; Pope, 1991), wherein all the reactive/conserved scalars are considered to be functions of a finite number, $n_r \geq 1$, of mutually-independent stochastic reference variables with a known joint PDF. Therefore, the problem is posed in terms of the advective-diffusive transport of the mapping functions rather than the evolution of the joint scalar PDF itself. The advantage of this approach lies in the fact that the expressions for the conditional velocity and dissipation terms (as deterministic functions of stochastic reference variables) follow from the choice of n_r and the joint distribution of the reference variables. Klimenko & Pope (2003) show that choosing a joint-Gaussian reference field leads to relatively straight-forward closures for the conditional velocity and dissipation terms. The value of n_r gives the 'dimensionality' of the system of MMC equations, which is computationally desirable (compared to PDF methods) only if $n_r < n_s$, where n_s is the total number of scalars to compute in the reactive-diffusive system. Various previous applications (Cleary & Kronenburg, 2007*b*,*a*) of the MMC framework with multi-step chemistry suggest that a selection of $n_r = 2$ proves sufficient to mimick the scalar fluctuations required to capture extinction and reignition.

In its general framework the suggested MMC model does not distinguish between the major and minor scalars (Klimenko & Pope, 2003) and any choice of major/minor scalars depends on how the underlying framework is interpreted (i.e. in CMC- or PDF-based terms). Thus, the CMC-compliant interpretation of MMC implies categorizing turbulent fluctuations (and species) into the aforesaid major and minor groupings. Herein the fluctuations in the major species are not restricted and are modelled using the mapping closure approach described above. Simultaneously, independent fluctuations are not permitted in the minor scalars and any minor fluctuations must be conditional on those in the major scalars. On the other hand, this 'major-minor' dichotomy is lost in the PDF-compliant interpretation of mapping closure (Klimenko, 2005) as it allows for minor fluctuations independent of those in the major scalars. It follows, therefore, that the PDF-compliant interpretation of MMC requires $n_r = n_s$, whereas for CMC-compliance n_r must at least be equal to the number of major scalars.

There have been a few recent examples (Wandel & Klimenko, 2005; Cleary & Kronenburg, 2007*b*,*a*) of the application of the MMC formalism to predict extinction and re-ignition of flames in homogeneous decaying turbulence. Wandel & Klimenko (2005) used stochastic MMC with single-step chemistry and one reference variable for mapping the mixture fraction. Conventional PDF mixing models with fixed dissipation time-scale ratios for all scalars were used to model the fluctuations of the minor scalars. While the results compared well with DNS data, the choice of dissipation time-scale ratios is not universal. A deterministic MMC model with a four-step chemical mechanism and reference variables for mapping mixture fraction and scalar dissipation (Klimenko, 2005) was used by Cleary & Kronenburg (2007*b*). The study employed three dissipation-like reference variables to represent the spectrum of time-scales associated with the turbulent dissipation process. These MMC computations showed marginal improvement in predicting extinction over double conditioning approaches with only one scalar dissipation variable and mixture fraction. However, the marginal improvements do not justify a significant increase in the computational complexity due to an increase in the dimensionality of the model to $n_r = 4$. In addition, lack of good agreement with the DNS data was due to the absence of a proper model of the correlation between the chemical source term (or temperature) and scalar dissipation during re-ignition. On the other hand, it has been shown that an MMC approach with reference variables for mixture fraction and sensible enthalpy can give excellent predictions for all species and captures the degree and onset of extinction/re-ignition nicely (Cleary & Kronenburg, 2007*a*). However, this approach, again, fails to take into account the feedback from scalar dissipation fluctuations to temperature changes. Thus, in absence of a model for this feedback, a presumption of the shape of the conditional PDF, $P(h_s|Z)$, and solution of the transport equation for $\langle h_s''^2|Z\rangle$, is required to *externally* impose the fluctuations on the conditional mean of sensible enthalpy. The inherent advantage of this MMC approach over the corresponding CMC calculation is the closure of the doubly conditioned dissipation terms, albeit modelling the joint $Z - h_s$ PDF remains uncertain.

It should be noted that using reference variables for sensible enthalpy and scalar dissipation simultaneously (in addition to mixture fraction) will still preclude any feedback mechanism between their respective fluctuations. As Kronenburg & Cleary (2008) recognised, generation of fluctuations around the means conditioned on Z is only possible if the MMC model is revised to attribute, what the authors call, a *dual* character to the reference variable for h_s. The *dual* nature implies that the reference variable mimics the statistics of the dissipation term, χ, in addition to that of h_s. The MMC modelling of extinction/re-ignition in the aforesaid study is fully closed with respect to the chemical source and dissipation terms and gives good predictions of the extinction and re-ignition phenomena. However, the assumption of homogeneous turbulence implies that any modelling of the convective velocity term was obviated in this study due to negligible spatial gradients of conditional means and the velocity term is set to zero.

For spatially evolving, inhomogeneous turbulent flows the assumption of negligibly small spatial gradients is no longer valid and providing closure for the convective velocity becomes necessary. According to the standard MMC formulation (Klimenko & Pope, 2003), the closure model of convective velocity is a linear combination of all the (normally distributed) reference variables and the modelling coefficients are known functions of the cross-correlation terms between the velocity and the respective major scalars. This means that the convective velocity model presumes Gaussian statistics for the velocity field. The imposed Gaussian shape oversimplifies the evolution of the flow in many instances and can cause an aphysical mismatch with the scalar statistics. In the next section, a new model is proposed for the convective velocity based on a more direct dependence on the scalar statistics and ensures consistency by re-deriving the drift coefficient in the governing MMC equations from first principles. The revised sub-model takes the form of a simple ordinary differential equation that is solved before the actual MMC computational routine. Details of the numerical implementation of this velocity modelling procedure within the MMC framework and the discussion of results thereof are laid out in the subsequent sections.

5.2 MMC formulation

The dimensionality of the model in the current MMC formulation is $n_r = 2$, where the mixture fraction, Z and sensible enthalpy, h_s are the first and second major scalars respectively. With reference to (2.1)-(2.3) the complete scalar set $\boldsymbol{\phi}$ can be seen as a combination of the subset of major scalars, $\boldsymbol{\phi}_{maj}$ and that of the minor scalars, $\boldsymbol{\phi}_{min}$. The subscript notation consistent with that introduced in Sec. 2.0.1

is also followed for the set of sample space variables, $\boldsymbol{\eta}$, of the scalars. In the conditional moment interpretation of MMC, fluctuations of the minor scalars away from their means conditioned on the major scalars are disallowed. This implies that the conditional means, $\langle \boldsymbol{\phi}_{min} | \boldsymbol{\phi}_{maj} = \boldsymbol{\eta}_{maj} \rangle$, are equivalent to determinable functions, $\boldsymbol{\phi}_{min}(\boldsymbol{\phi}_{maj})$. Therefore the joint PDF of all scalars, $P_{\boldsymbol{\phi}}$, can be computed by multiplying the marginal joint PDF of all major scalars, $P_{\boldsymbol{\phi}_{maj}}$, with delta-functions at the conditional means of the minor scalars.

The marginal joint PDF, $P_{\boldsymbol{\phi}_{maj}}$, is effectively solved for in the MMC approach. As described in the coming sections, the approach of solving for the scalar PDF (rather than presuming it *a priori*) also pays dividends in the velocity closure model. However, the solution of the joint PDF also requires the provision of the turbulent dissipation terms conditional on the major scalars. MMC uses the mapping closure (Chen *et al.*, 1989; Pope, 1991) approach to solve the joint PDF transport equation while facilitating the closure of the conditional dissipation terms simultaneously. Mapping closure involves mapping the physical (major) scalar field with the unknown joint PDF, to a stochastic reference field that has a known/prescribed distribution. As discussed earlier in Sec. 5.1, the dimensionality of the reference space is n_r and is given by $\boldsymbol{\theta} = \{\theta_1, \theta_2, ..., \theta_{n_r}\}$, with the corresponding sample space, $\boldsymbol{\xi} = \{\xi_1, \xi_2, ..., \xi_{n_r}\}$. Since $n_r = 2$ in the current MMC formulation, henceforth ξ_1, ξ_2 represent the stochastic reference-field counterparts of Z, h_s.

Finally, the requirement is to determine a set of mapping functions, $\mathbf{X} = \{X_1, X_2, ..., X_{n_s}\}$, such that the cumulative distributions of $\mathbf{X}(\boldsymbol{\theta})$ and $\boldsymbol{\theta}$ are the same. For illustration only, this can be expressed for a simplified case of uni-dimensional reference space ($n_r = 1$) as,

$$C_{\phi_I} = C_{\theta}, \tag{5.1}$$

where $C_{\phi_I} = \int P_{\phi_I} \cdot dX_I(\xi_1)$ and $C_\theta = \int P_{\theta_1} \cdot d\xi_1$ are the cumulative distribution functions (or CDFs) of the I^{th} scalar and the reference variable, respectively. Here the mapping functions have the same PDFs as the stochastically advected real scalars, i.e. $P_{\mathbf{X}} = P_{\boldsymbol{\phi}}$ and act as the latter's computational surrogates. This means that the differences between the actual spatio-temporal distributions of $\mathbf{X}$ and $\boldsymbol{\phi}$ are irrelevant so long as the statistical moments of the scalars are computed correctly. In other words, the mapping functions, $\mathbf{X}$, can be interpreted as the conditional averages of the physical scalars on an artificial stochastic reference field, i.e. $\mathbf{X}(\boldsymbol{\xi}) \equiv \langle \boldsymbol{\phi} | \boldsymbol{\theta} = \boldsymbol{\xi} \rangle$, with the prescribed joint PDF, $P_{\boldsymbol{\theta}}(\boldsymbol{\xi})$. Assuming that the cumulative distributions are non-pathological (continuous and monotonically increasing in $[0, 1]$), (5.1) gives a unique one-to-one mapping between the physical scalar and the stochastic reference variable. The same equation can be applied to compute the individual mapping for each scalar dimension separately and can be extended for multiple dimensions in $\boldsymbol{\xi}$-space. This one-to-one correspondence implies that the problem of solving the scalar PDF transport equation can be effectively posed in terms of the evolution equation for the mapping functions themselves.

For complete compliance with the joint scalar PDF transport equation, the equation for the evolution of the joint reference variable PDF, $P_{\boldsymbol{\theta}}$, is given by Klimenko & Pope (2003) as

$$\frac{\partial \bar{\rho} P_{\boldsymbol{\theta}}}{\partial t} + \boldsymbol{\nabla} \cdot (\mathbf{U} \bar{\rho} P_{\boldsymbol{\theta}}) + \frac{\partial A_k \bar{\rho} P_{\boldsymbol{\theta}}}{\partial \xi_k} + \frac{\partial^2 B_{kl} \bar{\rho} P_{\boldsymbol{\theta}}}{\partial \xi_k \partial \xi_l} = 0. \tag{5.2}$$

Here $\bar{\rho}$ models the ensemble averaged density. The advection-diffusion equation that governs the evolution of $\mathbf{X}(\boldsymbol{\xi})$ along spatio-temporal coordinates is referred to as the MMC equation (Klimenko & Pope, 2003) and it needs to be solved consistently with (5.2). The reader is referred to Sec. A.1 for the derivation of the generalised MMC equation. After primary closure assumptions, the MMC equation takes the following form for the I^{th} scalar,

$$\frac{\partial X_I}{\partial t} + \mathbf{U} \cdot \boldsymbol{\nabla} X_I + A_k \frac{\partial X_I}{\partial \xi_k} - B_{kl} \frac{\partial^2 X_I}{\partial \xi_k \partial \xi_l} = W_I / \rho_\xi. \tag{5.3}$$

Here, $\rho_\xi(\boldsymbol{\xi}) = \langle \rho | \boldsymbol{\xi} \rangle$ and $W_I = \langle \omega_I | \boldsymbol{\xi} \rangle$ are the mixture density and the chemical source term for the I^{th} species conditioned on the reference space. $\mathbf{U} = \langle \boldsymbol{u} | \boldsymbol{\xi} \rangle$ is the convective velocity vector conditional on the reference space and A_k, B_{kl} are the drift and diffusion coefficients in the MMC equation. The above equation governs the evolution of the mapping functions from initial and boundary conditions.

Thus, validity of (5.2) and (5.3) ensures that the joint PDF of the mapping functions (or surrogate scalars) satisfies the conventional scalar PDF transport equation. It should be noted that the present MMC approach requires the same (5.3) to be applied to all scalar mapping functions with no major-minor distinctions. This is in stark contrast to previous applications of mapping closure (Chen *et al.*, 1989; Pope, 1991; Girimaji, 1992; Mortensen & Andersson, 2005), where the technique was used to model the conditional scalar dissipation terms alone. Equation (5.3) has been applied to homogeneous turbulence previously (Cleary & Kronenburg, 2007*a*,*b*; Kronenburg & Cleary, 2008), but can be applied to inhomogeneous turbulent flows as well as is done in the present study. Also since (5.2) permits a broad range of solutions for $P_{\boldsymbol{\theta}}$, there need not be any fixed *a priori* assumptions about the shape of the PDF in the reference space.

Expressions used to compute the unconditional non-linear source terms, ω_I, for the chemical species depend on the flame-chemistry model employed in the present study and are described in Sec. 3.3. The full set of scalars, $\boldsymbol{\phi}$, modelled by the aforementioned MMC equation also includes the major scalars, viz. Z and h_s, in addition to the chemical species (or minor scalars). With reference to equations (2.17) and

(2.44), the expressions for the conditional source terms of the major scalars are given by, $W_Z = 0$ and $W_{h_s} = -\sum_\iota W_\iota \mathcal{H}_\iota^f$, where Σ_ι denotes the summation over the chemical species. Closure for this term in the MMC equation is provided using the first-order terms only, i.e. $W_I = W_I(\mathbf{X}(\boldsymbol{\xi}))$, since the fluctuations in the surrogate scalars, $\mathbf{X}$, are negligible with respect to the n_r-manifold. Closures for the unclosed velocity term and the drift and diffusion coefficients need to be consistent with the reference PDF transport equation. These closures can be determined for *any* reference space PDF prescription, with the *only* constraint that $P_{\boldsymbol{\theta}}$ satisfies (5.2). Here it is important to note that the stochastic reference variables represent the random fluctuations of the scalars in the MMC model. Therefore, one is free to choose any convenient description of this randomness in terms of the shape of PDF $P_{\boldsymbol{\theta}}$ and substitute that in (5.2) to obtain closures for the unclosed coefficients.

5.2.1 Modelling thermal effects on diffusivity

In real flames the diffusivities of the chemical species are not constant-valued but have a distinct temperature dependence. The thermodynamics model employed in the present study (cf. Sec. 3.2) accounts for this physical effect and the temperature-dependence of I^{th} scalar diffusivity, D_I, is given by (3.2). For the MMC implementation, incorporating this effect implies that D_I can no longer have a constant value in the reference space. Therefore, in order to employ existing closures for the MMC drift and diffusion coefficients that do not take the temperature-dependence of diffusivities into account, it is necessary to express B_{kl} in the form of conventional MMC diffusion coefficients without temperature-dependence. Thus,

$$B_{kl} = \frac{D_I}{\bar{D}} \cdot B_{kl}^0, \tag{5.4}$$

where B^0_{kl} is the conventional MMC diffusion coefficient with mean mixture fraction diffusivity, $\bar{D}$, and the 0-superscript denotes the lack of variation in the reference space. Henceforth, unless otherwise specified, the discussion on the modelling of the diffusion coefficients refers to the temperature-invariant B^0_{kl} values. It is understood that once B^0_{kl} is successfully modelled, one can revert back to the temperature dependence via (5.4). The reader is reminded that although D_I is not exactly the same for all species, the MMC differential diffusion term $\boldsymbol{\nabla}\cdot[\rho(D_I - D_k)\boldsymbol{\nabla}\theta_k]\partial X_I/\partial\xi_k$ occurring in the generalised MMC equation (6.7) is *not* modelled here (cf. Sec. A.1).

5.2.2 A_k closure

The MMC methodology allows for the PDF $P_{\boldsymbol{\theta}}$ to be selected as standard multivariate Gaussian (Klimenko & Pope, 2003), so that each one of the $\xi_1, \xi_2, .., \xi_{n_r}$ variables are stochastically independent and normally distributed with zero mean and unity variance. For this reference PDF, it can be shown (cf. Sec. A.3) that (5.2) remains satisfied, provided the MMC drift coefficient is given by

$$A_k = -\frac{\partial B_{kl}}{\partial \xi_l} + B_{kl}\xi_l + a_k, \tag{5.5}$$

where a_k satisfies the following PDE,

$$\frac{1}{\bar{\rho}}\boldsymbol{\nabla}\cdot(\mathbf{U}\bar{\rho}) + \frac{\partial a_k}{\partial \xi_k} - \xi_k a_k = 0. \tag{5.6}$$

(5.5) implies that the provision of the MMC diffusion coefficients, B_{kl}, is necessary to close the drift coefficients. Furthermore, the exact form for a_k is also not strictly known in the MMC framework and depends, via (5.6), on a closure model for the convective velocity term, $\mathbf{U}$. Hence, unless a suitable model for the convective velocity term is derived, closing the a_k (and therefore A_k) term is not possible. It should be stressed here that while models for the diffusion coefficients, B_{kl}, and convective velocity term, $\mathbf{U}$, need to follow certain consistency constraints[1], they do *not* rigorously follow from the mathematical framework for MMC. The MMC literature by Klimenko & Pope (2003) also provides conventional models for the B_{kl} and $\mathbf{U}$ terms for full closure of the MMC equation. However, these closures impose certain oversimplified and restrictive assumptions on the physics of turbulent non-premixed combustion. The coming sections explore these shortcomings and propose changes to the sub-models for B_{kl} and $\mathbf{U}$ and therefrom derive the model for a_k. These sub-models are then incorporated into (5.3) to get a fully-closed MMC framework for the present case of a spatially-evolving (inhomogeneous) turbulent jet flame.

5.2.3 B_{kl} closure

In order to provide closure for the MMC diffusion coefficients, it should be recalled (cf. Sec. 5.1) that MMC is a generalisation of the CMC concept that can (in principle) use any type of reference variables for conditioning. For well-chosen reference manifolds, where variance around the means conditioned on the reference variables is negligible, the (unclosed) scalar dissipation variable seen in the CMC equation (2.62) can be related to the MMC diffusion coefficient as,

$$N_{ij} = B_{kl} \frac{\partial X_i}{\partial \xi_k} \frac{\partial X_j}{\partial \xi_l}. \tag{5.7}$$

The reader is referred to Sec. A.2 for the full derivation of the above. It is easy to see that the above equation follows commutativity of the subscript indices, i.e.

---

[1] cf. (5.6) and (5.7)

$B_{kl} = B_{lk}$. Recall that B_{kl} can be expressed in the temperature-invariant form, B^0_{kl}, using (5.4). An analogous form for the dissipation variable is $N_{ij} = (D_I/\bar{D}) \cdot N^0_{ij}$, where $N^0_{ij} = \bar{D}\boldsymbol{\nabla}\phi_i \cdot \boldsymbol{\nabla}\phi_j$. Hence, the temperature-invariant form for (5.7) is given by

$$N^0_{ij} = B^0_{kl} \frac{\partial X_i}{\partial \xi_k} \frac{\partial X_j}{\partial \xi_l} \tag{5.8}$$

The above identity is used as the basis for deriving the closure of the MMC diffusion coefficients. To get rid of the unclosed terms, Favre-averaging (5.8) throughout yields,

$$\widetilde{N^0_{ij}} = \left\langle B^0_{kl} \frac{\partial X_i}{\partial \xi_k} \frac{\partial X_j}{\partial \xi_l} \right\rangle . \tag{5.9}$$

It is customary in mapping closure (Klimenko & Pope, 2003) to assume that B^0_{kl} is independent of $\boldsymbol{\xi}$, i.e. $B^0_{kl} = \overline{B^0_{kl}}$. This modelling implies that the B^0_{kl} coefficients remain unchanged under averaging and can be taken out of the $\langle\rangle$ operator in (5.9).

$$\widetilde{N^0_{ij}} = B^0_{kl} \left\langle \frac{\partial X_i}{\partial \xi_k} \frac{\partial X_j}{\partial \xi_l} \right\rangle . \tag{5.10}$$

The above reformulation of *removing* the diffusivity contribution is necessary in order to close the diffusion coefficients according to the models discussed in MMC literature. Matching of the diffusion coefficient B^0_{kl} with the averaged dissipation variable $\widetilde{N^0_{ij}}$ ensures the correct level of (unconditional) scalar fluctuations of scalars i and j. The derivatives in $\boldsymbol{\xi}$-space within the $\langle\rangle$ operator are easily determined once the mapping functions, $\mathbf{X}(\boldsymbol{\xi})$, are solved for using (5.3). Using the mean dissipation values from a RANS solver or a pre-computed DNS, the corresponding

MMC diffusion coefficients can be determined by solving (5.10) in matrix form for all scalars.

Recall that the above formulation for the diffusion coefficients holds only if they are presumed to be stochastically invariable. Evaluating this assumption requires an insight into the physical significance of the MMC diffusion coefficients and that can be clarified by using the above model in the limit of purely homogeneous turbulent scalar mixing. A further simplication of putting $n_r = 1$, with $\xi_1$corresponding to Z, is introduced to aid the clarity of presentation. For this reduced case, $N^0_{ij} = N^0_{11}$, $B^0_{kl} = B^0_{11}$ and $\widetilde{N^0_{11}} = B^0_{11}\left\langle(\partial Z/\partial\xi_1)^2\right\rangle$ using (5.10). Since, the turbulence is purely homogeneous and ξ_1 is a Gaussian of zero mean and unit variance, $\left\langle(\partial Z/\partial\xi_1)^2\right\rangle = \widetilde{Z''^2}$. Hence (5.10) takes the following form for homogeneous turbulence,

$$\widetilde{N^0_{11}} = B^0_{11}\widetilde{Z''^2} \tag{5.11}$$

Using the model for average scalar dissipation rate in homogeneous turbulent mixing (Spalding, 1971; Pope, 1985) from (2.36),

$$\widetilde{N^0_{11}} \sim \widetilde{Z''^2}/\tau, \tag{5.12}$$

where τ is the characteristic time-scale associated with integral scale turbulent eddies. Comparing (5.11) and (5.12) implies $B^0_{11} \simeq 1/\tau$, i.e. the MMC diffusion coefficient is a measure of the eddy turnover frequency in a homogeneous turbulent mixing process. Therefore, the assumption of a non-fluctuating B^0_{11} in $\boldsymbol{\xi}$-space really means that we are *fixing* the eddy turnover time-scale of the mixing process. For the special case of homogeneous turbulent mixing, this fixed value is roughly similar to the characteristic integral time-scale of turbulence. As explained earlier in Sec. 2.2.1, instantaneous scalar dissipation fluctuations are highly intermittent, with a wide quasi-lognormal distribution, that cannot be sufficiently characterised by any single spatial- or time-scale. Modelling these scalar dissipation fluctuations is crucial in predicting the extinction and re-ignition phenomena accurately. The diffusion coefficients (especially B_{11}^0) represent the mechanism of modelling the effects of the scalar dissipation fluctuations on the evolution of the scalar quantities in MMC. Assuming B_{11}^0 to have a fixed value in $\boldsymbol{\xi}$-space is therefore not sufficient to emulate the whole distribution of time-scales characteristic of the dissipation process. Klimenko (2003a, 2005) suggested the use of a 'dissipation-like' variable to model the fluctuations of the principal diffusion coefficient in $\boldsymbol{\xi}$-space as

$$B_{11}^0 = \overline{B_{11}^0}\varphi(\xi_2). \tag{5.13}$$

According to the above model, B_{11}^0 no longer simulates a fixed representative value of the turbulent mixing frequency but its complete (lognormal) distribution. Here ξ_2 represents the variable in reference space that causes the fluctuations in the dissipation rate in the MMC model. The function

$$\varphi(\xi_2) = exp(c_\alpha \xi_2 - {c_\alpha}^2/2) \tag{5.14}$$

describes the fluctuations of B_{11}^0 around its mean $\overline{B_{11}^0}$. Since ξ_2 is normally distributed, function $\varphi(\xi_2)$ is constructed so that the PDF of B_{11}^0 is lognormal with mean $\overline{B_{11}^0}$, irrespective of the value of the exponential coefficient, c_α. It is easy to deduce from (5.14) that the first two moments of φ are given by, $\langle \varphi \rangle = 1$ and $\langle {\varphi'}^2 \rangle = exp(c_\alpha c_\alpha) - 1$. Klimenko (2003$a$) has shown that the instantaneous scalar dissipation, N_{11}^0, of the mixture fraction, Z, is related to the conditional scalar dissipation, $\langle N_{11}^0 | Z = \eta_1 \rangle$ by $N_{11}^0 \simeq \langle N_{11}^0 | \eta_1 \rangle \varphi$. Using the moments of φ and the aforementioned approximation for N^0_{11}, the value of the exponential coefficient is determined as

$$c_\alpha{}^2 = ln\left(\frac{\langle N^{0''2}_{11}|\eta_1\rangle}{\langle N^0_{11}|\eta_1\rangle^2} + 1\right), \tag{5.15}$$

where $\langle N^{0''2}_{11}|\eta_1\rangle$ is the conditional variance of N^0_{11}.

As explained in Chapter 2, using mixture fraction and sensible enthalpy as the choice for the major, conditioning scalars in CMC ensures that the conditional fluctuations in the minor scalars are negligible. The same is not true of mixture fraction and scalar dissipation as the conditioning scalars. Keeping the conditional fluctuations at a minimum is necessary for the validity of the first-order closure of the chemical source term, W_I, in (5.3). Given this background, Kronenburg & Cleary (2008) present the dilemma of using the second reference variable, ξ_2, to represent the fluctuating behaviour of sensible enthalpy and scalar dissipation simultaneously. It should be re-iterated here that the reference variables represent the major scalars only notionally. Their real physical purpose in the MMC framework is to act as independent sources of randomness or stochastic behaviour. Thus, each system-defining major scalar is typically associated with a distinct reference variable. However, this need not be the case always. The authors (Kronenburg & Cleary, 2008) correctly recognise that while sensible enthalpy and scalar dissipation are used independently as major conditioning scalars in CMC literature, their stochastic behaviours bear a strong (negative) correlation. Therefore, generating fluctuations for both h_s and N^0_{11} using the same reference variable is completely valid in MMC, as long as the mapping functions/models for h_s and N^0_{11} are consistently derived/presumed. Since B^0_{11} (and therefore N^0_{11}) is modelled using (5.13), any reference variable ξ_2 can adopt the character of a dissipation-like variable. The notional association of ξ_2 with a physical quantity (viz. h_s) is unimportant here.

Finally, the model in (5.13) can be used to revise the closure for the diffusion coefficients, B^0_{kl}, as (Kronenburg & Cleary, 2008):

$$B^0_{11} = \overline{B^0_{11}} \cdot exp(c_\alpha \xi_2 - {c_\alpha}^2/2) \tag{5.16}$$

$$B^0_{12} = \overline{B^0_{12}} = B^0_{21} \tag{5.17}$$

$$B^0_{22} = \overline{B^0_{22}} \tag{5.18}$$

Here the overbar denotes the averaged values within the $\langle\rangle$ operator that are independent of the $\boldsymbol{\xi}$-space variables. These unknown $\overline{B^0_{kl}}$ values are computed by substituting the above model in (5.9) and solving the resulting 3×3 matrix equation. Unlike the standard B^0_{kl} model in (5.10), the $\varphi(\xi_2)$ exponential term occurring in the expression for B^0_{11} cannot be extracted outside the averaging operator. Hence the exponential dependency affects the averages of the gradients with respect to the ξ_1 coordinate. As mentioned above, fluctuations around mean temperature conditioned on the mixture fraction bear a strong negative correlation to the scalar dissipation fluctuations during the extinction/re-ignition process. This means that strong dissipation events lead to low temperatures due to the large strain imposed on the burning flamelet. The strength of the correlation between the scalar dissipation and temperature fluctuations reduces as the scalar dissipation values approach the extinction limit. Large fluctuations in scalar dissipation from the mean encountered by the burning flamelet at the extinction limit is indicated by the progressively large values attained by the $\left\langle N^{0''2}_{11}|\eta_1 \right\rangle / \langle N^0_{11}|\eta_1\rangle^2$ ratio in the expression for c_α in (5.15), which in turn is reflected in the value of $c_\alpha \to 0$. The c_α parameter is only indicative of the proximity to the extinction limit in terms of dissipation values and thus drives the dissipation fluctuations accordingly. However, it contains absolutely no feedback about the temperature level, without which predicting re-ignition is impossible. Hence the authors (Kronenburg & Cleary, 2008) introduce a simple correlation function, f_{corr}, that describes the degree of extinction/re-ignition based on the mean sensible enthalpy (or temperature) at stoichiometric conditions, into the expression for c_α. The revised c_α parameter is modelled as,

$$c_\alpha = C_f f_{corr} \left[ln \left(\frac{\left\langle N_{11}^{0''2} | \eta_1 \right\rangle}{\langle N_{11}^{0} | \eta_1 \rangle^2} + 1 \right) \right]^{1/2}, \tag{5.19}$$

where $f_{corr} = -\langle \hat{h}_s | \eta_1 = Z_s \rangle$ computed from the MMC at the previous computational step and C_f is a heuristic scaling constant for the model. The negative sign of f_{corr} ensures that the correlation between dissipation and sensible enthalpy fluctuations is modelled correctly. Even small increments in the value of the scaling constant cause an appreciably stronger exponential behaviour of $\varphi(\xi_2)$ leading to more lognormality of the dissipation fluctuations. Kronenburg & Cleary (2008) chose $C_f = 1$ in their MMC calculations for homogeneous decaying turbulence. However, for the present study it was found that using a constant value of $C_f = 1$ does not scale-up the correlation function well enough and value of 1.3 was chosen for the present implementation. Here, $\langle \hat{h}_s | \eta_1 = Z_{st} \rangle$ is conditional mean (at stoichiometric) of the sensible enthalpy normalised by the maximum at adiabatic flame temperature defined in (3.5).

5.2.4 U closure

In their derivation of the standard MMC formulation, Klimenko & Pope (2003) note that in traditional conditional moment closure studies (Kuznetsov & Sabelnikov, 1989; Klimenko & Bilger, 1999) it is customary to close the velocity term as a linear function of the conditioning scalars. Since the MMC involves conditioning based on reference scalars, the analogous MMC closure posits a linear dependence on all ξ_k to model the $\mathbf{U} = \langle \boldsymbol{u} | \boldsymbol{\xi} \rangle$ velocity term as

$$\mathbf{U} = \mathbf{U}^{(0)} + \mathbf{U}_k^{(1)}\xi_k \tag{5.20}$$

with

$$\mathbf{U}^{(0)} = \widetilde{\boldsymbol{u}} \tag{5.21}$$

and

$$\mathbf{U}_k^{(1)}\langle {\theta_k}^* {X_i}^* \rangle = \widetilde{\boldsymbol{u}''{\phi_i}''} \tag{5.22}$$

where $\widetilde{\boldsymbol{u}''{\phi_i}''}$ represents the Favre-averaged correlation of the convective velocity and i^{th} scalar fluctuations and the $*$-symbol denotes stochastic variables. It is important to remember here that the reference PDF $P_{\boldsymbol{\theta}}$ is presumed to be joint-Gaussian. Hence any $\mathbf{U}$-model linear in ξ-space implicitly presumes that the convective velocity field is Gaussian distributed like the reference variables. While the cross-correlation term provides the mechanism to account for the feedback between the velocity and scalar statistics in the model, the Gaussianity of the convective velocity is an additional (and sometimes unnecessary) constraint. It can grossly oversimplify the physical evolution of the flow, especially when the turbulent velocity field has not developed enough and shows strong local inhomogeneities, e.g. close to the nozzle in turbulent reacting jet flows. The presence of inhomogeneities in the initial scalar (and downstream velocity) distribution is characteristic of turbulent non-premixed jet flames. The reader is reminded that such flows typically involve forcing of the pure fuel and oxidiser streams into the combustion chamber, with each stream corresponding to a constant scalar concentration (normalised to Z) and constant downstream velocity value at the point of efflux. The initial scalar/velocity distributions can thus be modelled as double-δ PDFs, with peaks at the scalar-concentration/velocity values corresponding to the pure-fuel and pure-oxidiser limits. For the general case of multi-stream mixing with additional streams at intermediate values of Z, the initial scalar/velocity PDFs are modelled with as many δ-peaks. This implies that packets of fuel/oxidiser with different scalar-concentrations convect at different velocities depending on their stream of origin and as these fuel/oxidiser packets mix, their velocities and scalar-concentrations assume intermediate values together. In other words, the statistics of downstream convective velocity in the early mixing process are strongly correlated with the scalar distribution (represented by P_Z). Therefore, the velocity PDF evolves, just as the scalar PDF, from a double- or multi-δ initial condition and imposing an unnatural Gaussian distribution on it will not yield the correct mixing dynamics. Fig. 5.1 corroborates the physical correspondence between the velocity and scalar statistics close to the nozzle. The PDF of the downstream convective velocity values from the DNS at nozzle-exit shows a distinct tri-modal character, with peaks corresponding to the jet, pilot and oxidiser streams. On the other hand, by using the unconditional mean and variance values from the DNS, the Gaussian model predicts negative values of the convective velocity tantamount to an aphysical back-flow upstream. Truncating the Gaussian PDF at $u_x = 0$ will, in turn, cause unnaturally high values of velocity after correcting for the variance.

The unnecessary imposition of Gaussianity on the convective velocity can be avoided by recognising that its fluctuations correlate strongly with those of Z and that the Z-distribution is fully solved for in the MMC formulation. Instead of presuming the Gaussian shape of the velocity PDF *a priori*, it is better to model the velocity field by its average conditional on Z,

$$\mathbf{U} = \langle \boldsymbol{u} | Z \rangle, \tag{5.23}$$

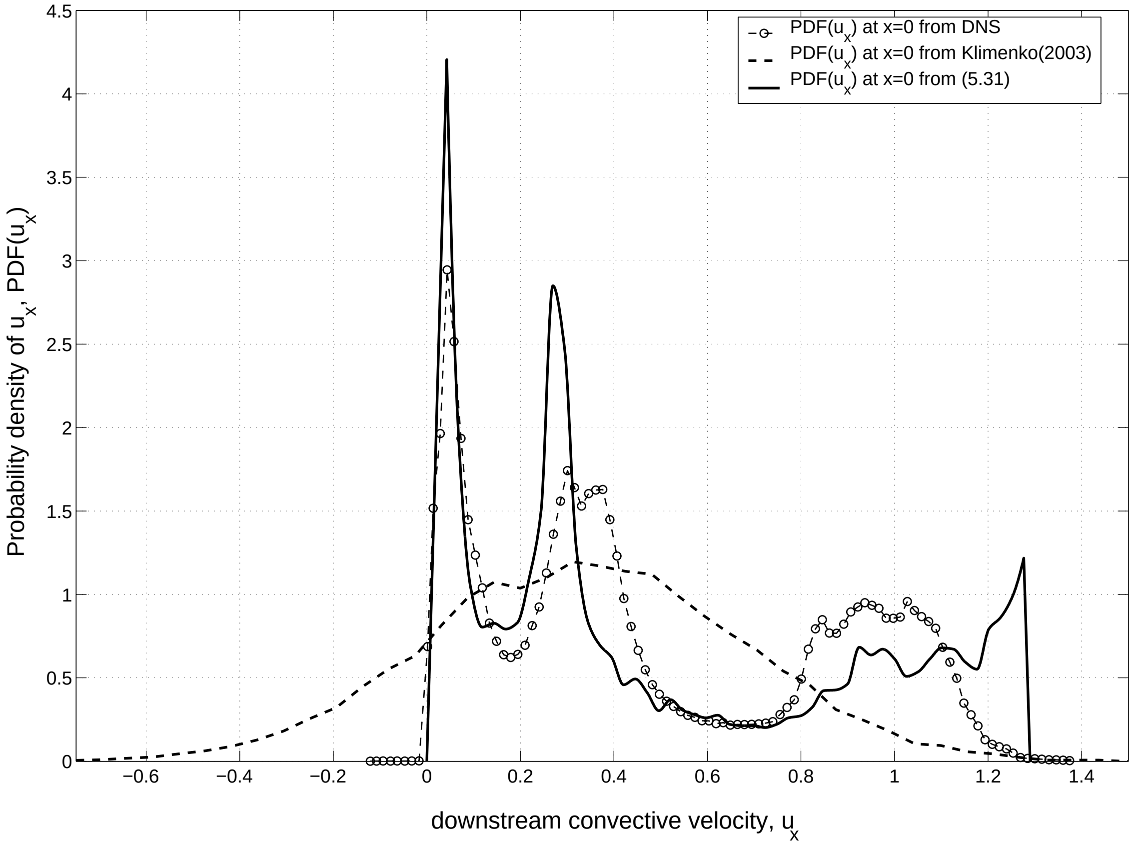

Figure 5.1: Comparison of the marginal velocity PDFs from the DNS, the Gaussian model in (5.20) and the revised model for the present study in (5.31) is shown at the jet-exit conditions, i.e. $x = 0$. The unconditional mean and variance of the Gaussian distribution correspond to actual DNS values at $x = 0$.

whereas the conditional variance, $\langle \boldsymbol{u}''^2 | Z \rangle$, is neglected. Using the standard conditional moment closure (Klimenko & Bilger, 1999) of velocity, the conditional velocity is then expressed as a linear function of the major mixture fraction variable instead of the underlying reference variables. Thus,

$$\mathbf{U} \simeq \widetilde{\boldsymbol{u}}(\mathbf{x},t) + (Z - \widetilde{Z}(\mathbf{x},t)) \frac{\widetilde{\boldsymbol{u}''Z''}(\mathbf{x},t)}{\widetilde{Z''^2}(\mathbf{x},t)}, \tag{5.24}$$

where the scalar statistics are represented by the fluctuating mixture fraction field as mentioned before. The coefficients in the linear model are functions of the ensemble

Favre-averages and correlations of Z and $\boldsymbol{u}$ that vary along spatio-temporal coordinates. Fig. 5.2 shows the joint PDF of the mixture fraction and the downstream convective velocity from the DNS, superimposed by convective velocity values modelled on the mixture fraction statistics in one and two physical dimensions. The figure shows that the two-dimensional implementation of the model in (5.24) can (partially) account for the conditional variance neglected in using the one-dimensional ensemble means. Nonetheless, (5.24) is clearly superior to the Gaussian model in predicting the $\langle \boldsymbol{u}|Z\rangle$ conditional mean. Further results and discussion on the comparison between these models can be found in Sec. 5.4.3.

It is important to note that the mixture fraction represents the first major scalar in the MMC framework, i.e. $Z \equiv \phi_1$, and the linear model in (5.24) can also be theoretically extended to incorporate the statistical dependence of convective velocity on secondary (e.g. h_s or more) major scalars. One can also extend the above model by adding non-linear terms involving higher moments and correlations of Z and $\boldsymbol{u}$. However, the standard closure approximation based on the single-conditioning of convective velocity on Z is most often considered sufficient in standard CMC/MMC literature (Kuznetsov & Sabelnikov, 1989; Klimenko & Bilger, 1999; Kim *et al.*, 2000; Devaud & Bray, 2003; Mortensen, 2005). This is mainly because the correlations between velocity and secondary major, conditioning scalars like h_s or χ are very weak compared to the magnitude of the turbulent scalar flux, $\widetilde{\boldsymbol{u}''Z''}$, in most turbulent non-premixed flames.

The stochastic mapping function for the mixture fraction, $X_1(\boldsymbol{\xi})$, is used as a surrogate for the actual turbulent field, Z, in the $\mathbf{U}$-model given by (5.24),

$$\mathbf{U}(\boldsymbol{\xi}) \simeq \widetilde{\boldsymbol{u}} + (X_1(\boldsymbol{\xi}) - \widetilde{Z})\frac{\widetilde{\boldsymbol{u}''Z''}}{\widetilde{Z''^2}}, \tag{5.25}$$

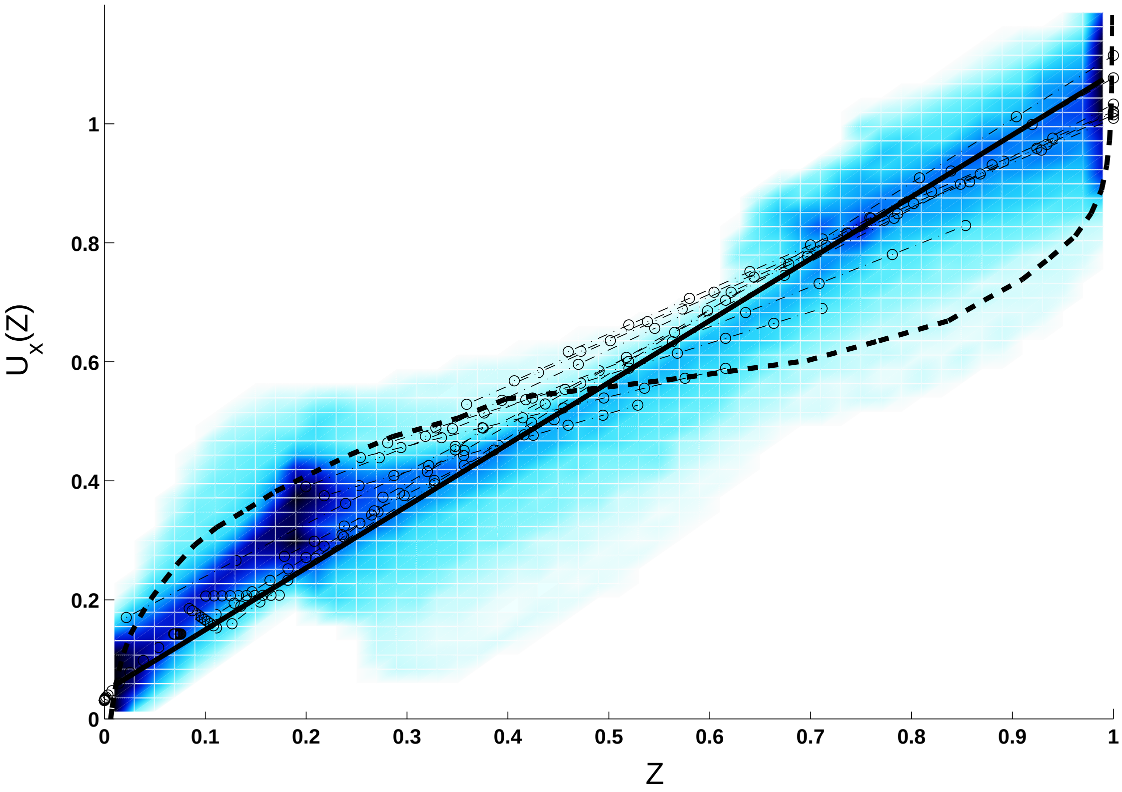

Figure 5.2: Comparison of the various velocity models in the composition space with the actual joint PDF of the mixture fraction and downstream velocity at $x = 0$. The dashed-dotted lines (with circles) indicate the velocity predictions from (5.24) based on local ensemble means/correlations at 40 locations along the cross-stream direction, i.e. mean/correlation values varying along y at $x = 0$. The solid line indicates the velocity prediction from (5.24) using ensemble averaging over the cross-stream direction, i.e. for constant mean/correlation values at $x = 0$. The dashed-line shows the result of the Gaussian model and its aphysical under-/over-predictions at $Z = 0, 1$ are not in view for presentation clarity.

The computational routine for (5.3) uses this velocity model as an input at each spatio-temporal step, by assigning $X_1(\boldsymbol{\xi})$ from the MMC solution at the previous step. This modelling ensures that the convective velocity PDF evolves in accordance with the scalar statistics computed using the MMC equation and is not limited to any prescribed (Gaussian) shape. Any aphysical mismatch between the scalar and velocity statistics is, thus, strictly avoided. Furthermore, as the $Z - \boldsymbol{u}$ joint PDF evolves into a bi-variate Gaussian with the downstream development (homogenisation) of turbulence, the above-mentioned linear approximation becomes increasingly equivalent to the conventional MMC **U**-model in (5.20).

A minor limitation of this model arises from the fact that unlike mixture fraction, the velocity field is a vector quantity, not a scalar. Statistics of only the dominant convective velocity component that forces the scalar mixing process are reflected in those of the scalar. As explained earlier, the principal convective mechanism for non-premixed reacting flows is provided by the downstream forcing of fuel and oxidiser jets. Therefore, the velocity component most strongly correlated with the evolution of the fuel-oxidiser mixing process is also aligned in the downstream direction. On the other hand, velocity components orthogonal to the downstream direction do not reflect the statistics of (or inhomogeneities in) the initial scalar mixing process and can be realistically expected to follow Gaussian dynamics. Thus for MMC involving more than one spatial dimensions (5.25) and (5.20) can be simultaneously used to model the downstream velocity and its orthogonal components, respectively.

5.2.5 a_k closure

As explained in Sec. 5.2.2, a joint-Gaussian $P_{\boldsymbol{\theta}}$ (with zero mean and unit variance) is presumed as the solution for the governing reference PDF equation. This solution is mathematically consistent with the form for the A_k term given by (5.5). The full expression for A_k includes the unclosed a_k term that is governed by the PDE in (5.6) and dependent on the convective velocity model for closure. Hence any revision in the modelling for **U** must be followed by a consistent modelling to close a_k. In the conventional MMC approach, Klimenko & Pope (2003) do not pose (5.6) for the a_k term explicitly. The authors implicitly substitute the model expressed in (5.20) for the convective velocity term in (5.6) and use the mean flow continuity condition to obtain the standard closure for the a_k term as,

$$a_k = \boldsymbol{\nabla} \cdot (\bar{\rho}\mathbf{U}_k^{(1)})/\bar{\rho}. \tag{5.26}$$

More recent studies (Cleary & Kronenburg, 2007*b*; Kronenburg & Cleary, 2008) employing fully-closed MMC of homogeneous decaying turbulence simply do not have to deal with the closure of the convective velocity term as the turbulence in that case is not spatially evolving. They set $\mathbf{U}_k^{(1)} \equiv 0$, which in turn nullifies a_k as well. However, for the present case of a spatially evolving, inhomogeneous turbulent flame, the a_k term is not negligible. It cannot be predicted by the model in (5.26) either, as the model is based on a presumed Gaussian velocity field. As described in the previous section on $\mathbf{U}$ closure, the Gaussian (downstream) convective velocity assumption will lead to an aphysical mismatch with the scalar statistics for evolving jet flows. Hence a model for the a_k term *consistent* with the revised convective velocity model in (5.25) has been derived here. Recall that the mathematical formulation for MMC provides only one PDE for determining the a_k variable. Since the reference-space for the present study is two-dimensional, closures for both $a_1(\boldsymbol{\xi}), a_2(\boldsymbol{\xi})$ need to be computed simultaneously. It should be noted here that the goal is to find the solution for (5.6) consistent with the model for $\mathbf{U}$. The actual form of the model presumed/derived for a_k is unimportant as long as it satisfies (5.6). Therefore, the following closure is proposed for a_k:

$$a_1 = a(\xi_1, \xi_2) \tag{5.27}$$

$$a_2 = 0 \tag{5.28}$$

Using the above in (5.6), the following one-equation submodel is obtained to close the a_k term in the expression for the drift coefficient in the governing MMC equation:

$$\frac{1}{\bar{\rho}}\boldsymbol{\nabla}\cdot(\mathbf{U}\bar{\rho})+\frac{\partial a}{\partial \xi_1}-\xi_1 a=0. \tag{5.29}$$

5.3 Numerical experiment

5.3.1 Model simplification

Equation (5.3) is the general MMC equation that describes the evolution of the mapping functions from their presumed initial distributions in all types of non-premixed turbulent flames. As described in Sec. 3.1 the non-premixed flame studied in this case is in a planar, spatially-evolving and inhomogeneous turbulent flow field. According to (4.2) the averaging operation for this flame involves averaging over the temporal and spanwise (z-coordinate) realisations. Therefore, in its present implementation (5.3) does not have any temporal or z-wise gradients and only the downstream (x-) and cross-stream (y-) variation of conditional statistics can possibly be predicted. However, a further simplification has been imposed on the problem domain, viz. of disregarding the variation of conditional statistics in the cross-stream direction as well. Besides the obvious reduction in computational demand, the two main reasons for enforcing this simplification are as follows:

- As explained in Sec. 3.4, large upstream regions of the Pantano (2004) flame geometry are quasi-laminar and the centre-line *turbulent* region of the jet is constrained to a width of only two- to three-nozzle diameters in the cross-stream direction. Computation of the turbulent scalar mixing in these regions is wasted unless the MMC cells that fall within the quasi-laminar region are merged with those where the turbulence intensities are higher. This reduces the number of MMC cells in the far downstream section as well, since a fixed

Cartesian grid with momentum/scalar fluxes and gradients orthogonal to the cell-boundaries is used to solve (5.3). Fixing the grid boundaries to the separation surfaces of the jet would solve this problem, but will require a transformation of the MMC equations resulting in unforeseen modelling problems for the convective and dissipation terms.

- The second reason for the simplification is a purely statistical consideration. A large (ideally infinite) number of independent realisations of a turbulent variable within the MMC cell is required to compute the averages reliably. The problem is made worse when computing conditional averages due to a reduction in the sample set on conditioning. Since unconditional Favre averages of various turbulent quantities are used as an input for the MMC combustion model, a larger number of MMC cells implies a reduction in the input data quality.

Due to both of the above reasons one MMC cell encompasses all the statistics along the cross-stream direction (in addition to the required spanwise and temporal coordinates). Therefore, the principal direction of spatial-evolution of the jet, i.e. the downstream, is chosen as the only indepedent coordinate in (5.3) over which the variations of the mapping functions are computed. For this one-dimensional MMC closure[2], equations (5.3), (5.25) and (5.29) take the following forms:

$$U_x \frac{\partial X_I}{\partial x} + A_k \frac{\partial X_I}{\partial \xi_k} - B_{kl} \frac{\partial^2 X_I}{\partial \xi_k \partial \xi_l} = W_I / \rho_\xi \qquad \forall\ k,l \in \{1,2\}, \tag{5.30}$$

$$U_x(\boldsymbol{\xi}) \simeq \widetilde{u_x} + \frac{\widetilde{u_x'' Z''}}{\widetilde{Z''^2}} \left(X_1(\boldsymbol{\xi}) - \widetilde{Z} \right), \tag{5.31}$$

---

[2] All references to 'one-dimensional MMC' indicate the downstream physical coordinate, but not the reference manifold.

$$\xi_1 a - \frac{\partial a}{\partial \xi_1} = \frac{1}{\bar{\rho}} \frac{\partial \left(U_x \bar{\rho}\right)}{\partial x}. \tag{5.32}$$

Terms $\widetilde{u_x}$, $\widetilde{Z}$ and $\widetilde{u_x''Z''}/\widetilde{Z''^2}$ are completely specified in terms of the ensemble averages from the DNS (or any RANS flow solver). Here, u_x is the (principal) streamwise component of the convective velocity vector, $\boldsymbol{u}$, and $U_x(\boldsymbol{\xi}) = \langle u_x | \boldsymbol{\xi} \rangle$ is its average conditioned on the reference space. The above equations along with (5.4), (5.5), (5.16)-(5.18) and (5.19) provide the complete theoretical MMC closure. The numerical implementation of these equations is illustrated in Fig. 5.3 and the details are discussed next in this section.

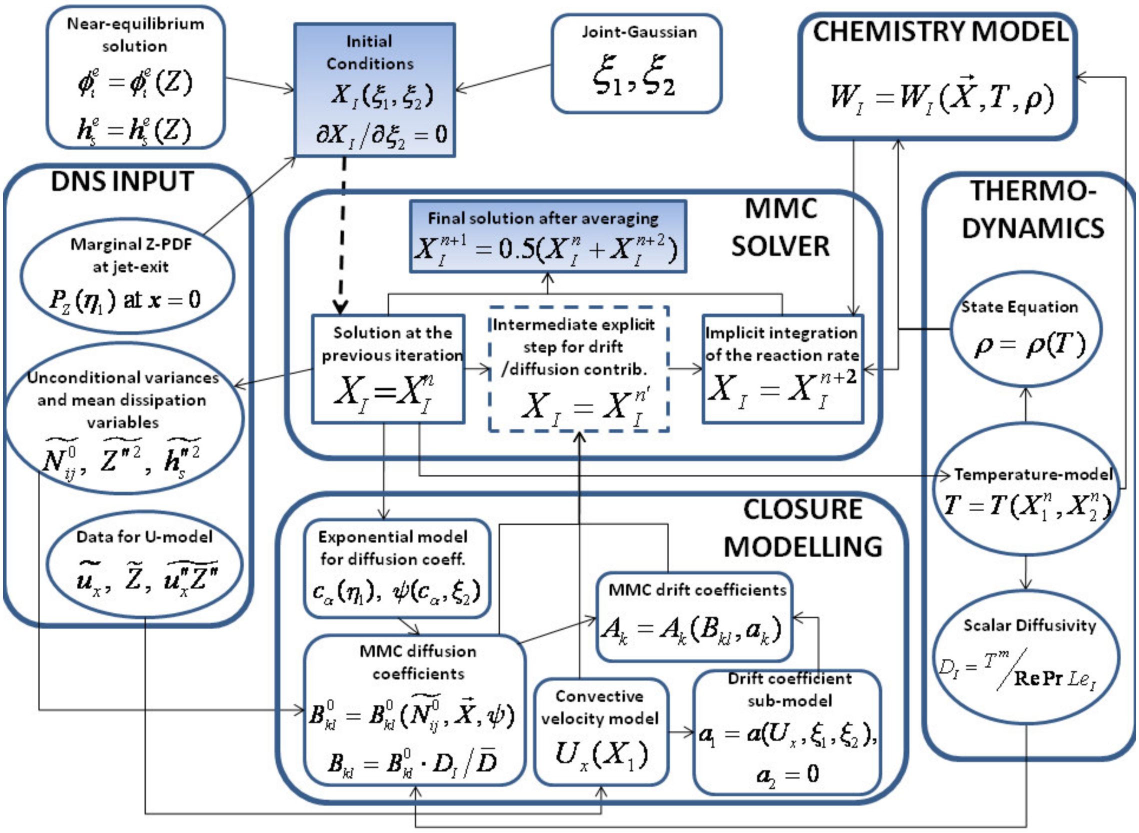

Figure 5.3: Schematic representation of the computational routines used to implement the MMC closure modelling in the present study. Shaded boxes indicate the presumed initial conditions at $x = 0$ and the final MMC solution at each downstream station. Arrow directions symbolise the information flow.

5.3.2 Initial conditions

Chemical species initialisation

The above mentioned closed system of partial differential equations represents an initial-value problem. Therefore, the initial values of the mapping functions corresponding to all the scalars need to be provided. Analogous to the initialisation used in the Pantano (2004) DNS, a one-dimensional laminar flamelet calculation was carried out to obtain the values of all species as functions of mixture fraction at equilibrium conditions, i.e. $\phi_\iota^e\,(Z)$. The flamelet solution for chemical species was obtained from the simplified steady flamelet equation of Peters (1984), i.e. using (2.54) without the transient term and replacing partial- with full-derivatives with respect to Z:

$$-\frac{\rho(T^e)}{Le_\iota} N_s \frac{d^2\phi_\iota^e}{dZ^2} = \omega_\iota\left(\phi_\iota^e, T^e(Z)\right), \qquad (5.33)$$

where $T^e(Z)$ is the Burke-Schumann profile for temperature dependent on the mixture fraction and $\rho(T^e)$ is computed from these temperature values using the gaseous equation of state. N_s is the stoichiometric value of the scalar dissipation at equilibrium chemistry and using Peters (2000) its value is given by $N_s = 4Z_s^2 D_f \,/\, (Re\delta^2)$, where the factor $1/Re$ occurs due to the use of non-dimensionalised quantities. The stoichiometric value of the mixture fraction diffusivity, D_f, is evaluated using (3.2) at the nondimensionalised adiabatic flame temperature, i.e. at $T^e(Z_s) = T_f$. $\delta = \delta_o/H$ is a non-dimensionalised measure of the diffusion thickness of the flame, where the value of $\delta_o = 0.05H$ is set by Pantano (2004).

Equation (5.33) represents a boundary-value problem by fixing the species concentration boundary values in the air and fuel streams at $Z = 0$ and $Z = 1$, respectively.

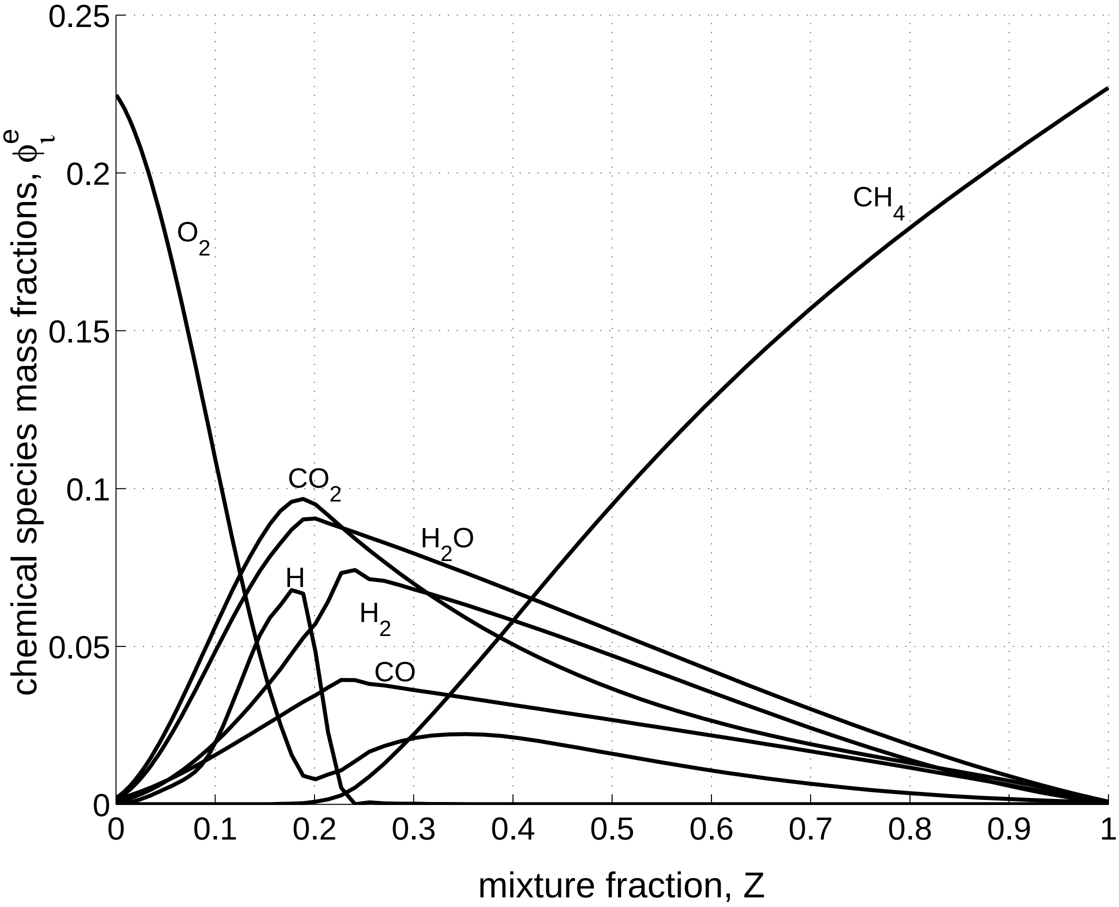

Figure 5.4: Near-equilibrium solution for the mass fractions of the chemical species as explicit functions of the mixture fraction determined using (5.33). The mass fractions of H_2 and H-radical have been scaled by factors of 50.0 and 500.0 for clarity of presentation.

A semi-implicit iterative method with central-differencing is followed to solve (5.33) on a Z-space grid uniformly discretised by 64 points. An initial guess of the species mass-fractions, as piece-wise linear Burke-Schumann type functions of Z, is used to start the computational procedure. The non-linear chemical source term on the right-hand side is computed explicitly from the solution at the previous iteration and left-hand side updates the solution implicitly using a simple tri-diagonal matrix inversion scheme with the pre-specified boundary conditions. The average of the updated and previous solutions is then fed back to the solver for the subsequent iterative process, until the percentage change accumulated during a single iteration in the stoichiometric value of the sensible enthalpy is less than 0.1%. The resulting quasi-equilibrium solution is smooth enough to initialise the species mass fractions as $\phi_\iota = \phi_\iota^e(Z)$ for the MMC computation. A similar initialisation is also used in the Pantano (2004) DNS and ensures physical consistency between it and the moment closure modelling calculations.

Sensible enthalpy initialisation

As specified in (3.4) and (3.5), the normalised sensible enthalpy is explicitly known as a function of the species mass fractions and temperature. Therefore, the aforementioned equilibrium values, $\phi_\iota^e(Z)$ and $T^e(Z)$, are used to initialise the sensible enthalpy as a function of Z, i.e. $\hat{h}_s = \hat{h}_s^e(Z) = \hat{h}_s^e(\phi_\iota^e, T^e)$.

The fuel and air stream termperatures and the temperature within the flame are specific to the DNS setup. These temperatures are non-dimensionalised by T_o as described in Sec. 3.2 and their values are given as $T_1 = 1.0$, $T_2 = 1.2$ and $T_f = 6.8$, respectively. Using these three characteristic temperature values and the corresponding near-equilibrium sensible enthalpy solution, $\hat{h}_s^e(Z)$, a planar model for temperature as a linear function of $\hat{h}_s$ and Z is constructed as

$$T = \sigma_0 + \sigma_1 \cdot Z + \sigma_2 \cdot \hat{h}_s, \tag{5.34}$$

where the modelling coefficients σ_0, σ_1 and σ_2 are given by

$$\frac{1}{h_{s_{max}}} \cdot \begin{pmatrix} 1 & 0 & h_s^e(T_2) \\ 1 & 1 & h_s^e(T_1) \\ 1 & Z_s & h_s^e(T_f) \end{pmatrix} \cdot \begin{pmatrix} \sigma_0 \\ \sigma_1 \\ \sigma_2 \end{pmatrix} = \begin{pmatrix} T_2 \\ T_1 \\ T_f \end{pmatrix}. \tag{5.35}$$

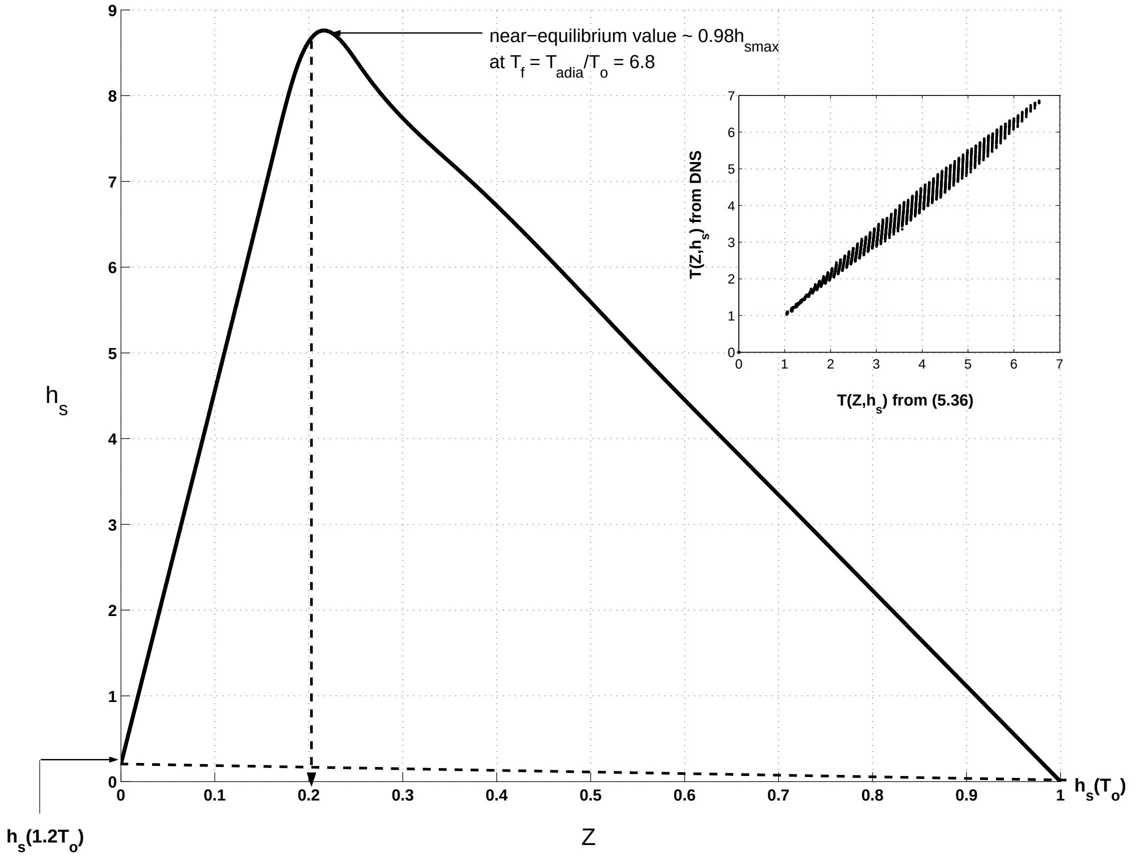

Figure 5.5: Near-equilibrium solution for the non-dimensionalised sensible enthalpy is plotted as a function of the mixture fraction. The three corner-values of the sensible enthalpy and mixture fraction, used to compute a planar function for temperature, are indicated. Inset: Scatter plot of the non-dimensionalised temperature values computed using the planar model in (5.35), i.e. $T(Z, \hat{h}_s) = 1.069 + 0.657\hat{h}_s h_{s_{max}} - 0.069Z$, with the temperature values from the DNS conditioned on the mixture fraction and sensible enthalpy at three streamwise locations, $x = 3H,\ 7.5H,\ 11.2H$.

The near-equilibrium sensible enthalpy values at the different non-dimensionalised temperatures in the above equation are computed using (3.4) and the values from the temperature model are plotted against DNS values in Fig. 5.5. As Fig. 5.5 suggests, the strong temperature-sensible enthalpy dependence is essentially thermodynamic in nature and, thus, does not change as the flow evolves in the downstream direction. Therefore, any x-wise variation in the $T(Z, \hat{h}_s)$ model can be safely neglected. Furthermore, the dependence (albeit weak) on the mixture fraction ensures that the initial difference between the cold-flow temperatures in the fuel and air streams is modelled correctly. The model ensures that temperatures above the burning flamelet solution and below the cold-flow values are not possible for any mixture fraction value.

Mixture fraction initialisation

Equation (5.30) describes the downstream spatial evolution of the mapping functions corresponding to all the scalars from their initial values presumed at the jet exit, i.e. at $x = 0$. For the MMC computation, the major scalars must be specified in terms of their surrogate mapping functions, $X_1(\xi_1, \xi_2) = \langle Z|\xi_1, \xi_2\rangle$ and $X_2(\xi_1, \xi_2) = \langle \hat{h}_s|\xi_1, \xi_2\rangle$, such that their joint-PDF corresponds to the inlet conditions of the Pantano (2004) flame DNS. As explained, a fully burning flamelet initial condition is assumed analogous to the DNS such that all species mass fractions and sensible enthalpy are known functions of the mixture fraction. In other words, Z is the only independently fluctuating, stochastic variable at the jet exit and its mapping function is determined to reflect the mixture fraction statistics at $x = 0$. The relationship between the statistics of the mapping function for Z and its actual statistics is given by an equality of their cumulative distributions in scalar and reference spaces. A preferred direction mapping procedure used by Klimenko & Pope (2003) and, more recently, by Kronenburg & Cleary (2008) is employed. This implies an ordering of the reference variables corresponding to the major scalars in a multi-dimensional reference manifold, i.e. when $n_r > 1$. As the primary dependence in turbulent diffusion flames is on the mixture fraction and secondary on the sensible enthalpy, the ordering of the corresponding reference variables reflects this. Therefore, the mapping function surrogate for the mixture fraction is initially presumed to be a function of ξ_1 alone, i.e. $X_1(\xi_1, \xi_2) = X_1(\xi_1)\,|_{x=0}$ and is solved for using the differential form of the cumulative distribution equality (5.1),

$$P_{\phi_1}\left(X_1(\xi_1)\right)\cdot\frac{dX_1\left(\xi_1\right)}{d\xi_1}=P_{\theta_1}\left(\xi_1\right) \tag{5.36}$$

,

with the boundary conditions given as,

$$X_1|_{\xi_1\to-\infty}=0 \quad \text{and} \quad X_1|_{\xi_1\to+\infty}=1. \tag{5.37}$$

The PDF $P_{\phi_1}\left(X_1\right)$ is specified using the mixture fraction statistics from the DNS at the jet exit as $P_{\phi_1}\left(X_1\right)=P_{\phi_1}\left(Z\right)|_{x=0}$ and $P_{\theta_1}=exp\left(-\xi_1^2/2\right)/\sqrt{2\pi}$ is the Gaussian with zero mean and unit variance. Mathematically, (5.36) is strictly valid only for $X_1\left(\xi_1\right)$ being a monotonically increasing function of ξ_1 for a non-pathological P_{ϕ_1}. The slope of the X_1 mapping function in the reference space is extremely sensitive to the values of P_{ϕ_1} and minor numerical errors in computing the former can seriously affect the quality of the presumed initial PDF. In order to ensure the smoothness and accuracy of the P_{ϕ_1} input, a larger number (1000) of points is used to discretise the reference variable ξ_1. To compute P_{ϕ_1}, the mixture fraction statistics for all locations upstream of $x=0.5H$ are utilised as opposed to the statistics at $x=0$ alone and are binned into 1000 points in the $[0,1]$ interval.

An implicit iterative scheme with central differencing is again used to solve (5.36) in the reference space. The stochastic reference variable, ξ_1, is discretised uniformly within the $-4\leqslant\xi_1\leqslant 4$ range as done in previous MMC studies (Cleary & Kronenburg, 2007*b*; Kronenburg & Cleary, 2008). As the reference variables are Gaussian distributed with zero mean and a unit variance their probability density is minuscule at over 4 standard deviations from the mean. Thus the $[-4,4]$ bounding interval is large enough to capture nearly all of the stochastic behaviour modelled by these

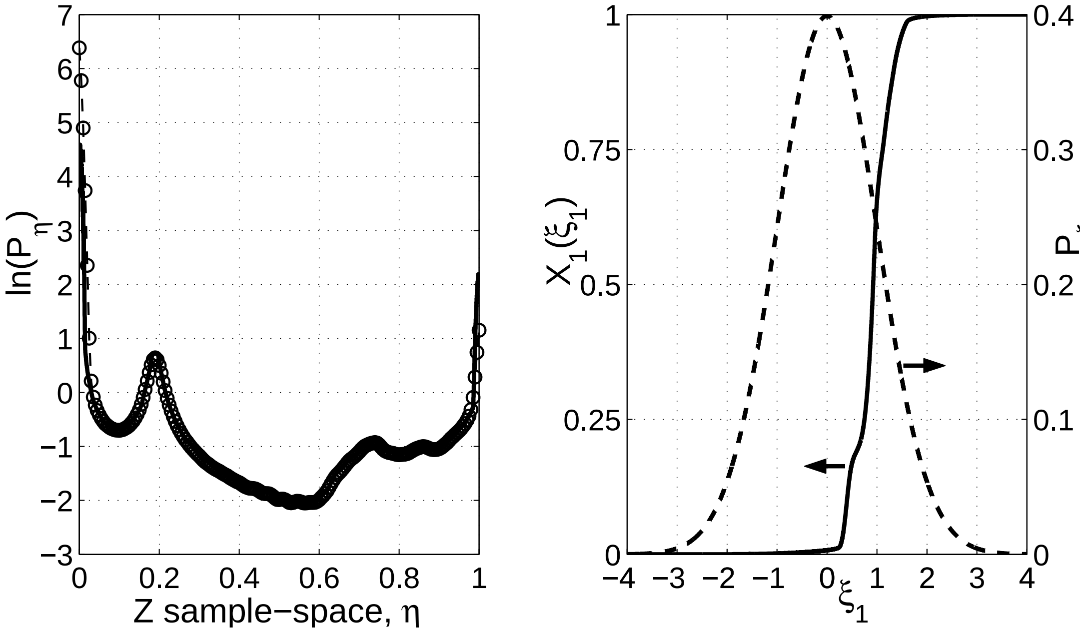

Figure 5.6: To the left: Semi-logarithmic plot of the marginal PDF for the mixture fraction, P_{ϕ_1}, at $x = 0$. The dashed-circles indicate the actual DNS data and the solid line is a reconstruction from the $X_1(\xi_1)$ solution of (5.36). To the right: The $X_1(\xi_1)$ mapping function solution of (5.36), with the marginal PDF, P_{ϕ_1}, specified from the DNS data (solid line). Gaussian PDF of zero mean and unit variance used in (5.36) (dashed line).

variables. The solution of (5.36) follows a predictive-corrective scheme similar to the one used for (5.33). The value of $X_1\left(\xi_1\right) = 0.5\left(1 + erf(\xi_1)\right)$ is used as the initial guess to start the computational procedure. The $X_1\left(\xi_1\right)$ mapping is used to update P_{ϕ_1} at every ξ_1 value after each iteration. Implicit tri-diagonal inversion using the updated P_{ϕ_1} and averaging the new and previous values of X_1 leads to an asymptotic convergence in $X_1\left(\xi_1\right)$ towards the final solution. Due to the sensitivity of the $dX_1/d\xi_1$ gradient to the $P_{\phi_1}\left(X_1\right)$ values and the large number of data points used to discretise the reference space, as high as $50,000$ iterations are required to resolve the mixture fraction mapping function accurately. A large number of grid-points to discretise the reference space is not feasible for a full MMC computation. Hence, the final $X_1(\xi_1)$ solution of (5.36) is mapped onto a smaller grid of 64×64 points in the (ξ_1, ξ_2)-space with $\partial X_1/\partial\xi_2 = 0$ as shown in Fig. 5.7. The $[-4, 4]$ bounding interval is again used for the MMC grid with clustering near $(\xi_1, \xi_2) = (0, 0)$ given by,

$$\xi_{1_k} = l_c \cdot erf^{-1}\left[\frac{2k - (n_\xi + 1)}{n_\xi - 1} \cdot erf\left(\frac{4}{l_c}\right)\right], \tag{5.38}$$

where the grid index, k, takes integral values from 1 to $n_\xi = 64$ and l_c is the clustering parameter. Progressively larger values of l_c reduce the clustering effect near $\xi_1 = 0$ and a value of 2.75 is chosen for the present purposes. The same clustering scheme is used to compute the grid points in the ξ_2-direction as well.

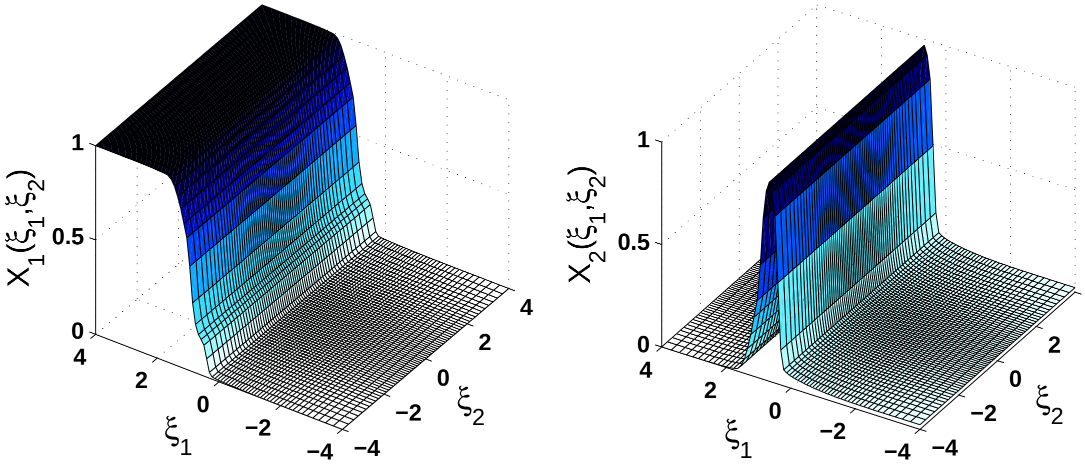

Figure 5.7: Initial the mapping functions for the mixture fraction (X_1) and the normalised sensible enthalpy (X_2) at $x = 0$. Mappings functions for sensible enthalpy and all minor scalars are initialised as equilibrium functions of X_1. Peak values of X_2 and all product species correspond to $X_1(\xi_1) = Z_s$ and $\partial X_I / \partial \xi_2 = 0$ for all $I \in \{1, .., n_s\}$.

It follows from the above that the joint-PDF of the major scalars, P_{ϕ_1,ϕ_2}, which is a necessary provision for the solution of the MMC equations, is equivalent to δ-PDFs along the $\hat{h}_s^e(X_1)$ function at the jet-exit conditions. The corresponding mapping functions for the sensible enthalpy and the chemical species are provided as $X_2(\xi_1, \xi_2) = \hat{h}_s^e(X_1(\xi_1, \xi_2))$ and $X_\iota(\xi_1, \xi_2) = Y_\iota^e(X_1(\xi_1, \xi_2))$ and are invariant in

ξ_2-space due to the aforementioned ξ_1-specific dependence. In conditional moment terms, it implies that the fluctuations in the minor scalars about their means conditioned on the mixture fraction are zero. Furthermore, the marginal sensible enthalpy PDF, $P_{\phi_2|\phi_1}$, shows single spikes along the $\hat{h}_s^e\,(Z = \eta_1)$ function and is, overall, trimodal with prominent peaks at the unmixed fuel, unmixed oxidiser and the burning pilot streams corresponding to $\hat{h}_s(T_1)$, $\hat{h}_s T_2$ and $\hat{h}_s T_f$ respectively.

5.3.3 Numerical scheme

CMC solution

It is important to note here that the singly- and doubly-conditioned CMC equations for species transport, given by (2.59) and (2.62) respectively, are also solved in the present study using the same overall numerical procedure employed for the MMC solution. The e_q and e_y terms in the CMC equations are closed by setting them to zero for reasons described earlier in Sec. 2.3.7 and first-order closure is used for the chemical source term. The unclosed dissipation variables and conditional velocity terms are taken directly from the DNS. The singly-conditioned (or CMC1) equations are solved for all chemical species (except nitrogen) and the normalised sensible enthalpy, whereas the doubly-conditioned (or CMC2) equations are used to compute the species concentrations only. The same near-equilibrium profiles for the chemical species and the sensible enthalpy used to initialise the MMC solution are employed as the initial conditions for solving CMC1. For the CMC2 implementation, planar profiles like the temperature model in (5.34) are constructed from the fuel-stream, oxidiser-stream and stoichiometric values of the species mass fractions. These planar profiles are then used to initialise the doubly-conditioned species mass fractions in the Z-$\hat{h}_s$ before the CMC2 solution. Results from the CMC1 and CMC2 calculations are presented and compared with those from the MMC implementation in Sec. 5.4.5.

MMC solver

For the initial conditions specified in Sec. 5.3.2, the fully closed set of MMC equations represented by (5.30) is solved for the mapping functions corresponding to the mass fractions of the fuel, oxidiser, products and intermediates simulated in the Pantano (2004) flame. Only nitrogen, which represents a chemically neutral species in the methane-air chemistry model employed presently, is not solved for using (5.3). Instead the conservation identity (3.8) is made use of to compute the mass-fraction of nitrogen from the MMC computed values of all other chemical species. A 3-step semi-implicit finite difference solver is used to solve (5.30), with an explicit step to compute the effects of convection/drift and diffusion and an implicit step to account for the chemical production term. A final averaging step is used to smoothen the mapping function profiles. All derivatives in the reference space are second-order accurate, the downstream-marching integration is first order accurate, and all ensemble (unconditional) mean statistics are taken from the DNS. Using this scheme, the MMC equation is discretised into the following three computational steps to evaluate the mapping function values at the $(n+1)^{th}$ grid point along the downstream coordinate from the data at the previous grid location:

$$\begin{aligned}
X_I^{n'} - X_I^n &= 2\Delta x \left(\mathbb{D}_F^n - \mathbb{D}_R^n\right)/U_x^n && (\textit{step } 1) \\
X_I^{n+2} - X_I^{n'} &= 2\Delta x W_I^{n+2}/\left(\rho_\xi^{n'} U_x^{n'}\right) && (\textit{step } 2) \\
X_I^{n+1} &= 0.5(X_I^{n+2} + X_I^n) && (\textit{step } 3)
\end{aligned} \tag{5.39}$$

where all terms with superscripts n, $n+1$ and $n+2$ are evaluated at the respective grid locations along the downstream coordinate. $X_I^{n'}$ is the intermediate value of the I^{th} scalar mapping function computed after taking only the convective/drift and diffusive effects into account and n' denotes the intermediate solution step. The MMC equation for the mapping function, X_1, of the mixture fraction does not have any source term. Therefore, its intermediate value, $X_1^{n'} = X_1^{n+2}$, and the density and convective velocity terms are updated between the first and second steps as $U_x^{n'} = U_x(X_1^{n+2})$ and $\rho_\xi^{n'} = \rho(T(X_1^{n+2}, X_2^n))$. Terms $\mathbb{D}_1^n$ and $\mathbb{D}_2^n$ represent the drift and diffusive components discretised using central-differencing in the reference space and take the following form at any point with indices p, q in the reference grid,

$$\begin{aligned}
\mathbb{D}_1^n \quad &= \quad A_{1_{p,q}}^n \left(X_{I_{p+1,q}}^n - X_{I_{p-1,q}}^n \right) / 2\Delta\xi_p \ + \\
&\quad\quad A_{2_{p,q}}^n \left(X_{I_{p,q+1}}^n - X_{I_{p,q-1}}^n \right) / 2\Delta\xi_q \\
\mathbb{D}_2^n \quad &= \quad B_{11_{p,q}}^n \left(X_{I_{p+1,q}}^n - 2X_{I_{p,q}}^n + X_{I_{p-1,q}}^n \right) / \Delta\xi_p^2 \ + \\
&\quad\quad 2B_{12_{p,q}}^n \left(X_{I_{p+1/2,q+1/2}}^n - X_{I_{p+1/2,q-1/2}}^n - X_{I_{p-1/2,q+1/2}}^n + X_{I_{p-1/2,q-1/2}}^n \right) / \Delta\xi_p \Delta\xi_q \ + \\
&\quad\quad B_{22_{p,q}}^n \left(X_{I_{p,q+1}}^n - 2X_{I_{p,q}}^n + X_{I_{p,q-1}}^n \right) / \Delta\xi_q^2.
\end{aligned} \tag{5.40}$$

$\Delta\xi_p$ and $\Delta\xi_q$ are the grid sizes at the p^{th} and q^{th} index position and do not depend on the reference-space direction along which the derivative is computed. Neumann boundary conditions are applied at the grid boundaries along $\xi_1, \xi_2 = 4, -4$. The first derivatives in the reference space are computed using the first-order accurate forward- or backward-differencing depending on the index position and the second derivatives are set to zero.

$$\left.\frac{\partial X_I}{\partial \xi_k}\right|_{\xi_k=+4} \simeq \frac{X_{I_{n_\xi}} - X_{I_{n_\xi - 1}}}{\Delta\xi_{n_\xi}}, \quad \left.\frac{\partial X_I}{\partial \xi_k}\right|_{\xi_k=-4} \simeq \frac{X_{I_1} - X_{I_0}}{\Delta\xi_0}, \quad \left.\frac{\partial^2 X_I}{\partial \xi_k \partial \xi_l}\right|_{\xi_k, \xi_l = +4, -4} \simeq 0 \tag{5.41}$$

The chemical production term in *step* 2 of (5.39) is expressed up to first-order accuracy as

$$W_I^{n+2} = W_I\left(\mathbf{X}^{n+2}\right) \simeq W_I\left(\mathbf{X}^{n}\right) + \sum_{J=1}^{n_s} \left(\frac{\partial W_I}{\partial X_J}\right)^n \cdot \left(X_J^{n+2} - X_J^{n'}\right). \tag{5.42}$$

The above expression is substituted back within *step* 2 and the resulting difference equation is solved for implicitly to yield the mapping function values at the $(n+2)^{th}$ grid position. The $\partial W_I/\partial X_J$ term indicates the rate of change of chemical production of a species due to changes in its concentration and is analytically derived from the Arrhenius rate expressions for the reaction sub-steps in the chemistry model described in Sec. 3.3. Finally, the solution is stabalised at the $(n+1)^{th}$ point by averaging the current and previous mapping function values. The last step is crucial in arresting the growth of any aphysical numerical fluctuations in the solution that may be introduced, in particular, by the numerical integration of the chemical source term in the previous step.

The x-wise discretisation employed in the DNS (cf. Sec. 3.1) was not found adequate for the stability of the downstream marching of the MMC solution. Therefore, every DNS grid cell in the downstream direction is further subdivided to ensure the numerical stability of the MMC solution procedure. All grid locations at $x \leqslant H$ are fractioned into 50 sub-steps to ensure that the species and sensible enthalpy fluctuations evolve correctly from the imposed equilibrium initial conditions. For $x \geqslant H$ downstream locations the sub-stepping is adaptively increased from a minimum of 30 fractional steps per DNS grid cell. The factor of increase is heuristically selected as 10 times the percentage of solution over-shoots or under-shoots in all scalars throughout the reference space. The over-/under-shoots are defined as the points on the reference space grid where the numerical solution takes values outside of the physical $[0, 1]$ interval. These local aphysical values rarely go above 1% of the total points in the reference space computed per scalar, resulting in no more than 40 sub-steps at any x-wise location $\geqslant H$. In the case of an under-shoot a preset value of 10^{-12} is assigned to the mapping function at that location and the over-shoot is corrected by the maximum value of the scalar mapping function at the previous step. In either case the chemical species mass-fractions are adjusted for continuity by normalising with the new non-unity total value. Intermediate sub-step values of the ensemble averaged quantities from the DNS that are used in the closure modelling of the MMC equations are calculated by linear interpolation between the two neighbouring DNS grid values along the x-coordinate.

Auxillary $a(\xi_1, \xi_2)$ computation substep

It may be recalled that full closure of the convective velocity requires the solution of a submodel (5.32) derived for $a(\xi_1, \xi_2)$. However, (5.32) can not be solved until the streamwise velocity gradient is specified. The dependence of the streamwise velocity on the mixture fraction through (5.31) implies that the equation for $a(\xi_1, \xi_2)$ is coupled with the MMC equation for the mixture fraction mapping function. Therefore, $a(\xi_1, \xi_2)$ cannot be known *a priori* without changing the form of (5.32). For this purpose, a computationally tractable form of (5.32) is derived by substituting the respective expressions for the $U_x(\boldsymbol{\xi})$ model and the streamwise gradient $\partial X_1/\partial x$ from (5.31) and (5.30) in (5.32) and collecting all the terms containing $a(\xi_1, \xi_2)$ on the left-hand side. In mathematical terms,

$$\left(\xi_1 + \frac{U_1}{U_x}\frac{\partial X_1}{\partial \xi_1}\right) a - \frac{\partial a}{\partial \xi_1} = \frac{1}{\bar{\rho}}\left[\frac{\partial \bar{\rho} U_0}{\partial x} + X_1 \frac{\partial \bar{\rho} U_1}{\partial x}\right] + U_1 \left(\frac{\partial X_1}{\partial x}\right)_{-a}, \tag{5.43}$$

where $(\partial X_1/\partial x)_{-a}$ is the streamwise gradient of the mixture fraction mapping function from (5.30) without the contribution of the $a(\xi_1, \xi_2)$ term that appears on the left-hand side of the above equation. The U_0 and U_1 notation is merely a convenient short-hand for the $\widetilde{u_x} - \widetilde{Z}\widetilde{u_x''Z''}/\widetilde{Z''^2}$ and $\widetilde{u_x''Z''}/\widetilde{Z''^2}$ terms, respectively. The right-hand side of (5.43) is computed from the $X_1(\xi_1, \xi_2)$ solution at the previous streamwise step, whereas the gradients of the ensemble-averaged U_0 and U_1 terms are specified from the DNS. The above represents a linear inhomogeneous partial differential equation where the right-hand side is a known function of the reference space variables and pre-computed ensemble averaged quantities. It is henceforth denoted by $f(\xi_1, \xi_2)$ for convenience. An analytical solution of the above is not possible and therefore a numerical procedure has been implemented to compute $a(\xi_1, \xi_2)$ *before* solving the main MMC equation (5.30) at each streamwise step. For the n^{th} streamwise grid position, the derivative in the reference space is approximated by second-order accurate central differencing to give,

$$\left(\frac{1}{2\Delta\xi_p}\right) a^n_{p-1,q} + \left[\xi_{1_p} + \left(\frac{U_1}{U_x}\frac{\partial X_1}{\partial \xi_1}\right)^{n-1}_{p,q}\right] a^n_{p,q} + \left(\frac{-1}{2\Delta\xi_p}\right) a^n_{p+1,q} = f^{n-1}_{p,q}. \tag{5.44}$$

This difference equation is solved using a fully implicit tri-diagonal matrix inversion method at each q index from 1 to n_ξ. Much like the $\partial X_1/\partial\xi_1$ term in (5.36), the gradient of $a(\xi_1, \xi_2)$ in the reference space is found to be very sensitive to the values of $f(\xi_1, \xi_2)$ and a finer grid is necessary to resolve it. Therefore, the matrix inversion is carried out over a one-dimensional ξ_1-grid uniformly discretised with 1000 points (i.e. index p takes values from 1 to 1000). Forward and backward differencing is used at the grid boundaries, $p = 1$ and $p = 1000$, respectively. The values of the known functions $\gamma(\xi_1, \xi_2)$ and $f(\xi_1, \xi_2)$ are linearly interpolated to the one-dimensional solution grid and the solution is averaged back on to the original reference space discretisation. It is important to stress here that unlike the cumulative distribution equation represented by (5.36), (5.43) is *linear* and does not require repeated matrix inversions for convergence. At each streamwise step, the tri-diagonal matrix inversion is done only once per q index to compute the $a(\xi_1)$ dependence. Consistency of the $a(\xi_1, \xi_2)$ term modelled using (5.32) with the actual downstream convective velocities from the DNS is evidenced in Fig. 5.8. Due to the linear time complexity of the tri-diagonal matrix algorithm (Golub & Van-Loan, 1996), the computational expense on the solution of (5.44) is insignificant compared to that on the actual MMC solver. Finally, the full $a(\xi_1, \xi_2)$ solution is used according to (5.28) to close the model for the drift coefficient, A_k, prior to the MMC solution procedure at every streamwise step.

Conditional moments and PDFs

The standard mapping closure is based on an equality of the cumulative probability distributions of the mapping function surrogates/models of the (major) scalars and their reference variables (Chen *et al.*, 1989; Pope, 1991; Klimenko & Pope, 2003) expressed in (5.1). Using this definition, the probability distributions of the modelled scalars and their reference variables are related as

$$P_{\boldsymbol{\phi}} = P_{\boldsymbol{\theta}} \cdot \left| \frac{\partial X_k}{\partial \xi_l} \right|^{-1} \tag{5.45}$$

where

$$\left| \frac{\partial X_k}{\partial \xi_l} \right|^{-1} = \begin{vmatrix} \frac{1}{\partial X_1/\partial \xi_1} & \frac{1}{\partial X_1/\partial \xi_2} \\ \frac{1}{\partial X_2/\partial \xi_1} & \frac{1}{\partial X_2/\partial \xi_2} \end{vmatrix} \tag{5.46}$$

is the Jacobian determinant of inverse derivatives of the major scalar mapping functions with respect to the reference space coordinates. The conditional moments of

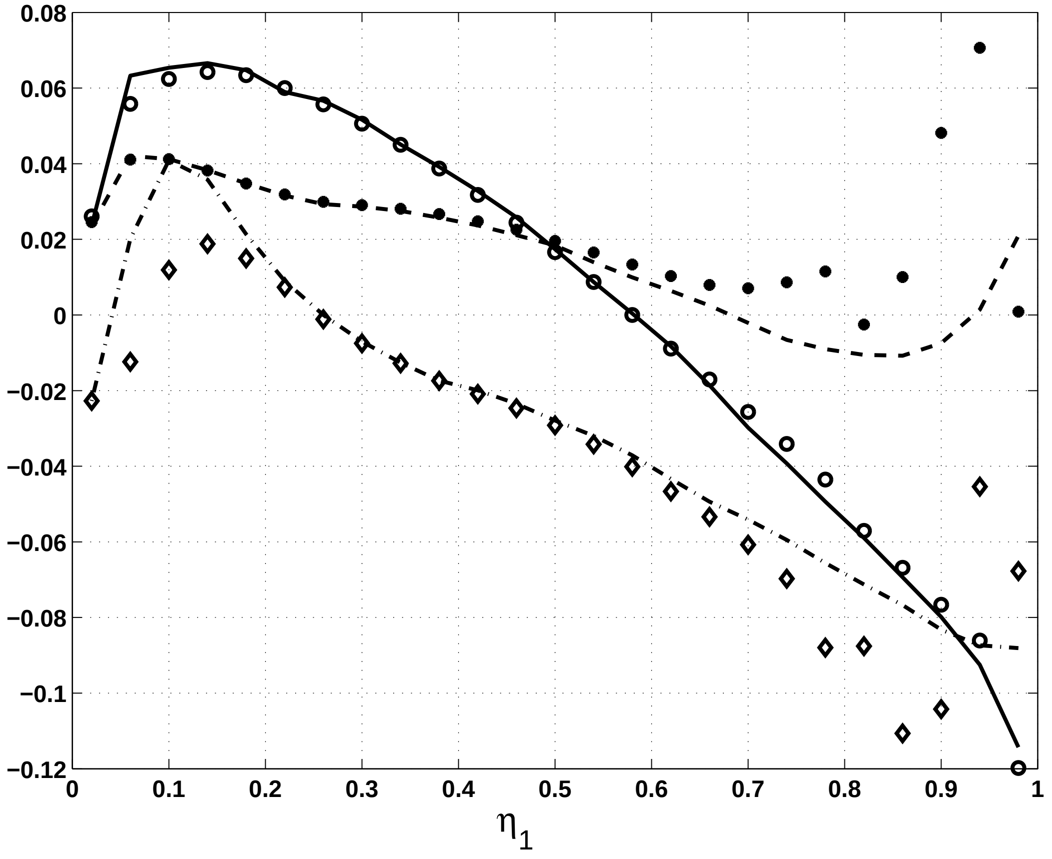

Figure 5.8: Comparison of the mixture fraction based conditional averages of the left-hand and right-hand sides of (5.32), using the $a(\xi_1, \xi_2)$ solution from the MMC and downstream velocity (and unconditional mean density) values taken from the DNS. Straight, dashed and dashed-dotted lines indicate the MMC computed $\langle \xi_1 a - \partial a/\partial \xi_1 | \eta_1 \rangle$ term for $x = 3H$, $7.5H$ and $11.2H$ downstream locations, respectively. Circle, asterisk and diamond symbols indicate the corresponding DNS computed values of the $\langle \bar{\rho}^{-1} \cdot \partial \left(u_x \bar{\rho} \right) / \partial x | \eta_1 \rangle$ term.

the scalars follow from the PDF computed in (5.45). While the above is the exact mathematical formulation to compute the modelled scalar PDF, its numerical implementation may not be always feasible on a coarse reference-space grid such as that employed for the MMC calculations. Further difficulties in implementation include:

- the presence of large regions of zero gradient in both ξ_1- and ξ_2-directions (e.g. in the mapping functions of minor product species) and

- transformation of the $\partial X_k/\partial \xi_l$ derivatives expressed as a function of (ξ_1, ξ_2) to $\partial \xi_l/\partial X_k$ expressed in terms of $(X_1, X_2) \equiv (\eta_1, \eta_2)$.

Due to these constraints, a consistent but numerically much more feasible technique is employed in the present study to compute the PDFs and conditional moments of surrogate scalars. It takes recourse to the basic mathematical definition of the joint probability distribution function of any number of stochastic variables, which can be expressed as,

$$P(\eta_1, .., \eta_k) \equiv P(\eta_1 \leqslant X_1^* \leqslant \eta_1 + d\eta_1, .., \eta_k \leqslant X_k^* \leqslant \eta_k + d\eta_k) \tag{5.47}$$

Here $\eta_1, .., \eta_k$ are the familiar sample space variables, while $X_1^*, .., X_k^*$ *do not* represent the scalar mapping functions on a fixed grid, but the stochastic values attained by the modelled scalars using the respective mapping functions. The stochastic values of the modelled scalars (for the present case of two reference variables) can be represented in mathematical terms as,

$$X_1^* = X_1(\theta_1^*, \theta_2^*), \qquad X_2^* = X_2(\theta_1^*, \theta_2^*). \tag{5.48}$$

An equivalent expression for the conditional moments derived from the stochastic reference variables is given by,

$$\langle \phi_I | \eta_1, .., \eta_k \rangle = \langle X_I(\theta_1^*, \theta_2^*) | X_1^* = \eta_1, .., X_k^* = \eta_k \rangle \tag{5.49}$$

The variables θ_1^* and θ_2^* in the above are uncorrelated stochastic reference variables with a joint Gaussian distribution of zero mean and unity variance. Since the joint

PDF of θ_1^* and θ_2^* is presumed, a pair of pre-computed random variables with the same joint-distribution can be used to simulate them. Given the pre-computed stochastic reference variables, equations (5.47)-(5.49) directly determine the modelled scalar moments and PDFs from first principles, circumventing the numerical problems posed by (5.45). In other words, the stochastic values attained by X_1^* and X_2^* are treated *as if* they were the actual instantaneous fluctuations of Z and $\hat{h}_s$ (respectively) from the DNS database while computing the moments and PDFs.

A standard pseudo-random number generating algorithm was used to calculate two uniformly distributed random variables with values within the $[0, 1]$ interval. These were transformed into Gaussian distributions with the aforesaid mean and variance values using the Central Limit Theorem, such that both variables remained decorrelated, i.e. $\langle \theta_1^* \theta_2^* \rangle = 0$. The values of each pre-computed Gaussian variable were computed in a sufficiently large number $(100, 000)$ to make sure that enough data are available to reproduce the PDFs and moments faithfully, without putting any significant computational burden on processing the data. All the $100, 000$ pairs of (θ_1^*, θ_2^*) values were stored in a binary format and were either loaded during the MMC solution to compute the conditional means (e.g. while calculating c_α from (5.19)) or while post-processing the MMC solution data. Linear interpolation between consecutive reference grid points was carried out to compute the mapping functions at sub-grid (θ_1^*, θ_2^*) values. Due to the exponential nature of decay of the Gaussian PDF away from the mean, not more than a few dozen stochastic values occurred beyond the $[-4, 4]$ interal. Therefore, enough points were available within the grid-range to model the scalar fluctuations and resolve the PDFs and moments accurately.

5.4 Closure modelling results

5.4.1 Modelling assumptions and realisability constraints

Firstly, the numerical constraints in MMC closure modelling warrant some discussion. It may be noted that the solution of the system of equations, represented by (5.9), does not ensure positive diffusion coefficients $\overline{B^0_{11}}$ and $\overline{B^0_{22}}$. The value of the diffusion coefficient for the sensible enthalpy in particular assumes negative values during the upstream development of the MMC solution. However, numerical stability for equation (5.3) generally requires all diffusion coefficients to be larger than or equal to zero, i.e. $B_{11} \geqslant 0$ and $B_{22} \geqslant 0$. The coefficient for the cross-correlation, B_{12}, may take negative values without compromising stability. More specifically, implicit or semi-implicit implementations of equation (5.3) are unconditionally stable if $|B_{12}| \leqslant \sqrt{B_{11} \cdot B_{22}}$ (int Hout & Welfert, 2007). The values of $\overline{B^0_{22}}$ and $\overline{B^0_{12}}$ are therefore set to zero if the solution of (5.9) yields negative values. If necessary, the B_{12} coefficient is adjusted after the thermal-correction of $\overline{B^0_{kl}}$ using (5.4), in order to meet the requirements for unconditional stability,

$$B_{12} = sgn[B_{12}]\sqrt{B_{11} \cdot B_{22}} \qquad \forall \ \frac{|B_{12}|}{\sqrt{B_{11} \cdot B_{22}}} > 1 \tag{5.50}$$

Fig. 5.9 shows the MMC diffusion coefficients, $\overline{B^0_{ij}}$, as function of downstream distance. It can be seen that the value for $\overline{B^0_{22}}$ (and therefore $\overline{B^0_{12}}$) must be constrained for $x \leqslant 6H$. As a consequence, (5.9) will not be satisfied and the correct value of dissipation cannot be imposed on the MMC simulations during this time. Hence, the predicted variance for normalized sensible enthalpy will not match the DNS data as can be seen in Fig. 5.10.

The evolution of the mixture fraction variance is well predicted initially, but the sen-

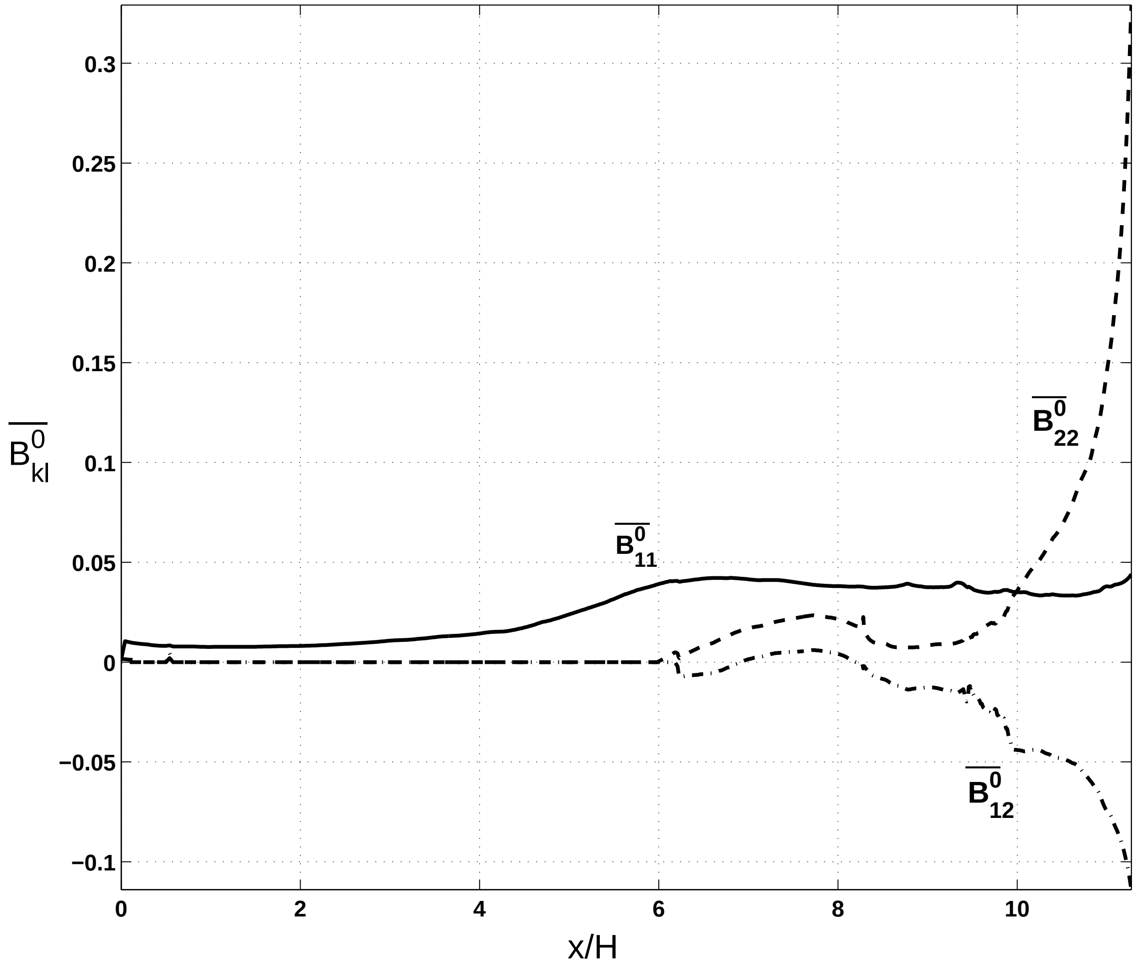

Figure 5.9: Downstream variation of the mean, temperature-invariant diffusion coefficients, $\overline{B^0_{kl}}$ computed using (5.9). $\overline{B^0_{22}}$ and $\overline{B^0_{12}}$ are constrained to zero till $x \leqslant 6H$ to maintain numerical stability.

sible enthalpy fluctuations are conspicuously lower at the upstream locations. This is consistent with the perception that negative diffusion coefficients would increase deviations from the mean value and omission of these negative values yields smaller variances than a perfect match with the DNS would require. The good predictions of mixture fraction variance in the upstream locations lead to good predictions of the shape of its marginal PDF, while underpredicted sensible enthalpy variances cause more deviations from DNS data (cf. Fig. 5.11). The statistics of the convective velocity follow that of the mixture fraction due to the former's dependence on Z

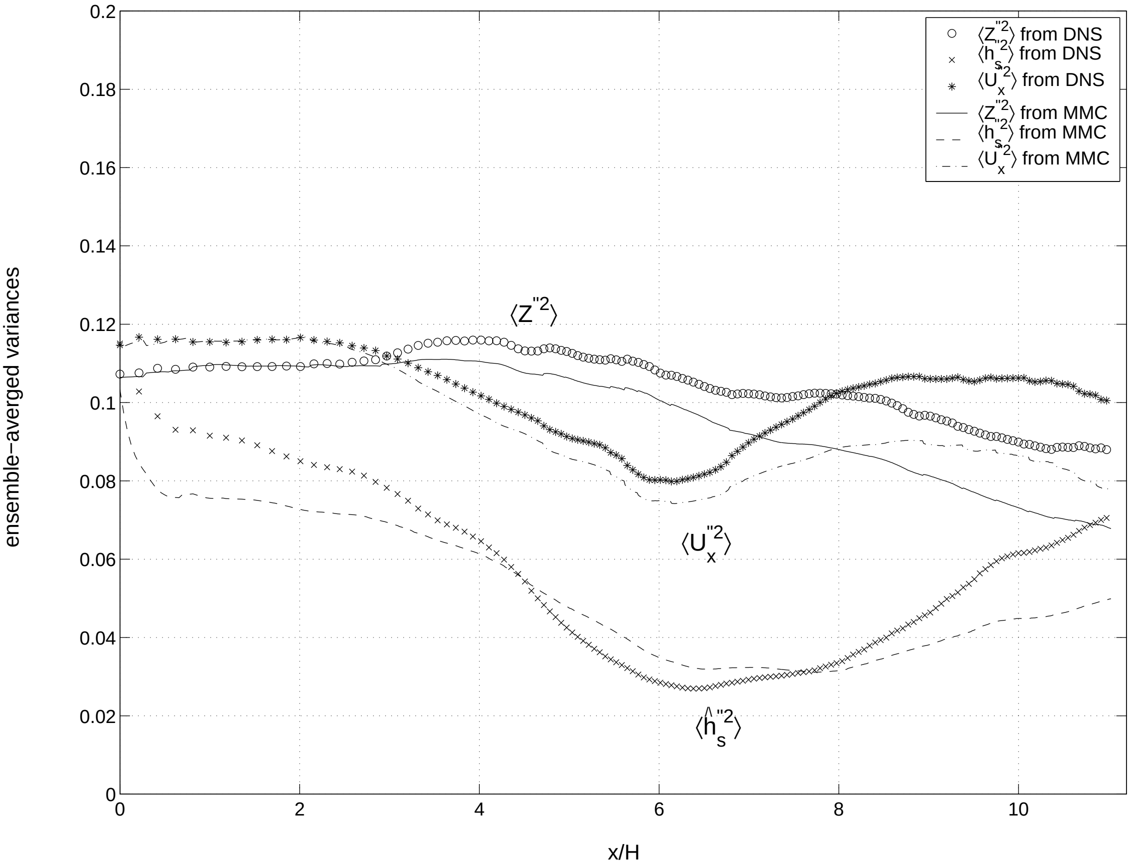

Figure 5.10: Downstream variation of the unconditional, ensemble-averaged variances of mixture fraction, sensible enthalpy and convective velocity computed from the MMC. The corresponding DNS values are supplied for comparison. Symbols used are specified in the legend.

through the model in (5.31). Gaussian velocity PDFs computed from the Klimenko & Pope (2003) model in (5.20) have been shown in Fig. 5.11 along with those from the revised model and the DNS results to stress the inaccuracy of the Gaussianity assumption for near-nozzle convection. The relatively narrow distribution of the modelled sensible enthalpy PDFs at the upstream locations (e.g. at $x = 3H$) can be partially explained by the underprediction of the variance and the mismatch of the diffusion coefficient. However, the divergence between the averaged statistics at later times is not under the influence of enforcing the numerical stability. The relatively larger variances of Z and $\hat{h}_s$ evidenced in the DNS at the far downstream locations is a consequence of the fresh amounts of air at $T_2 = 1.2$ entrained by the jet flow. While the MMC computation starts with exactly the same relative amounts of unmixed fuel and oxidiser/air as the DNS, much of the oxidiser is consumed in course of the spatial evolution of the flow. This is consistent with the stoichiometry of the modelled methane-air flame, where large amounts of air are required to burn a fraction of the methane present. This can be seen in Fig. 5.11 as a steady decay of the peak at $Z = 0$ in the predicted marginal PDF of the mixture fraction (and the corresponding decay in $\hat{h}_s$ PDF) along the downstream coordinate. The decay of the peak on the lean-side is also reflected in the statistics for the convective velocity. An attempt was made to model this phenomenon by externally enforcing a pre-determined mass-fraction of air on the mapping function for Z. However, this interfered with the natural evolution of the mixture fraction PDF and led to an aphysical suppression of the re-ignition process at the far downstream locations. The lack of a suitable model for air-entrainment represents the main shortcoming of the one-dimensional MMC closure in this study. Extending the MMC computations to two physical dimensions (cross-stream and downstream) seems the only way to improve upon these predictions.

Full MMC closure requires the provision of unconditional means of dissipation variables, $\widetilde{N^0_{11}}$, $\widetilde{N^0_{12}}$ and $\widetilde{N^0_{22}}$ at all downstream locations and the conditional scalar dissipation fluctuation term $\langle N^{0\,\prime\prime 2}_{11} | \eta_1 \rangle / \langle N^0_{11} | \eta_1 \rangle^2$ at $x = 0$. The unconditional mean dissipation variables used in the MMC closure are scaled by the ratios of the corresponding unconditional variances computed from the MMC and those from the DNS. In mathematical terms,

$$\widetilde{N^0_{ij}} = \widetilde{N^0_{ij}}_{DNS} \cdot \sqrt{\frac{[\widetilde{\phi''^2_i}\widetilde{\phi''^2_j}]_{MMC}}{[\widetilde{\phi''^2_i}\widetilde{\phi''^2_j}]_{DNS}}}, \tag{5.51}$$

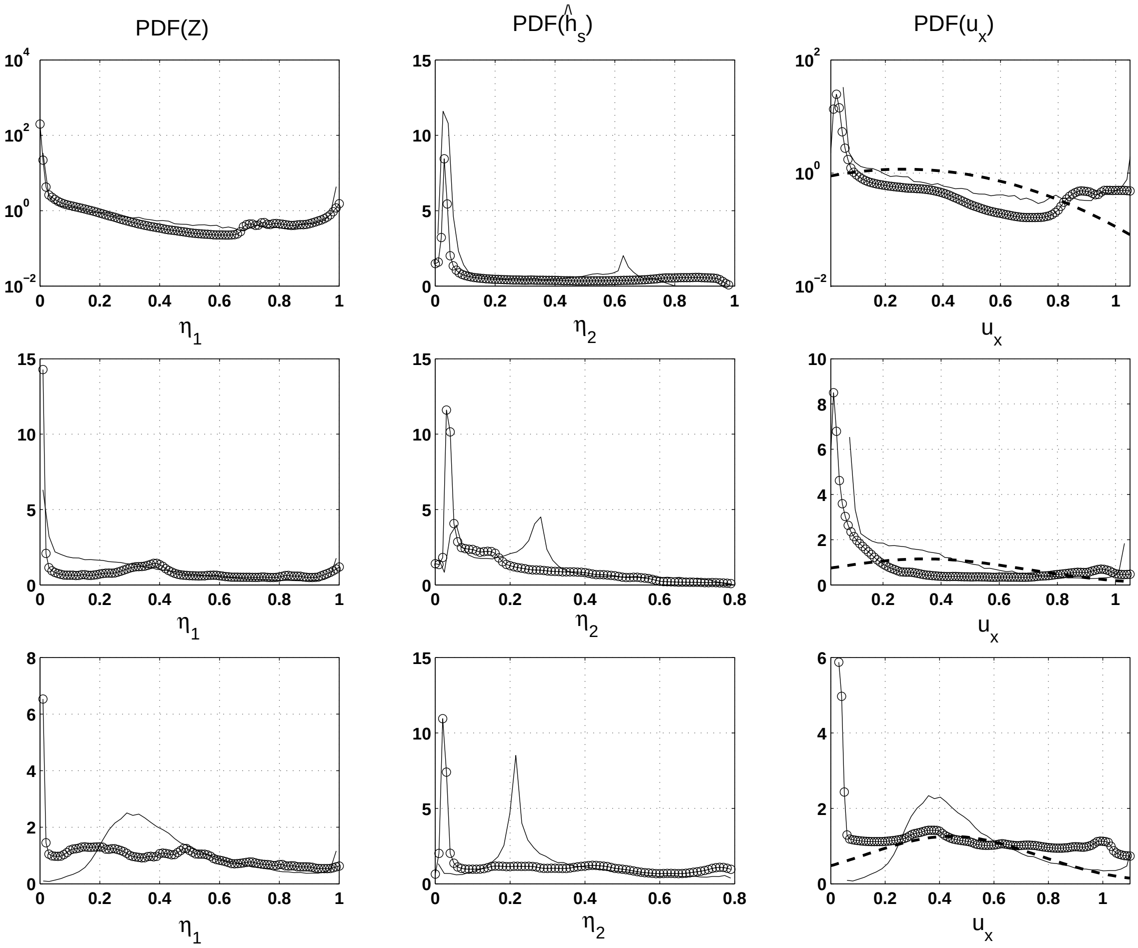

Figure 5.11: Marginal PDFs of the mixture fraction (left column), normalised sensible enthalpy (middle column) and the downstream convective velocity (right column) from the DNS and MMC computations are plotted at three stations along the streamwise coordinate. Circles denote the DNS values and solid lines are the MMC results. In addition, velocity PDFs from the Gaussian model in (5.20) have been plotted as the dashed-lines for comparison. The top row corresponds to $x = 3H$, middle to $x = 7.5H$ and the bottom to $x = 11.2H$.

where the DNS-subscript denotes the variance inputs from the DNS and the MMC-subscript denotes unconditional variances computed from the MMC solution at the previous computational step. Similar to the previous MMC study by Kronenburg & Cleary (2008), it was found that using the scaled value for the unconditional cross-dissipation term in (5.9) tends to result in $\overline{B^0_{22}} < 0$ adding to the aforementioned numerical realisability problems. Unlike established models for the passive and reactive scalar dissipation (Swaminathan & Bray, 2005), models for the cross-dissipation are not available in the combustion literature. To circumvent the problem, Kronenburg & Cleary (2008) suggest putting $\widetilde{N_{12}^0} = 0$ based on the observation that the magnitude of the cross-dissipation term is much less than that of the principal dissipation variable, $\widetilde{N_{11}^0}$ due to the former's change in sign around stoichiometric. The authors neglected all the cross-correlation terms and computed their $\overline{B_{11}^0}$ and $\overline{B_{22}^0}$ diffusion coefficients from a reduced 2×2 matrix in (5.9). However, this approach was found too limiting for the present purposes. Instead, the MMC computation in this study relaxes the constraint on the unconditional cross-dissipation to use half of the scaled $\widetilde{N_{12}^0}$ value and does not neglect the cross-correlation terms in the 3×3 matrix in (5.9). Errors due to these simplifications and numerical constraints do not have a strong effect on the predicted dissipation values, as evidenced by the good agreement between the predicted conditional dissipation profiles and the DNS values in Fig. 5.25. Specifically, reduction of the unconditional mean does not seem to affect the predictions for the cross-dissipation term especially at extinction. It should be noted that setting $\overline{B_{22}^0} = \overline{B_{12}^0} = 0$ to ensure numerical stability in the upstream locations does not imply that the doubly-conditioned dissipation rates, $\langle N_{ij} | \eta_1, \eta_2 \rangle$ assume zero values. Furthermore, once the temperature-invariant B_{kl}^0 coefficients are computed, the thermal effects are incorporated using (5.4).

Finally, the fluctuations of scalar dissipation are modelled in terms of the closure for the principal diffusion coefficient B_{11}^0 in (5.19). The initial estimate of c_α at $x = 0$ as a function of the mixture fraction is presumed at a constant value of -1.0, whereas the actual DNS values of c_α range from -0.5 to -1.6. Subsequent c_α values are computed directly from the MMC solution as it evolves along the downstream coordinate. As expected from previous studies (Kronenburg & Cleary, 2008), Fig. 5.12 shows that the mixture fraction dependence of c_α is small. However, unlike the previous study, large changes in the c_α values are not evidenced here and they remain

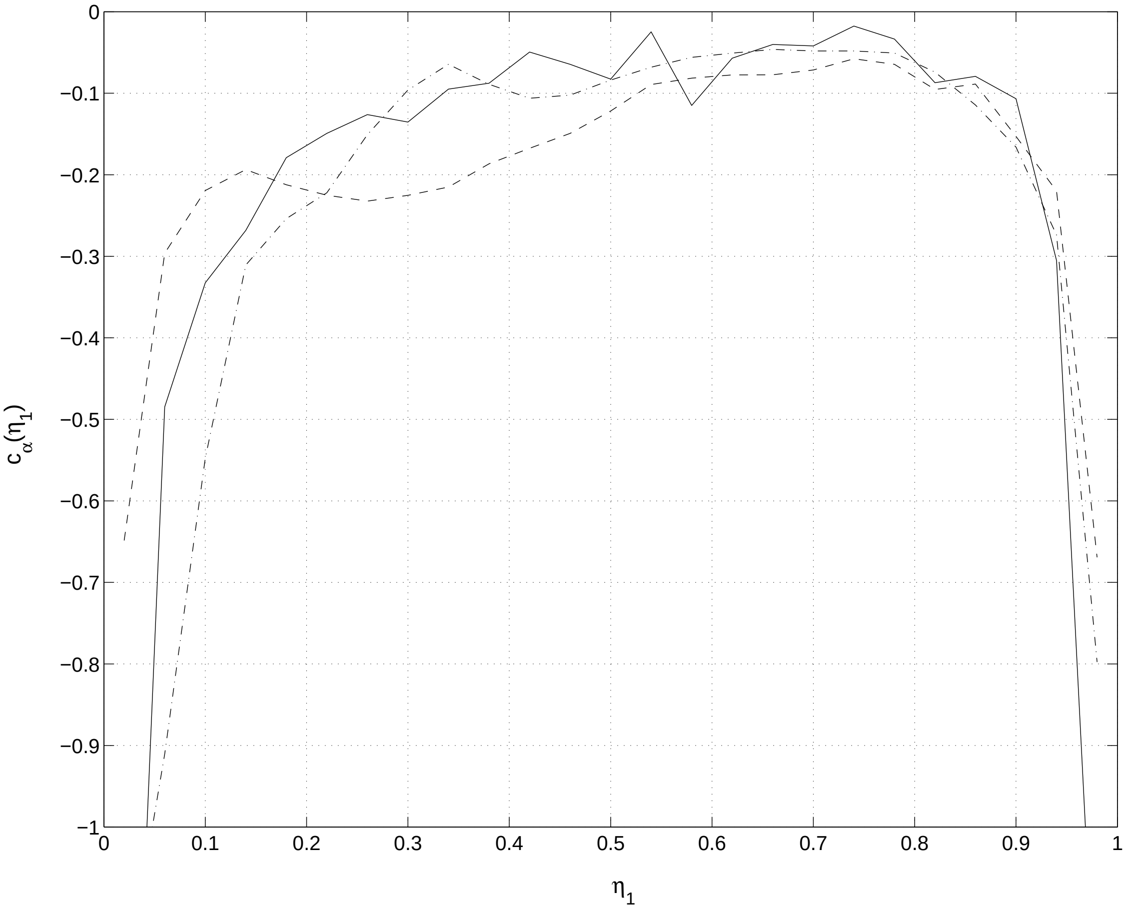

Figure 5.12: Variation of the c_α parameter as a function of the mixture fraction at three different stations along the downstream coordinate. Solid line indicates c_α at $x = 3H$, dashed line at $x = 7.5H$ and dashed-dotted line at $x = 11.2H$.

between -0.5 and -0.1 for most of the mixture fraction range throughout the evolution of the MMC solution. It should also be noted that the c_α values in the present MMC formulation have also been scaled by the $C_f = 1.3$ factor. Higher magnitude of c_α by itself (using (5.15)) is indicative of the increased intermittency of the dissipative process and consequent increases in the rate of extinction. However, the differences in the c_α values from the revised model (5.19) are small, since the correlation function f_{corr} decreases with increasing degree of extinction and this reduces the effective coefficient in the exponential function, φ, quickly. It is important to stress here that the current MMC implementation only requires the unconditional dissipation variables, $\widetilde{N_{ij}^0}$, and the turbulent scalar flux correlation, $\widetilde{u_x''Z''}$ as inputs for the modelling of the effects of turbulence in the spatially evolving jet on the reaction process. With the specification of these quantities, the modelling of the evolution in the $Z - h_s$ space is fully closed.

5.4.2 Predictions for major scalars

MMC models the evolution of all scalars in reference space and (5.3) ensures that the evolution of the probability distribution of the major scalars in real space will satisfy the joint PDF transport equation, (5.2). In this subsection only the modelling of the major scalars is analysed. For a better illustration of the method, Fig. 5.7 shows the mapping functions of mixture fraction, $X_1(\xi_1, \xi_2)$ and normalised sensible enthalpy, $X_2(\xi_1, \xi_2)$, at the start of the MMC simulation. Furthermore, colour contour plots of $X_1(\xi_1, \xi_2)$ and $X_2(\xi_1, \xi_2)$ at three different downstream locations are shown in Fig. 5.13.

As described in Sec. 5.3.2, Z is initialized as function of ξ_1 only, and a Heaviside-like function in ξ_1-space (cf. Fig. 5.6) results from a tri-modal PDF in real space, with the peak at the stoichiometric $Z_s = 0.2$ being much smaller than the peaks at the unmixed air/fuel limits. The ξ_1 location of the step largely determines the average value of the mixture fraction, $\widetilde{Z}$. As explained earlier, the normalized sensible enthalpy is initialized as a function of Z. The sensible enthalpy peaks at the ξ_1 value corresponding to $Z_s = 0.2$ and is independent of ξ_2 initially. The exponential dependence on ξ_2 (cf. (5.13)) leads to higher values of the diffusion coefficient, B_{11}^0, for low ξ_2. This causes more mixing evidenced in the smearing out of the mixture fraction gradients for negative ξ_2 values in Fig. 5.13 at $x = 3H$. Unlike the previous study by Kronenburg & Cleary (2008), the temperature dependence of diffusivity modelled in the present study plays a role in the evolution of the sensible

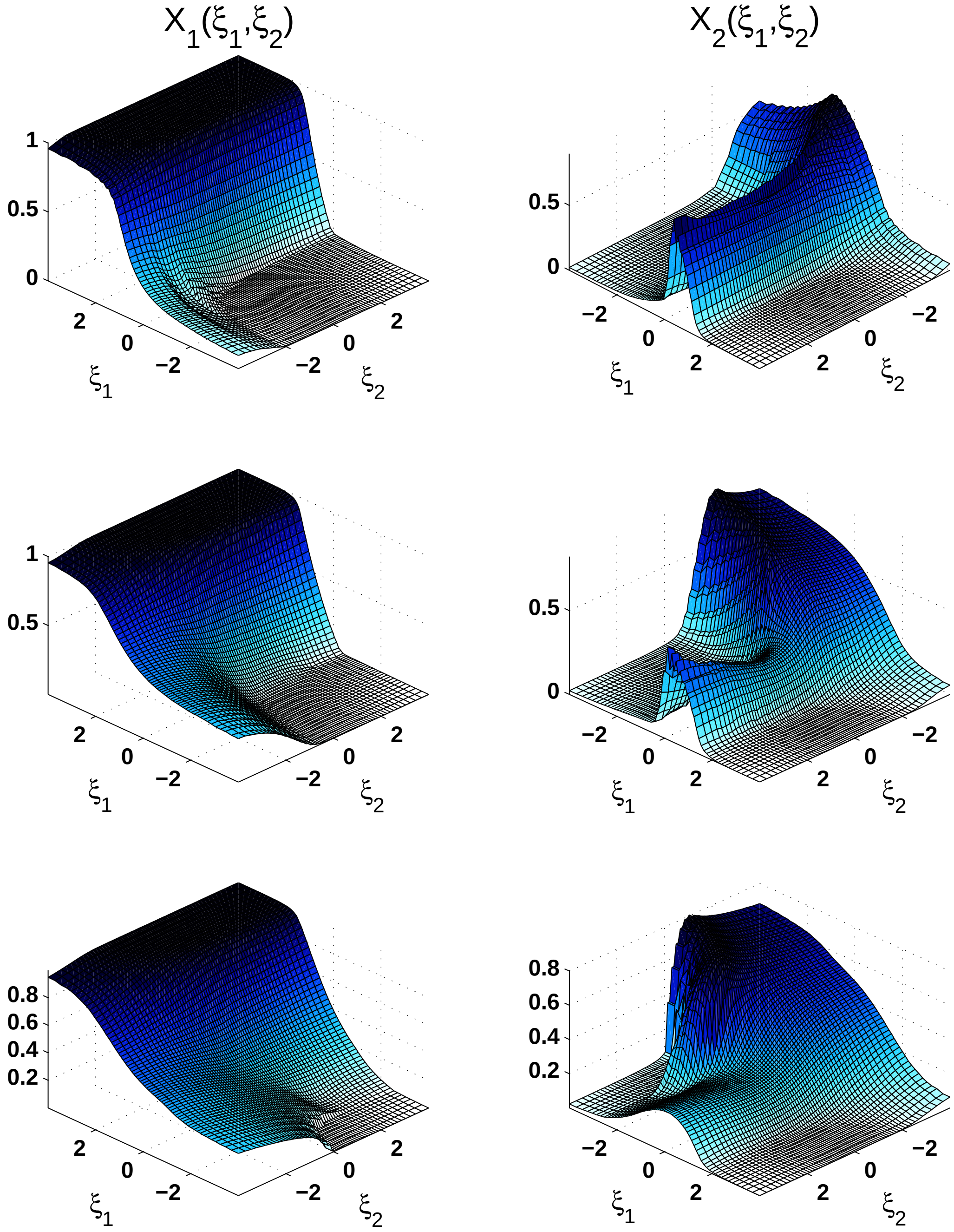

Figure 5.13: Evolution of the mapping function, $X_1(\xi_1, \xi_2)$, for the mixture fraction (left column) and, $X_2(\xi_1, \xi_2)$, for the normalised sensible enthalpy (right column) at three positions along the downstream coordinate. The ξ_1, ξ_2 axes have been reversed in $X_2(\xi_1, \xi_2)$ plots for better visibility. The top row corresponds to $x = 3H$, middle to $x = 7.5H$ and the bottom to $x = 11.2H$.

enthalpy mapping function. The reduction in temperature due to large B_{11}^0 values is only seen at the very outset of the MMC computation close to the nozzle, i.e. for $x < 3H$. The joint Z-$\hat{h}_s$ PDF at $x = 3H$ in Fig. 5.15, which has been computed for $[-0.25H, +0.25H]$ intervals around the mentioned locations, gives some indication of this initial reduction in temperature. However, this scenario is not sustainable further away from the nozzle, as the effect of large B_{11}^0 is substantially mitigated via (5.4) by the decrease in the temperature-dependent diffusivity and c_α values. Therefore, the temperature dependence of diffusivity modelled in the present study keeps the sensible enthalpy values high even at negative ξ_2, contrary to the previous study where such temperature dependence in negelected. As seen in the plots for $x = 7.5H$ in Fig. 5.13 the local extinction is achieved around $\xi_2 = 0$ near the centre of the domain inspite of the low B_{11}^0 values there. This is due to the dominance of the $\partial X_1/\partial \xi_1$ gradient in the region evidenced in Fig. 5.14. In this region, the net behaviour of the dissipation term, N_{11}, follows the gradient in ξ_1 space rather than the diffusion coefficient.

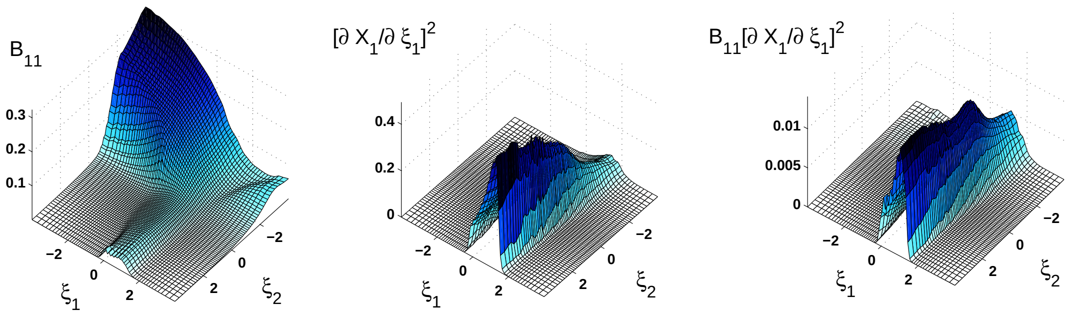

Figure 5.14: Surface plots of the MMC diffusion coefficient, (square of) the mapping function gradient in the ξ_1 direction and their product at $x = 7.5H$. The $B_{11}\left(\partial X_1/\partial \xi_1\right)^2$ product is the leading term in the MMC model for the scalar dissipation rate, N_{11}, in (5.7).

Due to the joint Gaussian distribution of the reference variables with peaks at $(\xi_1, \xi_2) = (0, 0)$, the probability density associated with temperature values in this region is extremely high. Therefore, any reduction of temperature in this region implies local extinction. On the other hand, re-ignition at $x = 11.2H$ is caused by an enhanced rate of mixing on the lean side of the mixture at negative ξ_1 values, leading to increased sensible enthalpy/temperature levels in that region. At the far downstream locations, the evolution of the X_2 mapping function is in the form of a front of high sensible enthalpy values (corresponding to the $Z = Z_s$ contour on X_1) moving along the ξ_2-coordinate from the negative to the positive end. This signifies the rapid consumption of the oxidiser in the absence of any fresh air-entrainment.

To facilitate the analysis of MMC, all results are transformed into the (η_1, η_2)-space using the technique introduced in Sec. 5.3.3. The resulting joint PDF, P_{ϕ_1,ϕ_2}, can be directly compared with DNS data. Fig. 5.15 demonstrates good qualitative agreement between the joint $Z-\hat{h}_s$ PDFs computed from the MMC solution and the DNS data at different streamwise locations, in particular around the stoichiometric mixture fraction. The key characteristic of the modelled joint PDF is the capability to capture the location of the extrema correctly. For better quantitative comparison, the joint PDFs are plotted along η_2 for constant mixture fraction values in Fig. 5.16. The model captures the size and locations (along the η_2-coordinate) of the peaks in the conditional enthalpy PDF at $Z = 0.1$ very well, especially at $x = 3H$ and $7.5H$. The bi-modal character of the conditional PDF is also well captured around stoichiometric and the location of the maxima is well approximated. A slightly wider distribution is noted in the DNS data and the more narrow MMC distribution can to some extent be associated with the aforementioned numerical constraints on the diffusion coefficients. A negative B_{22}^0 diffusion coefficient may not restrict the maximum normalized sensible enthalpy to around 0.75 at $x = 7.5H$, but allow higher values as evidenced in the DNS. Unlike the previous study by Kronenburg & Cleary (2008), where a similar situation was encountered, the narrowness of the MMC distribution in the present case is less pronounced. This may be due to the

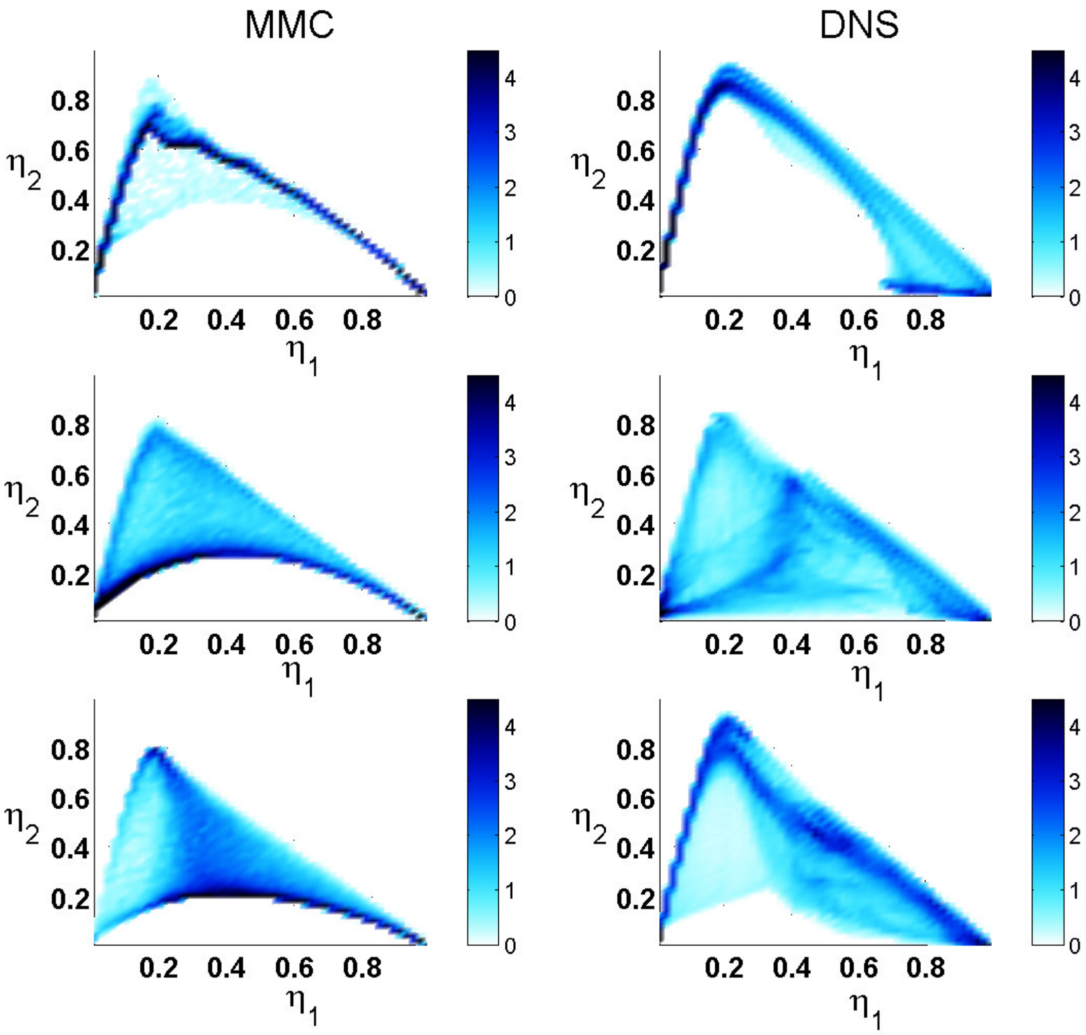

Figure 5.15: Evolution of the joint PDF of the mixture fraction and normalised sensible enthalpy, P_{ϕ_1,ϕ_2}, computed from the MMC model at three locations along the downstream coordinate is shown at the left. The corresponding DNS results are on the right. The top row corresponds to $x = 3H$, middle to $x = 7.5H$ and the bottom to $x = 11.2H$. All PDF values shown correspond to $\sqrt{min(P_{Z,\hat{h}_s}, 20)}$ for clarity of presentation and are computed for data in the $[x - 0.25H, x + 0.25H]$ interval.

relative lack of restriction placed on the cross-dissipation term that contributes to the diffusion in (η_1, η_2)-space. Fig. 5.16 shows an absence (in the DNS) of the high concentrations of low sensible enthalpy values predicted by MMC at the $x = 11.2H$ downstream location. This is consistent with the over-prediction of the conditional variance of sensible enthalpy at the same location in Fig. 5.17. This behaviour of the Pantano (2004) flame is quite anomalous because while the conditional variance at the stoichiometric mixture fraction drops from $x = 7.5H$ (extinction) to $x = 11.2H$ (re-iginition), it then re-grows to show good agreement with MMC predictions a little further downstream at $x = 13H$.

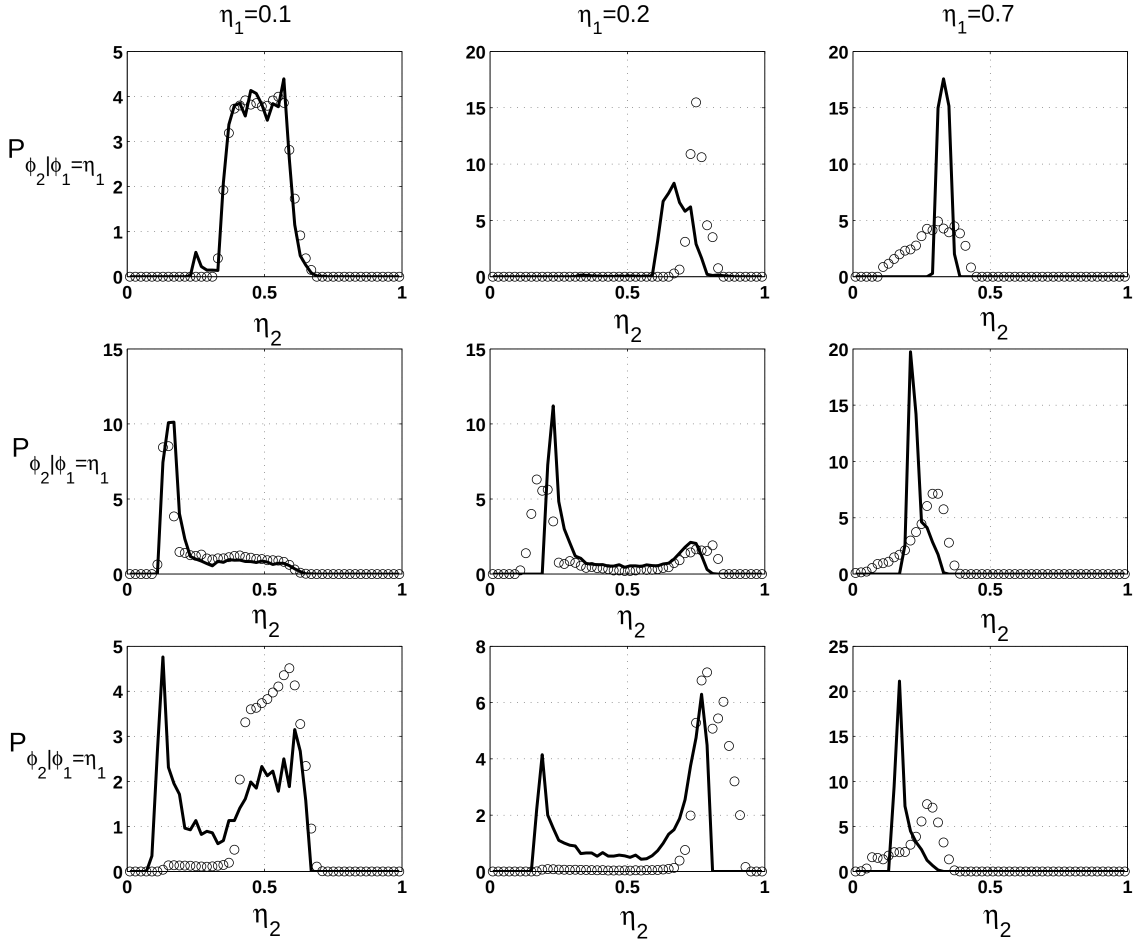

Figure 5.16: PDF of the normalised sensible enthalpy conditional on a fixed value of the mixture fraction, $P_{\phi_2|\phi_1}$. Results for $\eta_1 = 0.1$, 0.2 and 0.7 are arranged column-wise, whereas the rows correspond to $x = 3H$, $x = 7.5H$ and $x = 11.2H$ at the top, middle and bottom respectively. Statistics to compute the conditional PDFs have been gathered within the $[\eta_1 - 0.03, \eta_1 + 0.03]$ interval.

As Kronenburg & Cleary (2008) suggest, the coupling between large values of the diffusion coefficient, B^0_{11}, and low ξ_2 is an inescapable artefact of the present im-

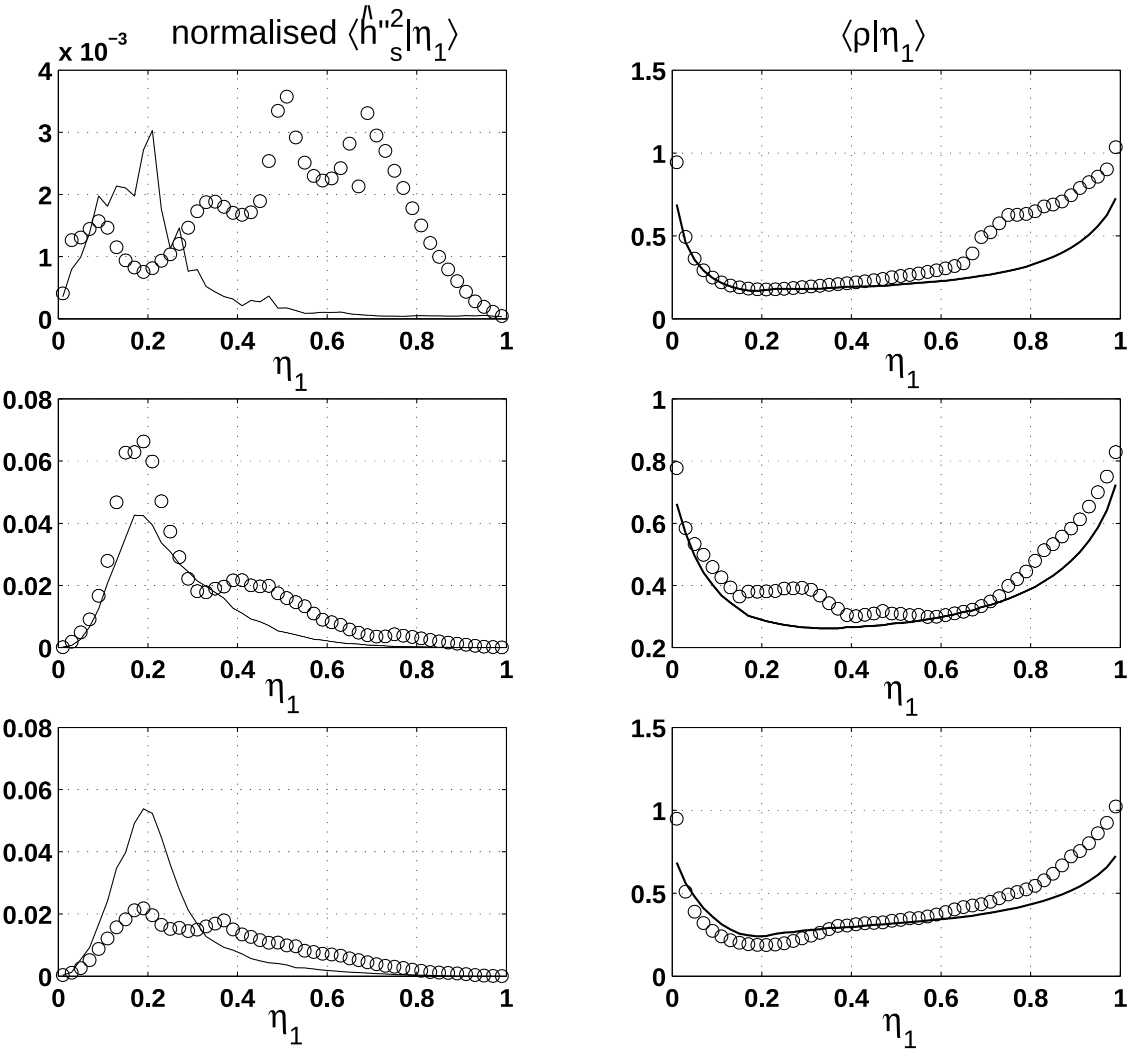

Figure 5.17: To the left: plots of the variance of the normalised sensible enthalpy conditional on the mixture fraction, $\langle \hat{h}_s''^2 | \eta_1 \rangle$ at different spatial locations. To the right: temperature-dependent value of the density computed from (3.6) conditional on the mixture fraction at different spatial locations. Circles denote the DNS values and solid lines are the MMC computed values. The rows correspond to $x = 3H$, $x = 7.5H$ and $x = 11.2H$ at the top, middle and bottom respectively.

plementation of the MMC model, with a major influence on the evolution of the $Z - \hat{h}_s$ PDF. The current implementation of MMC fixes high dissipation values to specific regions in the (ξ_1, ξ_2)-space. This is clearly aphysical because in real space the intermittent behaviour of scalar dissipation is not correlated with certain regions of low mixture fraction gradients. A mixture-fraction independent implementation of the dissipation intermittency model in MMC is desirable in removing these shortcomings. However, for the present deterministic MMC closure such coupling cannot be avoided and does not seem to strongly affect the modelling results.

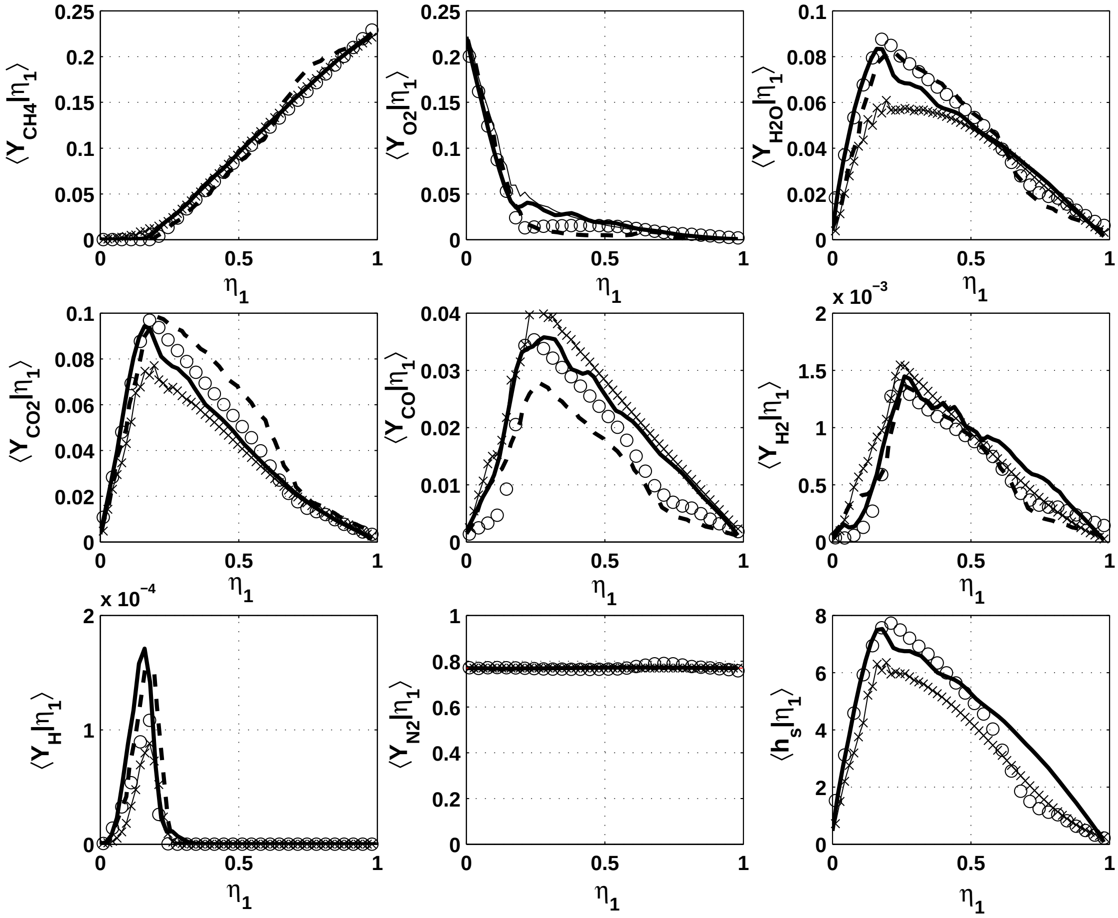

Figure 5.18: Comparison of the singly-conditioned (on Z) chemical species mass fractions and normalised sensible enthalpy from the MMC computation and those from the DNS at $x = 3H$. Results from the singly- (Z) and doubly-conditioned (Z, h_s) CMC computations have been included. The solid line, dotted line, crosses and circles correspond to the MMC, CMC2, CMC1 and DNS results, respectively. The doubly-conditioned CMC results have been weighted by the joint-PDF from the DNS.

MMC avoids many of the issues associated with the modelling of the conditional variance equation, since the conditional variance is solved implicitly and can be used as further quantitative measure for the performance of MMC. Fig. 5.17 compares the conditional variance of sensible enthalpy, $\langle \hat{h}_s''^2 | \eta_1 \rangle$, from MMC and DNS. The underprediction seen at $x = 3H$ for most of the mixture fraction range follows from an under-prediction of the unconditional variance (cf. Fig. 5.10), but agreement at $x = 7.5H$ is good for all mixture fraction values. As remarked earlier, the over-prediction of $\langle \hat{h}_s''^2 | \eta_1 \rangle$ at $x = 11.2H$ is because of the anomalous dip in the sensible enthalpy variance during the re-ignition phase, which rises back to the levels predicted by the MMC further downstream. A more common measure for the level of extinction is the conditional mean of sensible enthalpy at the stoichiometric mixture fraction or $\langle \hat{h}_s | \eta_1 = Z_s \rangle$. A plot of the variation of $\langle \hat{h}_s | Z_s \rangle$ with the downstream coordinate from the DNS and MMC computations is shown in Fig. 5.30. Furthermore, comparisons of the MMC and DNS conditional averages (with respect to Z) of the non-normalised sensible enthalpy at three different downstream stations can be found in Fig. 5.18-Fig. 5.20. The agreement between MMC and DNS is very good throughout the mixture fraction range for all three spatial locations and the same is reflected in the x-wise variation in Fig. 5.30. The general levels of extinction (at $x = 7.5H$) and re-ignition (at $x = 11.2H$) seem to be predicted well. The only issue seems to be the presence of a small trough in the conditional mean of the sensible enthalpy (reflected in all other product species) at stoichiometric during the extinction at $x = 7.5H$. This does not seem to be a physical effect and seems to be a DNS artefact. The level of extinction and the onset of reignition, albeit slightly delayed, are modelled fairly satisfactorily. Results for the conditional mean of the sensible enthalpy from the singly-conditioned CMC calculation are included here for comparison with the MMC predictions to re-iterate the need for doubly-conditioned approaches. The slight discrepancy in the level of extinction at $x = 7.5H$ is due to an underprediction of the enthalpy variance (Klimenko, 2004) discussed earlier and shown in Fig. 5.17. This is primarily caused by enforcing non-negative B_{22}^0 and the corresponding attenuation of sensible enthalpy fluctuations in the ξ_2-space (Kronenburg & Cleary, 2008). Fig. 5.17 also shows a comparison between the density conditional on the mixture fraction at three different spatial locations. The agreement is very good between the MMC and DNS values and the local temperature-dependent density changes are modelled well.

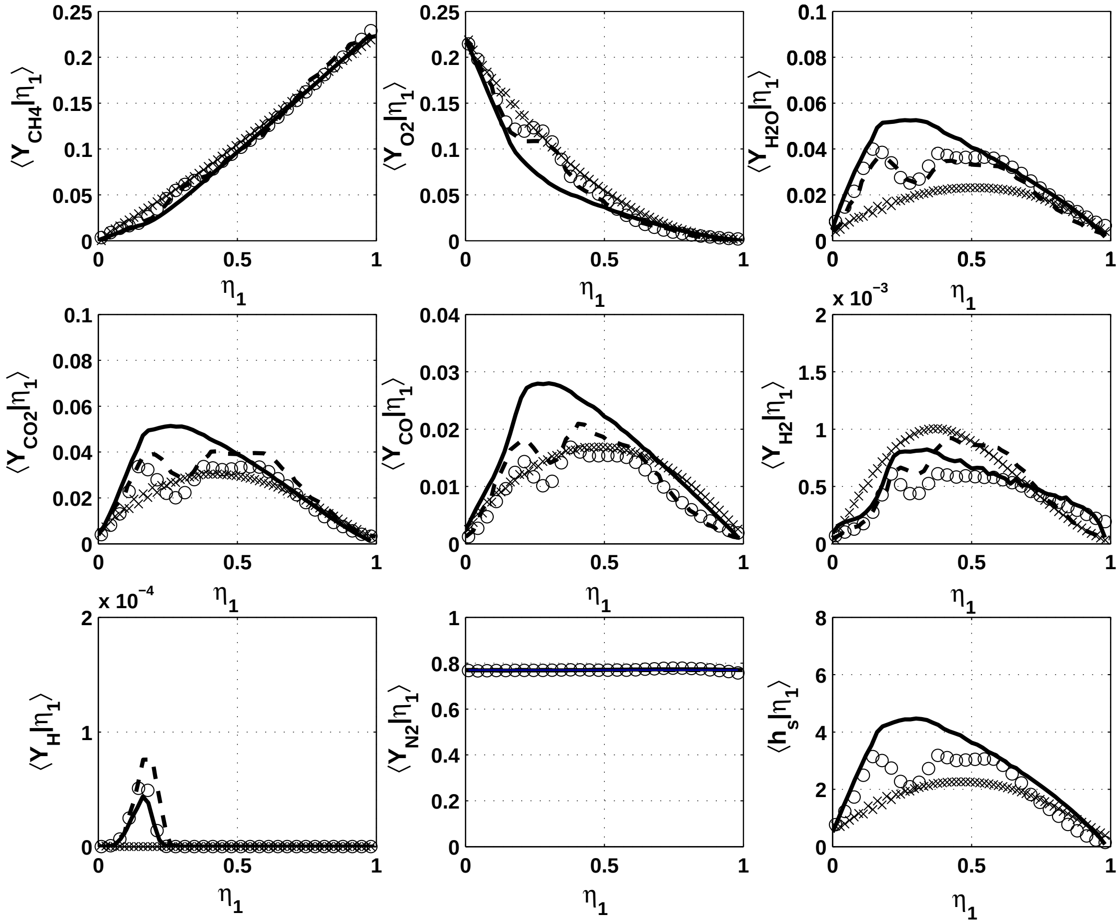

Figure 5.19: Comparison of the singly-conditioned (on Z) chemical species mass fractions and normalised sensible enthalpy from the MMC computation and those from the DNS at $x = 7.5H$. Results from the singly- (Z) and doubly-conditioned (Z, h_s) CMC computations have been included. The solid line, dotted line, crosses and circles correspond to the MMC, CMC2, CMC1 and DNS results, respectively. The doubly-conditioned CMC results have been weighted by the joint-PDF from the DNS.

5.4.3 Predictions for convective velocity

It may be recalled that the present case of a spatially evolving jet flame requires the provision of a model for the streamwise convective velocity and the consistent closure

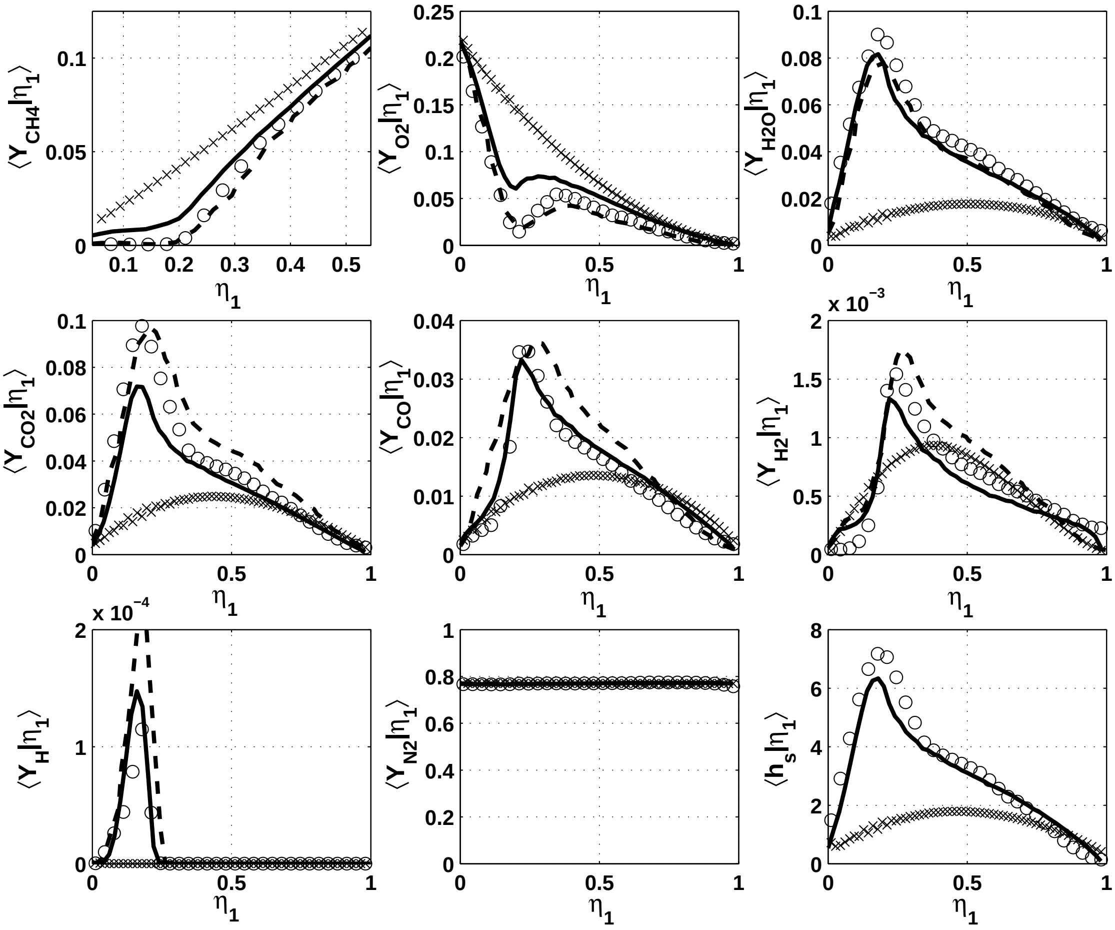

Figure 5.20: Comparison of the singly-conditioned (on Z) chemical species mass fractions and normalised sensible enthalpy from the MMC computation and those from the DNS at $x = 11.2H$. Results from the singly- (Z) and doubly-conditioned (Z, h_s) CMC computations have been included. The solid line, dotted line, crosses and circles correspond to the MMC, CMC2, CMC1 and DNS results, respectively. The doubly-conditioned CMC results have been weighted by the joint-PDF from the DNS.

of the drift coefficient in (5.3). A model for the convective velocity was proposed based on its conditional mean with respect to the mixture fraction (cf. (5.23)) and it was argued that the conditional mean can be expressed as a linear function of the mixture fraction even when the velocity-mixture fraction PDF is not joint-Gaussian. A consistent analytical one-equation sub-model for the $a_k(\xi_1, \xi_2)$ component of the MMC drift coefficient was derived in Sec. 5.2.5 and its solution was shown to be numerically feasible in Sec. 5.3.3. Nonetheless, the feasibility of the original convective velocity closure needs direct confirmation from the DNS data, and is evidenced in Fig. 5.21. As the figure clearly shows, the velocity model based on (5.31) approximates the actual conditional average very well at all downstream locations, even when the scalar turbulence is still nowhere close to being joint Gaussian. On the other hand, the standard MMC closure based on the Gaussian distribution of velocity fails to capture the conditional averages properly. Modelling the spread of a non-Gaussian U_x distribution using (5.20) also causes the aphysically high and low (even negative) velocity predictions seen in Fig. 5.21. It is important to stress here that evolution of the scalar turbulence towards joint-Gaussianity will strengthen the linearity approximation even further.

Fig. 5.21 also indicates that the conditional variance of convective velocity is quite low near the nozzle exit, which is consistent with the good model prediction in Fig. 5.1. The scatter around $\langle u_x | Z = \eta_1 \rangle$ increases with the downstream development of the flow, yet the alignment of the velocity-scalar PDF with the conditional mean remains strong. The evolution of the variance around $\langle u_x | \eta_1 \rangle$ in Fig. 5.1 can also be modelled using (5.31) by accounting for changes in the ensemble averaged velocity-mixture fraction means/correlations in the cross-stream direction that have been neglected here (cf. Fig. 5.2). This is possible in a two-dimensional MMC implementation. Nonetheless, the conditional mean approximation seems to give satisfactory results for the present case of one-dimensional MMC closure.

5.4.4 Doubly-conditioned dissipation variables

MMC provides implicit closures for two key quantities that appear in unclosed form in the doubly-conditioned moment closure formulation: the joint PDF of the conditioning scalars and the doubly conditioned dissipation terms. The modelling of the

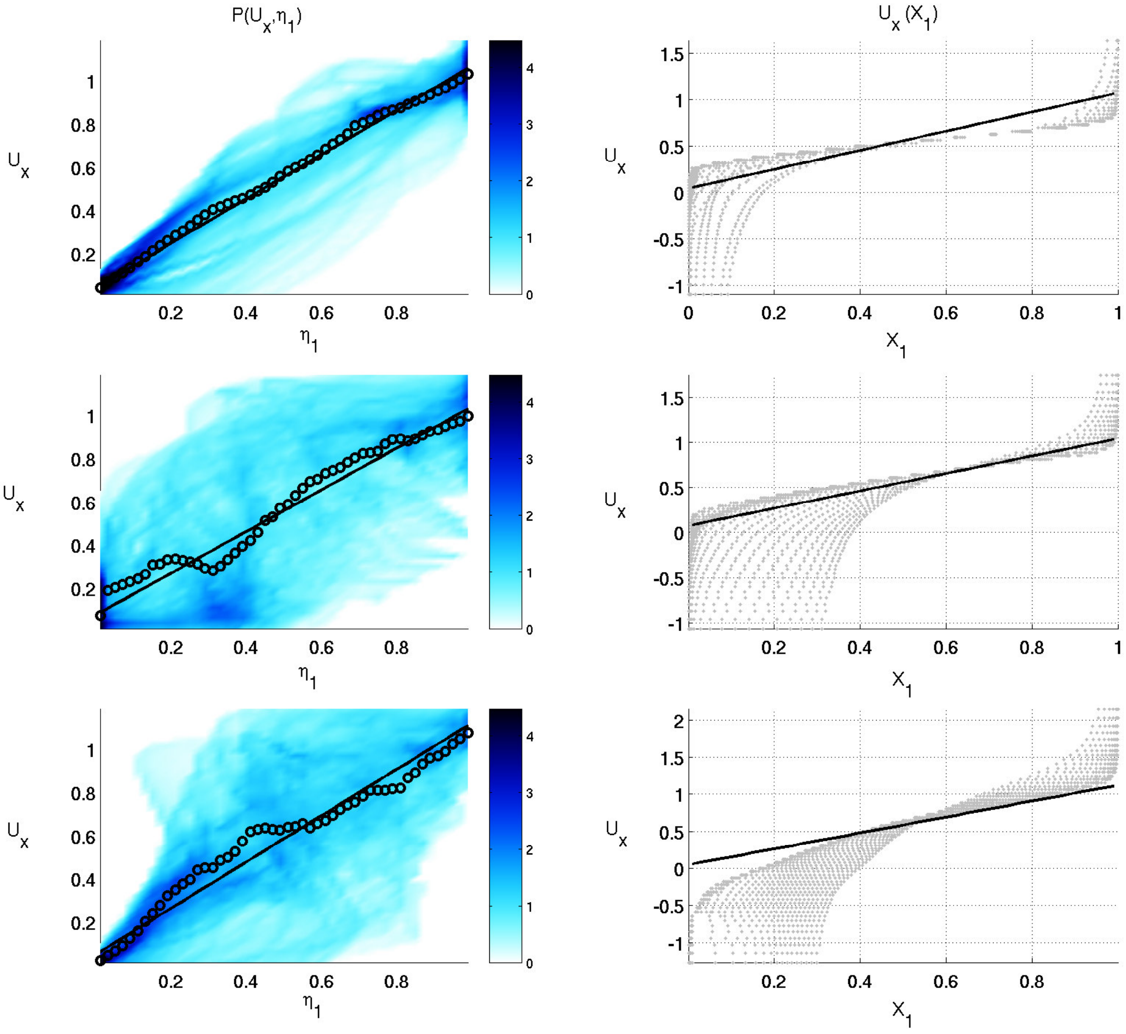

Figure 5.21: Left column: joint PDFs of the mixture fraction and the downstream convective velocity are shown at three locations along the downstream coordinate. All PDF values shown correspond to $\sqrt{min(P_{U_x,Z},20)}$ for clarity of presentation. The actual conditional mean, $\langle u_x|Z=\eta_1\rangle$, computed from the DNS is superimposed along with the convective velocity modelling result from (5.31). Circles and solid line denote $\langle u_x|Z=\eta_1\rangle$ and U_x from (5.31), respectively. Right column: modelled values of the streamwise velocity plotted against the mixture fraction mapping function at the same three locations. Dots indicate the values from the standard Gaussian model (5.20) by Klimenko & Pope (2003) and the solid line indicates values from (5.31). The top row corresponds to location $x=3H$, middle to $x=7.5H$ and the bottom to $x=11.2H$.

joint PDF has been addressed above and the dissipation terms are now compared with DNS data. The quality of the scalar dissipation modelling can be expected to mirror the strengths and weaknesses in the approximation of the joint PDF due to the intrinsic link between dissipation and PDFs. The doubly conditioned dissipation terms can be otained from (5.7) and can then be mapped onto the mixture fraction-sensible enthalpy-space.

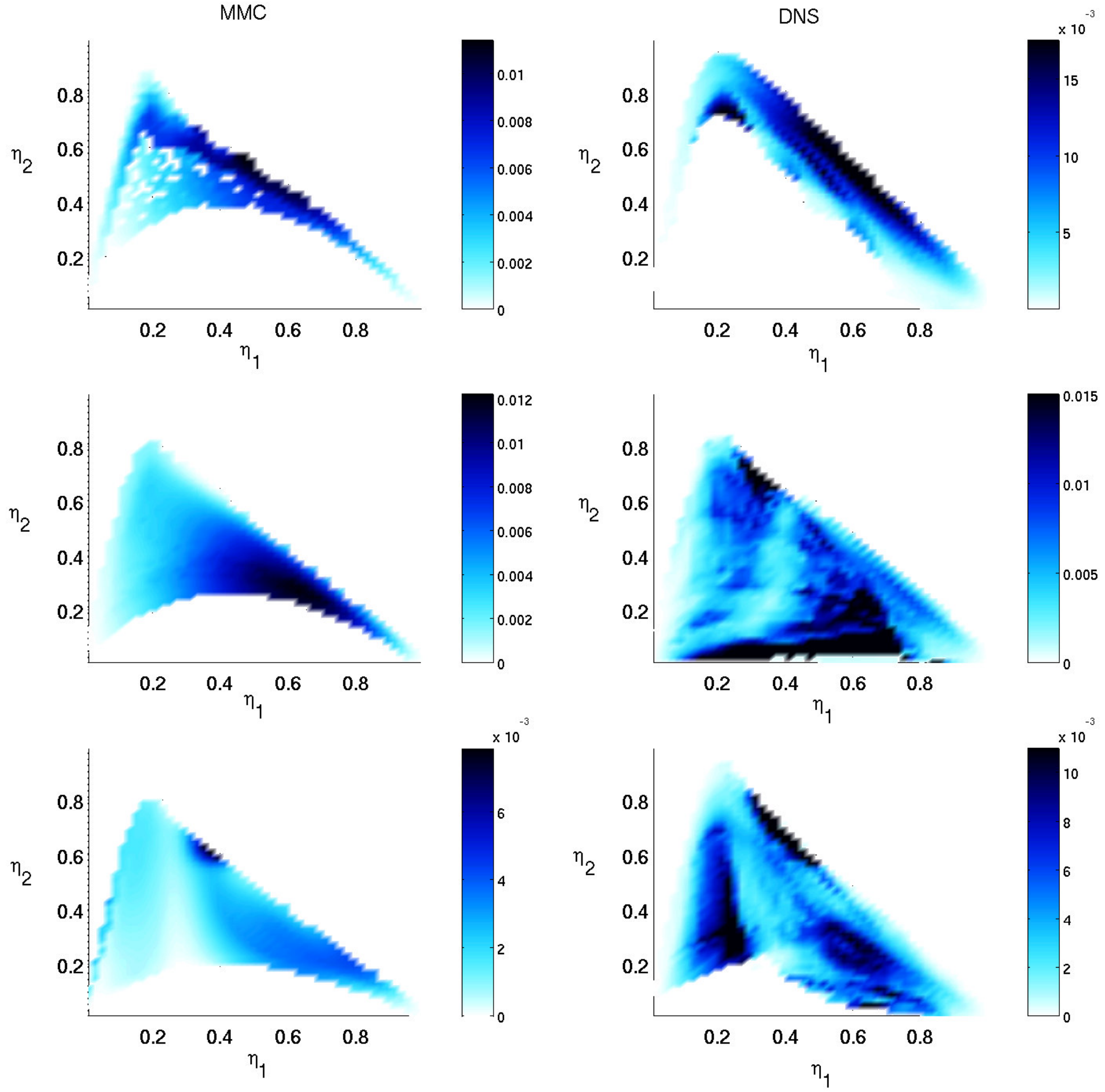

Figure 5.22: Evolution of the doubly conditioned dissipation rate of the mixture fraction, N_{11}, computed using (5.7) from the MMC model, is shown at three locations along the downstream coordinate in the left column. The corresponding DNS results are on the right. The top row corresponds to $x = 3H$, middle to $x = 7.5H$ and the bottom to $x = 11.2H$.

Fig. 5.22-Fig. 5.24 compare the modelled doubly conditioned dissipation of Z, $\hat{h}_s$

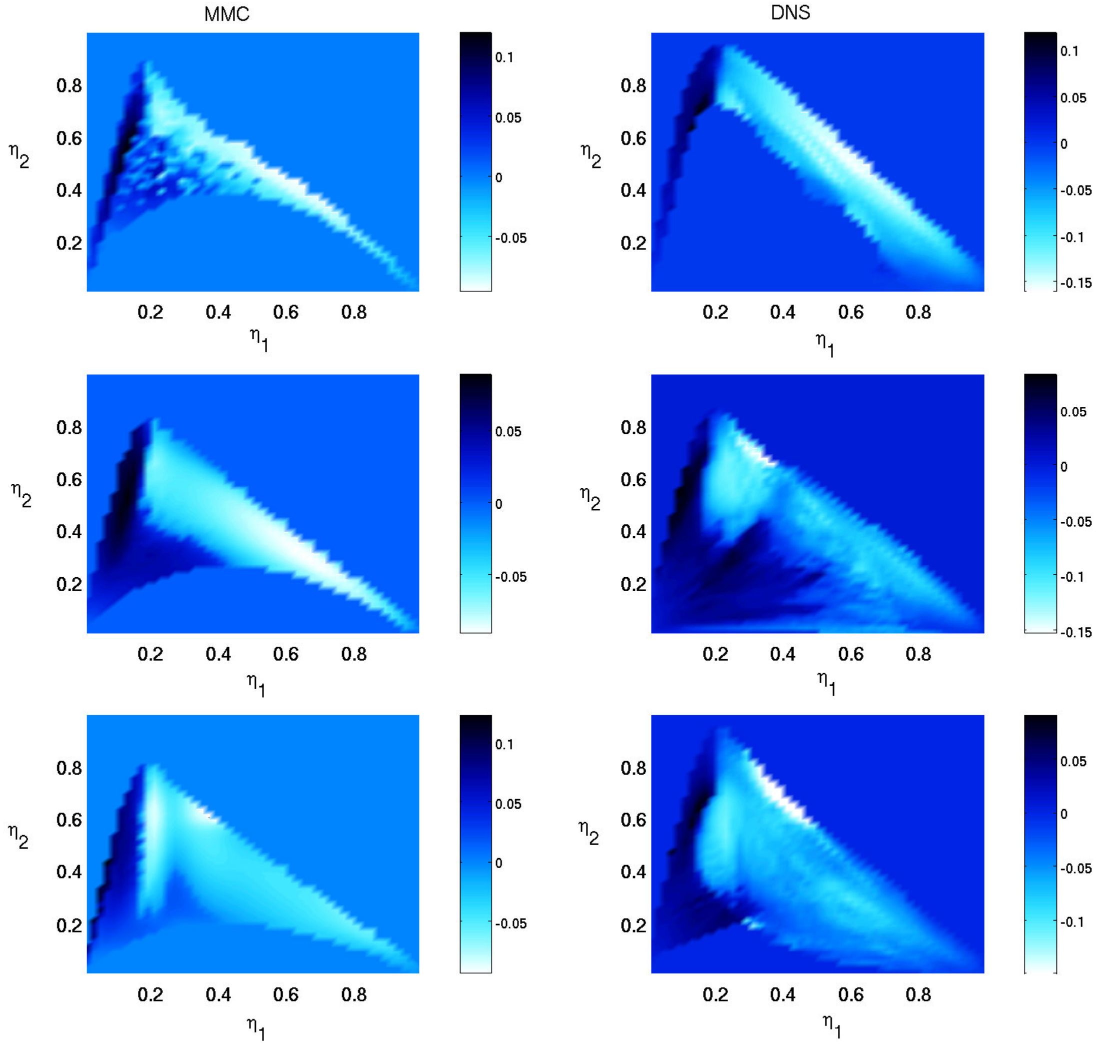

Figure 5.23: Evolution of the doubly conditioned cross-dissipation rate, N_{12}, computed using (5.7) from the MMC model, is shown at three locations along the downstream coordinate in the left column. The corresponding DNS results are on the right. The top row corresponds to $x = 3H$, middle to $x = 7.5H$ and the bottom to $x = 11.2H$.

and the cross-dissipation term with the DNS results at three different streamwise locations. MMC qualitatively approximates the trends in the evolution of the doubly conditioned dissipation rate variables. More quantitative comparisons between the MMC predictions and the DNS can be made in terms of the singly-conditioned means, $\langle N_{ij}|\eta_1\rangle$, shown in Fig. 5.25. There is excellent agreement between the MMC predictions and the DNS for all three dissipation variables at extinction ($x =$

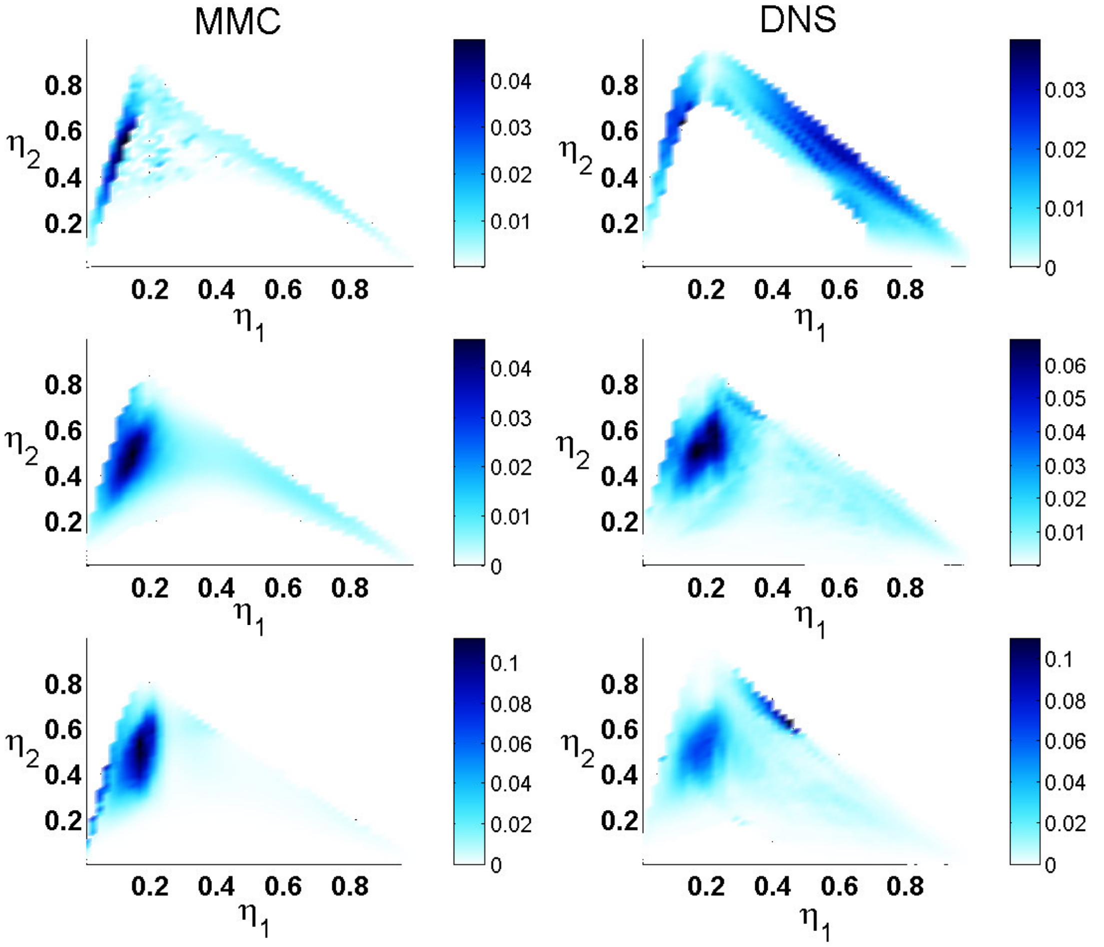

Figure 5.24: Evolution of the doubly conditioned dissipation rate of the sensible enthalpy, N_{22}, computed using (5.7) from the MMC model, is shown at three locations along the downstream coordinate in the left column. The corresponding DNS results are on the right. The top row corresponds to $x = 3H$, middle to $x = 7.5H$ and the bottom to $x = 11.2H$.

$7.5H$). In particular the evolution of the local minimum in the sensible enthalpy dissipation around stoichiometric is well captured. This would not be possible with conventional approaches (Swaminathan & Bilger, 1999; Kim *et al.*, 2004) that are normally based on flamelet assumptions which certainly do not hold in the presence of local extinction. The dissipation of the mixture fraction also captures the trends well and, unlike the previous study by Kronenburg & Cleary (2008), large increases in the scalar dissipation rate at low sensible enthalpy values are predicted in the present study. The qualitative trends captured by the cross-dissipation term in Fig. 5.23 and its conditional averages in Fig. 5.25 are satisfactory overall.

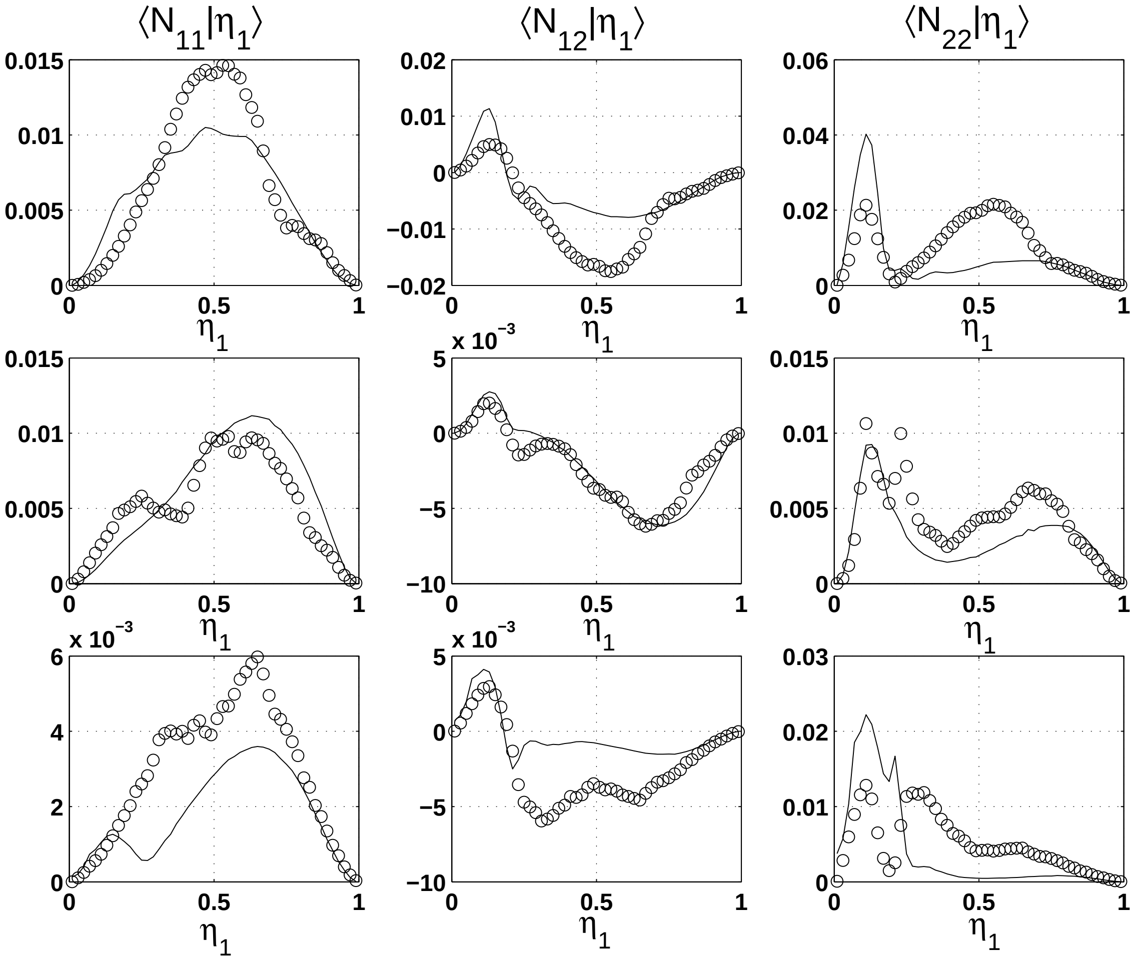

Figure 5.25: Plots of the singly conditioned (with Z) dissipation variables computed from the MMC solution with the DNS results for comparison at three downstream locations. The first, second and third columns correspond to variables $\langle N_{11}|\eta_1\rangle$, $\langle N_{12}|\eta_1\rangle$ and $\langle N_{22}|\eta_1\rangle$ respectively, while the top row corresponds to $x = 3H$, middle to $x = 7.5H$ and the bottom to $x = 11.2H$. Solid lines indicate modelling results and circles denote the DNS values.

5.4.5 Predictions for the minor scalars

Predictions of all reactive (minor) species are good at all spatial locations. Fig. 5.26-Fig. 5.29 compare the doubly conditioned mass fraction profiles of CH_4, H_2O, CO and the H-radical from the DNS (right) and MMC (left) at three different spatial locations qualitatively. For more quantitative comparisons between the MMC predictions and DNS results, the singly-conditioned (on Z) profiles of all the chemical species at the same three spatial locations are given in Fig. 5.18-Fig. 5.20.

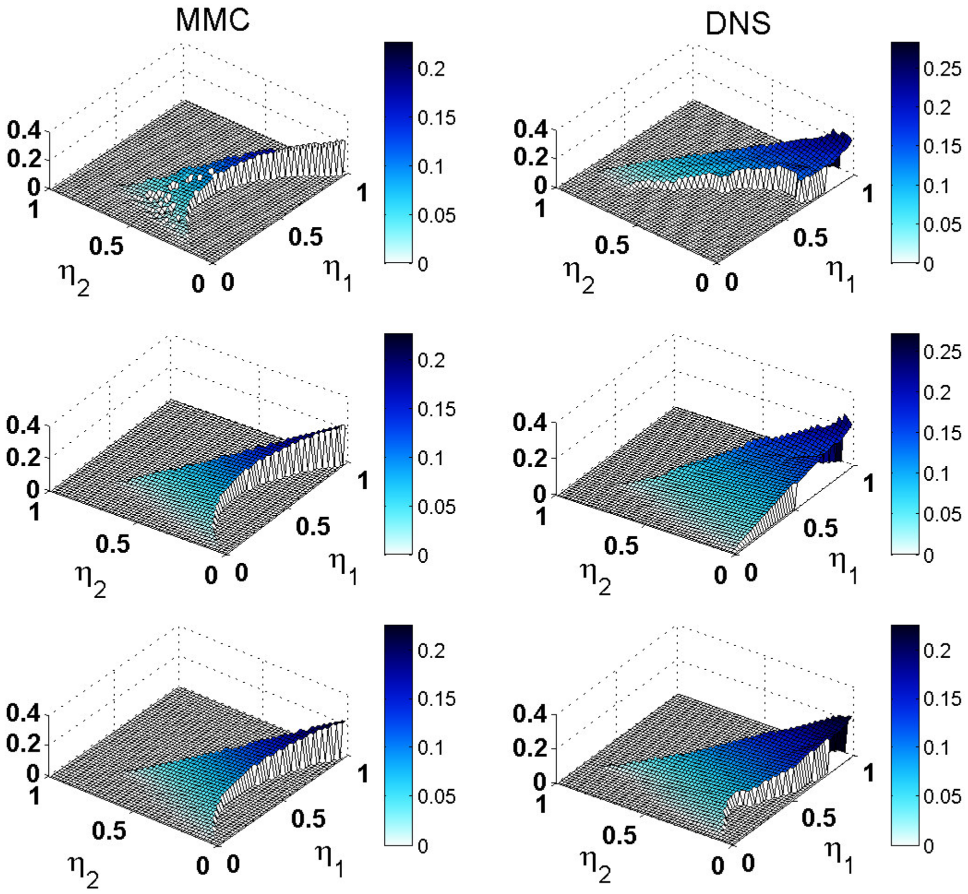

Figure 5.26: Comparison between the doubly conditioned means in η_1, η_2-space of CH_4 computed using the MMC closure (left) and computed from the DNS (right) at three spatial locations. The top row corresponds to $x = 3H$, middle to $x = 7.5H$ and the bottom to $x = 11.2H$.

Results from singly- and doubly-conditioned CMC computations have also been included for comparison. Solution profiles for the chemical species using doubly-conditioned CMC have been weighted by the PDFs taken from the DNS to give the

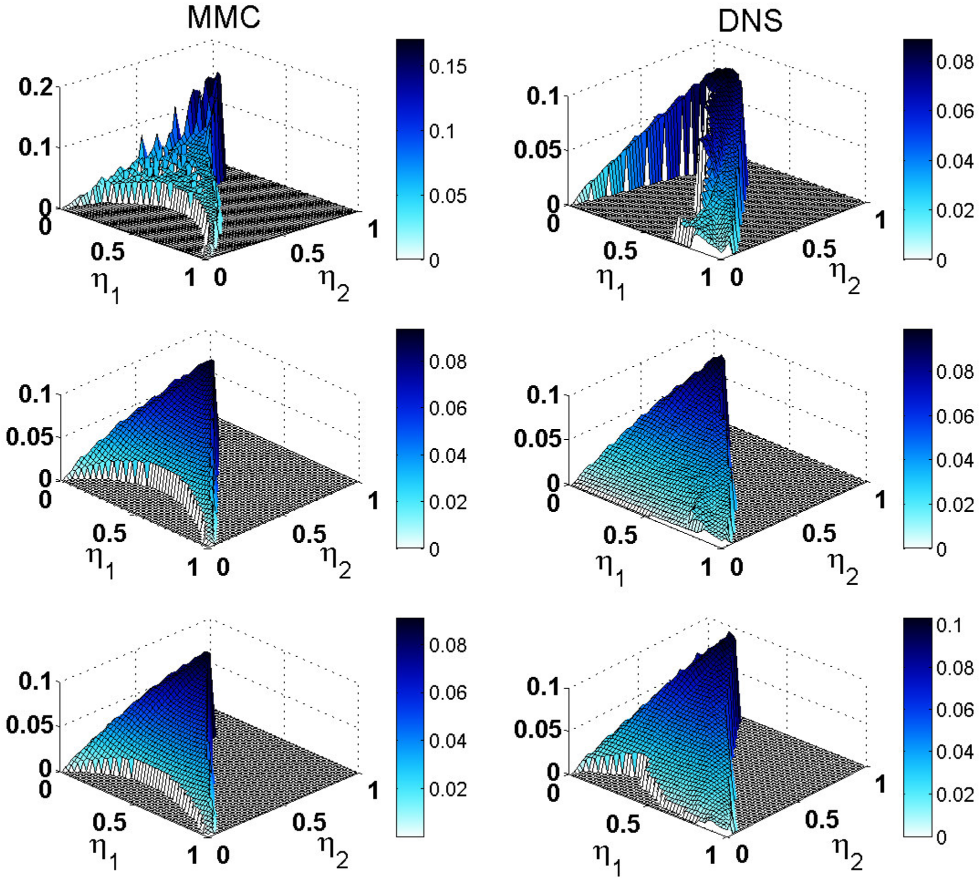

Figure 5.27: Comparison between the doubly conditioned means in η_1, η_2-space of H_2O computed using the MMC closure (left) and computed from the DNS (right) at three spatial locations. The top row corresponds to $x = 3H$, middle to $x = 7.5H$ and the bottom to $x = 11.2H$.

condional means in the mixture fraction space. Furthermore, one-dimensional plots of the downstream evolution of all minor scalars conditioned on the stoichiometric mixture fraction are shown in Fig. 5.30. Good agreement of the doubly conditioned quantities with DNS data implies that mixture fraction and normalised sensible enthalpy describe the turbulent scalar fluctuations well and that the chemical source term can be modelled with first order closure based on these doubly conditioned mass fractions. This is on expected lines since earlier studies (Kronenburg & Papoutsakis, 2005; Kronenburg & Kostka, 2005) on doubly conditioned moment clo-

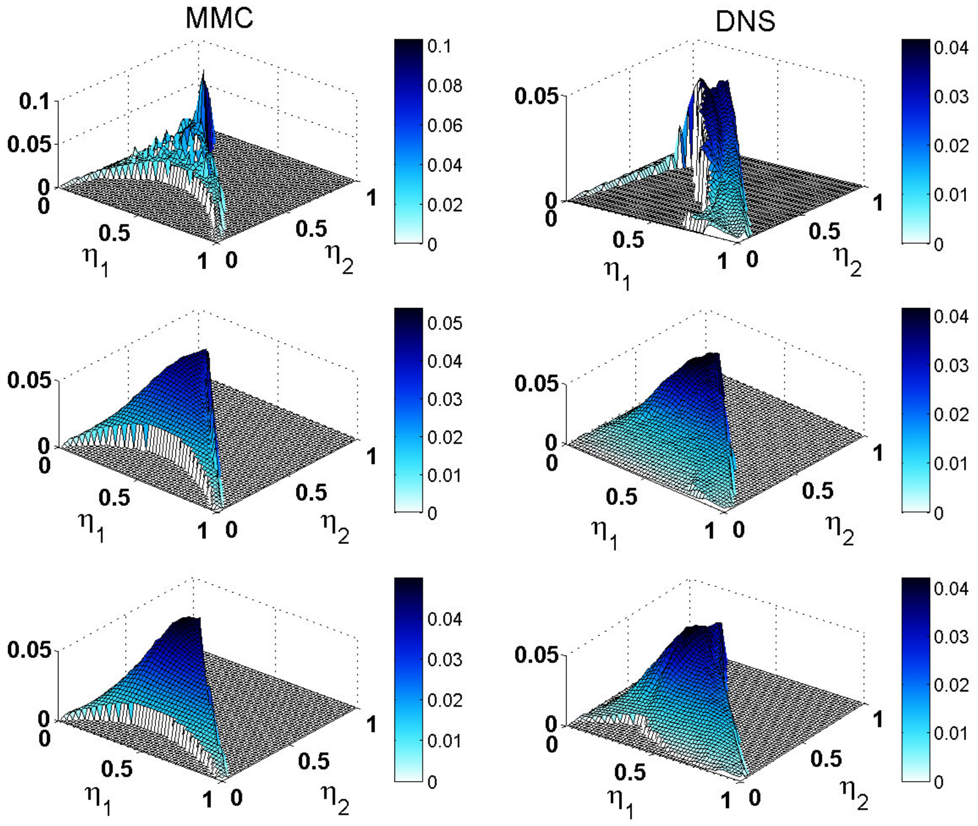

Figure 5.28: Comparison between the doubly conditioned means in η_1, η_2-space of CO computed using the MMC closure (left) and computed from the DNS (right) at three spatial locations. The top row corresponds to $x = 3H$, middle to $x = 7.5H$ and the bottom to $x = 11.2H$.

sure have amply demonstrated that the two major (or conditioning) scalars Z and h_s parameterise the composition space adequately and that fluctuations around the doubly-conditioned means are small. For the singly-conditioned quantities, agreement with the DNS is quite satisfactory, especially so for minor species like H_2 and the H-radical at both extinction and re-ignition. The insufficiency of the DNS data to compute the joint PDF during extinction (at $x = 7.5H$ leads to the aforementioned trough in the singly-conditioned profiles for all product species (except the H-radical). However, this seems an artefact of the DNS and lack of its prediction does not seem to be a shortcoming of the MMC computations. The trends in the

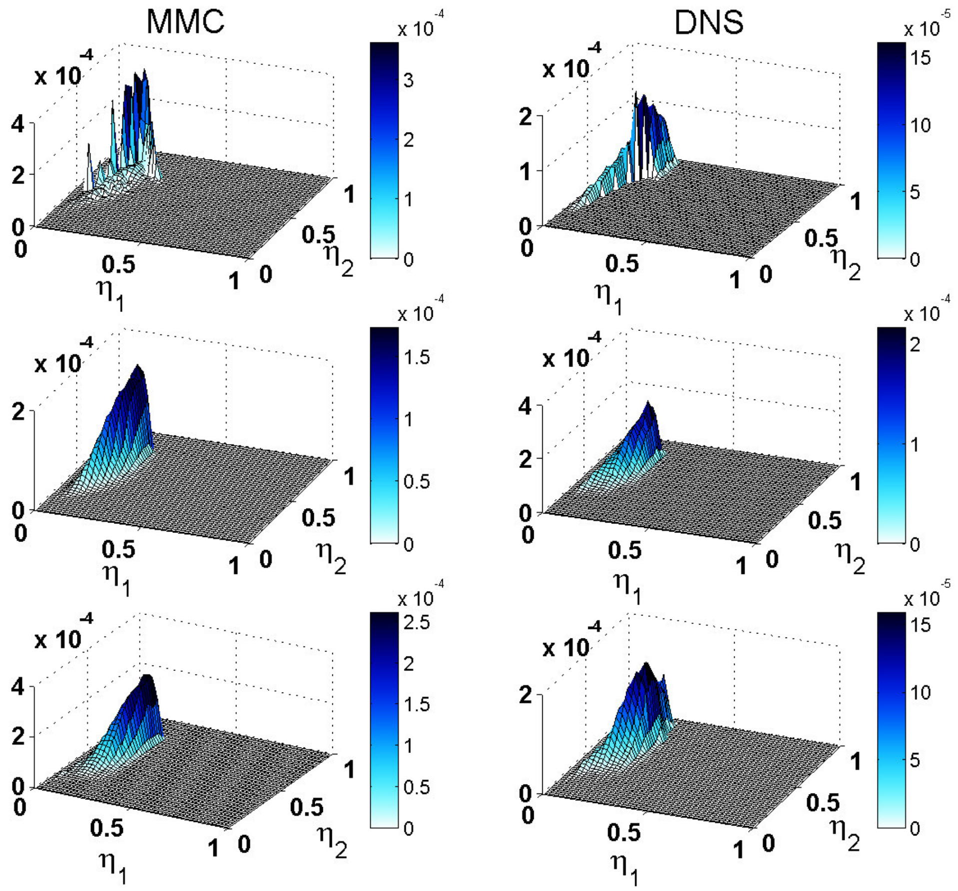

Figure 5.29: Comparison between the doubly conditioned means in η_1, η_2-space of H-radical computed using the MMC closure (left) and computed from the DNS (right) at three spatial locations. The top row corresponds to $x = 3H$, middle to $x = 7.5H$ and the bottom to $x = 11.2H$.

downstream evolution of the stoichiometric species mass fractions seem consistent with those shown by the sensible enthalpy and are fairly satisfactory.

The main conclusions of the studies on dissipation scaling and mapping closure are presented in the next chapter.

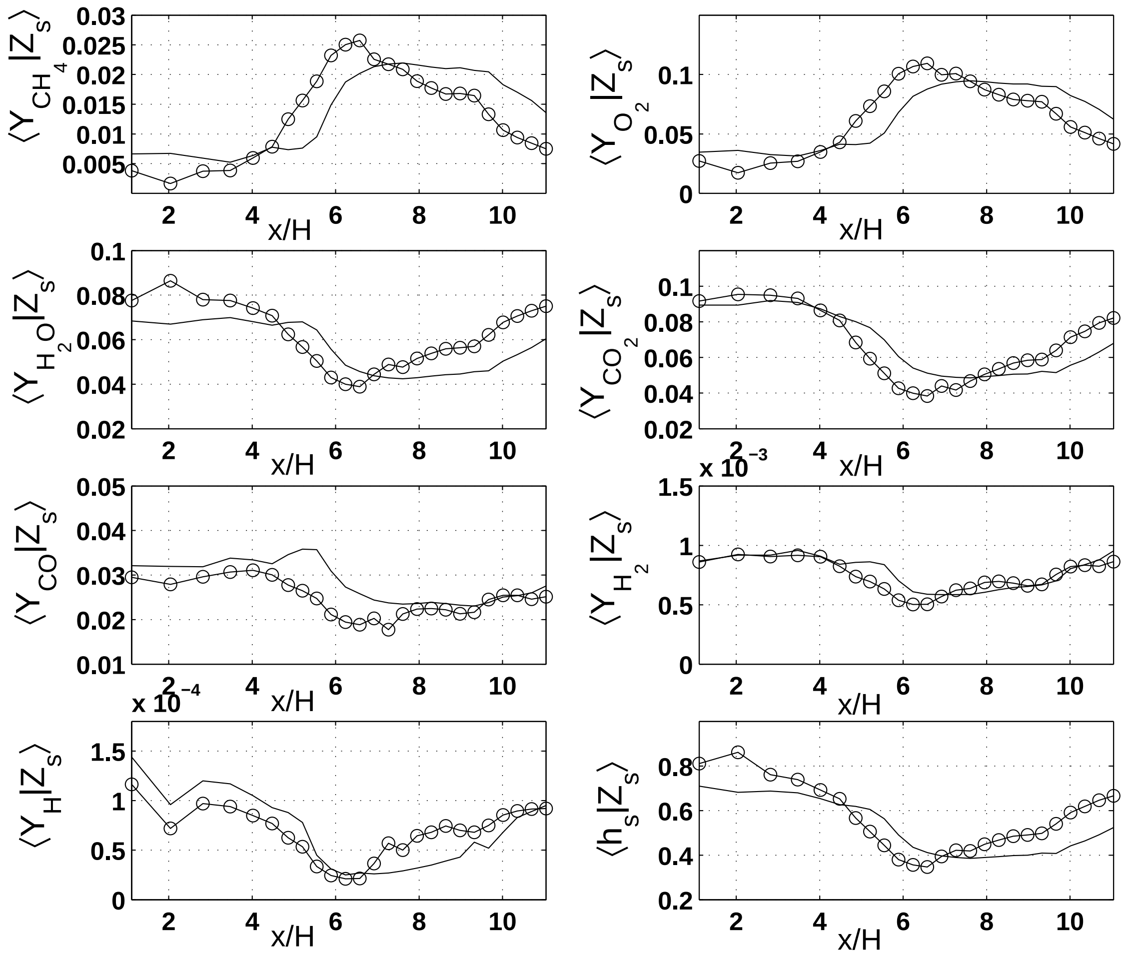

Figure 5.30: Downstream variation of the stoichiometric conditional means of all reactive scalars and the normalised sensible enthalpy. All conditional mean values have been computed after gathering the statistics for the species within the $[Zs - 0.03, Zs + 0.03]$ interval at 25 equidistant stations along the streamwise coordinate. Line plots indicate results from MMC and circles indicate DNS data.

Chapter 6

Conclusion

The chapter presents the conclusions of the numerical implementation of dissipation scaling methods and multiple mapping closure for the turbulent jet flame DNS by Pantano (2004) in the next two sections. Subsequently, potential areas of future research in both studies have been identified and explained.

6.1 Conclusions

6.1.1 Scalar dissipation scaling

The DNS database of Pantano (2004) of a turbulent reacting planar jet has been used to estimate the resolution requirements for scalar dissipation measurements and numerical simulations. It has been shown that the present database is sufficiently resolved in most regions of the flow for studying a highly intermittent variable like the scalar dissipation rate. The mean and instantaneous scalar dissipation length scales were determined by three different methods: spectral analysis, direct investigation of scalar dissipation structures and spatial filtering of the instantaneous mixture fraction field. Scalings and resolution criteria for experiments and simulations based on the easily measurable outer-scale Reynolds number, Re_δ, were then established.

The departure from Gaussian-statistics (in general) and the frequent occurrence of sub-Kolmogorov/Batchelor dissipation length-scales (in particular) are unaccounted for in the Kolmogorov's eddy-cascade picture (She, 1991). A supplementary physical model (She *et al.*, 1990; She, 1991) to explain these intermittency-related effects is introduced in Sec. 2.2.1. It is shown that the spatial-filtering technique can be used to recover the wide distribution of instantaneous scalar dissipation length scales that are important in accounting for the small-scale intermittency shown by χ and these are shown to be proportional to the local-minimum dissipation length scales. This seems to confirm the sufficiency criterion of χ-resolution based on the more stringent ${Re_\delta}^{-1}$ scaling as indicated by the estimates in Sreenivasan & Meneveau (1988), Yakhot (2003) and Sreenivasan (2004) when applied to reactive flows. The study shows that the assumption of exponential decay of intermittent χ peak-values with increasing filter-width holds. It thus allows the extrapolation to the 'fully-resolved' limit and an estimate of the actual resolution needs can be obtained.

It should be mentioned here that the stringent resolution criterion (primarily for DNS studies) suggested in the present study is limited to the resolution of scalar gradients or, equivalently, the scalar dissipation rate, which plays the key role in turbulent scalar mixing. Other physical quantities showing the same (or larger) degree of intermittent behaviour, such as enstrophy, have not been analysed here and the applicability of the suggested resolution criteria to these quantities is beyond the scope of this paper.

The Reynolds number scaling for the spectrally-recovered dissipation length scales is of the Kolmogorov type, while the scaling coefficient, Λ_0, was estimated to be of order of unity. This implies that the one-dimensional dissipation spectra are able to resolve the true Batchelor scales along the centreline of the evolving-jet, without any self-similarity assumptions and at low-to-moderate Reynolds number values. Notably, computation of instantaneous dissipation layer thicknesses also yields Batchelor scaling, with similar estimates of the scaling coefficient Λ_{3d} that are more conservative than other experimental estimates by Buch & Dahm (1998) and Su & Clemens (2003) for reasons explained in Sec. 4.2.3. However, it is not immediately clear why instantaneous dissipation layer thicknesses would not yield the $Re_\delta{}^{-1}$ scaling, evidenced using the spatial-filtering method. A probable explanation may be an inherent averaging involved in the process of computing dissipation contour thicknesses, which yields estimates of the average rather than the true instantaneous dissipation length-scales.

6.1.2 Mapping closure

The Multiple Mapping Conditioning approach has been used to model methane-air combustion in a spatially-evolving jet flame with local extinction and reignition due to turbulent strain. In the current MMC implementation, two reference variables are used representing mixture fraction and normalized sensible enthalpy and the strong correlation between sensible enthalpy and scalar dissipation fluctuations during the extinction process is exploited using the model for the MMC diffusion coefficients by Kronenburg & Cleary (2008). The second reference variable is implemented as a dissipation-like variable and a correlation coefficient is introduced to characterise the correlation between dissipation fluctuations and sensible enthalpy. This allows for correlating the scalar fluctuations of mixture fraction with those of the sensible enthalpy and generating conditional fluctuations of temperature about its mean. In addition, the level of scalar fluctuations is scaled up by a heuristic parameter and the effects of thermal fluctuations on the diffusion coefficients are accounted for. The differential rate of decay of scalar fluctuations of the chemical species is also controlled by incorporating their Lewis numbers. However, full effects of differential diffusion are not modelled here and their modelling is an area of future research. Furthermore, a linear model for the downstream convective velocity based on the mixture fraction is shown to hold for spatially evolving near-nozzle jet flows, where the scalar turbulence is strictly not joint-Gaussian. A consistent model for the MMC drift coefficients is derived and numerically implemented.

The evolution of mixture fraction and sensible enthalpy in reference space model their joint distribution well and results show good agreement with the DNS results. Similar to the previous study by Kronenburg & Cleary (2008), increased localized mixing of the mixture fraction in this case is an artefact of the deterministic implementation and stochastic MMC might remove this. However, a more important shortcoming of MMC closure in one physical dimension comes to light in the present study. This is the problem in accounting for air/oxidiser entrainment at far downstream locations. The MMC computation starts with a fixed amount of air and there is no mechanism to feed fresh air in to keep the mixture fraction PDF consistent with the real experimental/simulated flame.

Other modelling assumptions of reducing the unconditional cross-dissipation input, $c_\alpha = -1$ at $x = 0$, lack of differential species diffusion modelling and neglecting the conditional variance of convective velocity do not markedly affect the quality of the extinction/re-ignition predictions of the fully closed deterministic model presented here. The conditional variance of sensible enthalpy and the doubly-conditioned dissipation terms are implicitly modelled. The agreement of these quantities with DNS data is relatively good considering that other models employ inaccurate assumptions (for the conditional sensible enthalpy variance or convective velocity) or simply do not exist (for the doubly conditioned dissipation terms). Predictions of major and minor species are good and qualitatively comparable to similar preditions in earlier studies for homogeneous decaying turbulence by Cleary & Kronenburg (2007*b*) and Kronenburg & Cleary (2008).

6.2 Future Work

The present study on the analysis and modelling of the effects of dissipation intermittency represents an on-going research effort to better characterise this important physical quantity. A comparative analysis of spectral, level-set and spatial-filtering methods was done with a focus on isolating the regions of strongest dissipation intermittency for a highly resolved tubulent jet flame DNS. While these techniques are the most widely used in literature to measure the small-scale dissipative behaviour, the list is not exhaustive. As mentioned in Sec. 4.2, sophisticated pattern recognition algorithms (Kushnir *et al.*, 2006*a*,*b*) have been used recently with some success in doing similar numerical measurements of scalar dissipation and incorporation of this technique in the comparative analysis is potential area of future research. Further work may also include a deeper mathematical analysis of the level-set method described in Sec. 4.2 to study the inherent averaging of dissipation scales due to this method in more detail. An extension of the techniques described here to even more intermittent physical quantities associated with turbulence, like enstrophy, is also desirable.

The multiple mapping conditioning approach seems to be one of the most promising methods to model and predict the extinction and re-ignition effects of scalar dissipation fluctuations in turbulent jet flames. However, as the present study has shown, some shortcomings do exist in its one-dimensional (in physical space) implementation, most notable of which is the inability to account for the entrainment of fresh oxidiser at the far downstream locations. In other words, an 'unlimited' supply of air (simulated in the actual DNS) cannot be modelled in the one-dimensional implementation without compromising the average value of the mixture fraction. The only recourse is to extend the mapping closure to the cross-stream direction, where pure-air composition (i.e. $Z = 0$ value) can be enforced for the MMC cells farthest from the axis of the flame without affecting the statistics in the jet core. Another area of interest is modelling of the full effects of differential diffusion on minor species prediction that have been neglected in this case. Extensive research would also be required to revise the modelling of dissipation fluctuations for the two-dimensional MMC implementation, especially in tuning the magnitude of the important correlation function f_{corr} in MMC cells where the stoichiometric mixture fraction value is never achieved. Finally, the incorporation of a full RANS flow solver and suitable models for downstream and cross-stream velocity statistics, such as those presented in the present study, are required for a complete modelling of real, laboratory scale jet flames.

Appendix A

A.1 Derivation of MMC equations

The equation governing the balance between the advective-diffusive transport and chemical production of the I^{th} scalar is given by (2.6). After subtracting the scalar mass continuity terms and substituting for the diffusion flux term, J_j^I, from (2.8) the same can be written in gradient notation as,

$$\rho\frac{\partial\phi_I}{\partial t} + \rho\boldsymbol{u}\cdot\boldsymbol{\nabla}\phi_I - \boldsymbol{\nabla}\cdot(\rho D_I\boldsymbol{\nabla}\phi_I) = \rho\mathit{\Omega}_I(\boldsymbol{\phi}), \tag{6.1}$$

where $\mathit{\Omega}_I(\boldsymbol{\phi}) = \omega_I(\boldsymbol{\phi})/\rho$ is the chemical source term per unit mass and D_I is the molecular diffusivity of the I^{th} species. For flows with unity Lewis number, i.e. $D_I = D$, the above system of scalar transport equations can be transformed into the following transport equation for the joint-PDF of *all* scalars using well established techniques (Pope, 1985; Klimenko & Bilger, 1999; Pope, 2000):

$$\frac{\partial\bar{\rho}P_{\boldsymbol{\phi}}}{\partial t} + \boldsymbol{\nabla}\cdot(\bar{\rho}\boldsymbol{u}P_{\boldsymbol{\phi}}) + \frac{\partial\bar{\rho}\mathit{\Omega}_I P_{\boldsymbol{\phi}}}{\partial\eta_I} + \frac{\partial^2\bar{\rho}N_{IJ}P_{\boldsymbol{\phi}}}{\partial\eta_I\partial\eta_J} = 0, \tag{6.2}$$

where $N_{IJ} = D\boldsymbol{\nabla}\phi_I\cdot\boldsymbol{\nabla}\phi_J$ is the scalar dissipation rate variable for the $(I,J)^{th}$ combination of any two scalars, as defined in (2.35). Furthermore, by identifying a set of major scalars (cf. Sec. 5.2) and neglecting the fluctuations in the rest about their means conditional on the major scalars, the above PDF transport equation can be reduced to the major scalar space as,

$$\frac{\partial \bar{\rho} P_{\boldsymbol{\phi}_{maj}}}{\partial t} + \boldsymbol{\nabla} \cdot \left(\bar{\rho} \langle \boldsymbol{u} | \boldsymbol{\eta}_{maj} \rangle P_{\boldsymbol{\phi}_{maj}} \right) + \frac{\partial \bar{\rho} \langle \Omega_i | \boldsymbol{\eta}_{maj} \rangle P_{\boldsymbol{\phi}_{maj}}}{\partial \eta_i} + \frac{\partial^2 \bar{\rho} \langle N_{ij} | \boldsymbol{\eta}_{maj} \rangle P_{\boldsymbol{\phi}_{maj}}}{\partial \eta_i \partial \eta_j} = 0, \tag{6.3}$$

where $N_{ij} = D\boldsymbol{\nabla}\phi_i \cdot \boldsymbol{\nabla}\phi_j$ and lower-case indices i and j denote the set of major scalars only, consistent with the notation introduced in Sec. 2.0.1. A transport equation analogous to (6.3) for the evolution of the joint-distribution of arbitrarily chosen reference variables, $\boldsymbol{\theta}$, corresponding to the major scalars, has been proposed by Klimenko (2003*b*) and Klimenko & Pope (2003). The equation is introduced as (5.2) in the main text and is reproduced here for convenience,

$$\frac{\partial \bar{\rho} P_{\boldsymbol{\theta}}}{\partial t} + \boldsymbol{\nabla} \cdot \left(\bar{\rho} \langle \boldsymbol{u} | \boldsymbol{\xi} \rangle P_{\boldsymbol{\theta}} \right) + \frac{\partial \bar{\rho} A_k P_{\boldsymbol{\theta}}}{\partial \xi_k} + \frac{\partial^2 \bar{\rho} B_{kl} P_{\boldsymbol{\theta}}}{\partial \xi_k \partial \xi_l} = 0, \tag{6.4}$$

where $\langle \boldsymbol{u} | \boldsymbol{\xi} \rangle$ is the conditional mean of the convective velocity vector with respect to the reference space. A_k and B_{kl} are unknown functions of the reference variables and are termed as the MMC drift and diffusion coefficients (respectively) for reasons discussed later in the section. The reference PDF evolution equation (6.4) holds (in theory) for any arbitrary choice of stochastic reference variables and there exists a direct mathetmatical analogy between (6.3) and (6.4), such that variables $\langle \boldsymbol{u} | \boldsymbol{\eta}_{maj} \rangle$, $\langle \Omega_i | \boldsymbol{\eta}_{maj} \rangle$ and $\langle N_{ij} | \boldsymbol{\eta}_{maj} \rangle$ in the former correspond to $\langle \boldsymbol{u} | \boldsymbol{\xi} \rangle$, A_k and B_{kl} in the latter (Klimenko, 2003*b*). This analogy can be utilised to show that the scalar transport equation (6.1) used to derive (6.3) has a similar counterpart in the reference space as well. The form for the 'conservation' equation for the k^{th} reference variable consistent with the above evolution equation for $P_{\boldsymbol{\theta}}$ is given by,

$$\rho\frac{\partial\theta_k}{\partial t} + \rho\boldsymbol{u}\cdot\boldsymbol{\nabla}\theta_k - \boldsymbol{\nabla}\cdot(\rho D_k\boldsymbol{\nabla}\theta_k) = \rho A_k(\boldsymbol{\theta}), \tag{6.5}$$

where D_k is the diffusivity of the corresponding k^{th} major scalar and the drift coefficient, A_k, acts as the source term in the reference space. It may be recalled that the CMC equations are derived by conditional averaging of (minor) chemical species by the (major) scalars like mixture fraction and sensible enthalpy. On the other hand, MMC implies the conditional averaging of *all* scalars represented by (6.1) by using the transport equation (6.5) for the reference variables, instead of the major scalars themselves. The procedure of deriving the doubly-conditioned CMC equations by Kronenburg (2004) is followed here. Consistent with the CMC notation, the instantaneous scalar concentration, ϕ_I, can be split into the mean conditioned on the reference space, X_I and the fluctuation, X_I'' as

$$\phi_I = X_I(\boldsymbol{\xi}) + X_I'', \tag{6.6}$$

where $X_I(\boldsymbol{\xi})$ is the familiar mapping function realised as the conditional average in the reference space, i.e. $X_I(\boldsymbol{\xi}) = \langle\phi_I|\boldsymbol{\theta} = \boldsymbol{\xi}\rangle$. The spatio-temporal dependence in (6.6) has been omitted for clarity. Substituting (6.6) in (6.1), applying the chain rule of differentiation and using the conservation equation (6.5) for reference variables, we get a form for the MMC equation consistent with the CMC as

$$\begin{aligned}\langle\rho|\boldsymbol{\xi}\rangle\tfrac{\partial X_I}{\partial t} + \langle\rho\mathbf{u}|\boldsymbol{\xi}\rangle\cdot\boldsymbol{\nabla}X_I \;&=\; \langle\omega_I|\boldsymbol{\xi}\rangle - \langle\rho|\boldsymbol{\xi}\rangle A_k\tfrac{\partial X_I}{\partial\xi_k} + \\ &\quad \langle\rho|\boldsymbol{\xi}\rangle\langle D_I\boldsymbol{\nabla}\theta_k\cdot\boldsymbol{\nabla}\theta_l|\boldsymbol{\xi}\rangle\tfrac{\partial^2 X_I}{\partial\xi_k\partial\xi_l} + e_{q,MMC} + e_{y,MMC}\end{aligned} \tag{6.7}$$

with

$$e_{q,MMC} = \left\langle \boldsymbol{\nabla} \cdot [\rho D_I \boldsymbol{\nabla} X_I] + \rho D_I \boldsymbol{\nabla}\theta_k \cdot \boldsymbol{\nabla} \frac{\partial X_I}{\partial \xi_k} + \boldsymbol{\nabla} \cdot [\rho (D_I - D_k) \boldsymbol{\nabla}\theta_k] \frac{\partial X_I}{\partial \xi_k} \right| \boldsymbol{\xi} \right\rangle , \tag{6.8}$$

and

$$e_{y,MMC} = -\left\langle \rho \frac{\partial X_I''}{\partial t} + \rho \mathbf{u} \cdot \boldsymbol{\nabla} X_I'' - \boldsymbol{\nabla} \cdot [\rho D_I \boldsymbol{\nabla} X_I''] \right| \boldsymbol{\xi} \right\rangle \tag{6.9}$$

Equations (6.7)-(6.9) represent the generalised system of MMC equations. Term $\langle D_I \boldsymbol{\nabla}\theta_k \cdot \boldsymbol{\nabla}\theta_l | \boldsymbol{\xi} \rangle$ occurs as a coefficient of diffusion in reference space in (6.7), analogous to $\langle N_{ij} | \boldsymbol{\eta}_{maj} \rangle$ in the CMC equation. Therefore, it follows from the aforementioned correspondence between (6.3) and (6.4) that

$$B_{kl} = \langle D_I \boldsymbol{\nabla}\theta_k \cdot \boldsymbol{\nabla}\theta_l | \boldsymbol{\xi} \rangle. \tag{6.10}$$

Similarly, A_k is the coefficient of the term signifying convection/drift in the reference space in the above MMC equation. For clarity of presentation, the notation for the MMC drift and diffusion coefficients is kept consistent with the standard MMC form by Klimenko & Pope (2003). It is understood that each instance of A_k (or B_{kl}) refers to the drift (or diffusion) of the I^{th} scalar in the reference space.

Primary closure hypothesis for the $e_{y,MMC}$ term in (6.7) follows the same arguments as that for the corresponding CMC equation, namely that the set of conditioning reference scalars is large enough for the conditional fluctuations to be negligible. Hence, $e_{y,MMC}$ is easily set to zero for a sufficiently high dimensionality, n_r, of the reference manifold. Closure for $e_{q,MMC}$ also follows the CMC logic of neglecting the (first-order) gradients in the reference space, which are negligible at stoichiometric composition compared to the reactive-diffusive terms in (6.7). It should be noted that $e_{q,MMC}$ also contains the important differential diffusion term, $\boldsymbol{\nabla} \cdot [\rho(D_I - D_k)\boldsymbol{\nabla}\theta_k]\partial X_I/\partial\xi_k$, which may not be negligible for species whose Lewis number deviates significantly from unity. For the present MMC implementation, only the H-radical (and to a minor extent, H_2) have Lewis numbers appreciably lower than unity and the differential diffusion term ideally should not be neglected for them. However, the caveat is that their concentrations are also two-to-three orders of magnitude less than those of the other species (cf. Fig. 5.4) and, therefore, their first-order derivatives in the reference space will have a negligible influence on the primary MMC equation. Hence, setting $e_{q,MMC} = 0$ and $e_{y,MMC} = 0$ in the generalised MMC equation (6.7) results in the familiar form given by (5.3).

A.2 Derivation of N_{ij} in terms of B_{kl}

Using the general definition from (2.35), the scalar dissipation for a pair of major scalars denoted by indices i and j can be written in the standard repeated-index notation as

$$N_{ij} = D_I \frac{\partial \phi_i}{\partial x_p}\frac{\partial \phi_j}{\partial x_p} \qquad \forall \;\; p \in \{1, 2, 3\} \tag{6.11}$$

where repetition of index p denotes summation over it. Assuming a sufficiently large reference manifold such that fluctuations around the means conditioned on $\boldsymbol{\xi}$ are negligible, the scalars in (6.11) can be approximated by their conditional averages, i.e. $\phi_i \simeq \langle \phi_i | \boldsymbol{\theta} \rangle = X_i(\boldsymbol{\theta})$. In mathematical terms,

$$N_{ij} = D_I \frac{\partial X_i(\boldsymbol{\theta})}{\partial x_p} \frac{\partial X_j(\boldsymbol{\theta})}{\partial x_p}. \tag{6.12}$$

The mapping functions, X_i and X_j, are continuous and differentiable functions of the set of reference variables, $\boldsymbol{\theta}$. Therefore, applying the chain rule of differentiation on the mapping functions in (6.12) and denoting summation by repeated indices, we get

$$\frac{\partial X_i(\boldsymbol{\theta})}{\partial x_p} = \frac{\partial X_i}{\partial \theta_1} \frac{\partial \theta_1}{\partial x_p} + \frac{\partial X_i}{\partial \theta_2} \frac{\partial \theta_2}{\partial x_p} + .. = \frac{\partial X_i}{\partial \theta_k} \frac{\partial \theta_k}{\partial x_p} \tag{6.13}$$

and

$$\frac{\partial X_j(\boldsymbol{\theta})}{\partial x_p} = \frac{\partial X_j}{\partial \theta_1} \frac{\partial \theta_1}{\partial x_p} + \frac{\partial X_j}{\partial \theta_2} \frac{\partial \theta_2}{\partial x_p} + .. = \frac{\partial X_j}{\partial \theta_l} \frac{\partial \theta_l}{\partial x_p}. \tag{6.14}$$

The expanded gradient terms from (6.13) and (6.14) can be substituted back into (6.12) and re-arranged to obtain

$$N_{ij} = D_I \frac{\partial \theta_k}{\partial x_p} \frac{\partial \theta_l}{\partial x_p} \cdot \frac{\partial X_i}{\partial \theta_k} \frac{\partial X_j}{\partial \theta_l}. \tag{6.15}$$

Conditionally averaging (6.12) throughout with respect to the reference manifold, neglecting the conditional fluctuations of scalar dissipation, i.e. $N_{ij} \simeq \langle N_{ij} | \boldsymbol{\theta} = \boldsymbol{\xi} \rangle$ and replacing the repeated indices with the gradient notation gives,

$$N_{ij} = \langle D_I \boldsymbol{\nabla} \theta_k \cdot \boldsymbol{\nabla} \theta_l | \boldsymbol{\theta} = \boldsymbol{\xi} \rangle \frac{\partial X_i}{\partial \xi_k} \frac{\partial X_j}{\partial \xi_l}. \tag{6.16}$$

The term within the $\langle \rangle$ operator is identical to the expression for the MMC diffusion coefficient, B_{kl}, defined in (6.10). Finally, substituting B_{kl} for this term in (6.16) gives the important identity relating the scalar dissipation rate variable with the MMC diffusion coefficient,

$$N_{ij} = B_{kl}\frac{\partial X_i}{\partial \xi_k}\frac{\partial X_j}{\partial \xi_l}. \tag{6.17}$$

A.3 Derivation of a_k model

Consistent incorporation of the velocity model in the MMC formulation requires consistency with the governing equation for the scalar mapping functions and the reference PDF transport, represented by (5.3) and (5.2), respectively. This consistency can be acheived by substituting the aforesaid convective velocity model in the reference PDF equation and deriving the drift coefficient, A_k, in terms of the diffusion coefficients, B_{kl}, and the velocity model, $\mathbf{U}$, where the reference PDF is already presumed to be joint-Gaussian (Klimenko & Pope, 2003).

For the present case of a joint Gaussian reference PDF with zero mean and unity variance, its temporal derivative in (5.2) drops out, i.e. $\partial\bar{\rho}P_{\boldsymbol{\theta}}/\partial t = 0$. Similarly, the reference PDF remains unchanged in physical space and can be taken out of the spatial gradient term. Furthermore, the ensemble averaged density term, $\bar{\rho}$ is invariant in the reference space and can be taken out of the partial derivatives with respect to reference variables. Therefore, (5.2) takes the following form:

$$P_{\boldsymbol{\theta}}\boldsymbol{\nabla}\cdot(\mathbf{U}\bar{\rho}) + \bar{\rho}\frac{\partial A_k P_{\boldsymbol{\theta}}}{\partial \xi_k} + \bar{\rho}\frac{\partial^2 B_{kl} P_{\boldsymbol{\theta}}}{\partial \xi_k \partial \xi_l} = 0. \tag{6.18}$$

Since $P_{\boldsymbol{\theta}}$ is the PDF of n_r uncorrelated Gaussian reference variables, each with zero mean and unity variance, it can be mathematically expressed as,

$$P_{\boldsymbol{\theta}} = \frac{1}{2\pi} \cdot exp\left(-\frac{1}{2}\sum_{p=1}^{n_r}\xi_p^2\right) \tag{6.19}$$

and its first- and second-order derivatives with respect to arbitrary reference variables ξ_k and ξ_l are given by,

$$\frac{\partial P_{\boldsymbol{\theta}}}{\partial \xi_k} = -\xi_k P_{\boldsymbol{\theta}}, \qquad \frac{\partial^2 P_{\boldsymbol{\theta}}}{\partial \xi_k \partial \xi_l} = \left(\xi_k \xi_l - \boldsymbol{\delta}_{kl}\right) P_{\boldsymbol{\theta}}. \tag{6.20}$$

Here, $\boldsymbol{\delta}_{kl}$ is the Kronecker delta function. Using the product rule of differentiation and the identities in (6.20), the derivatives in the second and third terms of (6.18) can be expanded as,

$$\frac{\partial A_k P_{\boldsymbol{\theta}}}{\partial \xi_k} = P_{\boldsymbol{\theta}} \frac{\partial A_k}{\partial \xi_k} - P_{\boldsymbol{\theta}} \xi_k A_k \tag{6.21}$$

$$\frac{\partial^2 B_{kl} P_{\boldsymbol{\theta}}}{\partial \xi_k \partial \xi_l} = P_{\boldsymbol{\theta}} \frac{\partial^2 B_{kl}}{\partial \xi_k \partial \xi_l} + P_{\boldsymbol{\theta}} \left(\xi_k \xi_l - \boldsymbol{\delta}_{kl}\right) B_{kl} \tag{6.22}$$

Substituting all the derivative terms in reference space in (6.18) with the expressions given by (6.21) and (6.22) and cancelling $P_{\boldsymbol{\theta}}$ throughout,

$$\frac{1}{\bar{\rho}} \boldsymbol{\nabla} \cdot \left(\mathbf{U}\bar{\rho}\right) + \frac{\partial A_k}{\partial \xi_k} - \xi_k A_k + \frac{\partial^2 B_{kl}}{\partial \xi_k \partial \xi_l} + B_{kl} \left(\xi_k \xi_l - \boldsymbol{\delta}_{kl}\right) = 0. \tag{6.23}$$

Without any loss of generality, the above equation can be further simplified by assuming a convenient (but unclosed) form for the drift coefficient, A_k, given by

(5.5) in the main text (Klimenko & Pope, 2003). Substituting the expression for the MMC drift coefficient from (5.5) in (6.23) and cancelling out the redundant terms results in the generalised form of the equation for modelling the a_k term. This is given by (5.6) in the main text and is reproduced here

$$\frac{1}{\bar{\rho}}\boldsymbol{\nabla}\cdot(\mathbf{U}\bar{\rho})+\frac{\partial a_k}{\partial \xi_k}-\xi_k a_k=0. \tag{6.24}$$

As (5.6) suggests, the a_k term represents the contribution of the velocity modelling to the MMC drift coefficient and its closure is discussed in Sec. 5.2.5.

Bibliography

BARLOW, R.S. & KARPETIS, A.N. 2005*a* Measurements of scalar variance, scalar dissipation, and length scales in turbulent piloted methane/air jet flames. *Flow Turb. Combust.* **72**, 427–448.

BARLOW, R.S. & KARPETIS, A.N. 2005*b* Scalar length scales and spatial averaging effects in turbulent piloted methane/air jet flames. *Proc. Combust. Inst.* **30**, 673–680.

BATCHELOR, G.K. 1959 Small scale variation of convected quantities like temperature in a turbulent fluid. *J. Fluid Mech.* **5**, 113–133.

BATCHELOR, G.K. & TOWNSEND, A.A. 1949 The nature of turbulent motion at large wave-numbers. *Proc. R. Soc. Lond. A* **199**, 238–55.

BEER, J.M. 2000 Combustion technology developments in power generation in response to environmental challenges. *Prog. Energy Combust. Sci.* **26**, 301–327.

BILGER, R.W. 1976*a* The structure of diffusion flames. *Combust. Sci. Technol.* **13**, 150–170.

BILGER, R.W. 1976*b* Turbulent jet diffusion flames. *Prog. Energy Combust. Sci.* **1**, 87–109.

Bilger, R.W. 1980 Turbulent flows with nonpremixed reactants. In *Topics in Applied Physics: Turbulent Reacting Flows* (ed. P.A. Libby & F.A. Williams), pp. 65–111. Springer-Verlag.

Bilger, R.W. 1988 Structure of nonpremixed flames. *Proc. Combust. Inst.* **22**, 475–488.

Bilger, R.W. 1989 Turbulent diffusion flames. *Annual Review of Fluid Mechanics* **21**, 101–135.

Bilger, R.W. 1992 Advanced laser diagnostics: implications of recent results for advanced combustor models. In *Aerothermodynamics in Combustors* (ed. R.S.L. Lee, J.H. Whitelaw & T.S. Wung), pp. 3–16. Springer-Verlag.

Bilger, R.W. 2004 Some aspects of scalar dissipation. *Flow Turb. Combust.* **72**, 93–114.

Bilger, R.W., Pope, S.B., Bray, K.N.C. & Driscoll, J.F. 2005 Paradigms in turbulent combustion research. *Proc. Combust. Inst.* **30**, 21–42.

Bilger, R.W., Stårner, S.H. & Kee, R.J. 1990 On reduced mechanisms for methane air combustion in nonpremixed flames. *Combustion and Flame* **80** (2), 135–149.

Boersma, B.J. 1999 Direct numerical simulation of a turbulent reacting jet. In *Ann. Res. Briefs,* **CTR**, pp. 59–72. Stanford University.

Bogdanoff, D.W. 1983 Compressibility effects in turbulent shear layers. *AIAA J.* **21**, 926–927.

Borghi, R. 1988 Turbulent combustion modelling. *Prog. Energy Combust. Sci.* **14**, 245–292.

Bray, K.N.C. 1996 The challenge of turbulent combustion. *Proc. Combust. Inst.* **26**, 1–26.

Bray, K.N.C. & Peters, N. 1993 Laminar flamelets in turbulent flames. In *Turbulent Reacting Flows* (ed. P.A. Libby & F.A. Williams), pp. 63–113. Springer-Verlag.

Brethouwer, G. & Nieuwstadt, F.T.M. 2001 DNS of mixing and reaction of two species in a turbulent channel flow: a validation of the conditional moment closure. *Flow Turb. Combust.* **66**, 209–239.

Buch, K.A. & Dahm, W.J.A. 1996 Experimental study of the fine-scale structure of conserved scalar mixing in turbulent shear flows. Part 1. *J. Fluid Mech.* **317**, 21–71.

Buch, K.A. & Dahm, W.J.A. 1998 Experimental study of the fine-scale structure of conserved scalar mixing in turbulent shear flows. Part 2. *J. Fluid Mech.* **364**, 1–29.

Buckmaster, R.S., Clavin, P., Linana, A., Matalon, M., Peters, N., Sivashinky, G. & Williams, F.A. 2005 Combustion theory and modeling. *Proc. Combust. Inst.* **30**, 1–19.

Cant, R.S. 1999 Direct numerical simulation of premixed turbulent flames. *Phil. Trans. Royal Soc.* **357**, 3583–3604.

Cant, R.S. & Mastorakos, E. 2008 *An introduction to turbulent reacting flows*. Imperial College Press, London.

Cha, C.M., Kosály, G. & Pitsch, H. 2000 Doubly-conditional moment closure modelling of turbulent nonpremixed combustion. In *Ann. Res. Briefs,* **CTR**, pp. 129–140. Stanford University.

Cha, C.M., Kosály, G. & Pitsch, H. 2001 Modeling extinction and reignition in turbulent nonpremixed combustion using a doubly-conditional moment closure approach. *Phys. Fluids* **13** (12), 3824–3834.

Chen, H., Chen, S. & Kraichnan, R. H. 1989 Probability distribution of a stochastically advected scalar field. *Phys. Rev. Lett.* **63** (24), 2657–2660.

Cleary, M.J. & Kent, J. H. 2005 Modelling of species in hood fires by conditional moment closure. *Combust. Flame* **143** (4), 357–368.

Cleary, M.J. & Kronenburg, A. 2007*a* Hybrid multiple mapping conditioning on passive and reactive scalars. *Combust. Flame* **151** (4), 623–638.

Cleary, M.J. & Kronenburg, A. 2007*b* Multiple mapping conditioning for extinction and re-ignition in turbulent diffusion flames. *Proc. Combust. Inst.* **31**, 1497–1505.

Corrsin, S. 1951 On the spectrum of isotropic temperature fluctuations in isotropic turbulence. *J. Appl. Phys.* **22**, 469–473.

Dahm, W.J.A. & Southerland, K.B. 1997 Experimental assessment of Taylor's hypothesis and its applicability to dissipation estimates in turbulent flows. *Phys. Fluids* **9** (7), 2101–2107.

Dahm, W.J.A. & Southerland, K.B. 1999 Quantitative flow visualization via fully-resolved four-dimensional spatio-temporal imaging. In *Flow Visualization: Techniques and Examples* (ed. A. Smits & T.T. Lim), pp. 231–258. Imperial College Press, London.

Dahm, W.J.A., Southerland, K.B. & Buch, K.A. 1991 Direct, high resolution, four-dimensional measurements of the fine scale structure of Sc>>1 molecular mixing in turbulent flows. *Phys. Fluids A* **3** (5), 1115–1127.

Devaud, C.B. & Bray, K.N.C. 2003 Assessment of the applicability of conditional moment closure to a lifted turbulent flame: first order model. *Combust. Flame* **132** (1-2), 102–114.

Dimotakis, P. E. 2005 Turbulent mixing. *Ann. Rev. Fluid Mech.* **37**, 329–356.

Donzis, D. A., Sreenivasan, K. R. & Yeung, P. K. 2005 Scalar dissipation rate and dissipative anomaly in isotropic turbulence. *J. Fluid Mech.* **532**, 199–216.

Dopazo, C. 1975 Probability density approach for a turbulent axisymmetric heated jet, centerline evolution. *Phys. Fluids* **18(4)**, 397–404.

Frisch, U. 1991 From global scaling, *a la* Kolmogorov, to local multifractal scaling in fully developed turbulence. *Proc. R. Soc. Lond. A* **434**, 89–99.

Frisch, U. 1995 *Turbulence: The Legacy of AN Kolmogorov*. Cambridge University Press.

Frisch, U. & Vergassola, M. 1991 A prediction of the multifractal model: the intermediate dissipation range. *Europhys. Lett.* **14**, 439–444.

Gibson, C. H. 1991 Kolmogorov similarity hypotheses for scalar fields: sampling intermittent turbulent mixing in the ocean and galaxy. *Proc. R. Soc. Lond. A* **434**, 149–164.

Girimaji, S. S. 1992 On the modeling of scalar diffusion in isotropic turbulence. *Phys. Fluids A* **4** (11), 2529–2537.

Golub, G. H. & Van-Loan, C. F. 1996 *Matrix Computations*, 3rd edn. Johns Hopkins University Press.

Grant, H. L., Stewart, R. W. & Moilliet, A. 1962 Turbulent spectra from a tidal channel. *J. Fluid Mech.* **12**, 241–268.

Hanjalic, K. 1994 Advanced turbulence closure models: a view of current status and future prospects. *Int. J. Heat and Fluid Flow* **15**, 178–203.

Hawkes, E.R., Sankaran, R., Sutherland, J.C. & Chen, J.H. 2006 Scalar mixing in direct numerical simulations of temporally evolving plane jet flames with skeletal CO/H2 kinetics. *Proc. Combust. Inst.* **31**, 1633–1640.

Haworth, D. C., Drake, M. C., Pope, R. J. & Blint, R. J. 1988 The importance of time-dependent flame structures in stretched laminar flamelet models for turbulent jet diffusion flames. *Proc. Combust. Inst.* **22**, 589–597.

int Hout, K.J. & Welfert, B.D. 2007 Stability of ADI schemes applied to convection-diffusion equations with mixed derivative terms. *Appl. Numeric. Math.* **57** (1), 19–35.

Janicka, J. & Sadiki, A. 2005 Large eddy simulation of turbulent combustion systems. *Proc. Combust. Inst.* **30**, 537–547.

Kakhi, M. 1994 The transported probability density function approach for predicting turbulent combustion flows. PhD thesis, Imperial College London, Dept. Mech. Eng., Exhibition rd, London, SW7 2AZ.

Karpetis, A.N. & Barlow, R.S. 2002 Measurement of scalar dissipation in a turbulent piloted methane/air flame. *Proc. Combust. Inst.* **29**, 1929–1936.

Kempf, A., Lindstedt, R.P. & Janicka, J. 2006 Large eddy simulation of a bluff-body stabilized nonpremixed flame. *Proc. Combust. Inst.* **144**, 170–189.

Kerstein, A.R. 2002 Turbulence in combustion processes: modelling challenges. *Proc. Combust. Inst.* **29**, 1763–1773.

Kim, G., Kang, S., Kim, Y., Bilger, R.W. & Cleary, M.J. 2007 Conditional moment closure and transient flamelet modelling for detailed structure and NOx formation characteristics of turbulent nonpremixed jet and recirculating flames. *Combust. Theory Model.* **11** (4), 527–552.

Kim, R.W. & Williams, F.A. 1997 Extinction of diffusion flames with nonunity lewis numbers. *Journal of Eng. Math.* **31**, 101–118.

Kim, S.H. 2002 On the conditional variance and covariance equations for second-order conditional moment closure. *Phys. Fluids* **14** (6), 2011–2014.

Kim, S.H., Choi, C.H. & Huh, K.Y. 2004 Second-order conditional moment closure modeling of a turbulent $CH_4/H_2/N_2$ jet diffusion flames. *Proc. Combust. Inst.* **29**, 2131–2137.

Kim, S.H. & Huh, K.Y. 2002 Use of the conditional moment closure model to predict NO formation in a turbulent CH_4/H_2 flame over a bluff-body. *Combust. Flame* **130**, 94–111.

Kim, S.H., Huh, K.Y. & Bilger, R.W. 2002 Second-order conditional moment closure modeling of local extinction and reignition in turbulent non-premixed Hydrocarbon flames. *Proc. Combust. Inst.* **29**, 2131–2137.

Kim, S. H., Tao, L. & Huh, K. Y. 2000 Application of the elliptic conditional moment closure model to a two-dimensional nonpremixed methanol bluff-body flame. *Combust. Flame* **120** (1), 75–90.

Klimenko, A.Y. 1990 Multi-component diffusion of various mixtures in turbulent flow. *Fluid Dynamics* **25**, 327–334.

Klimenko, A.Y. 2003*a* MMC modelling and fluctuations of the scalar dissipation. In *Australian Symposium on Combustion*. Monash University, Melbourne, Australia.

KLIMENKO, A.Y. 2003*b* Modern modelling of turbulent non-premixed combustion and reduction of pollutant emission. In *CleanAir VII Symposium*. Lisbon, Portugal.

KLIMENKO, A.Y. 2004 Matching the conditional variance as a criterion for selecting parameters in the simplest MMC models. *Phys. Fluids* **16**, 4754–4757.

KLIMENKO, A.Y. 2005 Matching conditional moments in PDF modelling of non-premixed combustion. *Combust. Flame* **143** (4), 369–385.

KLIMENKO, A.Y. & BILGER, R.W. 1999 Conditional moment closure for turbulent combustion. *Prog. Energy Combust. Sci.* **25**, 595–687.

KLIMENKO, A.Y. & POPE, S.B. 2003 The modeling of turbulent reactive flows based on multiple mapping conditioning. *Phys. Fluids* **15** (7), 1907–1925.

KOLMOGOROV, A.N. 1941 The local structure of turbulence in incompressible viscous fluid for very large Reynolds numbers. *C. R. Dokl. Akad. Sci.* **URSS 30**, 301–305.

KOLMOGOROV, A.N. 1962 A refinement of previous hypotheses concerning the local structure of turbulence in a viscous incompressible fluid at high Reynolds numbers. *J. Fluid Mech.* **13**, 82–85.

KRONENBURG, A. 2004 Double conditioning of reactive scalar transport equations in turbulent nonpremixed flames. *Phys. Fluids* **16** (7), 2640–2648.

KRONENBURG, A. & CLEARY, M.J. 2008 Multiple mapping conditioning for flames with partial premixing. *Combust. Flame* **155** (1-2), 215–231.

KRONENBURG, A. & KOSTKA, M. 2005 Modeling extinction and reignition in turbulent flames. *Combust. Flame* **143** (4), 342–356.

KRONENBURG, A. & PAPOUTSAKIS, A.E. 2005 Conditional moment closure modelling of extinction and re-ignition in turbulent non-premixed flames. *Proc. Combust. Inst.* **30**, 759–766.

KUO, K.K. 1986 *Principles of Combustion*, 2nd edn. Singapore: John Wiley and Sons, Inc.

KUSHNIR, D., GALUN, M. & BRANDT, A. 2006*a* Fast multi-scale clustering and manifold identification. *Pattern Recognition* **39**, 1876–1891.

KUSHNIR, D., SCHUMACHER, J. & BRANDT, A. 2006*b* Geometry of intensive scalar dissipation events in turbulence. *Phys. Rev. Lett.* **97** (124502), 1–4.

KUZNETSOV, V.R. & SABELNIKOV, V.A. 1989 *Turbulence and Combustion*. Hemishphere, NY.

LELE, S.K. 1992 Compact finite difference schemes with spectral-like resolution. *J. Comput. Phys.* **103**, 16–42.

LESLIE, D. C. 1972 *Developments in the theory of turbulence*. Clarendon Press Oxford.

LIBBY, P. A. & WILLIAMS, F. A., ed. 1980 *Topics in Applied Physics: Turbulent Reacting Flows*. Springer-Verlag.

LINÁN, A. 1974 The asymptotic structure of counterflow diffusion flames for large activation energies. *Acta Astronaut.* **1** (7–8), 1007–1039.

LINDSTEDT, R.P. 2000 The modelling of direct chemical kinetic effects in turbulent flames. *Proc. Instn. Mech. Engrs.* **214**, 177–189.

LUMLEY, J.L. 1978 Computational modeling of turbulent flows. *Advances in Applied Mech.* **18**, 123–173.

Mathieu, J. & Scott, J. 2000 *An introduction to turbulent flow*. Cambridge University Press.

Mauss, F., Keller, D. & Peters, N. 1990 A Lagrangian simulation of flamelet extinction and re-ignition in turbulent jet diffusion flames. *Proc. Combust. Inst.* **23**, 693–698.

McBride, B.J., Gordon, S. & Reno, M.A. 1995 Coefficients for calculating thermodynamic and transport properties of individual species. *Tech. Rep.*. NASA.

Meneveau, C. & Sreenivasan, K.R. 1991 The multifractal nature of turbulent energy dissipation. *J. Fluid Mech.* **224**, 429–484.

Meyer, M.P. 2001 The Application of Detailed and Systematically Reduced Chemistry to Transient Laminar Flames. PhD thesis, Imperial College London, Dept. Mech. Eng., Exhibition rd, London, SW7 2AZ.

Mizobuchi, Y., Shinjo, J., Ogawa, S. & Takeno, T. 2005 A numerical study on the formation of diffusion flame islands in a turbulent Hydrogen jet lifted flame. *Proc. Combust. Inst.* **30**, 611–619.

Monin, A.S. & Yaglom, A.M. 1971 *Statistical fluid mechanics; mechanics of turbulence*, 1st edn. MIT Press.

Mortensen, M. 2005 Consistent modeling of scalar mixing for presumed, multiple parameter probability density functions. *Phys. Fluids* **17** (018106), 1–4.

Mortensen, M. & Andersson, B. 2005 Presumed mapping functions for Eulerian modelling of turbulent mixing. *Flow Turb. Combust.* **76**, 199–219.

Navarro-Martinez, S. & Kronenburg, A. 2007 LES-CMC simulations of a turbulent bluff-body flame. *Proc. Combust. Inst.* **31**, 1721–1728.

NELKIN, M. 1994 Universality and scaling in fully developed turbulence. *Adv. Phys.* **43** (2), 143–181.

NEWMAN, G.R., LAUNDER, B.E. & LUMLEY, J.L. 1981 Modelling the behaviour of homogeneous scalar turbulence. *J. Fluid Mech.* **11**, 217–232.

NOULLEZ, A., WALLACE, G., LEMPERT, W., MILES, R.B. & FRISCH, U. 1997 Transverse velocity increments in turbulent flow using the RELIEF technique. *J. Fluid Mech.* **339**, 287–307.

OBERLACK, M., ARLITT, R. & PETERS, N. 2000 On stochastic Damköhler number variations in a homogeneous flow reactor. *Combust. Theory Model.* **4**, 495–509.

OBOUKHOV, A.M. 1949 Struktura temperaturnovo polia v turbulentnom potoke. *Izv. Akad. Nauk SSSR Ser. Geofiz* **3**, 59.

O'BRIEN, E.E. 1980 The probability density function (PDF) approach to reacting turbulent flows. In *Topics in Applied Physics: Turbulent Reacting Flows* (ed. P.A. Libby & F.A. Williams), pp. 185–218. Springer-Verlag.

PANTANO, C. 2004 Direct simulation of non-premixed flame extinction in a methane-air jet with reduced chemistry. *J. Fluid Mech.* **514**, 231–270.

PANTANO, C., SARKAR, S. & WILLIAMS, F.A. 2003 Mixing of a conserved scalar in a turbulent reacting shear layer. *J. Fluid Mech.* **481**, 291–328.

PAPAMOSCHOU, D. & ROSHKO, A. 1988 The compressible turbulent shear layer: an experimental study. *J. Fluid Mech.* **197**, 453–477.

PETERS, N. 1984 Laminar diffusion flamelet models in non-premixed turbulent combustion. *Prog. Energy Combust. Sci.* **10** (3), 319–339.

PETERS, N. 1985 Numerical and asymptotic analysis of systematically reduced reaction schemes for hydrocarbon flames. In *Lecture Notes in Physics*, pp. 90–109. Springer.

PETERS, N. 1991 *Reduced kinetic mechanisms and asymptotic approximations for Methane-Air flames: Chapter 3*. Springer.

PETERS, N. 2000 *Turbulent Combustion*. Cambridge University Press.

PITSCH, H. 2000 Unsteady flamelet modelling of differential diffusion in turbulent jet flames. *Combust. Flame* **123**, 358–374.

PITSCH, H., CHA, C.M. & FEDOTOV, S. 2003 Flamelet modelling of non-premixed turbulent combustion with local extinction and re-ignition. *Combust. Theory and Modelling* **7**, 317–332.

PITTS, W.M., RICHARDS, C.D. & LEVENSON, M.S. 1999 Large- and scall-scale structures and their interactions in an axisymmetric jet. *Tech. Rep.* 6393. NIST.

POINSOT, T. & VEYNANTE, D. 2001 *Theoretical and Numerical Combustion*, 2nd edn. Philadelphia: R. T. Edwards Inc.

POPE, S.B. 1976 The implications of the probability equations for turbulent combustion models. *Combust. Flame* **27**, 299–312.

POPE, S.B. 1985 PDF methods for turbulent reactive flows. *Prog. Energy Combust. Sci.* **11**, 119–192.

POPE, S.B. 1991 Mapping closures for turbulent mixing and reaction. *Theor. Comput. Fluid Dyn.* **2**, 255–270.

POPE, S.B. 2000 *Turbulent Flows*, 1st edn., pp. 222–237. Cambridge University Press.

Pope, S.B. 2004 10 questions concerning the large eddy simulation of turbulent flows. *New J. Phys.* **6(35)**, 1367–2630.

Energy Review Report, U.K. 2006 The energy challenge. Department of Trade and Industry, HM Govt.

Rogerson, J.W., Kent, J.H. & Bilger, R.W. 2005 Conditional moment closure in a bagasse-fired boiler. *Proc. Combust. Inst.* **31**, 2805–2811.

Roomina, M.R. & Bilger, R.W. 2001 Conditional moment closure (CMC) predictions of a turbulent methane-air jet flame. *Combust. Flame* **61**, 87–102.

Saddoughi, S.G. & Veeravalli, S.V. 1994 Local isotropy in turbulent boundary layers at high Reynolds numbers. *J. Fluid Mech.* **268**, 333–372.

Schumacher, J., Sreenivasan, K.R. & Yeung, P.K. 2005 Very fine structures in scalar mixing. *J. Fluid Mech.* **531**, 113–122.

Seshadri, K. & Peters, N. 1988 Asymptotic structure and extinction of Methane-Air diffusion flames. *Combust. Flame* **73**, 23–44.

She, Z.-S. 1991 Physical model of intermittency in turbulence: near-dissipation-range non-Gaussian statistics. *Phys. Rev. Lett.* **66** (5), 600–603.

She, Z.-S., Chen, S., Doolen, G., Kraichnan, R.H. & Orszag, S.A. 1993 Reynolds number dependence of isotropic Navier-Stokes turbulence. *Phys. Rev. Lett.* **70** (21), 3251–3254.

She, Z.-S., Jackson, E., & Orszag, S.A. 1990 Intermittent vortex structures in homogeneous isotropic turbulence. *Nature* **344**, 226–228.

Sloan, D.G., Smith, P.J. & Smoot, L.D. 1986 Modeling of swirl in turbulent flow systems. *Prog. Enrg. and Combust. Science* **12**, 163–250.

Smith, N.S.A., Bilger, R.W., Carter, C.D., Barlow, R.S. & Chen, J.-Y. 1995 A comparison of CMC and PDF modelling predictions with experimental Nitric Oxide LIF/Raman measurements in a turbulent H2 jet flame. *Combust. Sci. Technol.* **105**, 357–375.

Smith, N.S.A., bilger, R.W. & Chen, J.-Y. 1993 Modelling of nonpremixed Hydrogen jet flames using a conditional moment closure method. *Proc. Combust. Inst.* **24**, 263–269.

Smooke, M.D. & Giovangigli, V. 1991 *Reduced kinetic mechanisms and asymptotic approximations for Methane-Air flames: Chapter 1*, pp. 1–28. Springer.

Spalding, D.B. 1971 Concentration fluctuations in a round turbulent free jet. *Chem. Engng. Sci.* **26** (1), 95–107.

Speziale, C.G. 1995 A review of Reynolds stress models for turbulent shear flows. *Tech. Rep.* 95-15. ICASE, NASA Langley, Virginia.

Sreedhara, S. & Lakshmisha, N. 2000 Direct numerical simulation of autoignition in a non-premixed turbulent medium. *Proc. Combust. Inst.* **28**, 25–34.

Sreenivasan, K.R. 1991 Fractals and multifractals in fluid turbulence. *Ann. Rev. Fluid Mech.* **23**, 539–600.

Sreenivasan, K.R. 2004 Possible effects of small-scale intermittency in turbulent reacting flows. *Flow Turb. Combust.* **72**, 115–131.

Sreenivasan, K.R. & Antonia, R.A. 1997 The phenomenology of small-scale turbulence. *Ann. Rev. Fluid Mech.* **29**, 435–472.

Sreenivasan, K.R. & Meneveau, C. 1988 Singularities of the equations of fluid motion. *Phy. Rev. A* **38** (12), 6287–6295.

SREENIVASAN, K.R. & STOLOVITZKY, G. 1996 Statistical dependence of inertial range properties on large scales in high-Reynolds-number shear flow. *Phys. Rev. Lett.* **77** (11), 2218–2221.

SU, L.K. 1998 Measurements of the three-dimensional scalar dissipation rate in gas-phase planar turbulent jets. In *Ann. Res. Briefs,* **CTR**, pp. 35–46. Stanford University.

SU, L.K. & CLEMENS, N.T. 2003 The structure of fine-scale scalar mixing in gas-phase planar turbulent jets. *J. Fluid Mech.* **488**, 1–29.

SWAMINATHAN, N. & BILGER, R.W. 1999 Study of the conditional covariance and variance equations for second order conditional moment closure. *Phys. Fluids* **11** (9), 2679–2695.

SWAMINATHAN, N. & BRAY, K.N.C. 2005 *Combust. Flame* **143**, 549–565.

TENNEKES, H. & LUMLEY, J.L. 1974 *A first course in turbulence*. MIT Press.

THEVENIN, D. 2005 Three-dimensional direct simulations and structure of expanding turbulent methane flames. *Proc. Combust. Inst.* **30**, 629–637.

TSURIKOV, M.S. & CLEMENS, N.T. 2002 The structure of dissipative scales in axisymmetric turbulent gas-phase jets. *AIAA J.* **0164**, 1–16.

TURNS, R.S. 1996 *An introduction to combustion: Concepts and Applications*. New York: McGraw Hill.

TURNS, S.R. 2000 *An Introduction to Combustion: Concepts and Applications*, 2nd edn. New York: McGraw Hill.

VAROQUIE, B., LEGIER, J.P., LACAS, F., VEYNANTE, D. & POINSOT, T. 2002 Experimental analysis and large eddy simulation to determine the response of non-premixed flames submitted to acoustic forcing. *Proc. Combust. Inst.* **29**, 1965–1970.

Vedula, P., Yeung, P. K. & Fox, R. O. 2001 Dynamics of scalar dissipation in isotropic turbulence: a numerical and modelling study. *J. Fluid Mech.* **433**, 29–60.

Vervisch, L. 2000 Using numerics to help the understanding of non-premixed turbulent flames. *Proc. Combust. Inst.* **28**, 11–24.

Veynante, D. & Vervisch, L. 2002 Turbulent combustion modeling. *Prog. Energy Combust. Sci.* **28**, 193–266.

Wall, C., Boersma, B.J. & Moin, P. 2000 An evaluation of the assumed beta probability density function sub-grid scale model for large eddy simulation of nonpremixed turbulent combustion with heat release. *Phys. Fluids* **12**, 2522–2529.

Wandel, A.P. & Klimenko, A.Y. 2005 Testing MMC mixing for Monte-Carlo PDF simulations. *Phys. Fluids* **17** (12), 128105.

Wang, G.-H., Barlow, R.S. & Clemens, N.T. 2007*a* Quantification of resolution and noise effects on thermal dissipation measurements in turbulent nonpremixed jet flames. *Proc. Combust. Inst.* **31**, 1525–1532.

Wang, G.-H., Karpetis, A.N. & Barlow, R.S. 2007*b* Dissipation length scales in turbulent nonpremixed jet flames. *Combust. Flame* **148**, 62–75.

Wang, L. & Peters, N. 2006 The length-scale distribution function of the distance between extremal points in passive scalar turbulence. *J. Fluid Mech.* **554**, 457–475.

Wang, L.-P., Chen, S. & Brasseur, J. G. 1999 Examination of hypotheses in the Kolmogorov refined turbulence theory through high-resolution simulations. Part 2. Passive scalar field. *J. Fluid Mech.* **400**, 163–197.

Warhaft, Z. 1980 The use of dual heat injection to infer scalar covariance decay in grid turbulence. *J. Fluid Mech.* **104**, 93–109.

Warhaft, Z. & Lumley, J.L. 1978 An experimental study of the decay of temperature fluctuations in grid generated turbulence. *J. Fluid Mech.* **88(4)**, 659–684.

Westbrook, C.K., Mizobuchi, Y., Poinsot, T., Smith, P.J. & Warnatz, J. 2005 Computational modeling. *Proc. Combust. Inst.* **30**, 125–157.

Williams, F.A. 1985 *Combustion Theory*, 2nd edn. Addison-Wesley Publishing Company.

Williams, F.A. 1994 The next 25 years of combustion theory. *Combust. Sci. Technol.* **98** (4), 361–366.

Yakhot, V. 2003 Pressure-velocity correlations and scaling exponents in turbulence. *J. Fluid Mech.* **495**, 135–143.

Yakhot, V. & Sreenivasan, K.R. 2005 Anomalous scaling of structure functions and dynamic constraints on turbulence simulations. *J. Stat. Phys.* **121** (5/6), 823–841.

Yeung, P.K., Donzis, D.A. & Sreenivasan, K.R. 2005 High-Reynolds-number simulation of turbulent mixing. *Phys. Fluids* **17**, 081703.

Yeung, P.K., Xu, S., Donzis, D.A. & Sreenivasan, K.R. 2004 Simulations of three-dimensional turbulent mixing for Schmidt numbers of the order 1000. *Flow Turb. Combust.* **72**, 333–347.